Development of 3D radiation measurement using IR imaging video bolometers for the study of radiation collapse in LHD

Ryuichi Sano

2015.03.04

Abstract

High density operation is preferred for a future fusion reactor since the fusion output is proportional to the density squared. Especially in magnetically confined plasmas, the energy confinement time increases with density. High density operation is also beneficial for the heat load reduction on plasma facing components called the divertor. At high density, the radiation loss is increased and the divertor heat load decreases. The maximum achievable density in a magnetically confined plasma is, however, limited by a density limit that has been expressed by semi empirical scaling, e.g. the Greenwald density limit for tokamaks and the Sudo limit for helical plasmas. The density limit of the tokamak is often accompanied by current disruption which can inflict much damage on the reactor and should be avoided. On the other hand, in helical plasmas, where large plasma current is not needed since the plasma is confined by the magnetic fields generated by external magnet coils, the radiation loss rapidly increases when the edge plasma density approaches the Sudo limit and finally, plasma collapses in a relatively benign manner due to the large radiation loss. Therefore, for the steady state operation of a fusion reactor, understanding of the physics mechanism of the density limit and the radiation collapse is quite important. In this study, the temporal evolution of the radiation collapse in helical plasmas of the Large Helical Device (LHD) is studied by using infrared (IR) imaging Video Bolometers (IRVB). Since the helical plasmas are characterized by a three dimensionally (3D) complicated shape, simple assumptions, such as e.g. axial symmetry, are not applicable and therefore a 3D approach is necessary. This thesis is composed of three parts, i.e., the development of the IRVB, the development of the 3D measurement and the investigation of the radiation collapse.

The IRVB has been developed for the measurement of 2D radiation profile patterns. The IRVB provides a distribution of the incident radiation on an IRVB foil. The IRVB has the advantage of having a large number of channels in a 2D array. This advantage is also beneficial for the 3D measurement. For the 3D measurement, in this study, three improvements have been applied to the IRVB. The first improvement is the selection of the material for the IRVB foil. The performance of the IRVB depends on the foil material. In this study the thermal characteristics of foil materials have been evaluated systematically. As the candidates of the foil material, Au, Pt, Ta, W were examined. These were illuminated by a He-Ne laser and their thermal characteristics were evaluated. Among these candidates Pt shows the best characteristics in the simultaneous achievement of high sensitivity and fast time response. According to the test results Pt has been selected. The second improvement is the foil calibration. The IRVB measurement as an absolute measurement requires a knowledge of the distribution on the foil of 3 foil parameters. However because two of the three parameters, foil thickness and emissivity, had not been evaluated, the IRVB measurement mainly served as a qualitative measurement. To evaluate the distribution of these two parameters, a new calibration technique has been developed. The calibration technique evaluates the effective thickness and effective emissivity distribution on the foil with a comparison between the 2D temperature which is measured from the laser illuminated foil, and the calculated 2D temperature using a Finite Element Method (FEM). The evaluated distribution of the effective foil thickness and the effective emissivity made possible for

the first time a quantitive measurement using an IRVB. The third improvement is the calculation of a projection matrix and the design of the fields of view of the IRVBs. The 3D measurement requires a 3D knowledge of the relation between each IRVB channels signal and 3D space. To obtain the relation, a calculation is made of the contribution of the radiation from each plasma volume element to the field of view of each IRVB channel. The fields of view of the IRVBs are designed to complete the coverage of the plasma using the calculated fields of view.

In this study two methods have been developed for the 3D radiation profile measurement. The first one is an algebraic reconstruction of the radiated power density from the IRVB images. For the algebraic reconstruction, Tikhonov regularization with the criterion of minimum Generalized Cross Validation (GCV) is employed as the reconstruction technique. The reconstruction has been numerically and experimentally examined. The simulated radiation profile using the EMC3-EIRENE code has been used as a numerical phantom in a numerical test of the reconstruction and has been reproduced with the reconstruction process. In reconstruction tests with experimental data which are taken before and after the plasma collapse, reconstruction results have responded to changes in the plasma condition. The first application to plasma measurements of a challenging 3D reconstruction has been performed. The reconstruction provides 3D radiation profiles as a quantitive 3D measurement. The time resolution of the 3D measurement is 20ms and the spatial resolution is roughly 5cm. Although a quantitative understanding of the reconstructed profile can be obtained by this algebraic reconstruction, a quantitative discussion of the reconstructed profiles relative to the changes in the plasma is still difficult. Therefore, another method of 3D model fitting has been developed to quantitatively investigate the physics mechanisms of the radiation collapse. Nine parameters have been selected to characterize the radiation profile, i.e. semi major and minor radius of radiation region, the center of radiation region, the width of radiation region, radiation intensity, the asymmetric factor for inboard-outboard asymmetry, the asymmetric factor for toroidal asymmetry, the local peaking factor and the specific size of the local peak. Using these nine parameters, the radiation is fitted to the model to minimize the mean square error between an experimental IRVB image and a synthetic IRVB image which is calculated from the model. The model fitting quantifies the temporal evolution of the radiation profile as the changes in the nine parameters. The time resolution of the model fitting is 40ms.

The developed 3D measurements have been applied to the study of the radiation collapse. Results of the model fitting show significant changes in the evolution of the radiation structure as model parameters change, during radiation collapse over a time period of 300 ms. The radiation region is minor radially localized before radiation collapse as the first step of the structure changes and the radiation region shrinks and radiation from the inboard side is significantly enhanced during radiation collapse. With changes in the radiation structure which are obtained by model fitting, it is possible to define the initiation of the radiation collapse, which has been difficult to define until now by using only the total radiation from the resistive bolometer.

To clarify the detail of the observed structure changes by the model fitting, algebraic reconstruction with Tikhonov regularization is also applied to the radiation measurement for the same plasma discharge. A result of the algebraic reconstruction shows that the inboard enhancement initiates at the vertically elongated cross section and then it is extended to the other poloidal cross sections along the Last Closed Flux Surface (LCFS). The inboard side of the vertically elongated cross section is at the nearest point to the wall.

The radiation structure of carbon II (426.7nm) and III (464.7nm) emission at the

timing of the shrinking and the inboard enhancement has also been investigated using a visible imaging spectrometer. The measurement result of the imaging spectrometer shows the carbon emission peak moves inward from the x-point and ergodic region towards the LCFS at that timing. It indicates that the shrinking and the inboard enhancement is related to the electron temperature. To clarify the relation, the electron temperature profile and the radiation profile which is obtained from the model fitting have been compared before and during the radiation collapse.

The comparison has provided a scenario of how the radiation structure changes during the radiation collapse as follows: When the electron temperature reduces, the radiation region starts to concentrate as the first step. As a second step, enhancement of the radiation from the inboard side and shrinking of the radiation region occur simultaneously. As a third step, the radiation region crosses the LCFS and the radiation power reaches a peak. Finally, the radiation region is concentrated at the center of the plasma. In this scenario, asymmetry in the radiation structure plays an important role. When the parallel transport is large enough, this kind of asymmetry cannot appear. To discuss the asymmetry, the mean free path at the plasma edge is investigated. At first, the mean free path decreases linearly with the electron density. This relation is changed before the initiation of the asymmetry. In this phase, the mean free path suddenly drops nonlinearly with increasing electron density. This behavior indicates that the asymmetry during radiation collapse is related to the reduction in parallel transport.

In this thesis, the IRVB measurement has become a quantitive measurement and is related to the 3D plasma space using a projection matrix calculation, through three improvements. Two methods for quantifying the 3D radiation structure have been developed with the improved IRVB measurement. In addition to a 3 dimensional tomography method, a nine parameter model quantifies the characteristics of the changes in the radiation structure during radiation collapse and algebraic reconstruction shows radiation collapse is initiated at the inboard side of the vertical cross section. Several events during the radiation collapse evolution have been observed for the first time from the model parameters and algebraic reconstructed profiles. By relating these events, a scenario for the radiation collapse has been obtained. That is the main result of this thesis. The developed IRVB improvement and 3D measurement techniques will also be applicable in the future to enhancing the understanding of radiation collapse and other radiation phenomena.

Contents

1 Introduction

1.1 Energy

1.1.1 Primary energy

The population of the world has doubled in the last 50 years [1]. Because the population and energy consumption are strongly correlated, an increase in the population will result in an increase in the energy consumption by simple logic. The energy consumption is also correlated with the ratio of the population between developing countries and advanced countries. In several advanced countries, the energy consumption per population is more than 10 times larger than that of developing countries[2] [3]. This indicates that the people who can be free to use energy, are just the people who live in advanced countries. Currently, the population of the advanced countries accounts for only about 17 % of the world [4] [5]. However, the predictable economic advancement in the developing countries will provide a significant growth in energy consumption. In the aspect of the energy production, the total primary energy supply has a high proportion of fossil fuels such as oil. The amount of deposits of fossil fuels is not close to being exhausted. However, when underground resources are exhausted at producing locations which are easy to handle, the cost of recovering underground resources becomes enlarged as the amount of deposits becomes smaller, because the recovery is usually performed in increasing order of difficulty. Additionaly, the cost of the transportation of resources or transmission of electrical energy are also becomes enlarged under the same situation, because transportation from distant places or foreign countries is needed in this situation. Therefore, the cost of power generation and transmission from underground resources becomes larger the more it is used. The same problem also applies to renewable energy, such as a solar power generation. renewable energy has a low power generation per area. Therefore, when all of the suitable place for a renewable energy plant are occupied, the plant will have to be placed in other places with extra costs. Current primary energies have the above problem without any advancement of technology. To handle the expected increase in the demand for energy in the future, a resource of energy which is not globally localized to specific regions and has a high power generation per area is preferred as a future energy resource.

1.1.2 Fusion

A candidate for the future energy resource is plasma fusion. Plasma fusion provides the high energy particles with a fusion process between two ionized light atoms. Several combinations of atoms are considered as fuels of the fusion process. A combination of the atoms which is attracting the most attention from researchers is deuterium and tritium. The process is described as

$$ {}^{2}_{1}D + {}^{3}_{1}T \longrightarrow {}^{4}_{2}He(3.5MeV) + n(14.1MeV). \tag{1-1-1} $$

In this reaction, the energy generated by fusion is distributed to the produced neutron and He atoms by the fraction of their weight. The high energy neutron is collected as a heat source to generate electricity. Because deuterium and tritium can be derived

from marine water, the fuel of the fusion is not localized to a specific area. The fusion process also does not require a large area. Therefore fusion potentially has large power generation from a small area. Therefore, in principle, a plasma fusion reactor is a good solution for handling future energy demands.

In a plasma fusion reactor, the fusion process takes place in a magnetically confined plasma. The fusion process is not available in ordinary conditions such as at room temperature, due to the mutual repulsion of the nuclei of atoms. Therefore a large number of atoms are confined in a small space by a magnetic field, and heated up by several energy sources to make an extreme condition which makes the fusion process available. For the achievement of a confined plasma with extreme conditions, many plasma confinement devices have been developed and produced usefull results.

The confinement of plasma in a small space is achieved by the magnetic field. Charged particles such as ions, have a characteristic to move along a magnetic field line. With this characteristics and closed field lines, devices for magnetic confinement confine the plasma. There are two prominent types of the magnetic confinement devices. The two types of devices have different methods of generating a magnetic field and different limitations on the increase of the plasma density which is favorable to fusion.

Tokamaks

Tokamak type devices are the mainstream of magnetic confinement devices. Tokamak devices confine the plasma using a magnetic field produced by the currents through poloidal coils and the plasma. Tokamak devices have a simple axially symmetric structure. These currents make twisted magnetic field lines which are required to confine the plasma without the instability of electric and magnetic fields. The main devices among tokamaks are JET, JT-60, T-3 and TFTR. Tokamak devices have an advantage in the capability of the enhancement of the ion temperature and have shown many significant results, such as observed ion temperature of 45keV in JT-60 [6]. Tokamak devices employ confine the plasmas using plasma current, which is usually driven by a toroidal electric field induced by ramping up the current through a center solenoid coil. Therefore, the long production of the plasma current only by induction is difficult. However, other mechanisms of plasma current drive, created by a pressure gradient (called bootstrap current), injection of neutral beams or electromagnetic waves, have been found to be considerable to the extent making a long burning reactor design possible. Because the current drive efficiency in the plasma is decreased with high plasma density, there is a problem that the efficiency of tokamak devices becomes lower of high plasma density.

Helical devices

Helical type devices have a large difference with tokamak devices in the method of generating the twisted magnetic field. Helical devices have twisted helical coils. The helical coils directly makes the twisted magnetic field. Therefore, helical devices do not have the limitation on the steady state operation due to the field generation. LHD in Japan is the main helical device. Because helical devices do not require plasma current for confinement, the plasma density in helical devices does not have a limitation by the plasma current. The plasma density is mainly limited by the density limit with radiation collapse which is described in Section 1.2.2.

1.2 Radiation

When the plasma is well confined by magnetic fields, radiation is one of major paths for energy loss from the plasma. Therefore, the total radiation power which is estimated from the measured data of the local radiation measurement, provides important information for studies of the power balance of the plasma between input power and power loss.

The local radiation power from an impurity is proportional to the electron density, the density of the impurity [7] and the cooling rate of the impurity which is a parameter depending on the electron temperature. The radiation measurement also provides information on the impurity behavior. This information is significantly useful for studies on impurity transport in the plasma. Additionally, the radiation is related to several behaviors and phenomena of fusion plasmas, such as radiation collapse. Radiation measurement is essential to understand these phenomena.

1.2.1 Radiation sources from plasma

Bremsstrahlung

When a charged particle is accelerated in a Coulomb field, radiation is emitted from the charged particle. This kind of radiation can be emitted from plasmas in fusion devices. For a full understanding of this process, quantum treatment is required. However, it can be treated classically with Gaunt factors which are corrections between classical results and quantum results.

The emission of power from a mono energetic electron accelerated by impact with an ion Coulomb field can be given as

$$\frac{dW(b)}{d\omega} = \begin{cases} = \frac{8Z^2e^6}{3\pi c^3 m^2 \nu^2 b^2} & (b << v/\omega) \\ = 0 & (b >> v/\omega) \end{cases} , \tag{1-2-1}$$

where b is the impact parameter which is defined as the length between the ion and the path of the electron, Z is the charge of the ion, e is the elementary charge, c is the light speed, m is the mass of thye electron and ν is the typical frequency. As an extension, the total emission power per unit time, unit volume and unit frequency range is given with the electron density, n_e, and the ion density, n_i, as

$$\frac{dW}{d\omega dV dt} = n_e n_i 2\pi\nu \int_{b_m in}^{\infty} \frac{dW(b)}{d\omega} b db. \tag{1-2-2}$$

Line radiation

In fusion plasma, many ions, atoms, molecules and electrons populate the whole space, these particles can be excited by interactions between these. When an excited ion or atom is deexcited, a photon is emitted which has the specific energy according to the energy gap between the excitation state and the end of the deexcitation process. The emission is called line radiation. The emission process and the excitation process are held in equilibrium for each excitation state in steady state plasma. The line radiation has a specific energy which depends on the species of the radiator and its charge state. Therefore the line radiation can be used for the identification of impurity species and their behavior.

In the LHD case, the line radiation from impurities is the strongest radiation source. Without any impurity injection, carbon and oxygen are the major radiators

from the plasma. Especially, because carbon is produced from carbon divertor plates which are striked with the plasma and easily enhanced with plasma discharges, carbon is important to control the plasma.

1.2.2 Radiative phenomena and operation

Plasma detachment

As a protection for components of a magnetic confinement device against the incident heat flux from the plasma, a divertor plate is employed at points striked by the plasma. The divertor plate is made from materials which have high heat resistance, such as carbon. However, as the plasma energy become high, the heat flux is enhanced. In the future, there are concerns that the heat flux will become unmanageably large with any materials. Therefore, reducing the heat flux is required to achieve future fusion devices.

An approach for the reduction is plasma detachment. The concept of the plasma detachment is to diffuse/dissipate the energy of the heat flux before approaching divertor plate. The process is achieved by several procedures.

Radiation collapse

The radiation collapse is a disruptive phenomena in the plasma. When radiation collapse occurs in a plasma, radiation power from the plasma is significantly increased and then the plasma is terminated. In helical devices, the density of the plasma is limited by the radiation collapse. When the electron density approaches the "Sudo density limit" $n_e^s = (PB/a^2R)^{0.5}$, the plasma is terminated by radiation collapse. Therefore, radiation collapse which plays a role as the proximate cause of the termination should be understood to achieve high density operation in helical devices.

1.2.3 Requirement for radiation measurement

These radiation phenomena and operation are important to achieve fusion devices. The radiation power from impurities in plasmas depends on the electron temperature and their density. Carbon is a major radiator of fusion devices which have carbon components such as LHD. The carbon emission mainly emanates from regions which have lower electron temperature around $100eV$, such as the ergodic edge region. The ergodic edge region is completely three dimensional. Therefore a good understanding of these radiation phenomena requires 3D measurements.

1.3 Tomography

1.3.1 Tomography

Tomography, which is the image reconstruction from projections, is a major field of the inverse problem study. The background of the tomography is Radon theory, which shows that the exact reconstruction is possible from omni-directional projections. Standard tomography is performed on the basis of the analytical inversion of the integral transform [8] [9]. As the field of computer science becomes larger, the tomography has been rapidly developed and extended as the technology of Computed Tomography (CT) with discretized numerical techniques. The advancement of the computer has made complicated techniques available such as matrix decompositions and fast iterative procedures of large size. Nowadays, tomography is an essential tool for an observation when

direct measurement is impossible. Tomography is widely used not only in the medical field but also in various scientific measurements.

1.3.2 Tomography in plasma studies

Around the 1980s, tomography started to be applied for the measurement of plasma properties in fusion devices. A lot of tomography measurements including the research with 2D imaging using neutron detector arrays in JET, have been perfomed and provided useful results [10]. Generally, the tomography measurement in fusion devices does not have complete angle measurement, due to strong limitations on the installation of measurement instruments. Therefore the tomography measurement in fusion devices easily is ill-conditioned. A large segment of tomography measurements in fusion devices is also performed as a passive measurement of the emission from plasma, unlike the active measurements such as X-ray transmission CT and Magnetic Resonance imaging (MRI).

1.4 Purpose of study

For future fusion devices, high density operation is required. However the plasma density is limited by radiation collapse in helical devices. Understanding radiation collapse is important for the achievement of high density operation in fusion devices. The purpose of this study is the development of a 3D measurement for the evolution of the radiation structure during radiation collapse such as how the radiation evolves and where the evolution is initiated.

Bibliography

[1] UN, World Population Prospects: The 2012 Revision

[2] International Energy Agency ,Kew World Energy Statistics 2014

[3] International Energy Agency ,World Energy Outlook 2013

[4] Agency for Natural Resources and Energy ,White Paper of Energy 2014 (in Japanese)

[5] Statistics Japan ,Statistics Report in the World 2014 (in Japanese)

[6] H. Kishimoto et al., Nucl. Fusion 45, 986(2005)

[7] B. J. Peterson et al., Nucl. Fusion 41, 519(2001)

[8] S. R. Deans, "The Radon Transform and Some of Its Applications" (2007)(Dover, New York, 2007)

[9] A. C. Kak and M. Slaney, Principles of Computerized Tomographic Imaging (IEEE Press, New York, 1987)

[10] L. C. Ingesson et al., Rev. Sci. Instrum. 75, 3696 (2004).

2 IRVB measurement

2.1 Radiation measurement

For a measurement of the radiation from the plasma, there are several candidates of measurement instruments. In this thesis, candidates should be chosen with a consideration of their characteristics and the target of the measurement.

2.1.1 Measurement instrument

2.1.2 Resistive bolometer

The bolometer is a kind of calorimeter. A resistive bolometer detects the temperature rise on the metal absorber as a change of resistance of a meander resistor which is placed behind of the absorber. The incident radiation power on the absorber is estimated from the change of resistance. The change of the resistance is obtained from the current on a Wheatstone bridge circuit.

When the radiation power irradiates the absorber, the temperature rise from the background temperature is given as

$$\frac{dT}{dt} = \frac{P_{RB}}{C\rho d S_{RB}} - \frac{T}{\tau_c}, \tag{2-1-1}$$

where T is the temperature rise from the background temperature on the absorber, d is the thickness of the absorber, P_{RB} is the total incident radiation power, C is a specific heat capacity, ρ is the density, S_{RB} is the area of the absorber and τ_c is the time constant of temperature rise and decay on the absorber. with the Equation 2-1-1, the power density of the incident radiation is given as

$$\frac{P_{RB}}{S_{RB}} = C\rho d S_b(\frac{dT}{dt} + \frac{T}{\tau_c}). \tag{2-1-2}$$

The power density can be calculated using the temperature change on the absorber. The sensitivity of the resistive bolometer depends on $C\rho d$. The C and ρ depends on the material of the absorber. When the absorber material is fixed, small d provides high sensitivity. However, the upper limit of the measurement range in terms of the wave length of radiation is determined by ρd. For measurement of plasma radiation which has X ray emission, d should be determined with a consideration of the measurement range. Current resistive bolometers for the radiation measurement from high temperature plasma use a gold absorber with a thickness of several micro meter to measure a large part of the radiation which includes X-rays.

The incident power on the resistive bolometer is determined as a line integrated value of the emission from the plasma along a sight line. The resistive bolometer is mainly used for the total radiation estimation from the line integrated power. The resistive bolometer is often used with a 1-D array of detectors. The measured data from multiple arrays of resistive bolometers has also been used in two dimensional tomography measurement[1] [2]. However, because several wires with vacuum feedthroughs are required for every channel, a huge channel array is difficult to realize.

In LHD, four resistive bolometer arrays have been installed on the outboard side of 6.5-L diagnostics port (20 channels), the inboard side of the 6.5-L diagnostics port (12 channels), the 8-O diagnostics port (16ch) and the 3-O diagnostics port (4 channels). One channel of these resistive bolometers is composed of an open detector and a blinded detector which is used as a reference channel as shown in Figure 2.2. Absorbers for resistive bolometers are made from $4\mu m$ gold foil. The maximum time resolution is 10ms. The sensitivity is 10 $\mu W/cm^2$.

2.1.3 AXUVD

The absolute Extreme Ultra Violet photodiode (AXUVD) is a measurement instrument using photo diodes. When photodiode are illuminated by radiation, the photodiode generates the charge per second, Q,. The charge, Q, is given as [3]

$$Q = QE \times N_{photons(\lambda)}, \tag{2-1-3}$$

where QE is the conversion efficiency of the photodiode with a particular wavelength and $N_{photons(\lambda)}$ is the number of the incident photons per second with the particular wavelength λ. With the charge, Q, the incident radiation power, P, as a function of the wave length is given as [3]

$$P(\lambda) = \frac{Q \times E_p}{QE}, \tag{2-1-4}$$

where E_p is the energy of a photon with the wavelength, λ, in electron volts. The AXUVD also requires 1-2 wires per channels. Therefore the AXUVD is not suitable for a huge array.

In LHD, AXUVD are used to measure soft X-ray (SX) and ultra violet (AXUVD) radiation from impurity ions and MHD activities. Seven 20ch AXUVD arrays are installed in the 3.5-U (SX $\times$2 and AXUV $\times$1), 6.5-U (SX $\times$2) and 8-O (SX $\times$2) diagnostic ports.

2.1.4 IR imaging Video Bolometer (IRVB)

An IR imaging video bolometer[4] is a measurement instruments for the radiation from plasmas with the pinhole projection principle. The IRVB consists of an aperture, thin metal foil and IR camera. When the radiation irradiates the IRVB foil through the aperture, the 2D temperature distribution is formed on the foil. The 2D temperature distribution is measured by the IR camera. The distribution of incident radiation power is calculated from the measured 2D teperature distribution. It is useful for the measurement of the radiation intensity and spatial distribution. The IRVB has the advantages of the large number of channels and simple components in the vacuum vessel. The advantage in the number of channels is suitable for the 3D measurement in this thesis. Therefore, the IRVB is chosen as the main measurement instrument in this thesis. The details of the IRVB are described in the next section.

2.2 IRVB measurement

The concept of the IRVB was proposed by B. J. Peterson [5]. The IRVB had been manufactured and installed in LHD since the 3rd experimental campaign of LHD(1999-2000). The number of installed IRVBs in fusion devices has been gradually increased. IRVBs have been used in LHD[6], JT-60U[7] and KSTAR with the thin bolometer foil which is made from Au as a screen of the pin-hole projection.

2.2.1 Heat equation on IRVB foil

When the plasma radiation is incident on the foil through the aperture, a 2D temperature distribution is formed on the foil and measured by an IR camera which is placed out of the vacuum vessels. The radiation power which is absorbed by the foil is given in terms of the temperature distribution on the foil by the following heat diffusion equation.

$$-\Omega_{rad} + \Omega_{bb} + \frac{1}{\kappa}\frac{dT}{dt} = \frac{\partial^2 T}{\partial x^2} + \frac{\partial^2 T}{\partial y^2} \tag{2-2-1}$$

$$\Omega_{rad} = \frac{P_{foil}}{kt_f}, \tag{2-2-2}$$

$$\Omega_{bb} = \frac{\epsilon\sigma_{SB}(T^4 - T_0^4)}{kt_f} \tag{2-2-3}$$

where T is the two dimensional temperature distribution on the foil, t_f is the foil thickness, k is the thermal conductivity, σ_{SB} is the Stefan-Boltzmann constant, ϵ is the emissivity of the foil, T_0 is the back ground temperature and κ is the thermal diffusivity of the foil. The incident radiation power, P_{foil}, on the foil is obtained by solving Equation 2-2-1 as an output of the IRVB measurement.

2.2.2 Characteristics

As for the mechanical characteristics of the IRVBs, the in-vessel and out-vessel components of the IRVB are not connected with any electrical wires. These components are connected with just the IR camera measurement of the foil. This characteristic simplifies the system and components for IRVBs. The performance of the IRVB, such as time resolution, strongly depends on the performance of the IR camera. Current typical IRVBs show time resolutions of 20-40ms.

As for the characteristics on the output of IRVBs, IRVBs provide the integrated radiation intensity of a large number of channels as a radiation image and the number of channels can be changed after the measurement within the resolution of the heat calculation. The integration is performed within the sight of each channel which has a pyramid beam shape. The characteristics provide large amounts of information on the plasma radiation, meanwhile, detailed considerations for the radiation structure require the accurate evaluation of the integration path that is with in the sight of each channel.

2.2.3 Previous IRVB studies in LHD

When solving Equation 2-2-1 to obtain the power distribution of the plasma radiation on the foil, the foil thickness t_f, emissivity ϵ, the thermal diffusivity, κ, and the thermal conductivity, k, on the foil are required. However these parameters are not uniform across the foil. So, the evaluations of these parameter's distributions are essential to calibrate the absorbed power from the temperature distribution on the foil. Therefore, evaluation techniques for foil parameters distribution is required for a quantitive IRVB measurement. In early IRVB studies IRVB foils were assumed as uniform and typical foil parameters are used in Equation 2-2-1. This assumption provides error in the measurement result. Therefore IRVB measurement was mainly used as a qualitative measurement. As a qualitative measurement, IRVBs are used for qualitative studies of radiation phenomena. For the study of radiation collapse, IRVB measurement had shown an asymmetric collapse which started from inboard side of the plasma[9].

In recent studies, the technique for evaluation on the distributions of several foil parameters has been developed. The distribution of the thermal diffusivity has been evaluated with LED illumination [10] and laser irradiation [11]. However, two parameters, foil thickness and emissivity, have not been evaluated for quantitive measurement. The evaluation of the two parameters is required to acheave a quantitive measurement.

2.2.4 Requirement for IRVB improvement

The measurement range of the photon energy for the IRVB is determined by the ability of the IRVB to stop high energy photons. An improvement of the ability which is determined by the foil material and thickness is required for future use on next-generation fusion devices such as ITER . An improvement on the performance of the IRVB such as sensitivity is also required for the 3D measurement which is described in a later section.

The Eq. 2-2-1 has four physical parameters of the foil. These parameters affect the performance of the IRVB. The thermal diffusivity, κ, and thermal conductivity, k, are determined with respect to the material of the foil as the thermal characteristics. The two parameters significantly effect the sensitivity and the time resolution of IRVBs. Therefore, the evaluation and selection of the foil material is very important for IRVB measurement. A comparison between thin Au and Pt foils has been made [12]. The study indicates that the Pt foil has higher sensitivity than the Au foil. However, other foil materials and thickness have not been evaluated systematically. It is necessary to evaluate and select the best foil material.

The 3D radiation measurement requires absolute values of the incident radiation power on IRVB foils, in other words, quantitive IRVB measruements are necessary. To acheve the quantitive measurement, the evaluation of the distribution of the un-evaluated foil parameters, the foil thickness t_f and emissivity ϵ, are required.

2.3 Flow of study

The purpose of this thesis is the development of 3D measurement tools for the evolution of the radiation structure during radiation collapse. Because the evolution is expected as a three dimensional change, measurement data which has the three dimensional information of radiation is required. The IRVB which can obtain the information from a three dimensional radiation structure as a two dimensional projection image, is employed as the main measurement instrument. To obtain three dimensional information from a two dimensional projection image, accurate understanding of the relation of these is strongly required. Therefore, in this thesis, improvements of the IRVB measurement and calculation of fields of view for IRVBs have been carried out to clarify the accurate relation between the three dimensional radiation structure and a two dimensional projection image. With the relation, two methods for three dimensional analysis, “3D algebraic inversion” and “3D function model fitting”, have been developed and applied for investigation of radiation collapse.

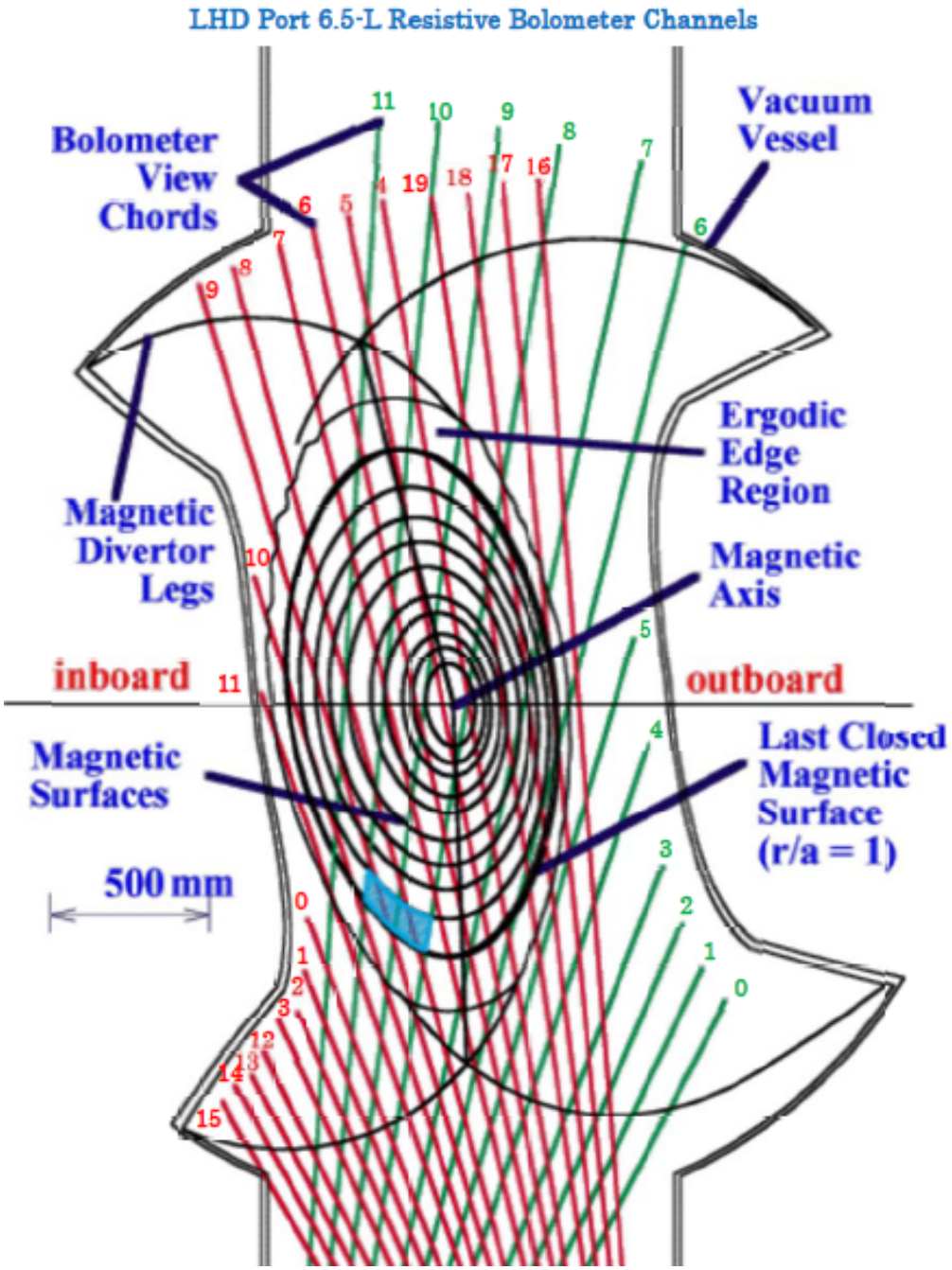

Figure 2.1: Sight lines for resistive bolometers on 6.5L diagnostics port [8]

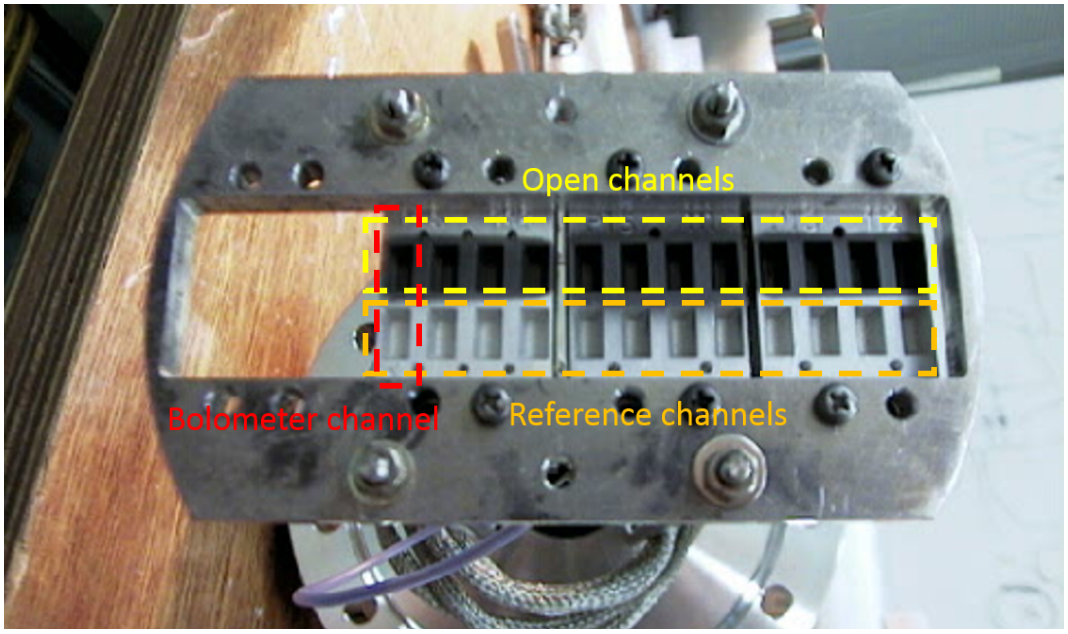

Figure 2.2: Picture of the resistive bolemeter array (photo by B. J. Peterson)

Bibliography

[1] A. W. Leonard et al., Rev. Sci. Instrum. 66, 1201(1995).

[2] S. Konoshima, et al., Plasma Phys. Control. Fusion 43, 7, 959(2001)

[3] International Radiation Detectors, 2527 West 247th Street Unit C, Torrance, CA 9055243, www.ird-inc.com

[4] B. J. Peterson et al., Rev. Sci. Instrum 74, 2040(2003)

[5] B. J. Peterson et al. Rev. Sci. Instrum 71, 3696(2000)

[6] B. J. Peterson et al., Rev. Sci. Instrum 74, 2040(2003)

[7] B. J. Peterson et al., Fusion Sci. Technol. 58, 412(2010)

[8] B. J. Peterson et al., Plasma Phys. Control. Fusion 45, 1167(2003)

[9] N. Ashikawa et al. Plasma Fusion. Res. 4, 437(2001)

[10] E. A. Drapiko et al. Rev. Sci. Instrum 81, 1873(2010)

[11] S.N. Pandya et al., Rev. Sci. Instrum 85, 054902 (2014).

[12] B.J. Peterson et al., Plasma Fusion Res. 5, 35 (2010).

3 Hardware installation and improvement

In this thesis, IR imaging video bolometers (IRVBs) have been used for radiation measurement. The IRVBs have been installed and improved as described in the following chapter.

3.1 IRVB installation in LHD

3.1.1 LHD

The Large Helical Device (LHD) located at the National Institute for Fusion Science (NIFS) is the largest helical device in the world. The LHD has been constructed to demonstrate the high performance of a helical plasma in a reactor relevant plasma regime.

For LHD, a pair of super conducting helical coils with the numbers of the toroidal and poloidal period $l/m = 2/10$ is employed to generate the magnetic field. The major and minor radii of the helical coils are 3.9m and 0.975m, respectively. The major and minor radii of the plasma are 3.9m and 0.5-0.65m, respectively. The maximum magnetic field produced by the helical coils is about 3T at R = 3.9m. As heating systems, 8 systems of Electron Cyclotron Heating (ECH) with a total heating capability of 2.5MW, 3 systems of Ion Cyclotron Resonance Heating (ICRH) with total heating capability 3 MW and 5 systems of Neutral Beam Injection (NBI) with a total heating capability of 23MW are installed in LHD. These heating systems are used in combination for each experiment[1].

Structure of LHD

The LHD has 10 toroidal sections with each having 36 toroidal degrees, and each section has several diagnostics ports for measurement instruments. All toroidal sections have upper (U), outer(O) and lower (L) diagnostics port. Additionally, the 1st, 6th, 7th and 10th sections have a tangential (T) port. Installation locations for measurement instruments are confined to the inside of these diagnostics ports.

3.1.2 IRVB installation

For previous IRVB measurements, three IRVBs had been installed at the 6-T port, the 6.5-U port and the 10-O port on the LHD. To enhance the measurement direction of the IRVB measurement and to increase the number of the IRVB channels for the development of a 3D tomographic measurement, an IRVB has been installed at the 6.5-L port as described below.

IR camera and IRVB foil for 6.5-L IRVB

The performance of the IRVB depends on the performance of the IR camera and the thermal characteristics of the IRVB foil. For the 6.5-L IRVB, a “SC655” IR camera (microbolometer type, manufactured by FLIR, measurement range on wavelength 7.5-13.5 μm, 50 frames per second with 640×480 pixels and 100 frames per second with

640×240). is used as an IR camera with a ZnSe IR window (manufactured by Fuji I-tec). The IRVB foil is manufactured from a $4\mu m$ Pt foil. The horizontal dimension of the foil is $150mm \times 110mm$. The foil has been constructed with a procedure described in Section 3.1.3. The magnetic field of the lower diagnostics port is expected to be higher than that of the outer and tangential port due to nearby superconducting coils. The "SC655" has a higher resistance to the magnetic field than IR cameras that have an Indium Antimonide detector type, because IR cameras that have the microbolometer type do not require any extra mechanical cooling. Therefore, the "SC655" IR camera has been chosen as the IR camera for 6.5-L IRVB.

Magnetic shielding box

The "SC655" IR camera has a higher resistance to the magnetic field than IR cameras which have mechanical cooling. However the uncovered "SC655" also can not be operated in an environment which has a high magnetic field. A magnetic shielding box has been employed to reduce the load of the magnetic field on the IR camera.

The shielding box has been made from electromagnetic soft iron. The external size of the shielding box is $200 \times 200 \times 470$.The shielding box has a double wall. The thickness of the inside-wall is 10mm and outside-wall is 6mm. For IRVB measurement, all components of the IR camera are confined in the shielding box.

In-vessel components

The IRVB foil which plays the role of the screen of the pin-hole projection and an aperture plate which plays the role of the pin-hole has been assembled in a metal pipe as in-vessel components. The aperture plate has been designed in later section 4.2.2. The metal pipe has been installed on a flange in the 6.5-L diagnostics port.

Setting for 6.5-L IRVB

The shielding box has been placed on a supporting rack which is fixed to the floor. The IR camera see the IRVB foil from inside of the shielding box with a gold mirror ($\phi 100mm$). Figure 3.10 shows a drawing of the setting of the 6.5-L IRVB.

Control system for 6.5-L IRVB

For the IRVB measurement, the IRVB should be remotely controlled from the control room of the LHD. The obtained data should also be transferred to the control room. Figure 3.12 shows the control system for the 6.5-L IRVB. The shielding box which confines the IR camera components is placed at the 6.5-L diagnostic port. The obtained signal is transferred by optical fiber with electric-optical conversion by a media link convertor which is also confined in the shielding box. Optical fibers are connected to an optical fiber assembly which is placed near the 6-T diagnostic port and has a direct connection to the control room. The transferred optical signal is converted to the electric signal with a media link convertor and introduced to a PC for control in the control room.

3.1.3 Construction of IRVB foil

An IRVB needs a thin metal foil as a screen of the pin-hole projection. IRVB foils are constructed by the following process. The IRVB foil is made from a thin Pt foil which is chosen by a selection described in Section 3.2. Regarding the 6.5-L IRVB, the dimensions of the Pt foil are $150mm \times 110mm \times 0.0025mm$. The foil is sandwiched by copper frames

for housing, which are shown in Figure 3.14. The thickness of each copper frame is 2mm, therefore the heat capacity of copper frame is much larger than that of the foil. The copper frames play the role as a heat sink to provide the boundary condition that the frame temperature is constant. The foil and copper frames are blackend to approximate their surface to an ideal blackbody using the carbon spray "Aerodag G" (manufactured by Acheson) The spray contains fine carbon particles and the isopropyl alcohol as a carrier. The blackened foil is illuminated using a 500W light to evaporate the isopropyl alcohol. This foil is used as an IRVB foil.

3.1.4 Foil calibration

For the IRVB measurement, data of the foil parameters are required. The foil parameters are not same as the typical values of the foil material, because of the forming processes of the thin foil reduces the thermal conductivity and the blackening processes provides high emissivity and less thermal conductivity. When typical values are used for the foil parameters, the resulting measurement can have a large error.

IRVB foils also have non-uniformity of their parameters on the foil. This non-uniformity is also introduced in the construction process, such as blackening by carbon spray introducing irregularity on thickness of the deposited carbon, stretching in the forming process of the foil leads to non-uniformity of the thickness and small holes. The non-uniformity results in errors in the results of IRVB measurement with miss-evaluation on the terms of Equation 2-2-1 as described on Section 2.2.4. The non-uniformity should be evaluated as effective foil parameters to avoid the miss-evaluation. In previous research, the uniformity is evaluated just for the foil thickness. However, the evaluation technique is a rough estimation with an assumption that the temperature on a foil pixel foil is not affected by the thickness on the adjacent pixel. The emissivity, which plays an important role in the loss of heat from a thin foil, is also not evaluated in the evaluation. This assumption and the lack of the evaluation provide a possibility of error in the IRVB measurement. To solve these non-typical and non-uniformity parameters problems, a new evaluation technique for the non-uniformity of the foil parameters is developed and applied on the foil as described later in Section 3.3, as a foil calibration which calibrates between the temperature distribution and the incident radiation on the foil.

3.1.5 IR camera and window calibration

In IRVB measurement, the incident radiation power on the foil is calculated from the temperature distribution measured by an IR camera. When an object is heated up, the object radiates the radiation which power is depending on the temperature, T, and the emissivity of the object. When the object has the emissivity which is close enough to 1, i.e. the object is a black body, the spectral radiant power, $E_{b\lambda}$, from object is based on the following Plancks-law Equation [2] [3].

$$E_{b\lambda} = \frac{2\pi h c_0^2}{\lambda^5(\exp(\frac{hc_0}{\lambda kT}) - 1)}, \tag{3-1-1}$$

where $h(= 6.6256 \times 10^{-34} J \cdots)$ is the Planck constant, k$(= 1.3805 \times 10^{-23} J/K)$ is the Boltzmann constant, and $c_0(2.998 \times 10^8 m/s)$ is the light speed in vacuum. The spectral radiant power, $E_{b\lambda}$ is the radiation power from a black body as a function of wavelength. The total radiation power from the object is obtained with following Stefan-Boltzmann

law Equation.

$$P_{obj} = \int_0^\infty E_{b\lambda} d\lambda = \sigma T^4. \tag{3-1-2}$$

The $\sigma(= 5.67 \times 10^8 W/(m^2 \cdot K))$ is the Stefan-Boltzmann constant. The IR camera converts the obtained total radiation power from the object into a digital level which is in arbitrary units. When the temperature of the object is calculated from the digital level, a transformation coefficient to the temperature from digital level is required. The obtained radiation by the IR camera changes with the distance from the object and the attenuation ratio of the path between the object and the IR camera as

$$P_{cam} = \frac{P_{obj} DA}{4\pi l^2},, \tag{3-1-3}$$

where P_{cam} is the obtained radiation by the IR camera, D is the attenuation ratio which is integrated over the whole path of the IR radiation, A is the area of the lens of the IR camera. The transformation coefficient depends on the distance from the object and IR camera and the emissivity of the object and the attenuation ratio of the path. The IR camera calibration is carried out to obtain the transformation coefficient with the same measurement setting with the actual IRVB measurement.

In the IR camera calibration, the temperature of a blackbody calibration source [M345 Blackbody calibration source, manufactured by MICRON] which is shown in Figure 3.16 is measured by an IR camera while changing the temperature considering the temperature range of the actual IRVB measurement. The surface of the calibration source can be assumed to have the same condition as the IRVB foil which surface is blacken by carbon. The distance between the IR camera and the calibration source is fixed at the same distance with the actual measurement and an IR window is placed in front of the IR camera. Figure 3.17 shows an IR calibration result for the 6.5-L IRVB with an IR camera (SC655 IR camera, manufactured by FLIR) and ZnSe IR window(IR window, manufactured by Fuji-Ideck). The distance between the IR camera and the IR window is 295mm and between the IR window and the calibration source is 1,689mm. The digital level of the plots, I, in Figure 3.17 are curve-fitted with the following quadratic function and fitting coefficients a_0, a_1 and a_2.

$$I = a_0 T^2 + a_1 T + a_2 \tag{3-1-4}$$

In this case, the obtained coefficients are $a_0 = 0.7812, a_0 = -320.88$ and $a_2 = 40924$. The transform function into temperature from the digital level is obtained with a quadratic formula using these fitting coefficients as

$$T = \frac{-a_1 + \sqrt{a_1^2 - 4a_0 a_2}}{2a_0}. \tag{3-1-5}$$

The obtained transform function is used in the actual IRVB measurement.

3.1.6 Incident power analysis from IR camera image

In IRVB measurement, the power density of incident radiation on the IRVB foil is calculated from a sequence of IR camera images which have a digital level as their unit. This calculation has several following processes, and these processes are carried out with the foil part in the IR camera image by the software IDL. At first, a noise filtering process is applied on the digital level of every IR camera pixel. A discrete Fourier-transform

is performed on the time evolution of the digital level at a camera pixel using an FFT routine as

$$G(k) = \sum_{i=0}^{N-1} I(i) exp(-j\frac{2\pi ki}{N}) \quad (0 \leqq k \leqq N-1), \tag{3-1-6}$$

where G(k) is Fourier spectrum, I(i) is digital level on the pixel, i is the index of the frame number, k is the frequency, N is the total number of samples and j is an imaginary number. To remove the noise spectrum from the Fourier spectrum, the following Butterworth filter of 5th order is applied with the Nyquist frequency, $f_n = 50Hz$. The kernel of the filter, K(k) and the filtered digital level are obtained as

$$K(k) = 1/(1 + (k/50)^10), \tag{3-1-7}$$

$$I_f(i) = \frac{1}{N} \sum_{k=0}^{N-1} K(k) G(k) exp(j\frac{2\pi ki}{N}), \tag{3-1-8}$$

Secondly, the filtered digital levels, $I_f(i)$, with the IR camera pixel are resampled with IRVB pixels which have the dimensions 5mm × 5mm (for 6.5-U and 6.5-L IRVB) or 2.5mm × 2.5mm square (for 6-T and 10-O IRVB). For the 6.5-L IRVB, the digital level image with camera pixels (200×100 camera pixels) is converted into a digital level image with IRVB pixels (15×11IRVB pixels). Thirdly, the image of the filtered digital level with IRVB pixel is converted into an image of the 2D temperature distribution using Equation 3-1-5 and the transform coefficients described in Section 3.1.5. Finally, the power density of the incident radiation on the foil is calculated from the 2D temperature distribution. This calculation is based on Equation 2-2-1. Equation 2-2-1 can be written with a discretization process and Crank-Nicolson method as

$$\begin{aligned} P_{foil(x,y,t)} = & - kt_f(\frac{T_{(x-1,y,t)} - 2T_{(x,y,t)} + T_{(x+1,y,t)}}{2\Delta x} + \frac{T_{(x,y-1,t)} - 2T_{(x,y,t)} + T_{(x,y+1,t)}}{2\Delta y}) \\ & + \epsilon_{(x,y)} \sigma_{SB} (T^4_{(x,y,t)} - T^4_0) \\ & + \frac{kt_{f(x,y)}}{\kappa_{(x,y)}} (\frac{T_{((x,y,t+1))} - T_{(x,y,t)}}{\Delta t}), \end{aligned} \tag{3-1-9}$$

where $T_{(x,y,t)}$ is temperature on the foil, x and y are indices of the IRVB pixel, t is an index of time, ΔX and ΔY are the pixel size of the IRVB with horizontal and vertical dimensions, respectively and Δt is the time step of the IRVB measurement. Equation 2-2-1 can't be applied directly to pixels on the foil edge, because of the temperature on the outside of the foil is not measured. Equation 2-2-1 is applied to edge pixels with an assumption that the temperature on the outside of the foil is the background temperature, T_0.

3.2 Improvement for IRVB (foil material)

In the IRVB measurement, the material and the thickness of the foil have a large influence on the performance of the IRVB such as the sensitivity and the time resolution. In a previous study, Au was chosen as the foil material. However, Au has a high neutron cross-section which leads to transmutation to Hg, therefore it is not suitable for the IRVB foil in a fusion reactor. Therefore, the foil material for the IRVB foil should be re-considered. The foil material has not been evaluated systematically. In this section,

candidates of the IRVB foil material have been evaluated and the best material among candidates has been selected to improve the performance of the IRVB.

3.2.1 Requirement for foil

IRVB foils must absorb high energy photons from plasma radiation. When photons entered an IRVB foil, photons lose their population as they move through in the direction of the thickness with the energy exerted on the foil. The attenuation ratio on the population of photons with the pathway length, depends on the foil material and the energy of the incident photons [5]. Therefore, the foil material and the thickness of the foil is should be chosen with consideration of the photon energy from the plasma radiation. The inverse of the sensitivity of the imaging bolometer with the absorbed energy is given by the noise equivalent power density (NEPD)In terms of the foil materials, the sensitivity depends on the thermal conductivity, k, thermal diffusivity, κ, and foil thickness, t_f. Also the foil temperature rise, ΔT, and the time constant for the temperature rise/decay, τ, with incidence radiation are related by the following equation with the case of weak radiation cooling.

$$\frac{1}{S_{IRVB}} \propto \frac{\kappa}{kt_f} \propto \frac{\Delta T}{\tau}, \tag{3-2-1}$$

The equation indicates higher ΔT and lower τ gives higher sensitivity on the IRVB. Therefore, evaluation of $\Delta T/\tau$ provides useful information to select the best foil material which provides the highest sensitivity of the IRVB. Normally, ΔT and τ can be calculated from k and κ which are obtained from a material database. However, in IRVB foil, k and κ can be changed by the manufacturing process of the IRVB foil. Therefore the foil material should be experimentally evaluated. In this section, candidates of the foil material are evaluated with ΔT and τ.

3.2.2 Candidates of foil materials

In this study, Pt, Ta and W are employed as candidates for IRVB foils. Typical physical parameters of these materials are described in Table 3.1. However, these physical parameter can be changed in manufacturing process of the foils. Therefore, these materials should be evaluated experimentally as manufactured foils. Criteria for selection of candidates are higher melting temperature than the expected and planned working temperature for the IRVB, high $\frac{\Delta T}{\tau}$ which is a rough index for the sensitivity of the IRVB foil and fine ability to stop high energy photons [4].

Table 3.1: Typical parameters of candidates for IRVB foil

	Thermal conductivity $(W/m \cdot K)$	Melting temperature (K)	Heat capacity $(J/kg \cdot K)$	Density (kg/m^3)	Thermal diffusivity (m^2/s)
Au	318	1064.4	129	19.3	0.127
Pt	71.6	1772.0	133	21.45	0.029
Ta	57.5	2996	140	16.6	0.020
W	173	3410	133	19.3	0.132

3.2.3 Making of samples for thermal characteristics evaluation

15 small foils are made with the following process, as samples for evaluation from the candidates with different thickness to evaluate their thermal characteristics. The nominal thickness of the small foils are Au (1.0, 2.5, 3.0, 5.0, 7.0, 10.0 μm), Pt (1.0, 2.5, 5.0, 7.5, 10.0 μm), Ta (5.0, 7.5, 10.0 μm) and W (10.0 μm). Dimensions of the small foils are 2cm $\times$ 2cm. Small foils are cut out from large metal foils which have 20cm x 20cm dimensions. A measurement of the thickness of these small foils has been carried out using two methods.

Measurement for foil thickness (average and local)

One of these methods is a measurement of the mean thickness by the weight of the foil. The weight of the small foils is measured by a micro balance. The mean thickness, $\overline{t_f}$, of the foil is calculated as;

$$\overline{t_f} = \frac{m}{A}, \tag{3-2-2}$$

where m is the measured weight of the foil and A is the area of the foil. The mean thickness, $\overline{t_f}$, is used as the foil thickness in this section.

As another measurement method for the foil thickness, local thickness measurement using (Scanning electron microscope) SEM is carried out to evaluate the local variation of the thickness of the foil. In this measurement, the cross section of the foil remaining from the process of cutting out the small foils is used. The cross section of the foil is placed with a 45 degree mounting angle on the SEM stage and observed using SEM. The thickness of the cross section is observed in the SEM image. This local measurement is carried out at three points on every foil.

Attenuation thickness

The attenuation length which is the thickness where the total number of the incident photons dropped to $1/e(= 63.2\%)$ is depends on the foil material. When the maximum absorbable photon energy for foils is defined as the maximum photon energy having less than 36.8% of the incident photons penetrate the foil, as is shown as Figure 3.18, the maximum energy for each foil sample can be calculated as Table 3.2. This parameter should also be considered in comparison among the candidate IRVB foils.

The small foils are mounted in copper gaskets as shown in Figure 3.19, and then small foils are blackened with carbon spray, "Aerodag G" (manufactured by Acheson). The small foils are placed on the copper frame to make the small foil array as shown in Figure 3.20. These mounted foils are used as the evaluation samples in this section.

3.2.4 Measurement of heat characteristics

The small foil array is placed in a vacuum chamber which is evacuated to less than 0.1 mTorr to remove the heat conduction cooling of the foil by air. Sample foils in the small foil array are heated with a chopped HeNe laser and their temperature measured by an IR camera to measure the thermal characteristics of the sample foil. The power of the HeNe laser is 12.5mW at the foil surface, the wave length is 633nm and the diameter of the laser spot is 1mm. The HeNe laser is chopped by a mechanical shutter with a pulse in Figure 3.23. The period of laser chopping is 12s (6s irradiation and 6s chopped). The used IR camera is an "OMEGA" IR camera (microbolometer type, manufactured by INDIGO, measurement range in wavelength 7.5-13.5 μm, 30 frame per second and 120 $\times$ 160 pixels). The IR camera is calibrated with the same procedure as described in

Table 3.2: List of the evaluation samples. Thickness of the evaluated foils, t_f, (a) nominal, (b) average (from weight), (c) local (from SEM), (e) Thermal conductivity, k, (f) thermal diffusivity, κ, of the foil and (g) maximum energy of stoppable photon.

Metal		Foil thickness(μm)			(e)k	(f)κ	(g)Photon energy
	(a)Nom.	(b)Ave.	(c)Loc.	(d)Var.	$W/(m \cdot K)$	$\times 10^{-6} m/s$	KeV
Au	1	0.83	1.2	$\pm$0.2	318	127	5.24
Au	2.5	0.96	2.3	$\pm$0.5	,,	,,	5.52
Au	3	2.7	2.5	$\pm$0.3	,,	,,	8.35
Au	5	4.88	6.5	$\pm$1.1	,,	,,	17.5
Au	7	7.14	6.5	$\pm$1.5	,,	,,	20.5
Au	10	12.2	11.5	$\pm$1.1	,,	,,	25.2
Pt	1	0.91	0.9	$\pm$0.2	71.6	25.1	5.52
Pt	3	0.72	1.3	$\pm$0.2	,,	,,	4.98
Pt	5	4.69	7.8	$\pm$1.8	,,	,,	17.9
Pt	7.5	7.21	7.3	$\pm$1.2	,,	,,	21.2
Pt	10	10.2	7.2	$\pm$2.0	,,	,,	24.4
W	10	8.32	7.6	$\pm$0.2	173	67.4	20.2
Ta	5	4.46	4.8	$\pm$0.3	57.5	24.7	15.6
Ta	7.5	8.18	13.1	$\pm$2.0	,,	,,	18.2
Ta	10	6.79	9.8	$\pm$3.3	,,	,,	17.3

Section 3.1.5. The IR camera is placed in front of a ZnSe IR window on the chamber at room temperature as shown in Figure 3.21. The IR camera signal is calibrated every experiment using a small carbon plate with an electrically heated wire which is shown in Figure 3.22.

Temperature measurement on center of foil

When the chopped laser is incident on the foil center, the foil temperature is rapidly changed. The change of the temperature on the foil center is measured by an IR camera. Figure 3.23 shows a pulse of the incident laser and the temperature rise from the background temperature on the foil center. Curve fitting is performed on the measured temperature change, T_c, with the following equation using a least square method with software the EXCEL (manufactured by Microsoft).

$$T_c(t) = \Delta T(1 - \exp(-\sqrt{\frac{t}{\tau}})). \tag{3-2-3}$$

This curve fitting provides two parameters, the time constant, τ, and the temperature rise, ΔT, as the thermal characteristics. This heating, measurement and curve fitting are carried out 20 times for each sample foil. The obtained parameters are used for comparison of the thermal characteristics in this section.

Foil temperature with laser irradiation

With the incident laser power on the foil surface, the heat diffusion equation on the foil can be written with polar coordinates as

$$\begin{cases} \rho c \frac{\partial T_1}{\partial t} = \frac{\partial}{r \partial r}(k t_f r \frac{\partial T_1}{\partial r}) + P_{laser} & (r \leq r_1) \\ \rho c \frac{\partial T_1}{\partial t} = \frac{\partial}{r \partial r}(k t_f r \frac{\partial T_1}{\partial r}) + P_{laser} & (r_1 < r) \end{cases}, \tag{3-2-4}$$

B.C.

$$\begin{cases} (r = r_1) & T_1(r_1) = T_2(r_1) \\ (r = r_2) & T_2(r_2) = T_0 \\ (r = r_1) & \frac{\partial T_1(r_1)}{\partial r} = \frac{\partial T_2(r_1)}{\partial r} \end{cases}. \tag{3-2-5}$$

T_1: Temperature of foil inside laser spot
T_2: Temperature of foil outside laser spot
T_0: Background temperature (= Temperature of the gasket)
ρ: Density of foil (kg/cm^3)
c: heat capacity of foil ($(J/kg \cdot K)$)
P_{laser}: Laser power density at foil surface(W/cm^2)
r_1: Radius of laser spot
r_2: Radius of gasket
t_f: Thickness of foil

When the foil temperature is in steady state, Equation 3-2-4 is written as

$$\begin{cases} T_1(r) = \frac{P_{laser}}{4kt_f}(r_1^2 - r^2) + \frac{P_{laser} r_1^2}{2kt_f} \ln \frac{r_2}{r_1} + T_0 & (r \leq r_1) \\ T_2(r) = \frac{P_{laser} r_1^2}{2kt_f} \ln \frac{r_2}{r_1} + T_0 & (r_1 < r) \end{cases}, \tag{3-2-6}$$

Temperature rise, ΔT, can be written with Equation 3-2-6 and r=0 (center of laser spot) as

$$\Delta T = T_1(0) - T_0 = \frac{P_{laser}}{4kt_f}(r_1^2) + \frac{P_{laser} r_1^2}{2kt_f} \ln \frac{r_2}{r_1} \tag{3-2-7}$$

3.2.5 Comparison and selection

Figure 3.24 and Figure 3.25 show the temperature rise, ΔT and time constant of the temperature rise/decay at the center of the foil versus foil thickness, respectively. Error bars in these figures are defined as the standard deviation of the measurement results with 20 measurements on each sample. For the same material, thinner foils show a higher temperature rise, ΔT, than thicker foils. For the same thickness foil, the Ta foil has the largest temperature rise among the candidates. Ta has the smallest thermal conductivity, k, among the candidates without the influence of carbon coating. Therefore, these results are consistent with Equation 3-2-7. The time constant, τ, of each material is in order from the shortest to the longest, Au,Pt,Ta, and W foil. However there is no observed strong dependence of the foil thickness up on the time constant. The index of the sensitivity of the IRVB foil, $\Delta T/\tau$, is also evaluated. Figure 3.26 shows the index of sensitivity of IRVB foil versus maximum energy of the stoppable photon by sample foils which is determined by foil material and thickness. For the same stoppable energy, Pt foil has the largest value of $\Delta T/\tau$ in all regions of the evaluated range on the stoppable energy. This behavior is consistent with theoretical prediction. Figure 3.27 shows k/κ which is proportional to $\Delta T/\tau$ as shown in Equation 3-2-1. In experimental results, the value of $\Delta T/\tau$ for the Pt foil is larger than twice that Au which is the conventional foil material. This result indicates, when foil thickness is determined with the target photon energy of the radiation, the Pt foil provides a larger sensitivity for the IRVB which is twice the conventional one without the dependence on the target photon energy. With

the results of this comparison, the conclusion is that Pt is the best material among the evaluated candidates and it provides more than twice as much sensitivity for the IRVB. Pt is used in the following section as the foil material.

3.3 Improvement for IRVB (foil calibration)

When the incident radiation power on the foil is calculated using the 2D temperature distribution, 2D distributions of the foil parameters are necessary which are the foil thickness, t_f, and the foil emissivity, ϵ, with the resolution of IRVB pixel. As a calibration between the incident power of radiation and the 2D temperature distribution, evaluation of the distribution of the foil parameters are carried out as described by the procedure in this section [6]. Because the foil is not considered as a multi layered foil in Equation 2-2-1 with two dimension, the effective thickness and the effective emissivity for the 2D calculation are required. The effective thickness and the effective emissivity are defined as parameters at which a pure Pt foil shows the same heat response with the evaluated foil. The foil calibration described in this section provides the effective thickness and the effective emissivity. In this calibration, the foil is divided into IRVB pixels or pixels which have the twice size of the IRVB pixel, and an assumption that the thicknesses and emissivity of these pixels are uniform in each pixel, is employed. In this section, a foil has the dimension with 9cm $\times$ 7cm $\times$ 2.5μm(nominal value), and pixels having double the IRVB pixel size are used for the description of the calibration procedure.

3.3.1 Calibration experiment

The foil calibration is carried out in a vacuum chamber which is evacuated to less than 0.1 mTorr to remove the heat conduction cooling of the foil by air. The evaluated foil is placed in the chamber and irradiated with a laser. The laser is a HeNe laser. The power of the HeNe laser is 11.5mW at the foil surface, the wave length of the laser is 633nm and the diameter of the laser spot is about 0.6mm. When a 2D temperature distribution is formed on the foil, the temperature distribution is measured by a IR camera which is a SC4000 camera (manufactured by FLIR, Indium Antimonide detector type, wavelength of 3-5μm, 420 frame per second and 320 $\times$ 256 pixels). The laser irradiation points are located on the center of the each pixel. The blue crosses in Figure 3.28 show the irradiation points and the red numbers show the irradiation point numbers.

3.3.2 Calibration flow

Figure 3.30 shows the calibration flow chart. This calibration procedure has three steps. As a first step, the 2D temperature distribution on the evaluated foil under laser irradiation is measured by the IR camera and curve fitted to a fitting function with three fitting parameters at all irradiation points. The fitting function is following modified Gausian function.

$$T(r) = T_0 + \Delta T \exp(\frac{-(r/w)^{2\alpha}}{2}) \tag{3-3-1}$$

The ΔT is the peak temperature of temperature distribution, r is the distance from the laser spot, w is the width of the peak and α is a shape factor.

As a second step, the temperature distribution is simulated using a finite element method (FEM) by changing the foil thickness in the FEM model. A curve fitting is performed to the simulated temperature distribution with the same fitting function and two fitting parameters and a fixed α which is obtained in the first step. The obtained

fitting parameters are compared between the simulated temperature and measured one to estimate the effective foil thickness at all irradiation points. As a third step, the same procedure as the second step is carried out but changing the foil emissivity to estimate the effective emissivity. The second and third steps are repeated as an iteration with feedback of the estimated distribution of the effective thickness and the effective emissivity into the FEM model until the estimated parameters converge to a distribution.

3.3.3 Comparison for foil parameters estimation

FEM model

In this calibration, the simulated temperature distribution with a 2D FEM model is employed for the comparison with the measured temperature distribution. All FEM analyses are carried out with the software ANSYS(developed by ANSYS). The FEM model is divided as described in Figure 3.28. The divisions are not the elements for the FEM analysis, the FEM analysis is performed with much smaller elements than the ones described in Figure 3.28. The foil thickness and the emissivity of the FEM model are changed individually for each division described in Fig.2. As the boundary condition of the FEM model, the temperature at foil edge and environment temperature for radiation simulation is fixed to room temperature (300K). The thermal conductivity of the foil is assumed as that of pure Pt, 71.6 $W/m \cdot K$. The initial thickness and emissivity is set as $2.5\mu m$ and 0.91 before the iterative calculation. The laser irradiation is simulated as a surface load. .

Comparison for thickness estimation

In the second step, described above with the 1st iteration, the foil temperature with laser irradiation is simulated using the initial emissivity with slight changes of the thickness. The simulated temperature is curve fitted to obtain the fitting parameters ΔT and w, at all irradiation points. The foil thickness at each irradiation point is estimated from these data by means of linear fitting in Figure 3.31(left), which shows the relation of $\Delta T/w$ with $1/kt_f$. Next, the FEM analysis was conducted using the obtained thickness distribution with a slight change of the emissivity. Figure 3.31(right) shows the relation of ϵ with the peak width w. A liner fitting is performed to this plot and projected the measured w on the line to estimate the emissivity at the irradiation point. The estimated distribution of the emissivity is given to the FEM model. The processes described above are reiterate until the estimated parameters converged to a distribution. The coefficients of determination between the nth estimated distribution and $(n-1)th$ estimated distribution is used as a criteria of the convergence. When the coefficient is larger than 0.95, the calibration analysis is judged as convergent.

3.3.4 Evaluated distribution of foil parameters

Figure 3.32 and Figure 3.33 show the behavior of the estimated effective thickness and effective emissivity. It shows that the estimated parameters converged with 5 iterations. When the evaluated distributions of effective parameters are given to the FEM model, the temperature distribution with the incident laser power is reproduced as Figure 3.34. It shows the calculation with the evaluated effective parameters well reproduces the measured temperature. Figure 3.35 and Figure 3.36 shows a 2D profile of the evaluated effective thickness and the effective emissivity. These figures show that the foil thickness and emissivity evaluated by this calibration do not correspond to the nominal values

because the FEM model did not take the influence of carbon coating and structural damage on thermal conductivity into account, and nominal thickness can have large error with manufacturing process of the foil. However, effective thermal response of the foil for the measurement of incident power distribution can be assessed with the estimation as shown in Figure 3.34. These results indicate that the evaluated effective parameters can be used as the calibration factor between the incident power and the formed temperature distribution. In the following chapters, this calibration is performed to evaluate the effective thickness and the effective emissivity on IRVB foils.

3.4 Imaging spectrometer

An imaging spectrometer is a spectrometer with a two dimensional detector array. The imaging spectrometer has been installed on the 7-O diagnostics port in LHD with the direction viewing the divertor plasmas. It has also been used for radiation measurement to identify the difference in behaver of radiation among impurities and fuels. The imaging spectrometer has a total of 130 fibers array (10×13). Radiation from the plasma is focused on each fiber by a lens unit. The array provides a 130 channel array as in Figure 3.36. The radiation focused on the fiber is transmitted to a spectrometer and analyzed with each spectrum. The output of the imaging spectrometer had never been calibrated by any absolute calibration. In this study, an absolute calibration has been carried out. The detail of the absolute calibration is described in the next chapter. The calibrated imaging spectrometer is supplementarily used to measure radiation collapse.

3.4.1 Calibration analysis for imaging spectrometer

In this thesis, the imaging spectrometer which is installed in the 7-O diagnostics port is used to support the developed 3D measurement for radiation collapse. Measurement data of the imaging spectrometer is absolutely calibrated with the following processes.

In imaging spectrometer measurement, measured data by the imaging spectrometer is outputted as a digital level which is an arbitrary unit on the CCD image. The digital level should be converted to incident radiation power on the lens with a calibration factor. A calibration analysis has been carried out to obtain the calibration factor. To take reference data for the calibration analysis, emission from an integrating sphere is measured by the imaging spectrometer as shown in Figure 3.38. The calibration data is taken with an exposure time for the CCD of 5s, known incident power for every wavelength $P_{calib,\lambda}$ and no diaphragm on the incident power. The measured data by the imaging spectrometer is obtained as a raw data image which is shown in Figure 3.39. In the Figure, the data of the channel appears as a spot. The X axis of the image is wavelength and the Y axis is the index of the channel for the imaging spectrometer. Using pixels in the image, the digital level of the i-th channel with a wavelength is written as

$$Q_{j,\lambda} = \frac{\sum_{a=a_0}^{a_j+\Delta a} \sum_{b=b_0}^{b_\lambda+\Delta b} S_{(a,b)}}{\Delta\lambda\Delta a}, \tag{3-4-1}$$

where $S_{(a,b)}$ is the digital level at the pixel $(x, y) = (a, b)$, a_j and b_j are the edge pixel of the spot for the j-th channel, Δa is the width of the spot with the unit of the pixel, $\Delta\lambda$ is the width of the spot with the unit of wavelength and $Q_{j,\lambda}$ is the mean digital level of the j-th channel and wavelength λ. The unit of $Q_{j,\lambda}$ is the digital level per nm(wavelength). When the general calibration factor between the incident power P_λ and $Q_{j,\lambda}$ with a 1s exposure time, a wavelength and no diaphragm is defined as $A_{(j,\lambda)}$, it can be given as

$$\Delta t_{calib} P_{calib,\lambda} = A_{(j,\lambda)} Q_{(calib,\lambda)}, \tag{3-4-2}$$

$$A_{(j,\lambda)} = \frac{\Delta t_{calib} P_{calib,\lambda}}{Q_{(calib,\lambda)}}, \tag{3-4-3}$$

where $\Delta t_{calib} (= 5s)$ is the exposure time for the calibration experiment. Equations 3-4-4 and 3-4-5 can be rewritten as a specific calibration factor $A_{exp(j,\lambda)}$ for each experiment, as

$$\Delta t_{exp} P_{exp,\lambda} = A_{exp(j,\lambda)} Q_{exp,\lambda}, \tag{3-4-4}$$

$$A_{exp(j,\lambda)} = \frac{A_{(j,\lambda)} \Delta\lambda}{\Delta t_{exp} D_{slit}} = \frac{\Delta t_{calib} P_{calib,\lambda} \Delta\lambda}{\Delta t_{exp} D_{slit} Q_{(calib,\lambda)}}, \tag{3-4-5}$$

where Δt_{exp} is the exposure time for an experiment and D_{slit} is the diaphragm effect by the slit. The specific calibration factor is calculated with each experimental setting and used for the conversion to the radiation power from the digital level.

3.5 Summary of chapter

To develop a 3D measurement, the following improvements in hardware of the IRVB have been carried out.

A new IRVB was installed at the 6.5-L diagnostics port in LHD. To improve IRVB performance, candidates of the IRVB foil material (Pt, W, Ta ,Au) are evaluated in their thermal characteristics with laser irradiation. The evaluation indicates Pt has the best thermal characteristics among candidates and provides twice the sensitivity of Au which was the material for previous IRVB measurements.

To acheave quantitive IRVB measurment, a foil calibration technique for the foil thickness and the emissivity has been developed. The technique provides a distribution of the parameters and makes the quantitive measurement available.

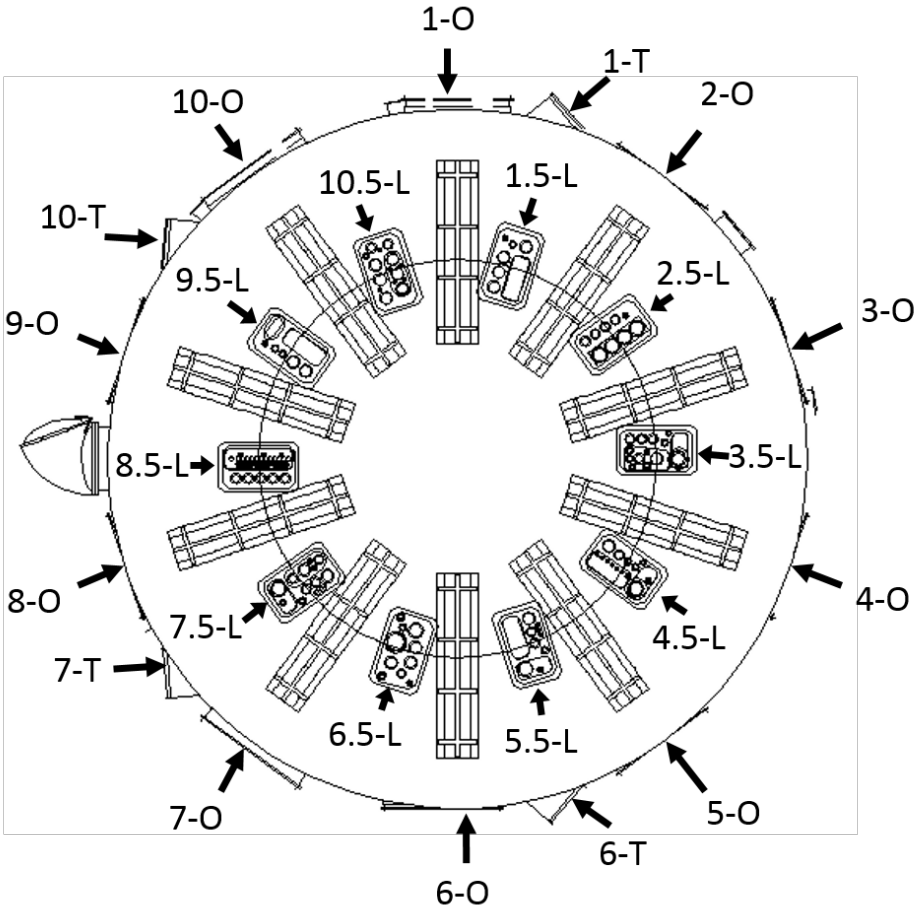

Figure 3.1: Location of diagnostics ports in LHD. U-ports are placed on opposite side of L-ports.

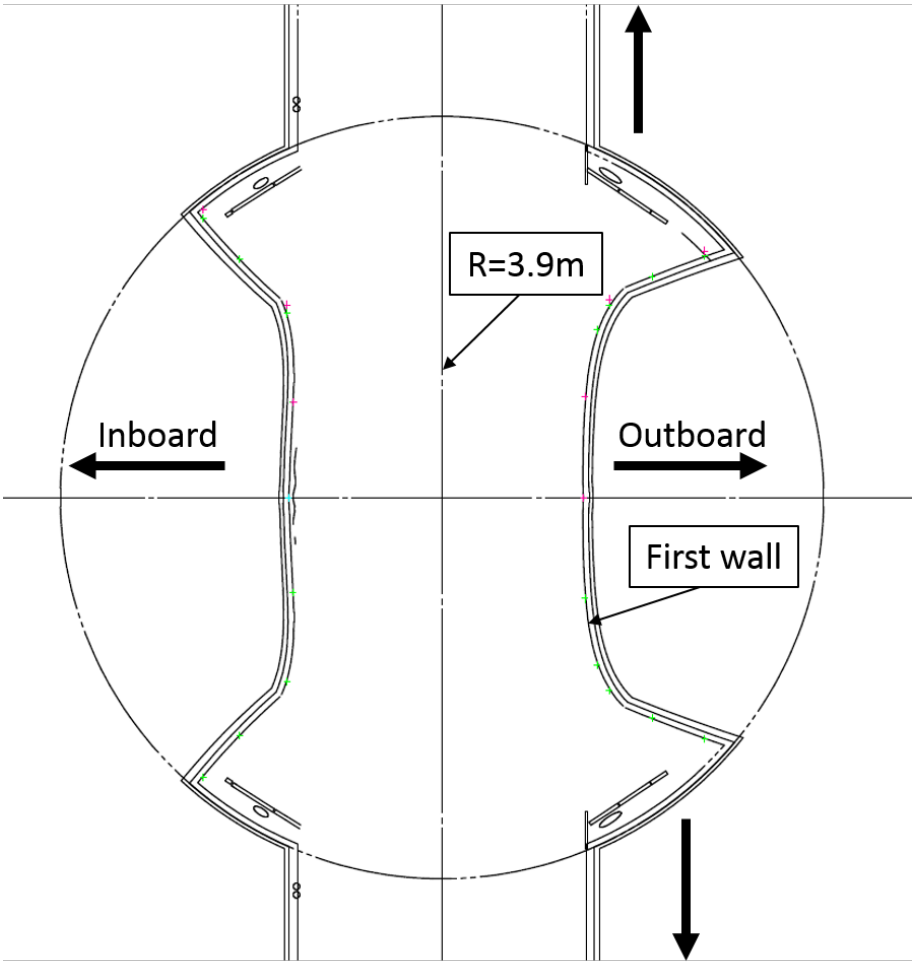

Figure 3.2: A poloidal cross section of the LHD at $\phi = 0°$

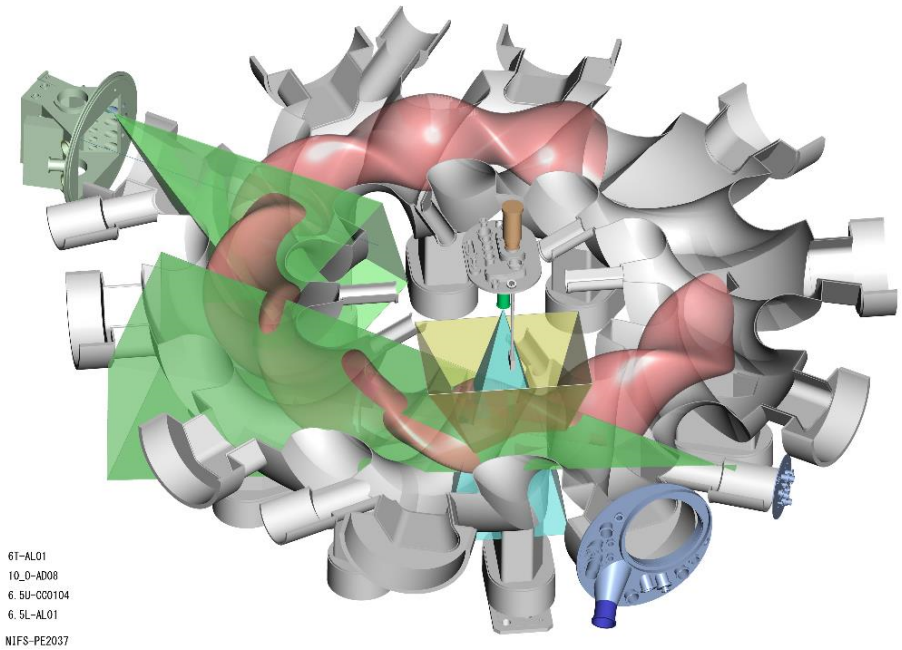

Figure 3.3: Outline drawing for 4 IRVB Fields of view(FoV)

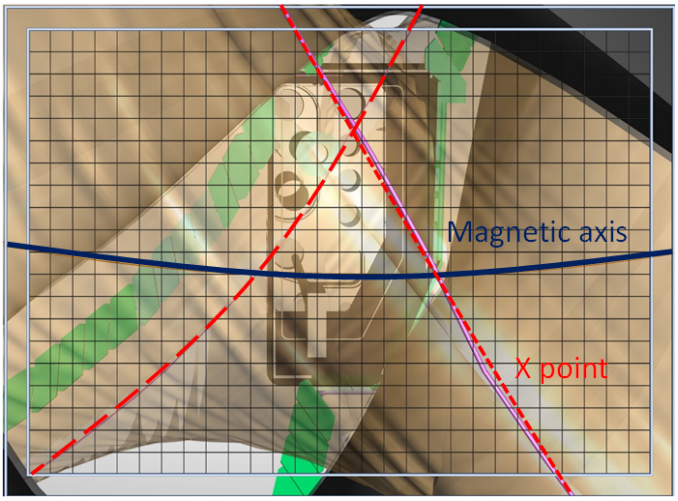

6.5-L IRVB
(lower)

30x22=
660 ch

Figure 3.4: FoV for 6.5-L IRVB

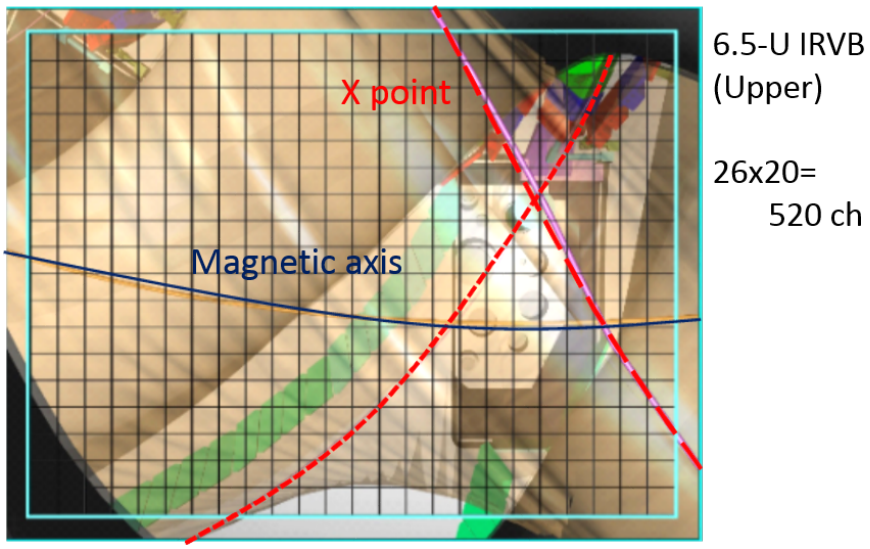

Figure 3.5: FoV for 6.5-U IRVB

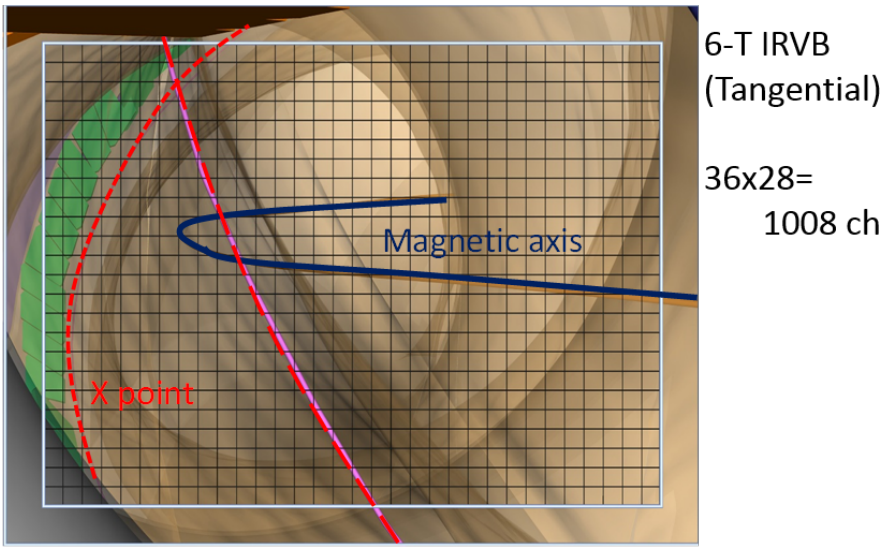

Figure 3.6: FoV for 6-T IRVB

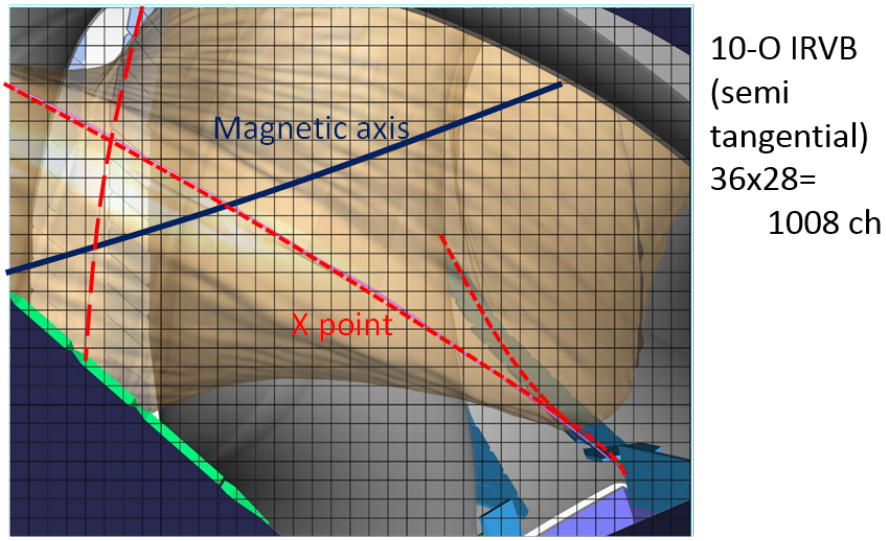

Figure 3.7: FoV for 10-O IRVB

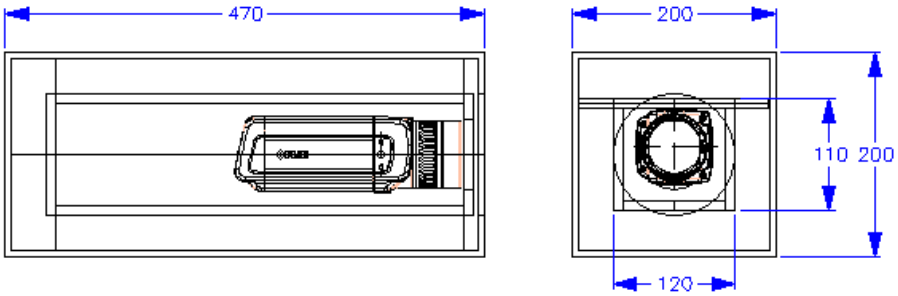

Figure 3.8: Drawing of 6.5-L shielding box

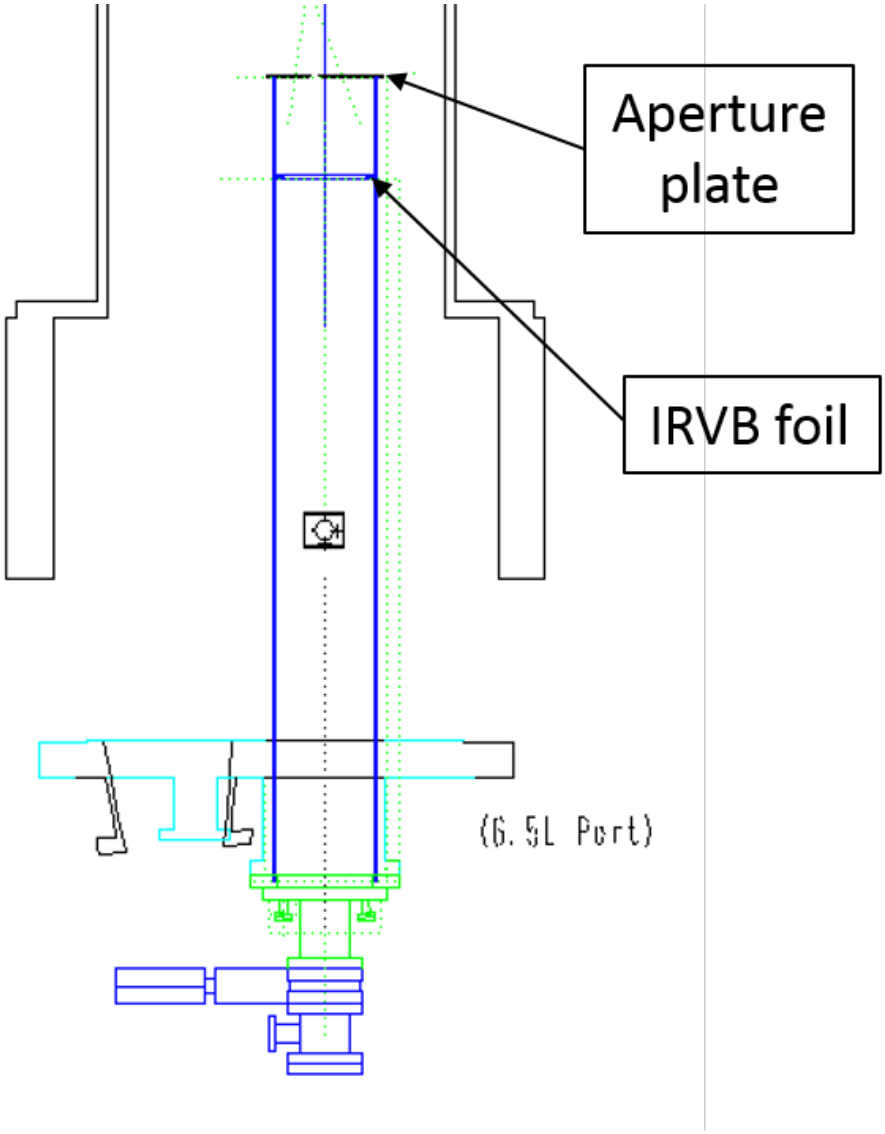

Figure 3.9: Drawing of invessel components for 6.5-L IRVB

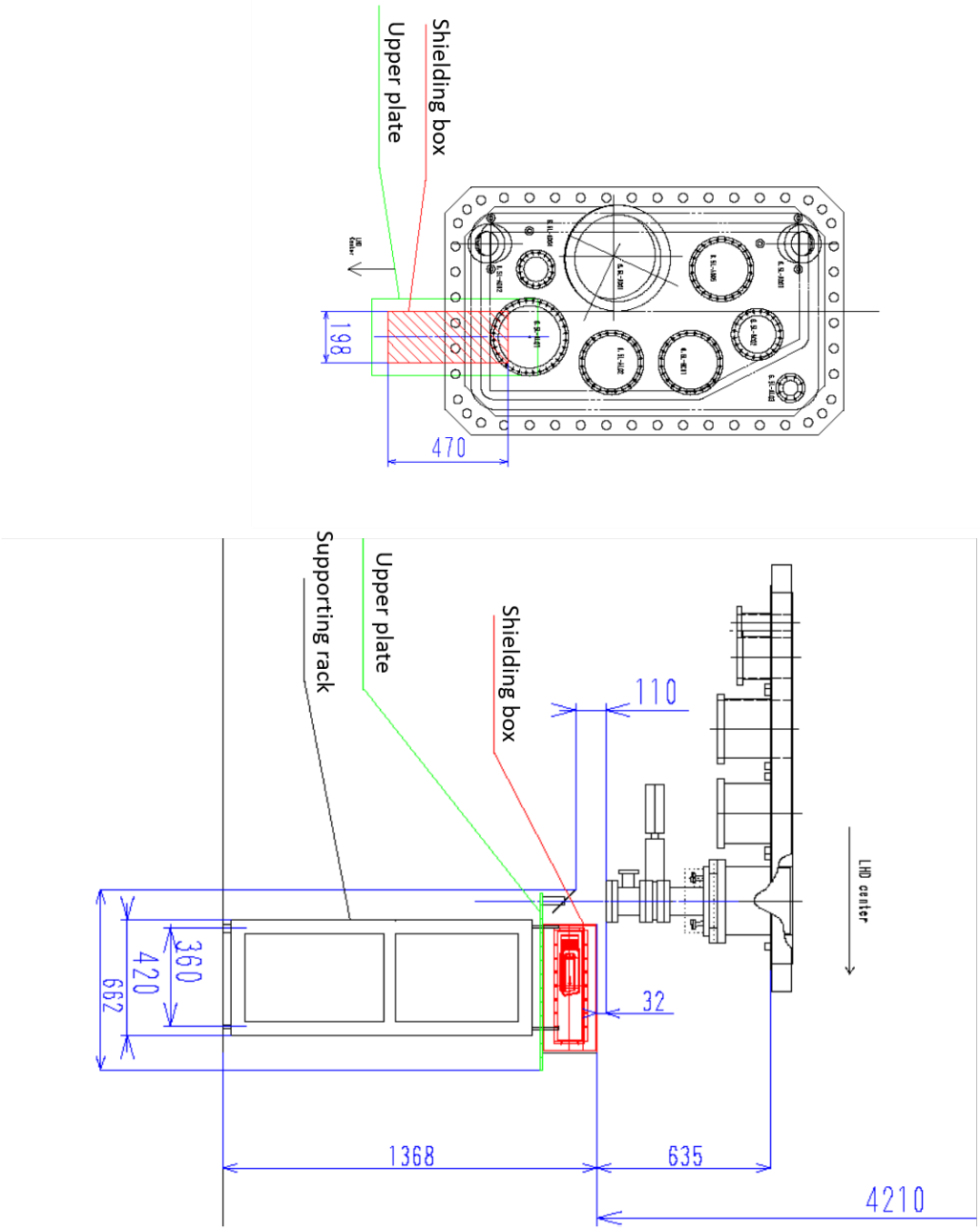

Figure 3.10: Drawing of setting for 6.5-L IRVB

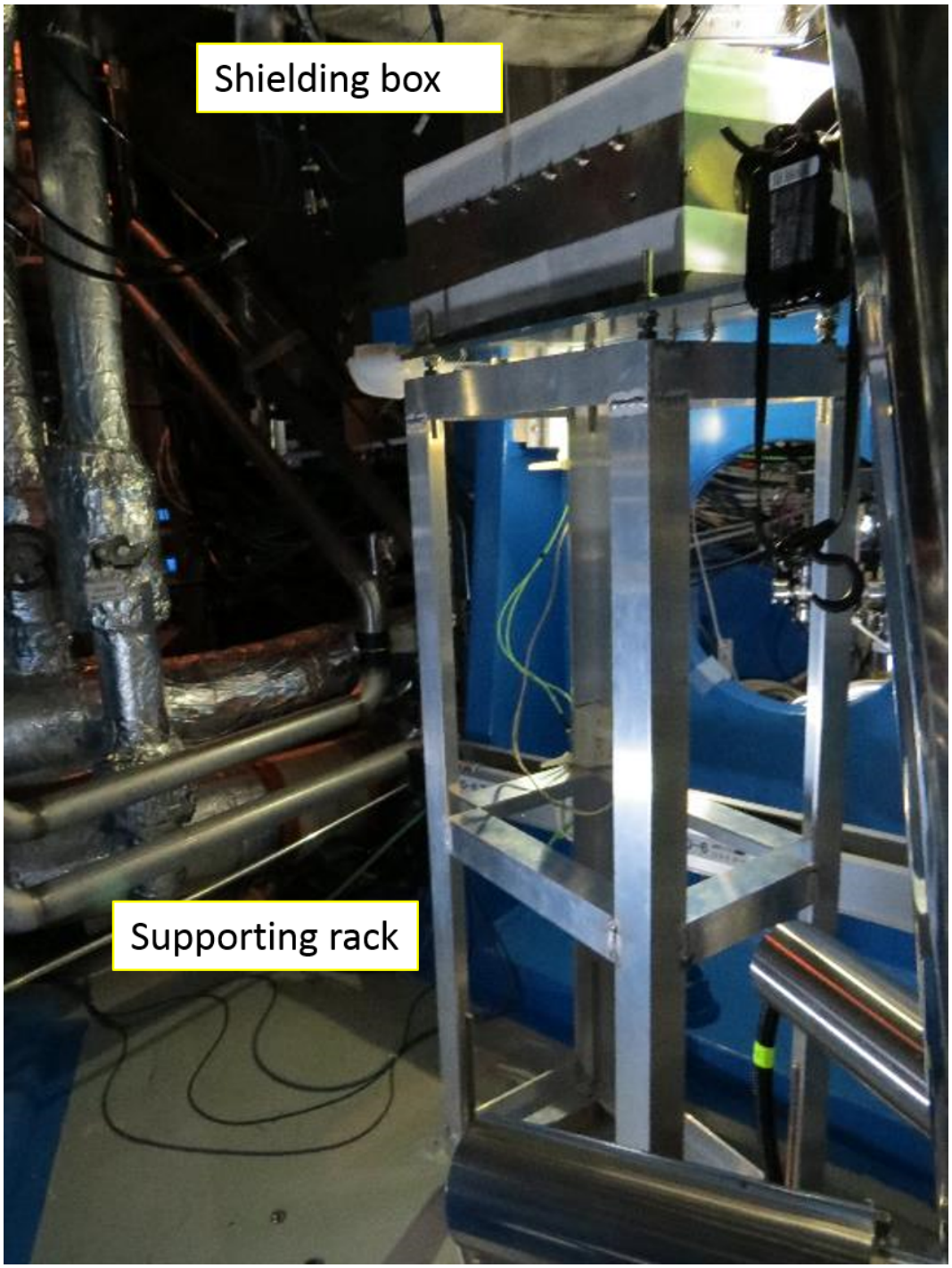

Figure 3.11: Picture of 6.5-L IRVB

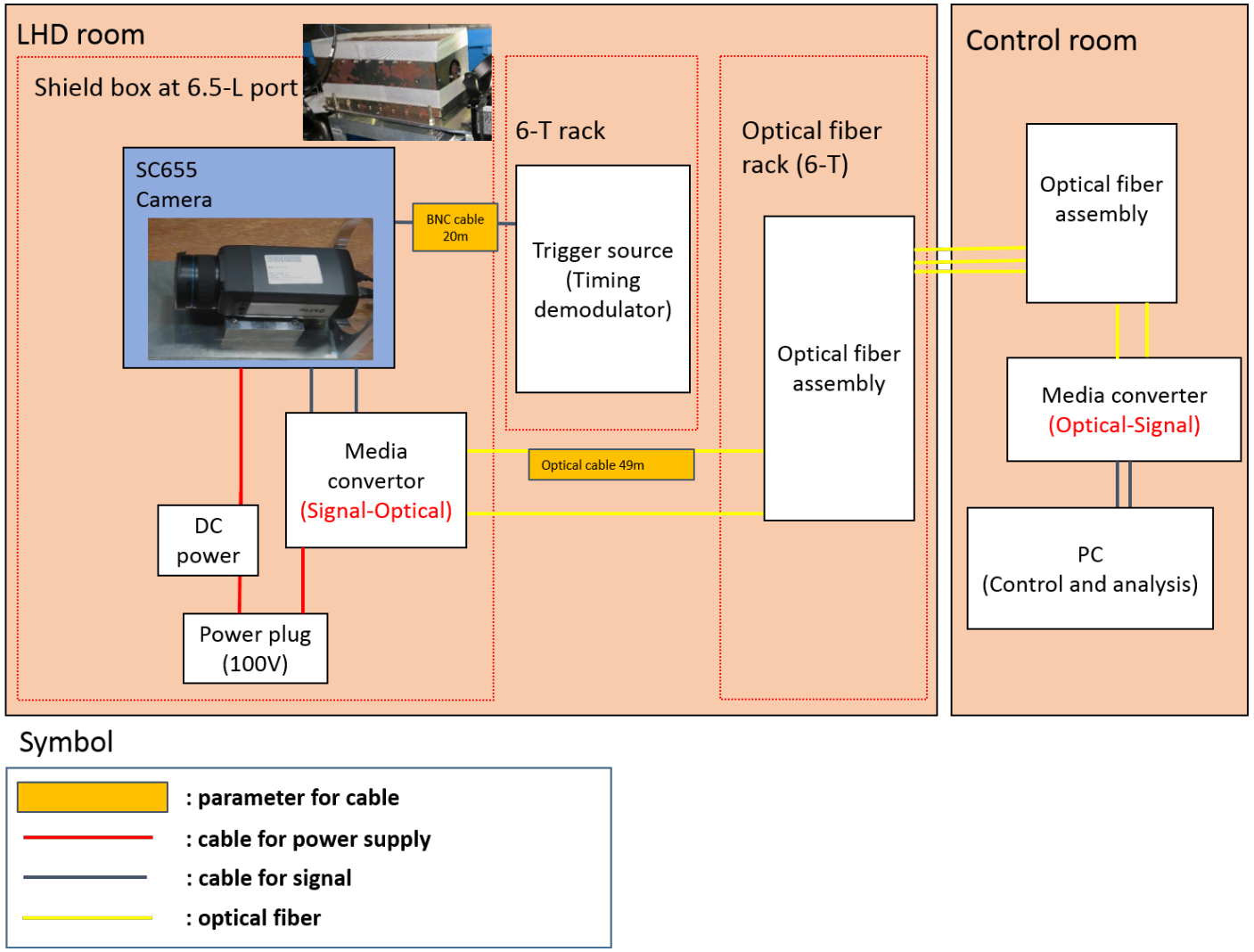

Figure 3.12: System diagram for 6.5-L IRVB

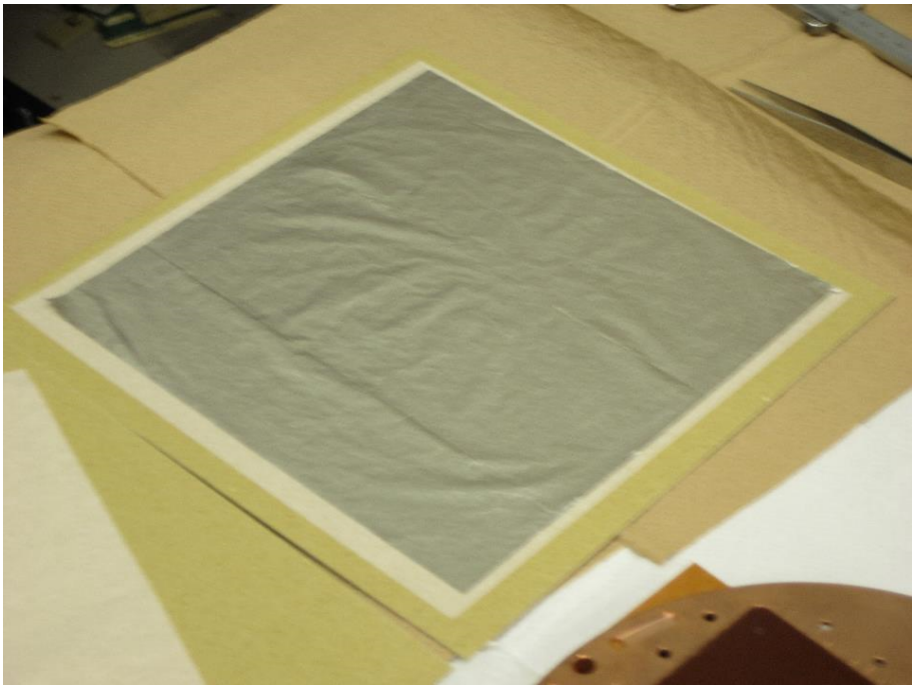

Figure 3.13: Thin metal foil for IRVB foil

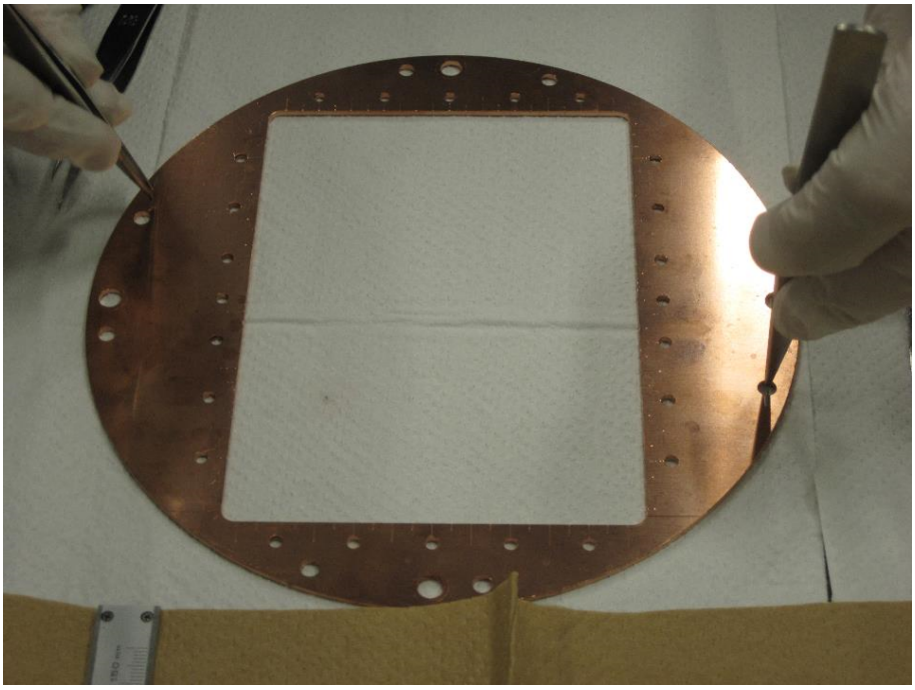

Figure 3.14: Copper frame for foil housing

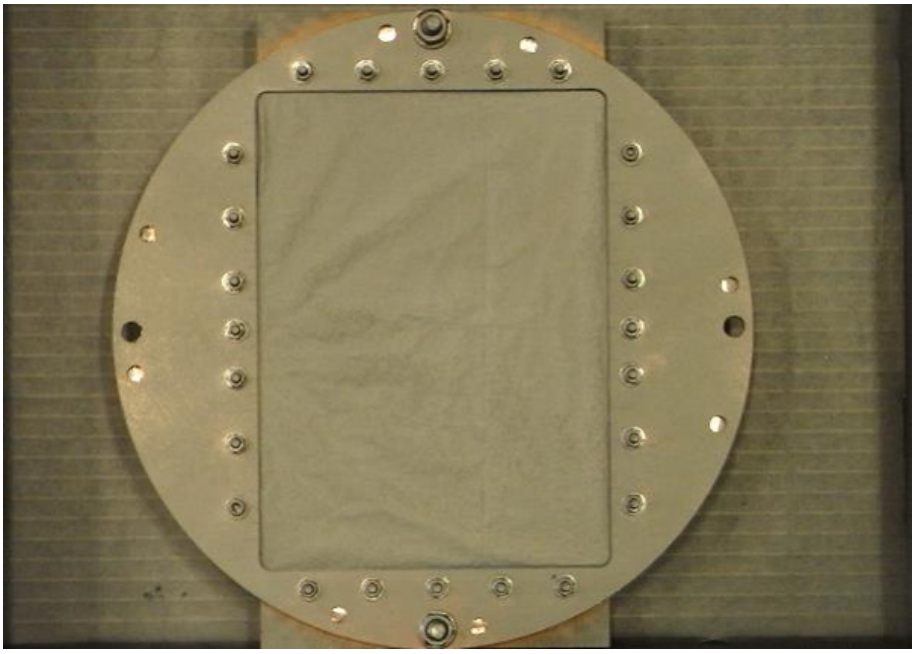

Figure 3.15: Blackened foil by carbon spray

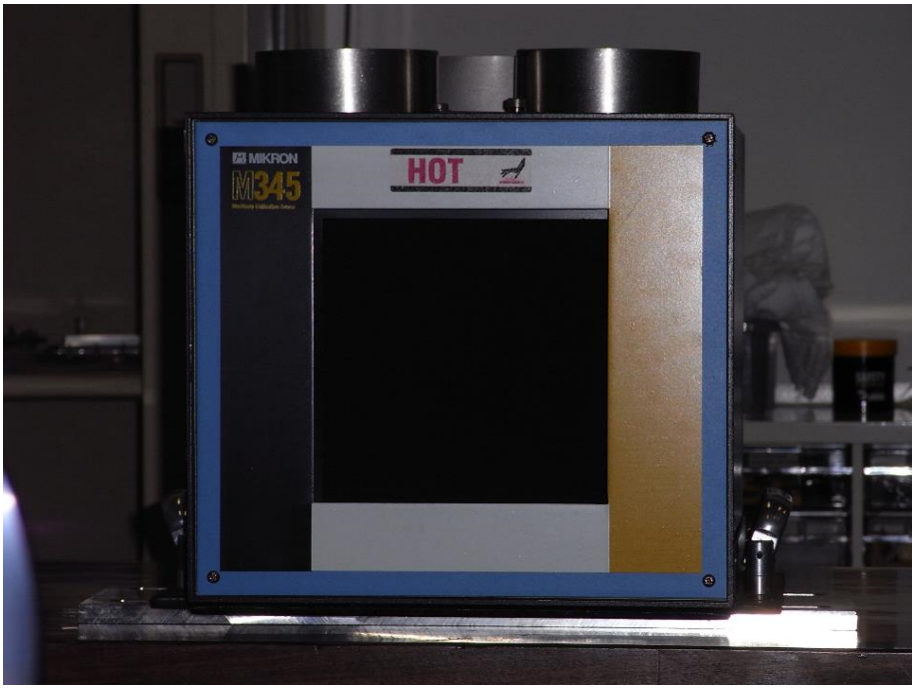

Figure 3.16: Blackbody calibration source

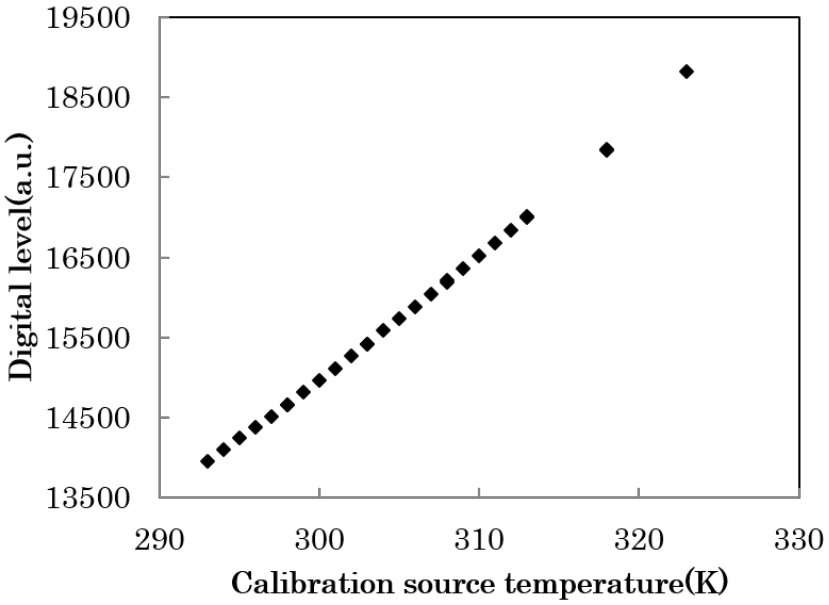

Figure 3.17: IR camera calibration result with IR camera (SC655) for 6.5-L IRVB

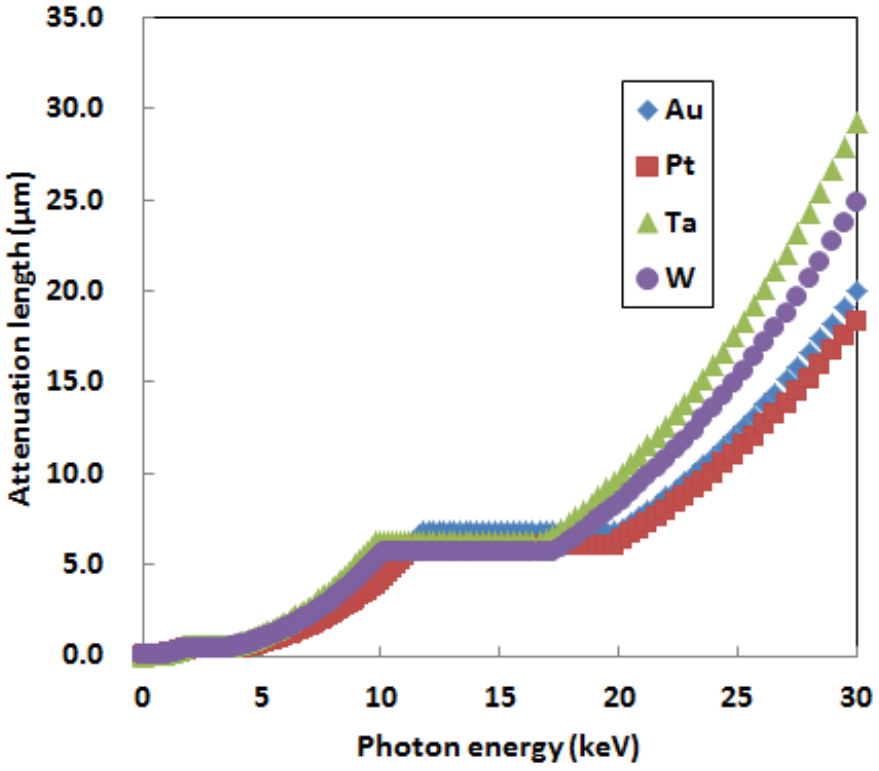

Figure 3.18: Maximum energy of absorbable photon versus foil thickness

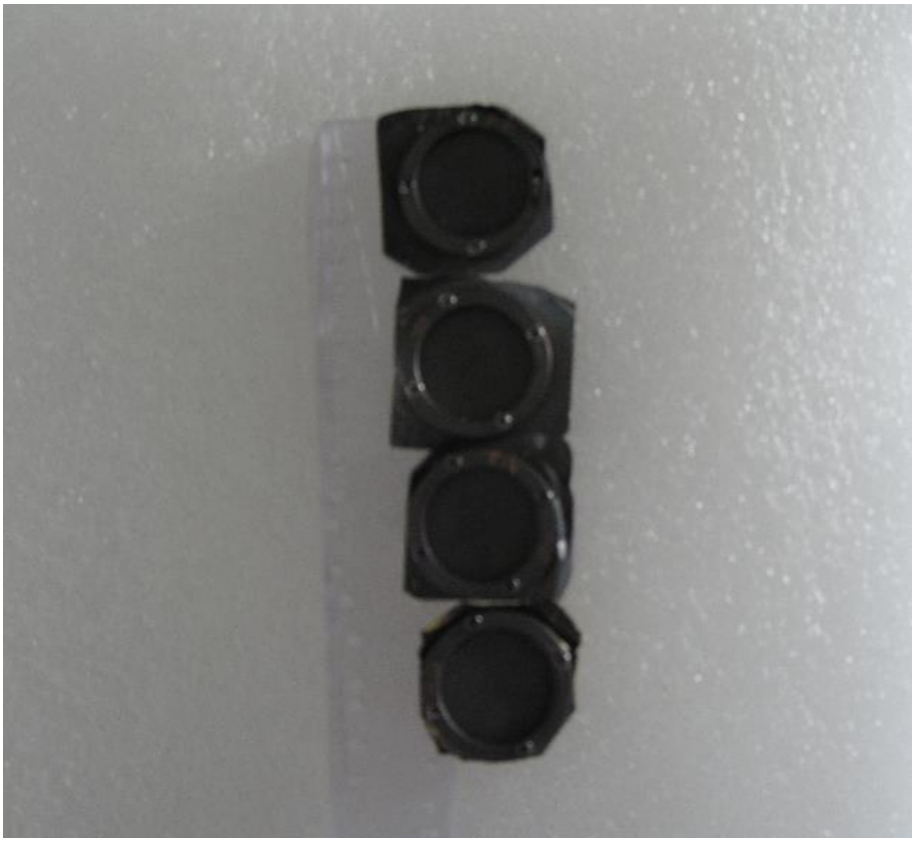

Figure 3.19: Mounted small foil with copper gasket

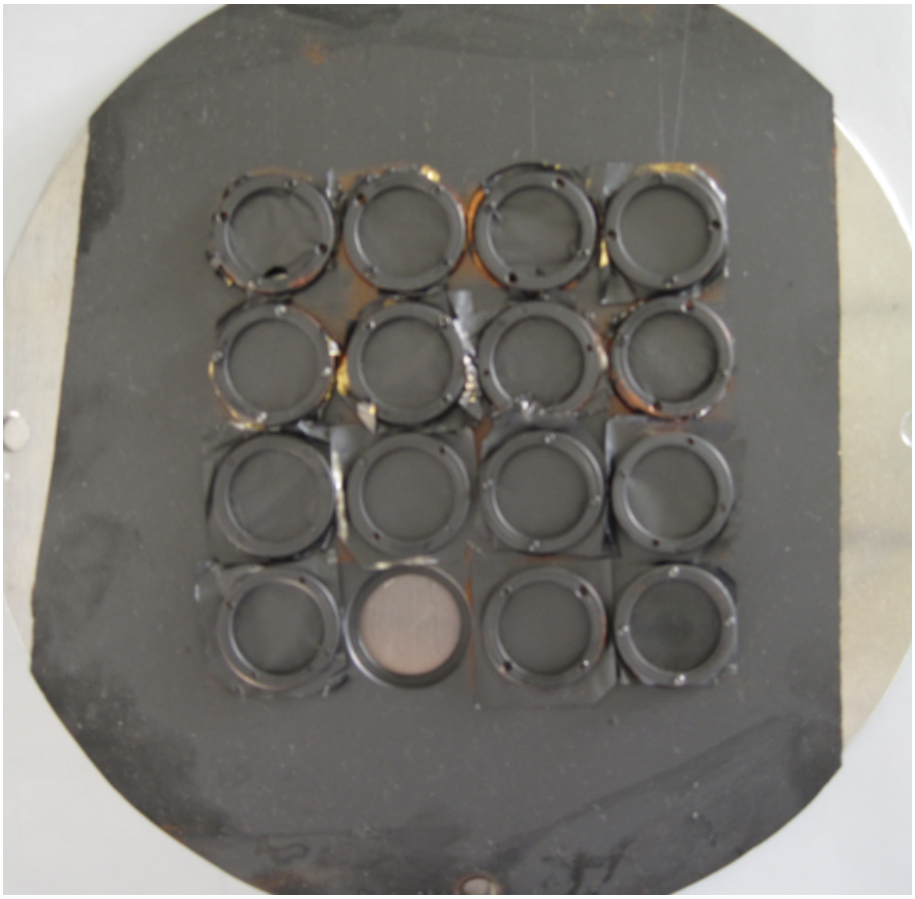

Figure 3.20: Array of blackend small foils

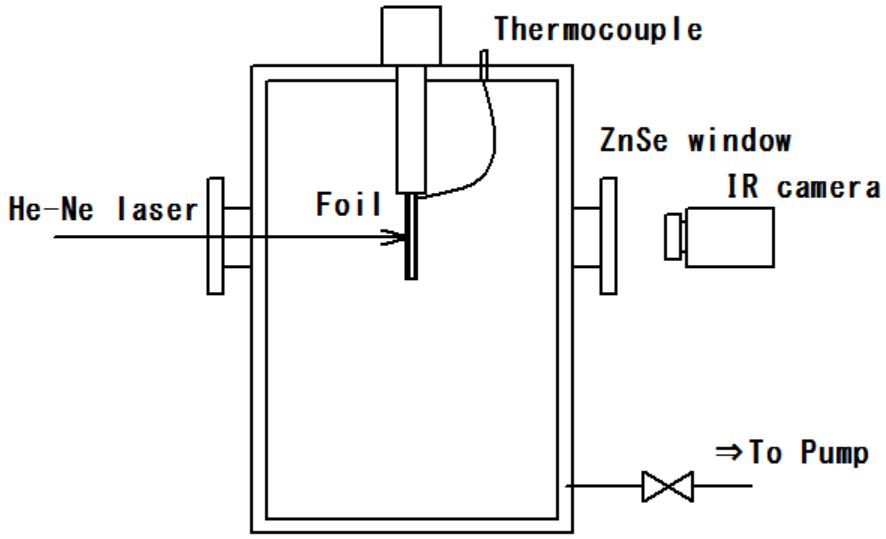

Figure 3.21: Setting for measuement of heat characteristics

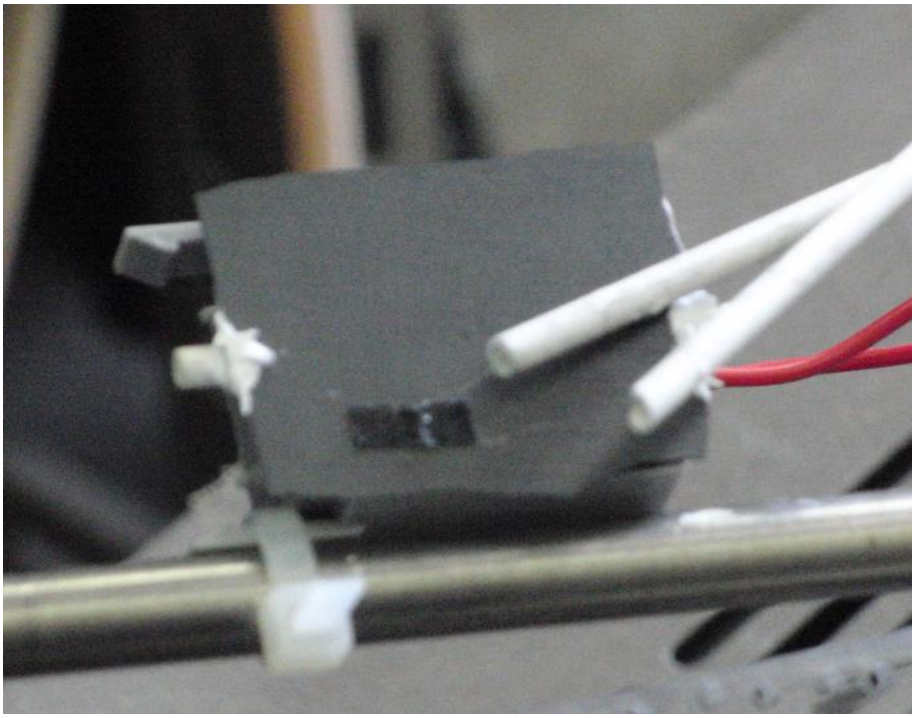

Figure 3.22: Small heat source for IR camera calibration

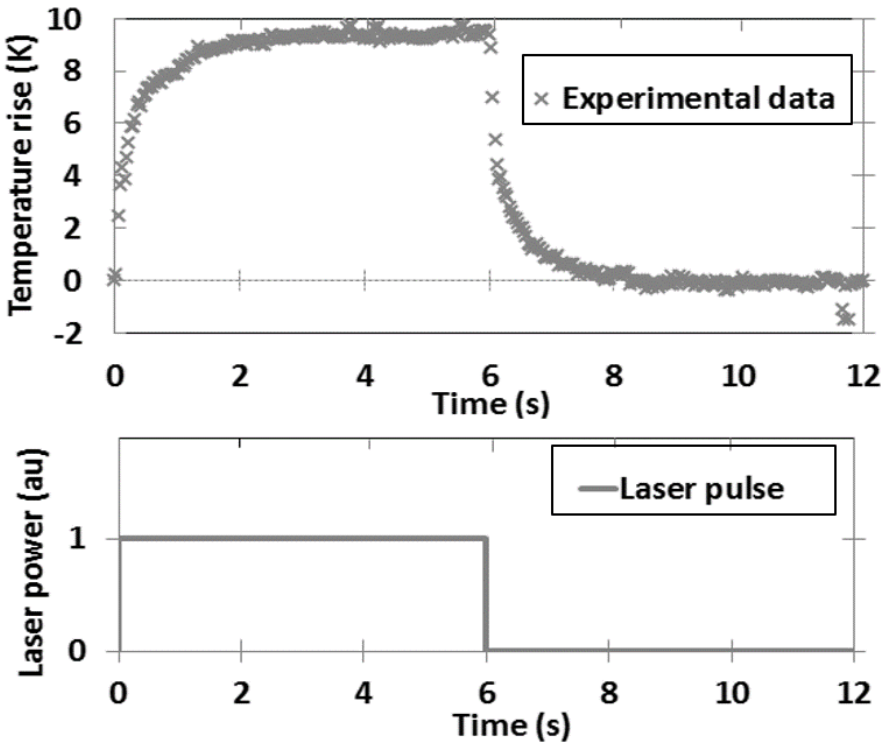

Figure 3.23: Chopped laser pulse at foil surface

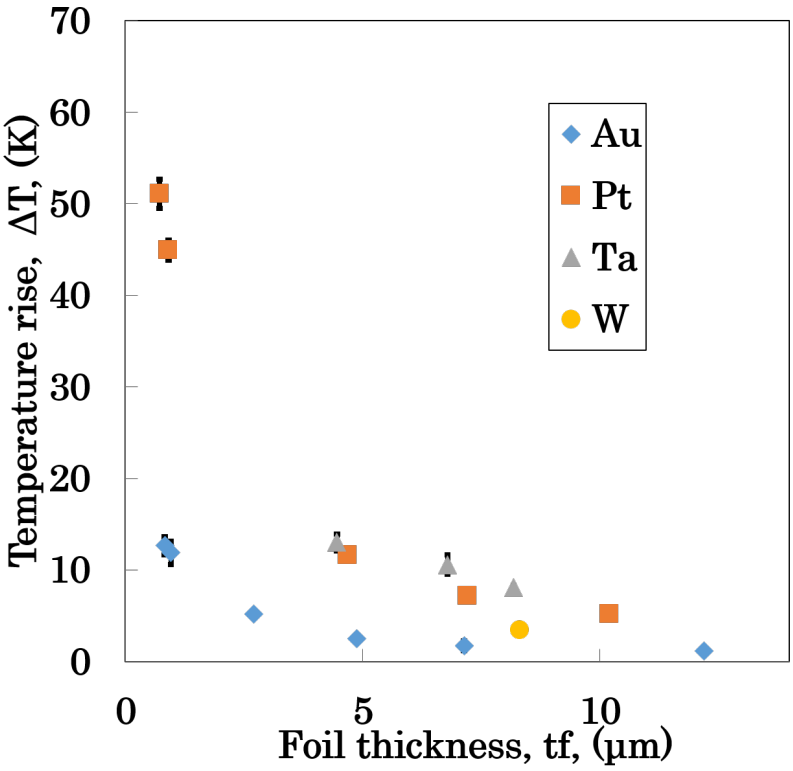

Figure 3.24: Temperature rise from room temperature with laser irradiation versus foil thickness

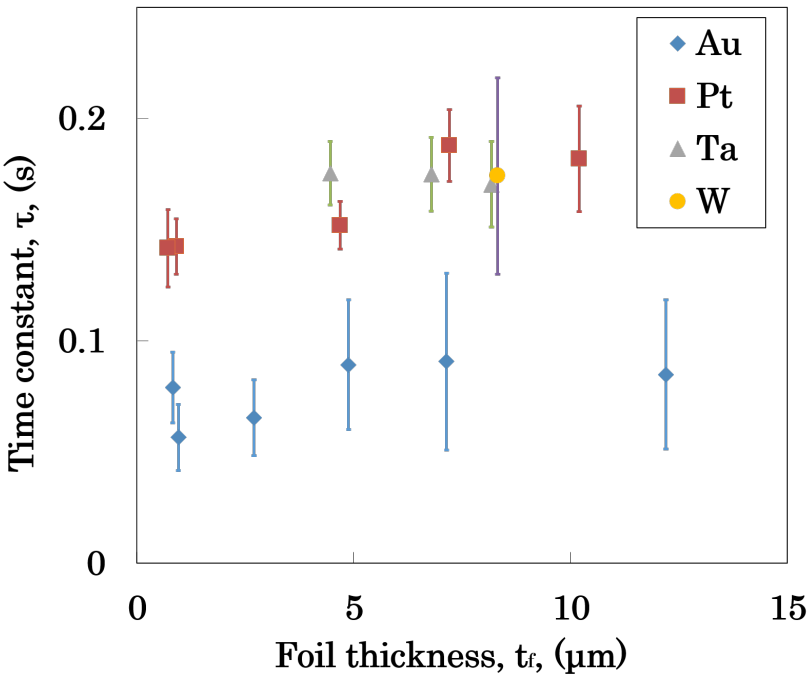

Figure 3.25: Time constant of temperature rise/decay with laser irradiation versus foil thickness

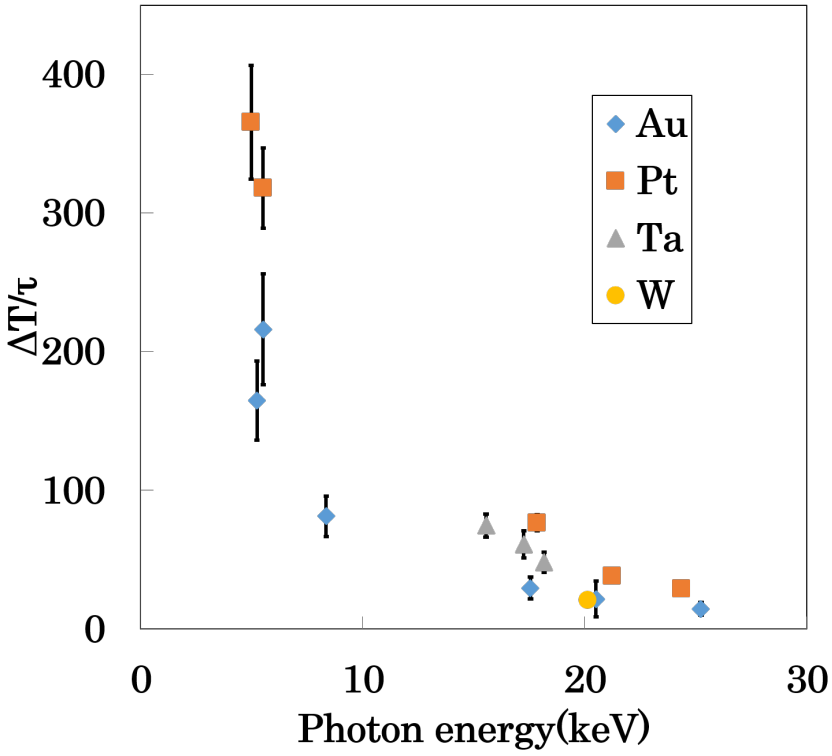

Figure 3.26: Index of sensitivity of IRVB foil versus maximum energy of stoppable photon

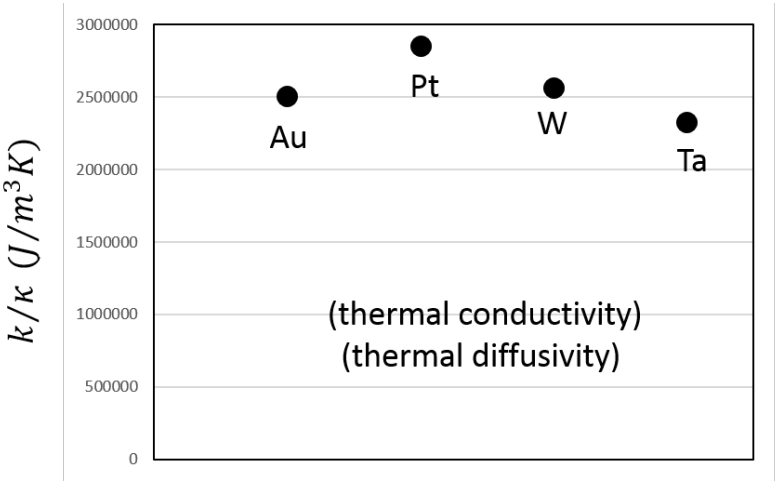

Figure 3.27: Theoretical value of thermal characteristics

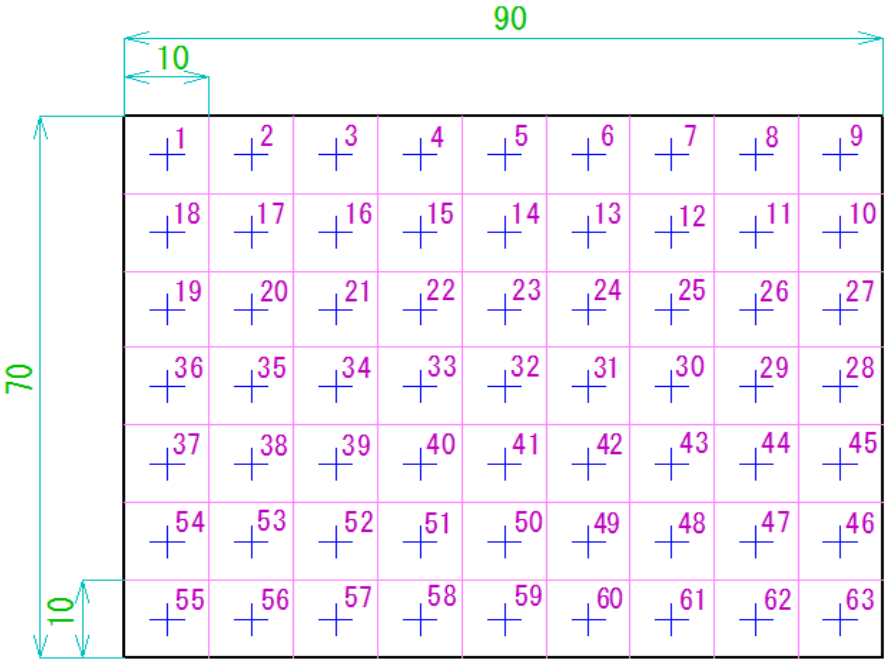

Figure 3.28: Irradiation points on the evaluated foil

Figure 3.29: Setting for foil cariblation setting

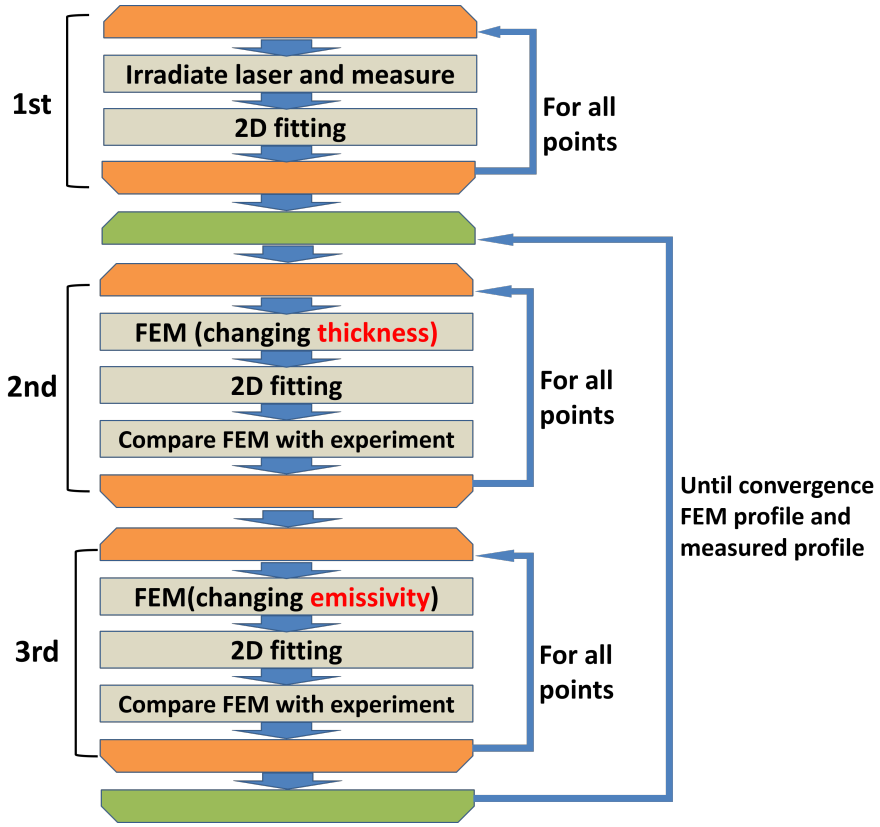

Figure 3.30: Foil calibration flow chart

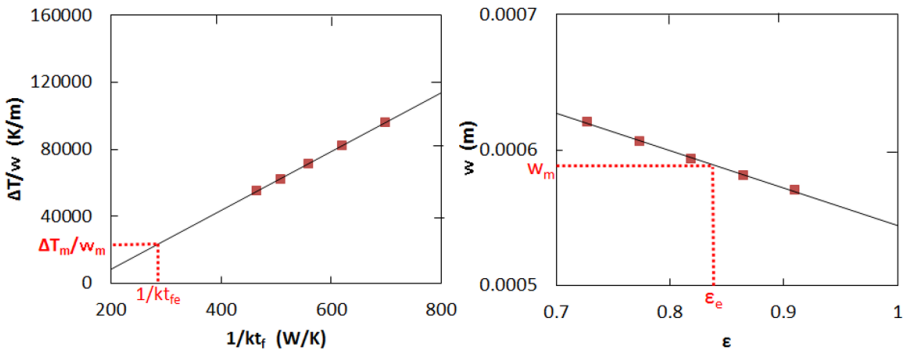

Figure 3.31: Estimation from fitting parameters. For thickness (left) and emissivity (right), at irradiation point 32(foil center). ΔT_m and w_m are measured values. t_{fe} and ϵ_e are estimated values.

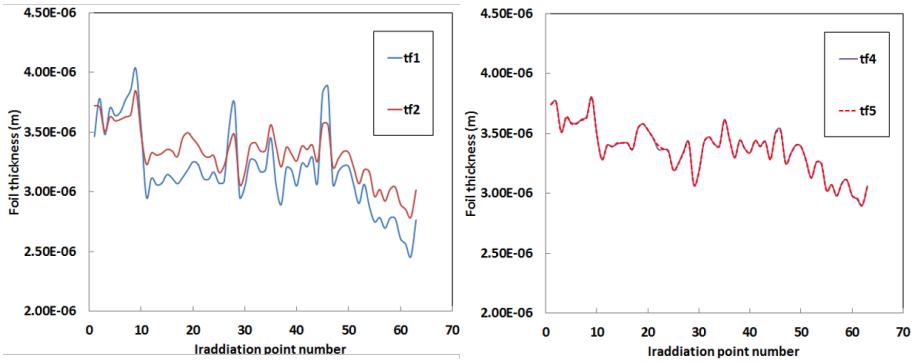

Figure 3.32: Distribution of the evaluated effective thickness on the IRVB foil

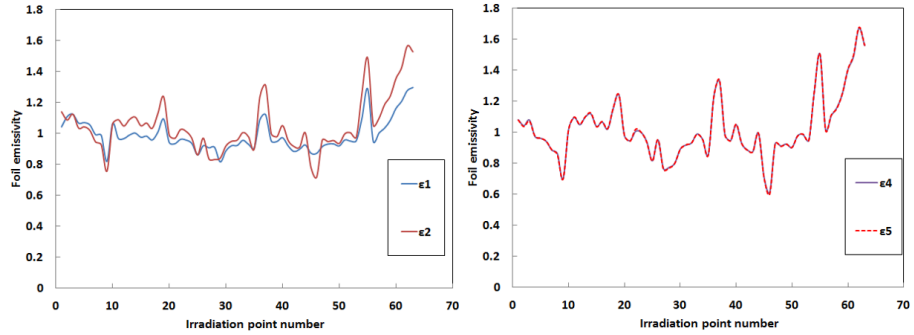

Figure 3.33: Distribution of the evaluated effective emissivity on the IRVB foil

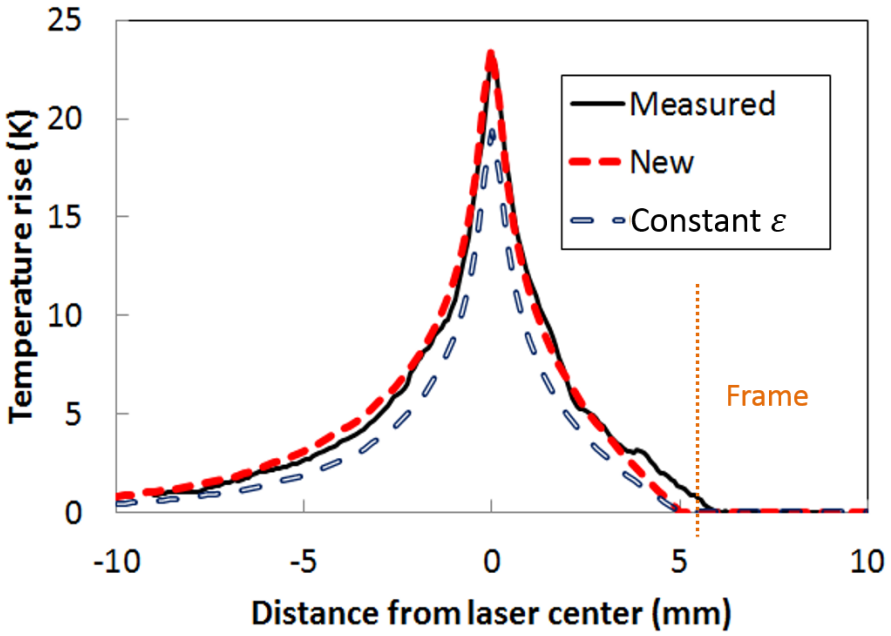

Figure 3.34: Temperature distribution with laser irradiation. Measured temperature(black), calculated temperature with evaluated parameters using new calibration technique(red) and calculated temperature with evaluated parameters using conventional technique(blue)

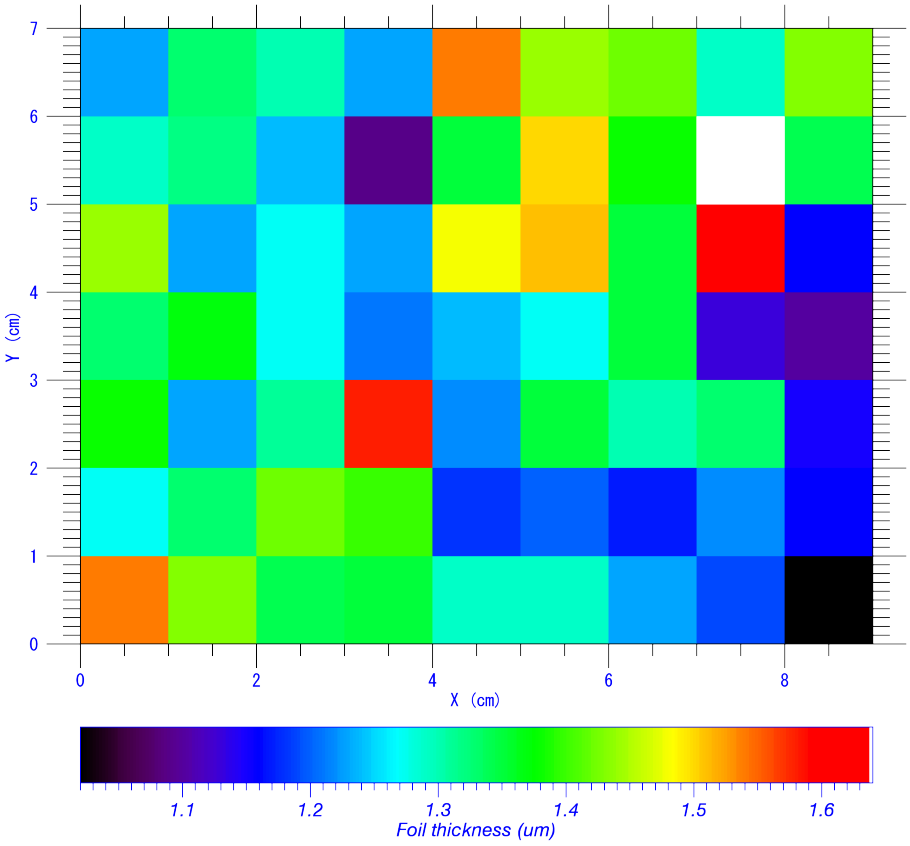

Figure 3.35: Estimated distribution of effective thickness

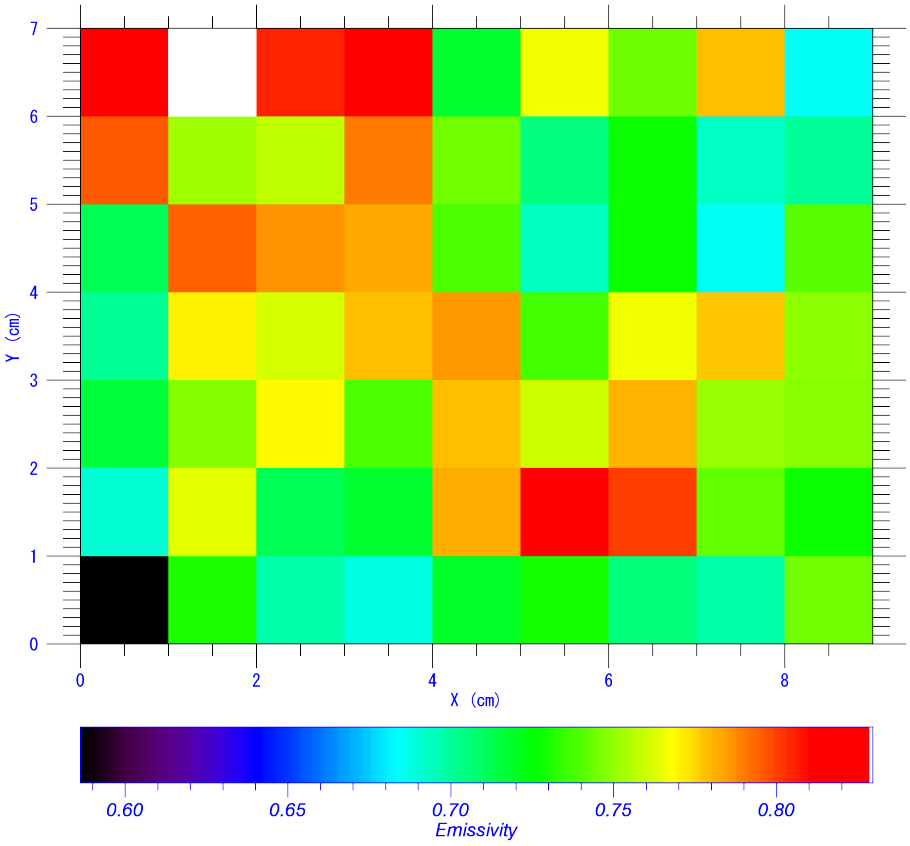

Figure 3.36: Estimated distribution of effective emissivity

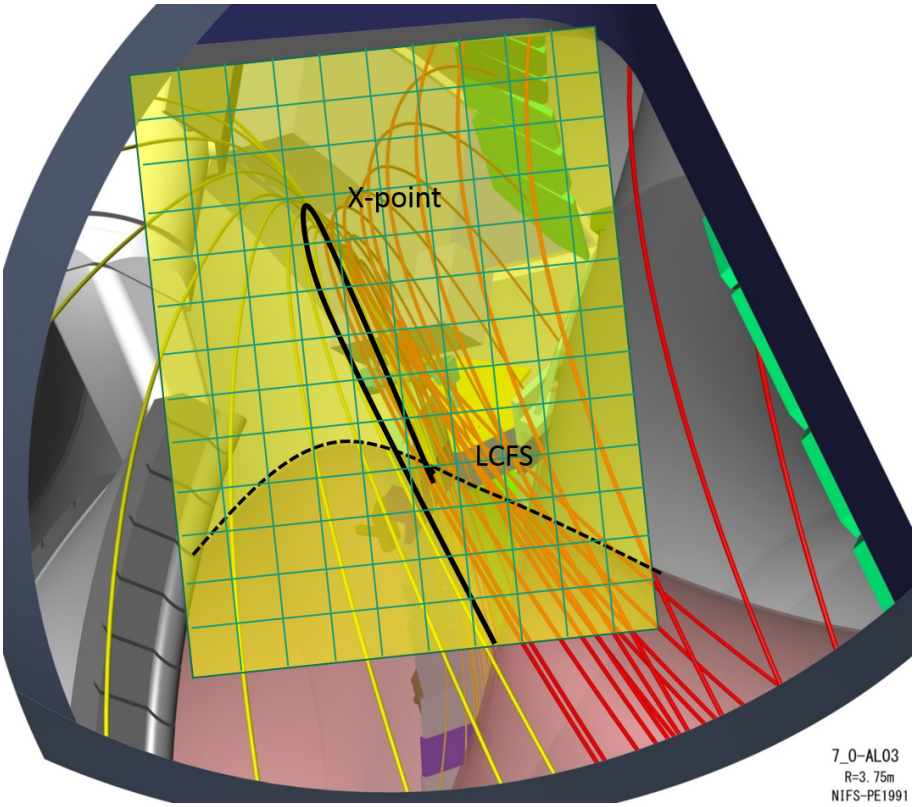

Figure 3.37: Field of view and channels for 7-O imaging spectrometer. Red and yellow lines are magnetic field lines. Black line is X point. Black dashed line is LCFS.

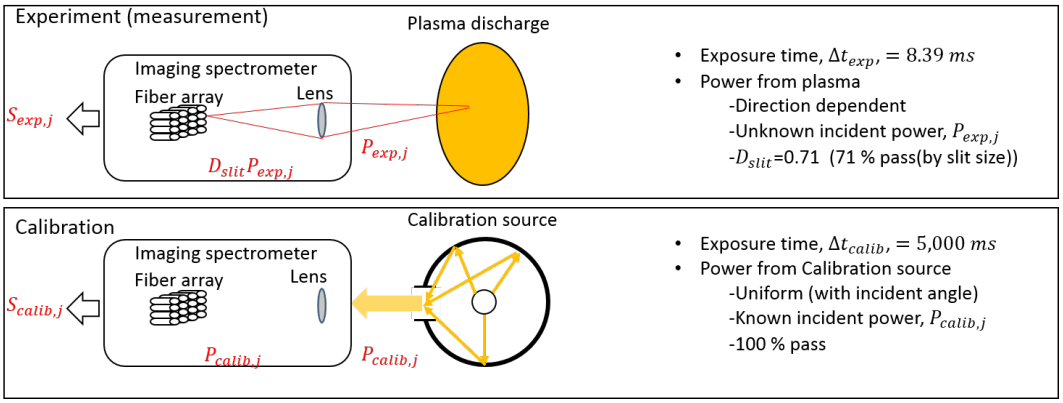

Figure 3.38: Comparison between calibration and experiment

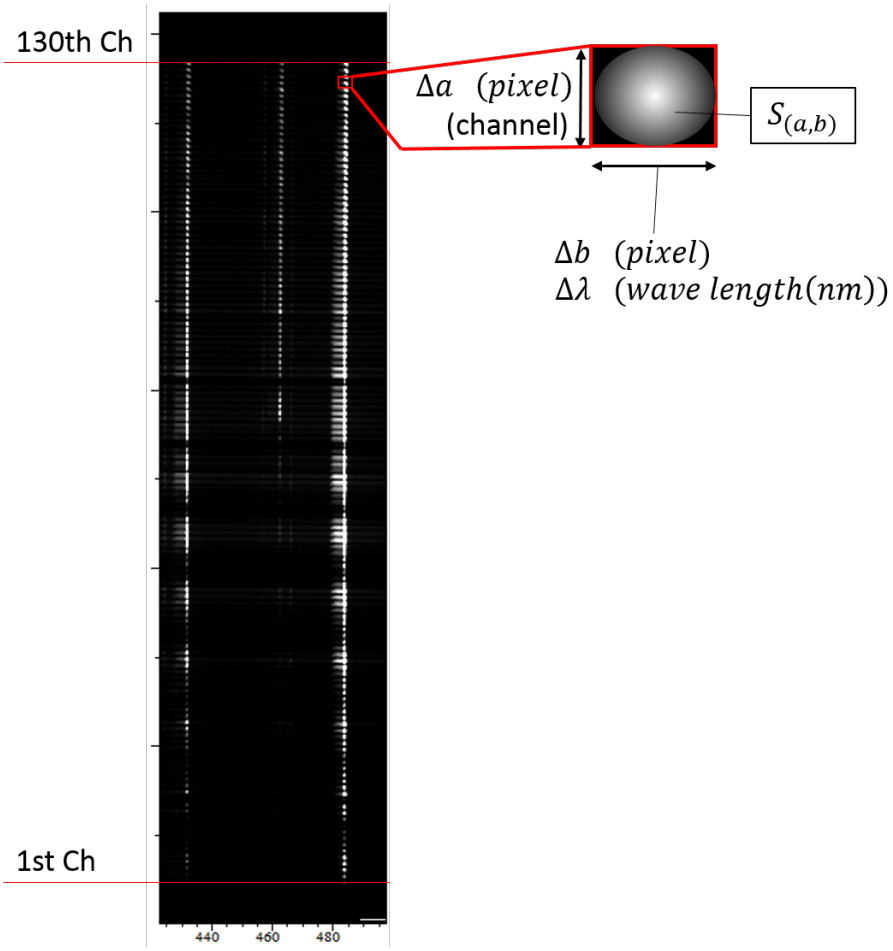

Figure 3.39: Raw data image of imaging spectrometer

Bibliography

[1] A. Komori et al., Fusion Sci. Technol., 58, 1(2009)

[2] The Japan Society of Mechanical Engineers, "Heat transfer" (The Japan Society of Mechanical Engineers, Tokyo, 2005) (in Japanese)

[3] B. J. Peterson et al., Plasma Fusion Res. 2, S1018(2007)

[4] G. B. Rybicki et. al., (1979) Radiative Processes in Astrophisics (Wiley vch, Weinheim, 1985)

[5] Center for X-ray Optics, Lawrence Berkeley . National␣Laboratory,␣USA.␣http://henke.lbl.gov/optical_constants/atten2.html

[6] R. Sano et al., Plasma Fusion Res. 7, 2405039(2012)

4 Three dimensional tomographic analysis for radiation measurement

In this chapter, tools for 3D radiation measurement are developed for utilizing IRVBs for investigating the radiation collapse. IRVBs can observe the radiation integrated along the sight of each channel which has a pyramid beam shape. Measuring the 3D profile of the radiation source from the IRVB data requires accurate relations between these with a consideration of the broadened lines of sight. In the following sections, a measurement system with IRVBs is designed and examined. A complicated procedure of calculating the projection matrix between the 3D helical object and IRVB pixels is established with regard to the fields of view of the IRVBs and used for appropriating the geometrical layout of IRVBs. With a selected geometry, numerical tools for 3D tomography are developed in two approaches, that is, a straightforward algebraic approach of imaging and a parametric model fitting approach for feature extraction. The effectiveness of the tools is examined on some simulated projection data and also on typical experimental data of LHD. The simulation code EM3-EIRENE is used as a standard. A method of relative calibration among IRVBs is contrived for successfull 3D tomography.

4.1 EMC3-EIRENE impurity behavior model

EMC3-EIRENE is a code for simulating three dimensional edge transport in the equilibrium state of LHD plasma. The EMC3-EIRENE is a combination of the EMC3 code [1] and the EIRENE [2] code. EMC3 handles the fluid equations of electrons and ions with their energy and momentum. The EIRENE code is the transport code of neutral particles and based on the Boltzmann equation with collisional reactions such as ionaization and recombination. The EMC3-EIRENE code can handle the behavior of particles and facing components under the magnetic field.

In LHD, the EMC3-EIRENE code is used for the simulation of impurity transport outside of the last closed flux surface (LCFS). The simulation provides several plasma parameters and the emission from an impurity, such as the electron temperature and the radiation from carbon with each charge state. Since the results of this simulation code have a spatial resolution finer than the plasma voxels which are defined in Section 4.2, the resolution is reduced to that of the plasma voxels. Also, in this thesis, the total emission profile of carbon is used as a numerical phantom of the tomographic reconstruction test and given a role as a standard of the radiation profile. In Figure 4.15 (Section 4.4)a typical phantom is shown on its 2D profile in the vertical poloidal cross section of LHD with the voxellation of 3D image region which is described in the next section. The simulated profile has been calculated in the region without the divertor leg under the 3.9 m magnetic axis configuration, with an upstream electron density of $3.98 \times 10^{19} m^{-3}$, and an upstream electron temperature of $1.51 \times 10^{2} eV$. The narrow structure observed in the boundary region of plasma is an important test target for developing the tomographic imaging system in both hardware and software.

4.2 Measurement system with IRVBs in LHD

When 3D imaging is performed with measurement data that have information on the spatially integrated profile of the object, the solution space and the observation space should be defined. In the IRVB system of LHD, the solution space is a region of interest defined in the LHD plasma, and the observation space is defined on the pixels of the IRVB foils. The two spaces are correlated through a matrix called the projection matrix, whose elements relate each plasma-voxel to each IRVB pixel. The projection matrix is equivalent in substance to the fields of view (FoVs) of the IRVBs. From the standpoint of numerical analysis, the measurement system is composed of these three parts.

4.2.1 Region of interest and voxellation

The region of interest in LHD plasma is divided into voxels having the following dimensions in cylindrical coordinates: major radial, R, 5 cm (54 divisions); vertical, Z, 5 cm (52 divisions); toroidal, ϕ, 1° (360 divisions) for a total of 1,010,880 voxels. This division provides voxels of approximately cubic shape with about 5-centimeter sides. The width of the thinnest part of the LHD edge ergodic region can be covered nearly by one of these voxels. When the fields of view of the four IRVBs installed separately in LHD are combined into a single 3D tomography system, assumptions are applied to the plasma structure with an additional purpose of decreasing the size of the image reconstruction.

Firstly, the helical periodicity of the plasma structure is assumed in the toroidal direction. In addition, the radiation source $S(r, \phi, z)$ in plasma is assumed to repeat itself every half period of magnetic field (18 degrees toroidally) with a symmetry of

$$S(r, \phi, z) = S(r, \pi/5 - \phi, -z) \tag{4-2-1}$$

Under this assumption, the fields of view of IRVBs located at different toroidal positions can be combined in image reconstruction as if all of them exist in a single half field period. Secondly, plasma-voxels in the region where no plasma is expected, such as near the wall, is neglected by masking. The mask in each poloidal cross section is an ellipse which will cover the radiation region expected from the EMC3-EIRENE simulation. The total number of plasma-voxels is decreased to 323,760 by the masking and furthermore, to $16,188 (= 323,760/20)$ by the above assumptions of periodicity and symmetry. Plasma behaviors consistant with the assumptions appear in EMC3-EIRENE simulations. However, it has been reported that the assumptions are invalidated in some plasma conditions of LHD such as discharges in which magnetic islands appear. Therefore the above design of the region of interest cannot be applied to plasmas in such kinds of discharges particularly with magnetic island configulations. In this thesis, the plasma voxellation in the region of interest, which is relieved by masking and with the assumptions, is used for 3D measurement.

4.2.2 Calculation of projection matrix for IRVBs

For the 3D measurement with the IRVB system, it is required to obtain a projection matrix that correlates the region of interest with the IRVB pixels, which are defined on the IRVB foils. Because each IRVB has a field of view with a pyramid beam, which is introduced by a small aperture, the projection matrix cannot be handled simply as a line integration along the sight path. The projection matrix is calculated as illustrated in Figure 4.2 [4].

Firstly, the volumes of all the plasma-voxels seen by each IRVB pixel are calculated as in Figure 4.2(a). In the present IRVB installations on LHD, the FoV of each pixel goes

through a square aperture with 4mm or 8mm sides. The FoV is calculated by tracing the sight-line every 1cm step, from the center of pixel to the center of aperture until the line hits the first wall. The width of the FoV after passing through the aperture is calculated as

$$\begin{aligned} w(i) &= l_{ap}\frac{i\Delta x - x_c}{l_{(ap-pix)} - x_c} \\ x_c &= \frac{l_{ap-pix}l_{pix}}{l_{pix} + l_{ap}}, \end{aligned} \tag{4-2-2}$$

where l_{ap} is the length of the aperture side, l_{pix} is the length of the IRVB pixel side, l_{ap-pix} is the distance between the aperture and the foil, $\Delta x(= 1cm)$ is the step size of tracing, and i is the index of the step. When the small FoV volume of size $(w(i) \times w(i) \times \Delta x)$ is in a plasma voxel, the volume is judged as a seen volume. This calculation requires that the small FoV volume is sufficiently smaller in size than the plasma voxel in order to provide sufficient accuracy. The width $w(i)$ will become larger with the step number, i. When $w(i)$ become larger than Δx, the FoV is divided into pieces with equal vertical and horizontal widths. Secondly, the solid angles from the obtained small FoV volumes to each IRVB pixel are calculated as in Figure 4.2(b). The purpose is to estimate what percentage of the total emission at the small volume reaches the IRVB pixel. Because some portion of the view from the seen voxel to the IRVB pixel is blinded by the aperture edge, the solid angle Ω is calculated by removing the blinded angles.

After the first and second steps are carried out for all the IRVB pixels, the element of the projection matrix which defines the influence of the emission from the n-th plasma voxel to the m-th IRVB pixel is obtained as

$$h_{m,n} = \sum_k \frac{V_{k,m,n}\Omega_{k,m,n}}{4\pi}, \tag{4-2-3}$$

where $V_{k,m,n}$ is the volume of the k-th small FoV volume, $\Omega_{k,mn}$ is the solid angle from the k-th volume to the m-th IRVB pixel and k is the volume index on the inside of the n-th voxel. When Δx is small enough, the projection matrix is determined by the aperture and pixel sizes, l_{ap}, l_{pix}, the distance between aperture and foil, the position of the aperture, and the position of the foil. Projection matrices are calculated for the four installed IRVBs and combined in a single matrix with the assumption of helical periodicity and symmetry given by Equation 4-2-1.

The projection matrix so-obtained provides two pieces of information. One of these is the information about the influence of the emission at each plasma-voxel on each pixel of the four IRVBs and is useful for tomographic analysis. The other is the information about the total number of non-visible plasma-voxels, which are defined as voxels that cannot be measured by any IRVBs. When the n-th plasma-voxel is non-visible, the projection matrix has a property of

$$h_n = \sum_m h_{m,n} = 0, \tag{4-2-4}$$

since all the elements of the n-th column are zero. This equation means that no IRVB has a FoV on the n-th plasma-voxel.

4.2.3 FoV design using projection matrices

Using Equation 4-2-4 as a criterion, the FoVs of four IRVBs have been designed to diminish the number of non-visible plasma-voxels. When a 3D radiation distribution is

reconstructed from IRVB images, it is desirable that all the plasma-voxels in the region of interest are seen by at least one IRVB. The FoVs have been designed with the following procedure. The projection matrix for each IRVB has been calculated repeatedly with small changes in the aperture position and also in the distance between the foil and the aperture. In this calculation, the sizes of aperture and pixel and the positions of foil were fixed. The combinations of the aperture position and the foil-aperture distance have been selected to make the total number of non-visible voxels nearly zero in the combined projection matrix. For the selected combinations, the FoV of each IRVB and the combined FoV are demonstrated in Figures 4.3 - 4.4 and Figure 4.5 in a binary plot discriminating the non-visible voxels.

In these figures and in the subsequent figures, the 3D distribution in LHD is plotted in a lexicographical sequence of poloidal cross sections with one degree increment of toroidal angle, starting with $\phi = 0.5^\circ$ at the upper left corner (vertical cross section) and ending with $\phi = 17.5^\circ$ at the lower right corner (horizontal cross section). The left and right sides of the cross section are the inner and outer sides of the torus, respectively. In Figure 4.5, one finds that a few voxels are still non-visible (black). These remaining non-visible voxels are in the walls and do not have any significant influence on the image reconstruction. Figure 4.6 shows the distribution of the total number of sight-lines that pass through each voxel. The total number was obtained by counting non-zero elements in the corresponding column of the projection matrix of each IRVB and by summing the counts over four IRVBs. It is observed that the sight-lines are dense in the core region of torus and sparse in the boundary region. The selected FoVs have been used in the IRVB measurement.

4.3 Nonparametric inversion by algebraic methods

As an analysis tool for the 3D radiation measurement, the algebraic method of tomographic inversion has been developed. For this analysis, the measument system described in Section 4.2 is employed as a 3D tomographic imaging system. The tomography system provides 3,196 measurement data as pixel values of four IRVBs, from which a 3D radiation profile is obtained on 16,188 plasma-voxels. Therefore, the system of tomography is specified with a projection matrix having a large size of $3,196 \times 16,188$.

4.3.1 Linear equation for inversion

When the source, s_n, at the n-th voxel is measured with a system which has an influence, $h_{m,n}$, from the n-th source voxel to the m-th measurement data, the obtained data p_m is expressed as

$$p_m = \sum_n h_{m,n} s_n. \tag{4-3-1}$$

The inverse calculation is a procedure to obtain a source profile from the measurement data and used in various fields such as medical CT [5]. Let us adopt an N-dimensional vector $\mathbf{S}$, an M-dimensional vector $\mathbf{P}$, and an $M \times N$ dimensional matrix H whose elements are s_n, p_m and $h_{m,n}$ respectively. Then, Equation 4-3-1 can be conveniently expressed in the following form:

$$H\mathbf{S} = \mathbf{P}. \tag{4-3-2}$$

$$\mathbf{S} = \begin{bmatrix} s_1 \\ \vdots \\ s_N \end{bmatrix}, \mathbf{P} = \begin{bmatrix} p_1 \\ \vdots \\ p_M \end{bmatrix}, \qquad \mathbf{H} = \begin{bmatrix} h_{1,1} & \cdots & h_{1,N} \\ \vdots & \ddots & \vdots \\ h_{M,1} & \cdots & h_{M,N} \end{bmatrix} \tag{4-3-3}$$

In the case of the measurement system of the IRVBs, $\mathbf{S}$ is a plasma radiation profile descretized with the plasma-voxels, $\mathbf{P}$ is a set of signals on IRVB pixels and H is the projection matrix. Equation 4-3-2 can be considered as a linear equation for unknown $\mathbf{S}$. When the number of unknowns, N, is smaller than the number of equations, M, it is said that the linear equation is "overdetermined". With the opposite condition, it is said that the linear equation is "underdetermined". Generally, an underdetermined equation is difficult to be "solved". In this thesis, the tomography with the measurement system of IRVBs is an underdetermined problem as far as the algebraic method are concerned. In this chapter, the least squares approach [5], [6] is described only for the underdetermined case of $M < N$.

4.3.2 Tikhonov regularization

Least squares method

With respect to Equation 4-3-2, the mean of the squared errors is written as

$$\Lambda(\mathbf{S}) \equiv (1/M)\|H\mathbf{S}-\mathbf{P}\|^2 = (1/M)(H\mathbf{S}-\mathbf{P})^T(H\mathbf{S}-\mathbf{P}) = (1/M)[\mathbf{S}^T(H^TH)\mathbf{S}-2\mathbf{P}^THS+\mathbf{P}^T\mathbf{P}] \tag{4-3-4}$$

for a projection matrix H and a data vector $\mathbf{P}$ that are disturbed with errors in evaluation and measurement, respectively. Because the source profile $\mathbf{S}$ that minimizes the square error $\Lambda(\mathbf{S})$ is required in the least squares method, let us differentiate the objective function $\Lambda(\mathbf{S})$ with the vector $\mathbf{S}$:

$$\frac{\partial}{\partial \mathbf{S}}\Lambda(\mathbf{S} = \frac{2}{M}(H^TH\mathbf{S} - H^T\mathbf{P}). \tag{4-3-5}$$

For the right side to be equal to a zero vector, we have

$$(H^TH)\mathbf{S} = H^T\mathbf{P}. \tag{4-3-6}$$

which is the so-called normal equation in the least squares method. If the inverse matrix $(H^TH)^{-1}$ existed, the least squares solution $\hat{\mathbf{S}}$ would be given as $\hat{\mathbf{S}} = (H^TH)^{-1}H^T\mathbf{P}$. However, whenever the linear equation 4-3-2 is underdetermined with $M < N$, the inverse $(H^TH)^{-1}$ does not exist as $detH^TH = 0$; the solution of Equation 4-3-5 is indefinite. This situation leads us to the Tikhonov idea of minimization under constraint.

Pseudo-inverse solution and TSVD

The Singular Value Decomposition (SVD) of H is given as

$$H = U\Sigma V^T, \tag{4-3-7}$$

$$U = [\mathbf{u_1}, \mathbf{u_2}, \cdots, \mathbf{u_M}], \tag{4-3-8}$$

$$V = [\mathbf{v_1}, \mathbf{v_2}, \cdots, \mathbf{v_M}], \tag{4-3-9}$$

Here U is an $M \times M$ matrix whose column vectors $\mathbf{u}_i$ (left singular vectors) are orthonormal with $\mathbf{u}_i^T\mathbf{u}_j = \delta_{i,j}$, and V is an $N \times M$ matrix whose column vectors $\mathbf{v}_i$ (right

singular vectors) are orthonormal with $\mathbf{v}_i^T\mathbf{v}_j = \delta_{i,j}$. The matrix Σ is a diagonal matrix with diagonal elements σ_i (singular values), which are arranged in descending order ($\sigma_1 \geq \sigma_2 \geq \cdots \geq \sigma_M \geq 0$). When H is a square matrix and fully ranked, the solution of Equation 4-3-2 can be obtained as

$$\hat{\mathbf{S}} = H^{-1}\mathbf{P}. \tag{4-3-10}$$

However the inverse matrix H^{-1} never exists for the non-square matrix H. A generalized method is to adopt the pseudo-inverse matrix H^+ and to write the solution as

$$\hat{\mathbf{S}}^+ = H^+\mathbf{P}. \tag{4-3-11}$$

Here, H^+ is produced from the SVD of H as

$$H^+ = V\Xi U^T. \tag{4-3-12}$$

where Ξ is a diagonal matrix whose diagonal elements are the reciprocals of the singular values, $1/\sigma_i$, and zeros for $\sigma_i = 0$ (smaller than the computer epsilon in practice). Equation 4-3-11 can be written as a series expansion of the following form:

$$\hat{\mathbf{S}}^+ = \sum_{i=1}^{M^+} \frac{\mathbf{u}_i^T\mathbf{P}}{\sigma_i}\mathbf{v_i}, \tag{4-3-13}$$

where M^+ is the number of non-zero diagonal elements of H^+. It is noted that the orthonormal vectors $\mathbf{v}_i$ work as the bases of the source profile $\hat{\mathbf{S}^+}$, and that the inner products $\mathbf{u}_i^T\mathbf{P}$ are the components of $\mathbf{P}$ in the directions of $\mathbf{u}_i$, that is, the orthonormal vectors $\mathbf{u}_i$ work as the bases of the projection data $\mathbf{P}$. So, the expansion coefficients $\mathbf{u}_i^T\mathbf{P}/\sigma_i$ may be interpreted as the solution in $U - V$ space that has been generated by the SVD of the projection matrix H. Additionally, it is known that $\hat{\mathbf{S}}^+$ is the least squares minimal norm solution of the linear equation $H\mathbf{S} = \mathbf{P}$.

Apparently, this pseudo-inverse solution $\hat{\mathbf{S}}^+$ is weak on the measurement noise which is implicitly contained in $\mathbf{P}$. When the noise is explicitly written by replacing $\mathbf{P}$ with $\mathbf{P} + \mathbf{e}$, Equation 4-3-13 becomes

$$\hat{\mathbf{S}}^+ = \sum_{i=1}^{M^+} \frac{\mathbf{u}_i^T(\mathbf{P}+\mathbf{e})}{\sigma_i}\mathbf{v_i} = \sum_{i=1}^{M^+} \frac{\mathbf{u}_i^T\mathbf{P}}{\sigma_i}\mathbf{v_i} + \sum_{i=1}^{M^+} \frac{\mathbf{u}_i^T\mathbf{e}}{\sigma_i}\mathbf{v_i}. \tag{4-3-14}$$

The second term in the right side, which represents the effect of noise, tends to increase when the singular value σ_i decreases faster than $\mathbf{u}_i^T\mathbf{e}$ with the increase of i . Particularly, in the pseudo-inverse solution, which uses all the singular values larger than the computer epsilon, the noise will easily be enhanced. Therefore, the ratio of the maximal and minimal singular value, σ_1/σ_M, namely the condition number, is a useful parameter to guess the strength of noise enhancement in the inversion. From this viewpoint on Equation 4-3-13, truncating the solution $\hat{\mathbf{S}}^+$ with an appropriate cut-off term number M_c instead of $M^+(M_c < M^+)$ looks useful to get a good effect of noise suppression. This method of inversion is called the method of truncated SVD (TSVD)[7].

Advance to Tikhonov regularization

Another approach to avoid the noise effect is to take a formulation of minimization under constraint. Let us consider that a cost function $\phi(\mathbf{S})$ should be minimized under the constraint that the mean of the squared errors $(1/M)\|H\mathbf{S} - \mathbf{P}\|$ is equal to a constant.

One may imply that the constant corresponds to the magnitude of the noise contained in the measurement data $\mathbf{P}$. With respect to the underdetermine equation $H\mathbf{S} = \mathbf{P}$, this determination of the solution is called the regularization. The solution so-regularized s obtained by minimizing the following Lagrange function $\Lambda(\mathbf{S})$ in place of Equation 4-3-4:

$$\Lambda(\mathbf{S}) = (1/M)\|H\mathbf{S} - \mathbf{P}\|^2 + \gamma\phi(\mathbf{S}), \tag{4-3-15}$$

where γ is an unknown positive-valued constant. Contrary to the Lagrange theorem, the unknown constant is attached to the second term in inverse problem theory and called the regularization parameter. As the value of γ is increased, the effect of regularization becomes larger. Also, the cost function $\phi(\mathbf{S})$ is often called the penalty function. When the squared norm $\|\mathbf{S}\|^2$ is chosen for $\phi(\mathbf{S})$, the regularization is called the Tikhonov regularization [8]. The solution is obtained as follows.

$$\frac{\partial}{\partial \mathbf{S}}\Lambda(\mathbf{S}) = \frac{\partial}{\partial \mathbf{S}}[\frac{1}{M}\|H\mathbf{S} - \mathbf{P}\|^2 + \gamma\|\mathbf{S}\|^2] = \frac{2}{M}(H^T H\mathbf{S} - H^T\mathbf{P}) + 2\gamma\mathbf{S}, \tag{4-3-16}$$

For the right side to be a zero vector, we have an equation

$$(H^T H + M\gamma I)\mathbf{S} = H^T\mathbf{P}. \tag{4-3-17}$$

where I is the N-dimensional identity matrix.

In contrast to Equation 4-3-6, the inversion of the coefficient matrix in this extended normal equation becomes meaningful owing to the added identity matrix term. Therefore, we obtain the solution

$$\hat{\mathbf{S}} = (H^T H + M\gamma I)^{-1} H^T\mathbf{P}. \tag{4-3-18}$$

With the singular decomposition of H in Equation 4-3-7, the solution can be rewritten in the form of a series expansion

$$\hat{\mathbf{S}} = \sum_{i=1}^{M} w_i(\gamma)\frac{\mathbf{u}_i^T\mathbf{P}}{\sigma_i}\mathbf{v}_i \tag{4-3-19}$$

with

$$w_i(\gamma) = \frac{1}{1 + M\gamma/\sigma_i^2}. \tag{4-3-20}$$

In comparison with Equation 4-3-13, the meaning of Equation 4-3-19 is clear. From the definition of the singular value series in SVD, it is noted that, with the increase of i, $w_i(\gamma)$ decreases monotonically with the singular value σ_i. Accordingly, the Tikhonov solution in Equation 4-3-19 is a modification of the truncated SVD solution, using the window function $w_i(\gamma)$. When the coefficient matrix H is ill-conditioned with a large condition number σ_1/σ_M, $w_i(\gamma)$ decreases rapidly as a function of i and, as a result, the large-i terms where the noise contained in $\mathbf{P}$ is enhanced otherwise are well truncated. The same effect of noise suppression is obtained when the regularization parameter γ is increased. While the singular value series σ_i of H is the property of the measurement system of IRVBs, the regularization parameter γ should be appropriately chosen for a good regularization of the solution. To choose the optimal value of γ, the Generalized Cross Validation (GCV) is effective as a criterion [9]. The GCV is given by

$$GCV(\gamma) = \frac{\varepsilon^2(\gamma)}{[1 - \frac{1}{M}\sum_{i=1}^{M} w_i(\gamma)]^2}. \tag{4-3-21}$$

where ε^2 denotes the mean square error between the projection data $\mathbf{P}$ (the set of IRVB images) and the projection of the reconstructed profile $\hat{\mathbf{S}}$, that is,

$$\varepsilon^2(\gamma) = \frac{1}{M}\|H\hat{\mathbf{S}} - \mathbf{P}\|^2. \tag{4-3-22}$$

As a function of γ, $GCV(\gamma)$ takes a minimum when the monotonical decrease of $\varepsilon^2(\gamma)$ is compensated by a faster decrease of the denominator. The value of γ minimizing $GCV(\gamma)$ provides the optimal reconstruction $\hat{\mathbf{S}}$ in a statistical sense. The Tikhonov regularization with the criterion of minimum GCV is the standard method of inversion and has also been used for nuclear fusion research [10] [11] [12].

Equation 4-3-19 also means that, as well as the pseudo-inverse and TSVD regularizations, the Tikhonov regularization keeps the linearity of $\hat{\mathbf{S}}$ as a function of the data vector $\mathbf{P}$. Once the SVD of H is achieved, the calculation of $\hat{\mathbf{S}}$ is direct (not iterative) and easy for the change of $\mathbf{P}$, that is, for the purpose of pursuing the time evolution of plasma. On the other hand, the linearity allows the reconstructed emissivity profile to take negative values. To avoid the appearance to negative values, it is necessary to use nonlinear methods such as the maximum entropy method [13] and the Hopfield neural network [14], which need iterative procedures of calculation.

Within the scheme of linearity, the Tikhonov regularization can be extended by introducing the Laplacian matrix. The identity matrix, I, is replaced by the Laplacian matrix C as $\phi(\mathbf{S}) = \|C\mathbf{S}\|^2$, which is a direct evaluation of the roughness of the reconstructed profile. While $\|\mathbf{S}\|^2$ and the entropy function lead to a sort of smoothing due to the properties of the convex function, the minimization of the roughness leads to an effective smoothing (a good statistical stability) of the reconstructed profile. The Laplacian matrix C is calculated with regard to the geometry of the 3D reconstruction region in LHD. When the Laplacian matrix is used, the Tikhonov regularization is often called the Phillips regularization. With the penalty function $\phi(\mathbf{S}) = \|C\mathbf{S}\|^2$, the Tikhonov solution in Equation 4-3-18 becomes

$$\hat{\mathbf{S}} = (H^T H + M\gamma C^T C)^{-1} H^T \mathbf{P}. \tag{4-3-23}$$

With $A = HC^{-1}$, this solution is rewritten as

$$\hat{\mathbf{S}} = C^{-1}(A^T A + M\gamma I)^1 A^T \mathbf{P}. \tag{4-3-24}$$

Then, with the singular value decomposition

$$HC^{-1} = U\Sigma V^T \tag{4-3-25}$$

the solution can be rewritten as

$$\hat{\mathbf{S}} = \sum_{i=1}^{M} w_i(\gamma)\frac{\mathbf{u}_i^T \mathbf{P}}{\sigma_i} C^{-1}\mathbf{v}_i \tag{4-3-26}$$

with

$$w_i(\gamma) = \frac{1}{1 + M\gamma/\sigma_i^2}. \tag{4-3-27}$$

It should be noted that the singular values σ_i and vectors $\mathbf{u}_i$ and $\mathbf{v}_i$ are those of HC^{-1}, and that the bases of the solution are changed from $\mathbf{v}_i$ to$C^{-1}\mathbf{v}_i$, which are not orthonormal in general. The linearity of the solution with respect to the measurement data is conserved. The Phillips regularization has also been applied to 2D tomography by tangential view in the Textor tokamak [15], [16] and LHD [17].

In this thesis, the study focuses on the linear regularization of Tikhonov-Phillips for the first success of the 3D tomography of LHD plasma. The negative values that may appear in the reconstructed profile should rather be advantageous for revealing the deficiencies in calculating the projection matrix, H, and in calibrating the system of IRVBs.

4.4 Development of algebraic methods for 3D tomography

In this chapter, the 3D tomographic inversion with Tikhonov-Phillips regularization is examined on numerical phantoms. The Laplacian matrix C is extended for image reconstruction in the 3D helically bounded region of interest, and a numerical technique is developed to get the inverse matrix of C, which is very large in size.

4.4.1 Test of Tikhonov regularization with identity matrix

The algebraic method of Tikhonov with the identity matrix is examined on the image reconstruction of large size with respect to the 3D tomography system of IRVBs. Using the projection matrix calculated in Section 4.2, the software is tested on some numerical phantoms of simple 3D structure and with a simulated profile from EMC3-EIRENE. The flow of the numerical simulation is as follows.

Step1 Projection from a given 3D profile

As the first step, projection images, $\mathbf{P}_o$, are calculated from a given model profile $\mathbf{S}_o$ as

$$\mathbf{P}_o = H\mathbf{S_o}. \tag{4-4-1}$$

To simulate the projection data $\mathbf{P}$, at four IRVBs, each of the calculated projection images is corrupted with a zero-mean additive Gaussian noise which has a standard deviation as large as 10 percent of the mean value of projection image. The values of standard deviation are comparable with those observed in actual IRVB measurement without plasma discharge.

Step2 Reconstruction from projection images (tomographic inversion)

As the second step, tomographic inversion from the projection images is carried out with the Tikonov regularization method. The reconstructed profile $\hat{\mathbf{S}}$ is compared with the original profile of the phantom $\mathbf{S}_o$ The accuracy of reconstruction is evaluated with a normalized error $\delta^2(\gamma)$ which is defined as

$$\delta^2(\gamma) = \frac{\|\hat{\mathbf{S}} - \mathbf{S}_o\|^2}{\|\mathbf{S}_o\|^2}. \tag{4-4-2}$$

Step3 Projection from the reconstructed profile

As the third step, 4 IRVB images $\hat{\mathbf{P}}$ are calculated from the reconstructed profile $\hat{\mathbf{S}}$ as $\hat{\mathbf{P}} = H\hat{\mathbf{S}}$ and compared with the original projection $\mathbf{P}_o$ and the noise corrupted data $\mathbf{P}$. The recovered projection $\hat{\mathbf{P}}$ should be similar to the original $\mathbf{P}_o$ and also fit the data $\mathbf{P}$ in a reasonable manner. The reconstructed and original projections should be matched for reasonable calculations. Fitting to the data is evaluated in the mean square error $\epsilon^2(\gamma)$ and the GCV, which are given by Equations 4-3-21 and 4-4-2. The value of regularization parameter, γ, minimizing the GCV is chosen as its optimal value.

The uniform, tube, thin tube and core radiation profile shown in Figure 4.8 have been employed as phantoms $\mathbf{P}_o$. A profile produced by the EMC-3 EIRENE simulation code of impurity behavior and shown in Figure 4.9 has also been employed as another phantom. Figures 4.10-4.13 shows the results of the inversion for the regularization parameter, γ, that has been optimized with GCV. These reconstructed profiles have a large number of positive and negative artifacts due to the ill-condition of Equation 4-3-2. However, these profiles are similar to the original profiles in features such as the location of the strongest radiation and the outline of the 3D structure. Table 4.1 shows an evaluation of the reconstruction results. Since the error between the projections of the model and the reconstructed profile is small enough, it can be stated that the calculations have been achieved reasonably. However, the normalized reconstruction errors δ^2 are large and evaluated as around 0.80. The total radiation is reproduced with around 10 percent error.

In these simulations, the criterion of minimum GCV has worked well. It has been found that the value of γ chosen with GCV provides reasonable reconstruction for the IRVB tomography system in LHD. Figure 4.7 shows the behavior of $GCV(\gamma)$, $\epsilon^2(\gamma)$ and the normalized reconstruction error $\delta^2(\gamma)$ in reconstructing the EMC3-EIRENE phantom. While $\epsilon^2(\gamma)$ monotonically decreases with γ, $GCV(\gamma)$ is minimized for a value of γ. The γ value corresponds closely to the minimum of $\delta^2(\gamma)$, which provides the best reconstruction of the original profile. This result shows that the GCV is effective for the optimization of γ. The SVD of the matrix H has been achieved with the function "LA_SVD" of the software IDL. The condition number was 3.96×10^6.

Table 4.1: Results of reconstruction in numerical tests of Tikhonov regularization. Table elements are reconstruction error δ^2, projection error between original and reconstructed ϵ^2, total numbers of negative voxels and positive voxels in the reconstructed profile, total radiation power in original (model) and reconstructed profile.

	Uniform	Tube	Thin tube	Core	Simulated
Error in profile, δ^2	0.413	0.728	0.832	0.461	0.85
Error in projection, ε^2	0.048	0.052	0.056	0.052	0.051
Number of positive voxels	15714	11463	9899	11343	9249
Number of negative voxels	59	1973	2634	1527	2906
Total radiation (original) (MW)	54.3	14.5	7.81	16.4	1.75
Total radiation (reconstructed) (MW)	48.6	14.9	7.25	14.0	1.81

4.4.2 Laplacian matrix for regularization

The Tikhonov regularization can be extended with the Laplacian matrix C (Phillips regularization) in order to suppress noisy artifacts in the reconstructed profile. The matrix C for the 3D tomography system in LHD is calculated with the following procedure.

Laplacian matrix calculation

In Figure 4.14, the essential part of the Laplacian matrix in the 2D case is shown as a visual map in the real space. Each center pixel has -4 and its four adjacent pixels have

1. This essential form is modified into 3D form for 3D tomography. The 3D form has -6 at the center voxel and 1 at its six adjacent voxels as in Figure 4.15. When the voxels are scanned sequentially along R, Z and ϕ axes in the 3D reconstruction region of LHD, the k-th voxel is given a value Δ_k as follows:

$$\Delta_k \begin{cases} = -6 & (k = 936r + 18z + \phi) \\ = 1 & (k = 936r + 18z + \phi \pm 1) \\ = 1 & (k = 936r + (18 \pm 1)z + \phi) \\ = 1 & (k = 936(r \pm 1) + 18z + \phi) \\ = 0 & (otherwise) \end{cases} \tag{4-4-3}$$

for the integer indices $r = 0 \sim 53$, $z = 0 \sim 51$, and $\phi = 0 \sim 17$ in the directions of the major radius R, the vertical coordinate Z, and the toroidal angle ϕ, respectively. Here we have $936 = 52 \times 18$ in relation to the $Z - \phi$ scan. The 3D reconstruction region is helically twisted and outlined by masking. Whenever the adjacent voxel goes outside of the region corresponding to the r and z ranges, the center voxel is added with 1. Additionally, when the adjacent voxel with $\phi \pm 1$ goes outside of the reconstruction region, a voxel at $z = 52 - z$ is added with 1 using the toroidal symmetry, which is expressed by Equation 4-2-1.

From the resultant series of voxel values Δ_k , we have the matrix C of 3D Laplacian operation. Its original is a $50,544$-dimensional square matrix C_o with the following elements $c^o_{i,j}$:

$$c^o_{i,j} \begin{cases} = -6 & (j = i) \\ = 1 & (j = i \pm 1) \\ = 1 & (j = i \pm 18) \\ = 1 & (j = i \pm 936) \\ = 0 & (otherwise) \end{cases} \tag{4-4-4}$$

for $i = 1 \sim 50,544$, as illustrated in the upper part of Figure 4.16. Then, this original matrix is modified according to the masking which was described in Section 4.2. When the k-th voxel is masked in the real space of LHD, both the k-th column and row are masked and cut off as in the lower part of the same figure. If any element in the masked $k-th$ column has a positive value, the diagonal element on the row to which the positive-valued element belongs is added with 1. With this procedure, the $16,188$-dimensional square matrix of the 3D Laplacian operation has been produced for the helically twisted volume of the LHD plasma.

Inverse of Laplacian matrix

Equations 4-3-25 and 4-3-26 indicate that the modification into the Phillips regularization needs the inverse matrix of the 3D Laplacian matrix C obtained above. However the Laplacian matrix is a huge matrix ($16,188 \times 16,188$), the calculation of the inverse matrix easily has a computational error. Therefore, two methods are examined.

The first method is a direct calculation of C^{-1}. The calculated C^{-1} is provided for the SVD in Equation 4-3-25 and used again for calculating the expansion bases $C^{-1}\mathbf{v}_i$ in Equation 4-3-26.

The second method is an inverse calculation with the Cholesky decomposition [18]. In general, a matrix of the form A^TA is symmetric and positive definite. Thus, the matrix C^TC in Equation 4-3-23 can be decomposed to the Cholesky form

$$C^TC = R^TR, \tag{4-4-5}$$

where R is an upper triangular matrix. With this relation, the solution in Equation 4-3-23 becomes

$$\hat{\mathbf{S}} = (H^T H + M\gamma R^T R)^{-1} H^T \mathbf{P}. \tag{4-4-6}$$

This equation is formally the same as Equation 4-3-23, having the matrix R in place of C. Analogically, the SVD

$$HR^{-1} = U\Sigma V^T \tag{4-4-7}$$

allows one to rewrite the right side of Equation 4-4-6 as

$$\hat{\mathbf{S}} = \sum_{i=1}^{M} w_i(\gamma) \frac{\mathbf{u}_i^T \mathbf{P}}{\sigma_i} R^{-1} \mathbf{v}_i \tag{4-4-8}$$

with

$$w_i(\gamma) = \frac{1}{1 + M\gamma/\sigma_i^2}. \tag{4-4-9}$$

Here, it should be noted that the singular values σ_i and the singular vectors $\mathbf{u}_i$ and $\mathbf{v}_i$ are those of HR^{-1}; they are different from only those of HC^{-1} in Equation 4-3-25 but also those of H in Equation 4-3-17. The GCV expression in Equations 4-3-21 and 4-3-22 remains valid for the inversion problems that are defined with the new matrices HC^{-1} and HR^{-1}.

Based on Equation 4-3-23, the solutions in Equations 4-3-26 and 4-4-8 are the same as long as the inverse matrices C^{-1} and R^{-1} and the related SVDs are accurately calculated. One expects that a significant difference in computational accuracy may appear between C^{-1} and R^{-1} as the size of the $N \times N$ matrices C and R becomes large. While the Laplacian matrix C tends to be ill-conditioned, it is expected that the upper triangular matrix R remains so well-conditioned that the inverse R^{-1} is easily calculated. Comparison has been made using the software IDL. The Cholesky decomposition of $C^T C$ and the calculation of C^{-1} and R^{-1} have been carried out using the LA_CHOLDC function and the LA_INVERT function, respectively. The inverse calculation has been examined on the normalized square errors, which are defined as

$$\varepsilon_1^2 = \frac{\|C^{-1}C - I\|^2}{\|I\|^2}, \varepsilon_2^2 = \frac{\|R^{-1}R - I\|^2}{\|I\|^2} \tag{4-4-10}$$

using the Frobenius norm of matrix. Results of calculation show $\varepsilon_1^2 = 0.36$ and $\varepsilon_2^2 = 5 \times 10^{-15}$, that is, a failure and a success in calculating the inverses C^{-1} and R^{-1}, respectively. Hereafter, the second method using the Cholesky decomposition is employed for the Phillips regularization of image reconstruction. The condition number of the matrix HR^{-1} was 1.35×10^{15}.

4.4.3 Effect of Laplacian matrix in numerical simulation

To evaluate the effect of adopting the Laplacian matrix, the same numerical test of inversion as in Section 4.4 has been carried out.

Numerical simulation

The model profiles and the noise-corrupted projection data in Section 4.4 have been employed again. Figure 4.17-4.19 and Table 4.2 show the results of the inversion for the values of γ which have been optimized with the criterion of minimum GCV. The reconstructed profiles have a remarkable tendency in reconstruction quality. The reconstructed profiles of uniform and core models in Figure 4.17(a) and Figure 4.18(d)

are fine and show the high reproducibility of the original profiles with much decreased reconstruction error and with higher fidelity to the projection data. A similar improvement is observed also on the tube model. On the thin tube model and on the simulated model of EMC3-EIRENE, however, the reconstructed profiles are smoothly broadened. In spite of a good effect of diminishing noisy artifacts, the spatial resolution is lowered and insufficient to recover the narrow profiles. The values δ^2 and ϵ^2 are similar with those of the tests using the identity matrix. The behavior indicates that the inversion technique with the Laplacian matrix is suitable for smooth and broad profiles.

Table 4.2: Results of reconstruction in numerical tests of Tikhonov regularization with Laplacian matrix. Table elements are reconstruction error δ^2, projection error ϵ^2, total numbers of negative and positive voxels in reconstructed profile, total radiation powers in original (model) and reconstructed profiles.

	Uniform	Tube	Thin tube	Core	Simulated
Error in profile, δ^2	0.031	0.637	0.863	0.080	0.846
Error in projection, ε^2	0.006	0.041	0.058	0.018	0.054
Number of positive voxels	16188	11190	9756	11776	9023
Number of negative voxels	0	2988	3612	1526	2834
Total radiation (original) (MW)	54.3	14.5	7.25	16.4	1.75
Total radiation (reconstructed) (MW)	54.4	16.5	9.40	14.8	2.19

4.5 Parametric inversion by function model fitting

3D tomographic imaging with the above algebraic methods provides a quantitive measurement of the distribution and intensity of radiation. When the 3D measurement is applied to the measurement of the evolution of radiation structure, local changes having structures larger than artifacts can be identified. However, the evolution of 3D radiation structure is completely three dimensional, and a global understanding of the evolution is difficult, being disturbed by the artifacts which haphazardly appear. Therefore, the least squares fitting of a 3D function model with few parameters is developed as an alternative method to characterize the spatial evolution of the radiation structure. The fitting is not made to the algebraically reconstructed 3D profile but to the measured IRVB images directly. The fitting technique is a useful technique of computed tomography, which is represented by the series expansion model fitting well known in nuclear fusion studies. When we build up a 3D function model suitable for the helical structure of LHD plasma, the parameter estimation is nonlinear and has to be iteratively achieved.

The calculated projection matrix enables the calculation of synthetic IRVB images from a given 3D radiation profile. For the synthetic images to match well with the measured IRVB images, the 3D function model must be similar to the actual profile of the radiation in the plasma discharge. In this section, a function model is built up and an iterative procedure of parameter estimation is investigated as an effective tool of 3D measurement. The technique is used to trace the evolution of the 3D radiation structure in parameters during the radiation collapse in LHD.

4.5.1 Model parameters

To have an effective modeling and to handle the model fitting with short calculation time, the total number of model parameters should be minimized. In this model fitting, the following parameters are employed.

Figure 4.20 shows a radiation profile simulated by the EMC3-EIRENE code. The simulated profile shows an elliptic shape. Therefore, an ellipse is employed as the base shape of the model. To produce the elliptic shape, the following 5 parameters are introduced into the model.

a: Semi-major radius of ellipse (m)
b: Semi-minor radius of ellipse (m)
w:Width of radiation region
R: Center of ellipse(m) (in the major radial direction)
c: Radiation intensity (W/cm^3)

The simulated profile also shows asymmetry between the inboard and outboard side. The previous study indicates that the radiation collapse has such asymmetry. Therefore, a parameter is introduced to describe the asymmetry.

γ_{in-out}: Asymmetric factor (inboard and outboard)

The simulated profile also shows strong or broad radiation around the X-points. A parameter for peaking is introduced.

γ_{peak}: Peaking factor
d_X: Location of peak

Figure 4.21 shows the total radiation intensity at each poloidal cross section in the simulated profile. The total radiation is not uniform with toroidal angle. It indicates that the radiation profile has toroidal asymmetry. Therefore, a parameter for toroidal asymmetry is introduced.

$\gamma_{toroidal}$: Asymmetric factor (Toroidal)

These nine parameters are employed for the model.

4.5.2 Definition of 3D function model

The radiation model is defined with the above nine parameters as the following equations with the cylindrical coordinate system of the LHD (r, z, ϕ),

$$S_{model}(r,z,\phi) = \begin{cases} 0 & (PP(r,z,\phi) < (1-w)^2) \\ c(1+\gamma_{in-out}cos(\frac{(r-R)\pi}{2(R-r_e)}))(1+ & \\ \gamma_{peak}XX(r,z,\phi))(1+\gamma_{toroidal}cos(2\phi)) & \\ & ((1-w)^2 \geq PP(r,z,\phi) \geq 1^2) \\ 0 & (1^2 < PP(r,z,\phi)) \end{cases} \quad (4\text{-}5\text{-}1)$$

$$XX(r,z,\phi) = exp(-\frac{((r-R)cos(\phi) - (z \pm a(1-d_X w))sin(\phi))^2}{2(d_X wa)^2}), \quad (4\text{-}5\text{-}2)$$

$$PP(r,z,\phi) = \frac{((r-R)cos(\phi) - zsin(\phi))^2}{b^2} + \frac{((r-R)sin(\phi) - zcos(\phi))^2}{a^2}, \qquad (4\text{-}5\text{-}3)$$

where r_e is the innermost location of the ellipse on the $r-$axis. a, b, R, w, γ_{in-out}, γ_{peak}, $\gamma_{toroidal}$, d_X and c are used as free parameters.

4.5.3 Procedure of 3D function model fitting

To estimate model parameters from four measured IRVB images, an iterative method has been developed in a least squares scheme. The least squares scheme is carried out with scanning in each discretized space of two parameters with all possible regression to handle the function model which is too complecte to handle with a gradient method. The function model fitting is carried out regarding the normalized square error ϵ_n^2 between each measured IRVB image, $\mathbf{P}_{measured}$, and the corresponding IRVB image, $\mathbf{P}_{model}^{(i)}$, from the 3D radiation model, $\mathbf{S}_{model}^{(i)}$, in the i-th iteration. The ϵ_n^2 is given as

$$\epsilon_n^2 = \|(\frac{\mathbf{P}_{measured}}{p_{measured,max}} - \frac{\mathbf{P}_{model}^{(i)}}{p_{model,max}^{(i)}}\|^2, \qquad (4\text{-}5\text{-}4)$$

where the normalization factors $p_{measured,max}$ and $p_{model,max}^{(i)}$ are the maximum values of $\mathbf{P}_{measured}$ and $\mathbf{P}_{model}$. The model parameters are so few that their values can be determined even from one IRVB image. The model fitting procedure is shown in Figure 4.22 and executed sequentially for each of IRVBs by taking into account the intensity gaps among 4 IRVBs. The obtained values of each model parameter are averaged afterwards. The details are as follows.

Step1 Nine model parameters $[a_0, b_0, R_{center,0}, w_0, \gamma_{in-out,0}, \gamma_{peak,0}, \gamma_{Toroidal,0}, d_{X,0}, c_0]$ are set to initial values, and the initial model $\mathbf{S}_{model}^{(0)}$ and the corresponding $\mathbf{P}_{model}^{(0)}$ are calculated with these initial parameter values.

Step2 Two model parameters are chosen and scanned the discretized parameter space to minimize the square error ϵ_n^2 while the other parameters are fixed to the initial values. This 2-parameter search is carried out individually for other 2-parameter sets except c.

Step3 ϵ_n^2 is calculated for the obtained set of eight parameters $[a_1, b_1, R_{center,1}, w_1, \gamma_{in-out,1}, \gamma_{peak,1}, \gamma_{Toroidal,1}$ through the "Step 2". When the ϵ_n^2 is smaller than the its initial value, the eight model parameters are renewed. Otherwise, eight parameters are adjusted to minimize ϵ_n^2 on the straight line between the initial parameter values and the obtained ones in eight dimensional space.

Step4 The remaining parameter c is scanned and chosen to minimize the "un-normalized" mean square error

$$\epsilon^2 = \|\mathbf{P}_{measured} - \mathbf{P}_{model}\|^2, \qquad (4\text{-}5\text{-}5)$$

because c influences just the radiation intensity. Then, one arrives at a renewed model $\mathbf{S}_{model}^{(1)}$ and the corresponding $\mathbf{P}_{model}^{(1)}$

Step5 The above whole process is repeated using the obtained values of nine parameters for the initial values in "Step 1", until all parameters converge.

In this flow, the parameters $[a, b, R_{center}, w, \gamma_{in-out}, \gamma_{peak}, \gamma_{toroidal}, d_X]$ are free from the influence of c. Therefore, this least squares procedure is handled as a function model

fitting with $8+1$ model parameters. In this model fitting, the resulting paramters are quasi-optimal due to the instability in the solution. The instability grows as the number of free paratemers is increased. In the measurement of the time evolution of radiation, to suppress the influence of the instability, this model fitting is carried out for each IRVB and then the results are averaged over four IRVBs and also over the sequence of the timing.

4.5.4 Validation of function model

The function model fitting is validated with the radiation profile simulated by the EMC3-EIRENE code. The result of the fitting test is shown in Figure 4.23. The reconstructed profile in Figure 4.23 (b) is similar to the original profile displayed in Figure 4.23 (a) in features such as asymmetry and shape. In fine structures, there are differences. One finds that the reconstructed profile is similar to the smoothed original profile, which is displayed in Figure 4.23 (c). In other words, the modeling succeeds in a kind of feature extraction. This good behavior is attributed to the small number of model parameters. When the number of parameters is increased, the fine structure of the radiation profile may tend to be recovered, but an excessive increase may lower the effect of feature extraction.

For example, in the model in Equation 4-5-6, let us take the γ_{in-out} term and add higher order terms of the cosine function as

$$(1+\gamma_{in-out,1st}cos(\frac{(r-R)\pi}{2(R-r_e)})+\gamma_{in-out,2nd}cos(2\frac{(r-R)\pi}{2(R-r_e)})+\gamma_{in-out,3rd}cos(3\frac{(r-R)\pi}{2(R-r_e)})+\cdot) \tag{4-5-6}$$

in order to recover the details in the in-out asymmetry of the profile. Figures 4.24 shows the changes of the normalized mean square error ϵ_n^2 and the Akaike information criterion (AIC) [19] with the order number n, respectively, in two of the IRVBs. In disregarding a constant term, AIC is defined here as

$$AIC(n) = Mln\epsilon_n^2 + 2(n+9+1), \tag{4-5-7}$$

and evaluated for each IRVB. Then, M is the number of pixels of each IRVB. Figure 4.24(a) indicates that the increase of n leads to the monotonical decrease of ϵ_n^2, which means higher fidelity to the measured IRVB images. Meanwhile, AIC is minimized for the 3rd and 7th order. This result suggests that the 3rd and 7th order is best and that the true radiation profile possesses a detailed structure in the γ_{in-out} cosine expansion. However, the lowest order is employed hereafter as it is suitable for characterization of the radiation structure.

4.6 Projection matrix calculation for imaging spectrometer

The imaging spectrometer described in Section 3.4 can be used for estimating the parameters of 3D function model in Equation 4-5-1. When the function model is fitted to the measurement data of the spectrometer, calculation of a projection matrix is required concerning the peculiar geometry and FoV of the spectrometer. The method of calculation is similar to that for a single IRVB, which is described in Section 4.2.2. Instead of the aperture of an IRVB, the imaging spectrometer has a round lens unit to expand the FoV. So, the calculation has been carried out by following a little different procedure.

At first, an assumption is employed to handle a cone beam sight with cubic elements. The imaging spectrometer has a fiber array as a channel array. The sight of each

channel has a cone beam shape, the fiber crosssection being expanded by the lens unit. The assumption is that the cone beam shape of the sight is a quadrangular pyramid with the same volume. Under this assumption, the projection matrix for the imaging spectrometer can be calculated with a procedure similar to that of the IRVBs.

The sight is calculated by tracing a line with every 1cm step from the center of the lens unit until they hit the first wall, with a direction defined by the positions of a fiber and the lens unit. The side width of a cross section on the quadrangular pyramid, $w_s(n)$ at the n-th step of the tracing is given as,

$$w_s(n) = \sqrt{(n\Delta x \frac{c_{4050} l_f - l_{lens}}{2x_{4050}})^2 \pi} \tag{4-6-1}$$

where $\Delta x (= 1cm)$ is the step size of the tracing, $c_{4050} (= 1,200)$ is the magnification of the lens unit at a typical distance $x_{4050} (= 4,050mm)$, l_f is the radius of the fiber core and l_{lens} is the radius of the lens unit. When a small volume of the FoV step $(w_s(n) \times w_s(n) \times \Delta x)$ is in a plasma voxel, the volume which is a part of the plasma-voxel is judged as a seen volume. When $w_s(n)$ is larger than Δx, the FoV is divided equally vertically and horizontally in the same way described in 4.2.2. The solid angle from the center of the seen volume to the lens is calculated as shown in Figure 4.25. A element of the projection matrix is calculated as Equation 4-2-3. The calculated matrix is used for fitting the function model to the measurement data of the imaging spectrometer.

4.7 Experimental inversion from IRVB images and relative calibration

4.7.1 Experimental inversion by Tikhonov regularization

In the inversion from experimental data of IRVBs, the algebraic method of Tikhonov has been examined. With the procedure of calculation in Section 4.4 except step 1, IRVB images observed in two specific cases of discharge have been analyzed. One is a set of four IRVB images with edge localized radiation, which was obtained in an equilibrium state of the plasma before radiation collapse. Another is a set of images with core concentrated radiation, which was obtained after radiation collapse. Figures 4.26 and Figure 4.27 show raw images, background subtracted images and final digitalized images in two cases. The pixel numbers in the digitalized images, that is, the numbers of projection values, are $36 \times 28 (= 1,008)$ in 10-O port, $36 \times 28 (= 1,008)$ in 6-T port, $26 \times 20 (= 520)$ in 6.5U port, and $30 \times 22 (= 660)$ in 6.5L port. The total of these pixel numbers is the number of projection values M in the reconstruction analysis.

Figures 4.28-4.29 show the results of the experimental inversion by the Tikhonov regularization method with the identity matrix. In comparison between the reconstructed profiles in two cases, it can be confirmed that the Tikhonov method succeeds in revealing a meaningful difference between the profiles before and after collapse. However, some strange structures are observed in the edge region. For example, the reconstructed profile after the collapse has high radiation peaks on the outboard side of the horizontal cross section ($\phi = 17.5°$) and at the lower edge of the vertical cross section ($\phi = 0.5°$). As the high peak at $\phi = 17.5°$ is observed also in the numerical test with the core radiation phantom as in Figure 4.8(d), it might be spuriously produced by the ill-condition of the equation and the layout of sight-lines which are few in the boundary region. However, the high peak at $\phi = 0.5°$ is not observed in the numerical test. In addition, there are a

larger number of negative artifacts than in the numerical test. These new artifacts that appear in experimental results may be attributed to the intensity gaps in IRVB signals. In other words, some IRVB signals are enhanced with a factor which comes from the unrefined setting and environment of IRVBs, for example, the reflection of IR emission by components that exist between the IRVB foil and the IR camera. To evaluate the factor, a relative calibration has been carried out as described below.

Relative calibration among IRVBs

For experimental data analysis, the projection data **P** should have consistency among the IRVBs. The four IRVBs had already been calibrated in each component of the IRVB such as the IR camera and the bolometer foil. However, some IRVBs showed smaller or larger intensity in comparison to the intensity expected from the projection matrix H. In other words, IRVB signals are enhanced by a factor for each IRVB. To evaluate the factor, a relative calibration has been carried out as follows. The relative calibration is a matching between the intensity ratio among experimental IRVB images (6.5-U, 6.5-L, 6-T and 10-O) and the intensity ratio among model IRVB images. As the experimental images, the images after radiation collapse are employed. A model which has been optimized by the procedure of 3D function model fitting described in Section 4.5 is employed. Figures 4.30 - 4.31 show an example of the set of experimental IRVB images and model images for relative calibration. The total intensity of each of IRVB images, $\overline{P_k}$, is calculated from the model profile with the following equation,

$$\overline{P_k} = \sum P_{k,j}. \tag{4-7-1}$$

where k is the camera index and j is the pixel index of the IRVB. The total intensity of the corresponding experimental IRVB image, $\overline{P_{exp,k}}$ is also calculated with Equation 4-7-1. If the model and experimental radiation profiles have similar structures, the IRVB images should have similar shapes and strength ratios of $\overline{P_k}$ among IRVBs. The relative calibration factors, f_k, are calculated using these total intensities as

$$f_k = \frac{\overline{P}_{k,model}/\overline{P}_{1,model}}{\overline{P}_{k,exp}/\overline{P}_{1,exp}}. \tag{4-7-2}$$

In this study, images of the 6.5-U IRVB are used as the reference images for calculating $\overline{P}_{1,model}$ and $\overline{P}_{1,exp}$ as reference images. The f_k is calculated in several discharges and averaged for each IRVBs. The calculated factors are as follows.

$f_1 = 1.00$ (for 6.5-U IRVB)
$f_2 = 2.07$ (for 6.5-L IRVB)
$f_3 = 1.048$ (for 6-T IRVB)
$f_4 = 1.23$ (for 10-O IRVB)

With this relative calibration, the IRVB image **P** is corrected by multiplying these factors to the experimental IRVB images. Figures 4.32-4.33 and Figures 4.34-4.35 show the calibrated IRVB images and the results of Tikhonov reconstruction for the same discharge and timing as those in Figures 4.28-4.29. In the reconstructed profiles, the spurious high peak at the lower edge of the vertical cross section almost disappeared while the negative values are weakened with a significant decrease of the number of negative values. The relative calibration is applied to all the subsequent experimental reconstructions.

4.7.2 Effect of Laplacian matrix in experimental inversion

The Tikhonov regularization with the Laplacian matrix has also been examined in image reconstruction from experimental data. The IRVB images calibrated above have been employed again as the test data. Figures 4.36-4.37 show the reconstructed profiles before and after radiation collapse. In comparison with Figures 4.33 and 4.35, it is seen that the reconstructed profile after collapse looks better in a smoothed and centralized radiation profile, and that the profile before collapse has some helical structures broadened in both positive and negative values. Improvement of spatial resolution is a remaining subject of numerical analysis study.

4.8 Summary of chapter

To define the relation between the 3D radiation structure and the 2D IRVB images, a projection matrix has been calculated with geometrical consideration under the assumption of the toroidal periodicity and symmetry of the LHD plasma. With respect to four pyramid beam cameras, which are set in separate positions in the helical torus, the difficulty of calculation has been overcome, and a method of calculation has been established. Using the calculated projection matrix, the fields of view of four IRVBs have been designed to get good coverage of the whole plasma region. For the appropriated fields of view, the numerical technique of 3D tomographic imaging has been developed and examined in two approaches algebraic and model fitting toward the primary target of measuring the radiation collapse.

The standard algebraic method of Tikhonov and its extension with the Laplacian matrix have worked reasonably in both numerical simulation and experimental data analysis with the statisitical criterion of minimum GCV. A method of calculating the Laplacian matrix has been developed for the 3D boundary of a helical plasma, and the matrix inversion of large size has been achieved using the Cholesky decomposition. The Tikhonov regularization of the original form has proved advantageous to get a spatial resolution good enough for resolving the narrow radiation profile of LHD plasma in the equilibrium state. Adopting the Laplacian matrix has brought an effective diminishment of noisy artifacts with a loss of resolution. The linearity of the algebraic methods that allows the reconstructed images to have negative values has rather been useful to detect the deficiency of the measurement system and has lead to the relative calibration of IRVBs, which is a key-point of this tomographic imaging with IRVBVs.

A practical 3D function model has been designed with regard to the 3D helical structure of radiation, which has an elliptic shape in the poloidal cross sections and toroidal asymmetry in the half period of magnetic field. The iterative procedure of the model fitting to IRVB images has worked well in numerical simulation on the EMC3-EIRENE phantom, for which the modeling has been checked with AIC. The modeling is expected to provide a useful characterization of the 3D radiation structures and their evolution. The established method of calculating the projection matrix has been applied to the imaging spectrometer for the purpose of the characterization by a spectral measurement.

The 3D imaging techniques developed and examined are applied to the analysis of LHD experiment data in the following chapter.

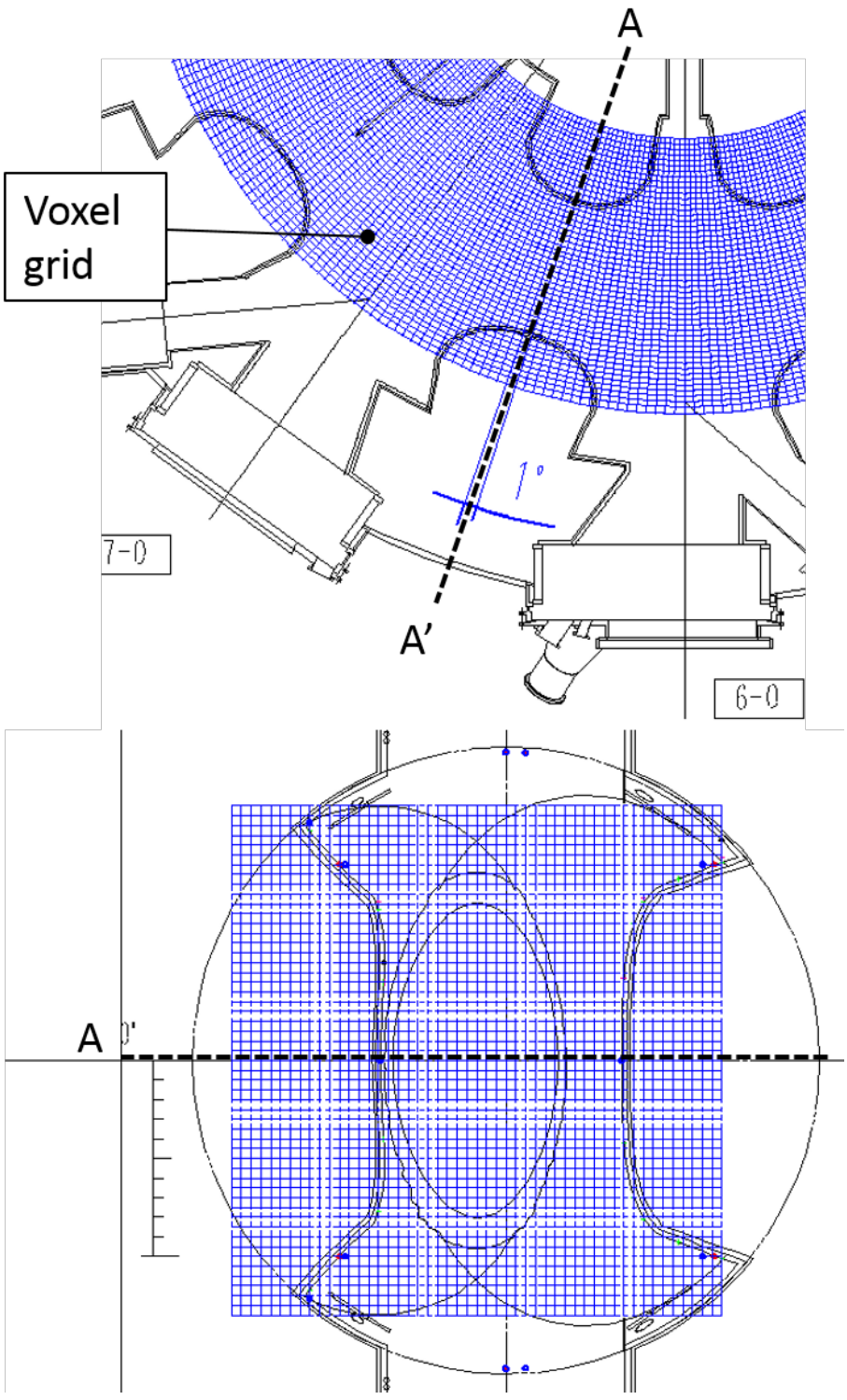

Figure 4.1: Voxel grid with cylindrical coordinates: major radial, R, 5 cm (54 divisions); vertical, Z, 5 cm (52 divisions); toroidal, ϕ, every 1° (360 divisions)

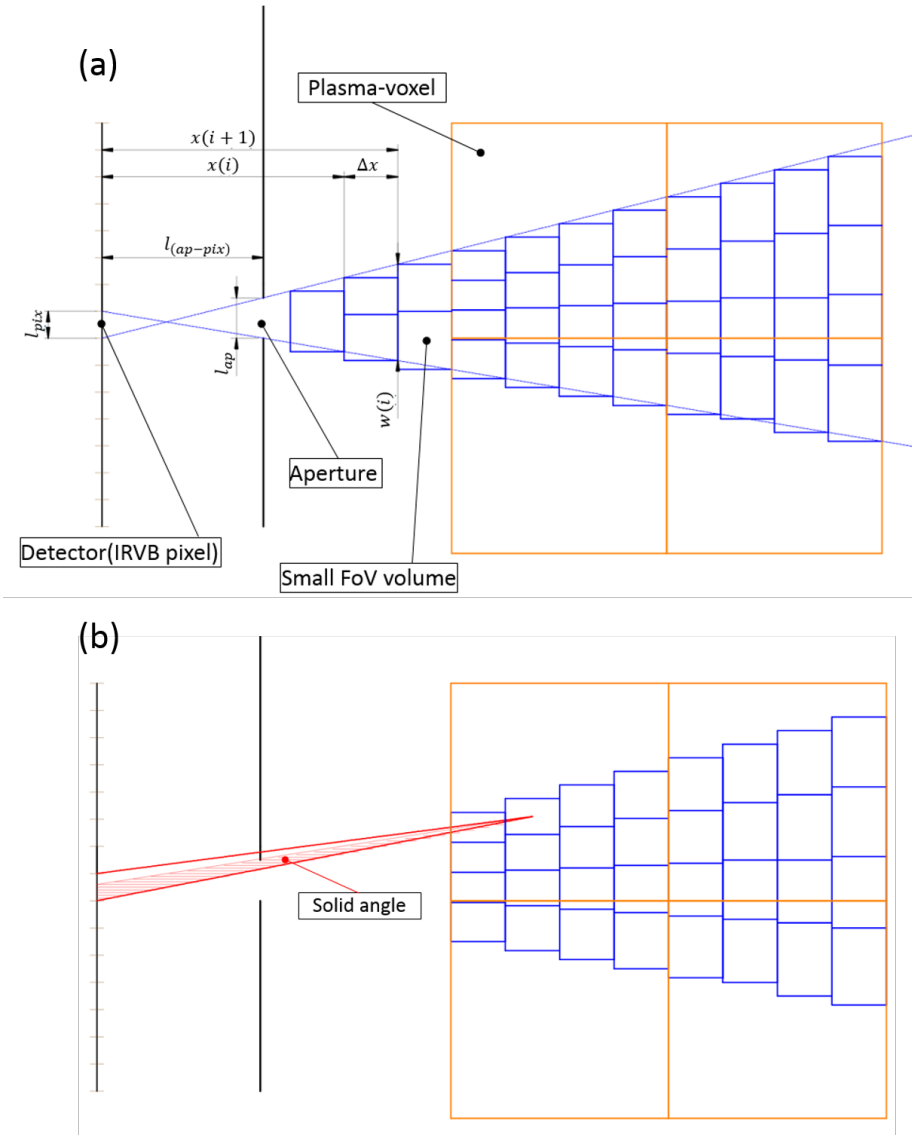

Figure 4.2: Projection matrix calculation. (a) Volume calculation for seen voxel, (b) Solid angle calculation from seen voxel to IRVB pixel).

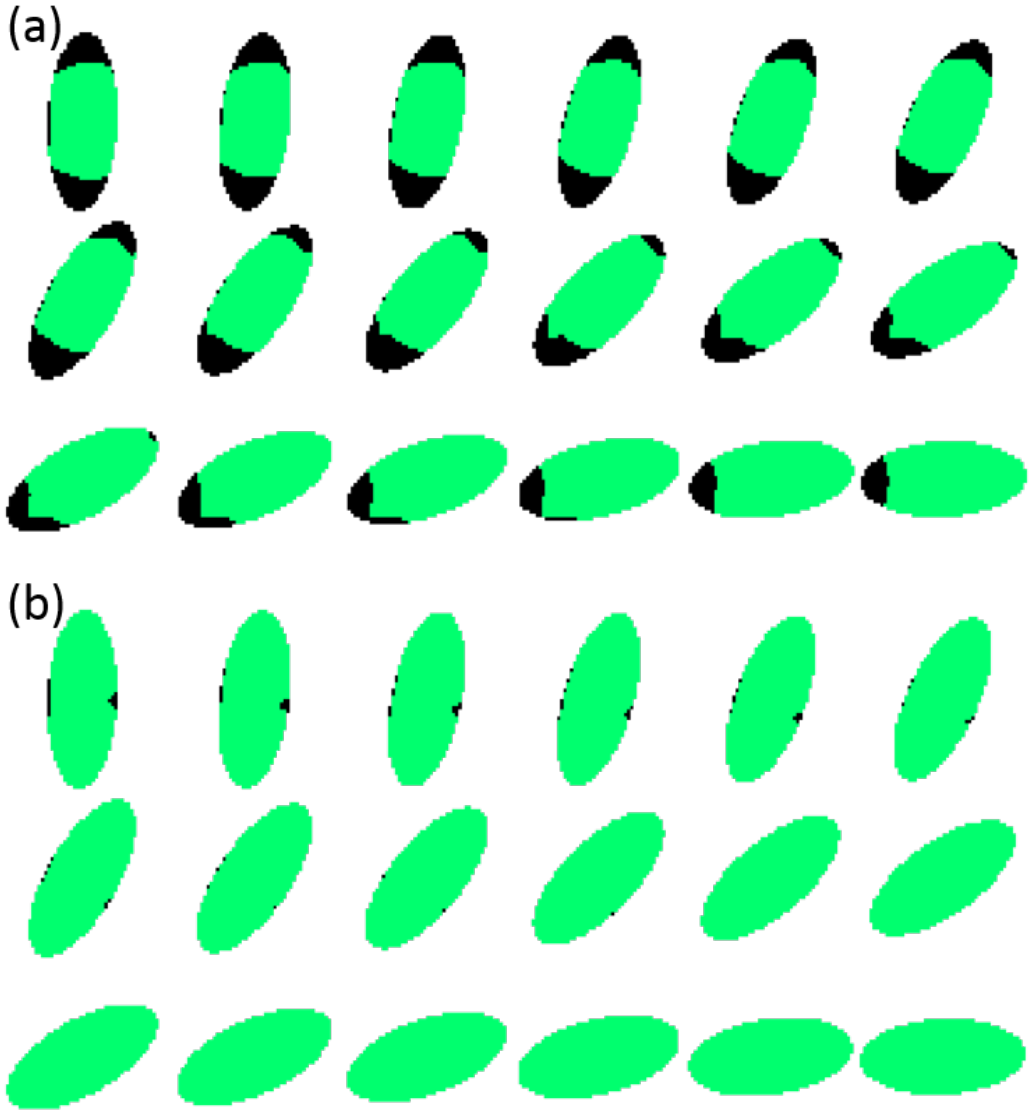

Figure 4.3: Selected FoVs of four IRVBs: (a) 6-T IRVB, (b) 10-O IRVB. Visible plasma voxel (green), non-visible plasma-voxel (black) and masked region (white).

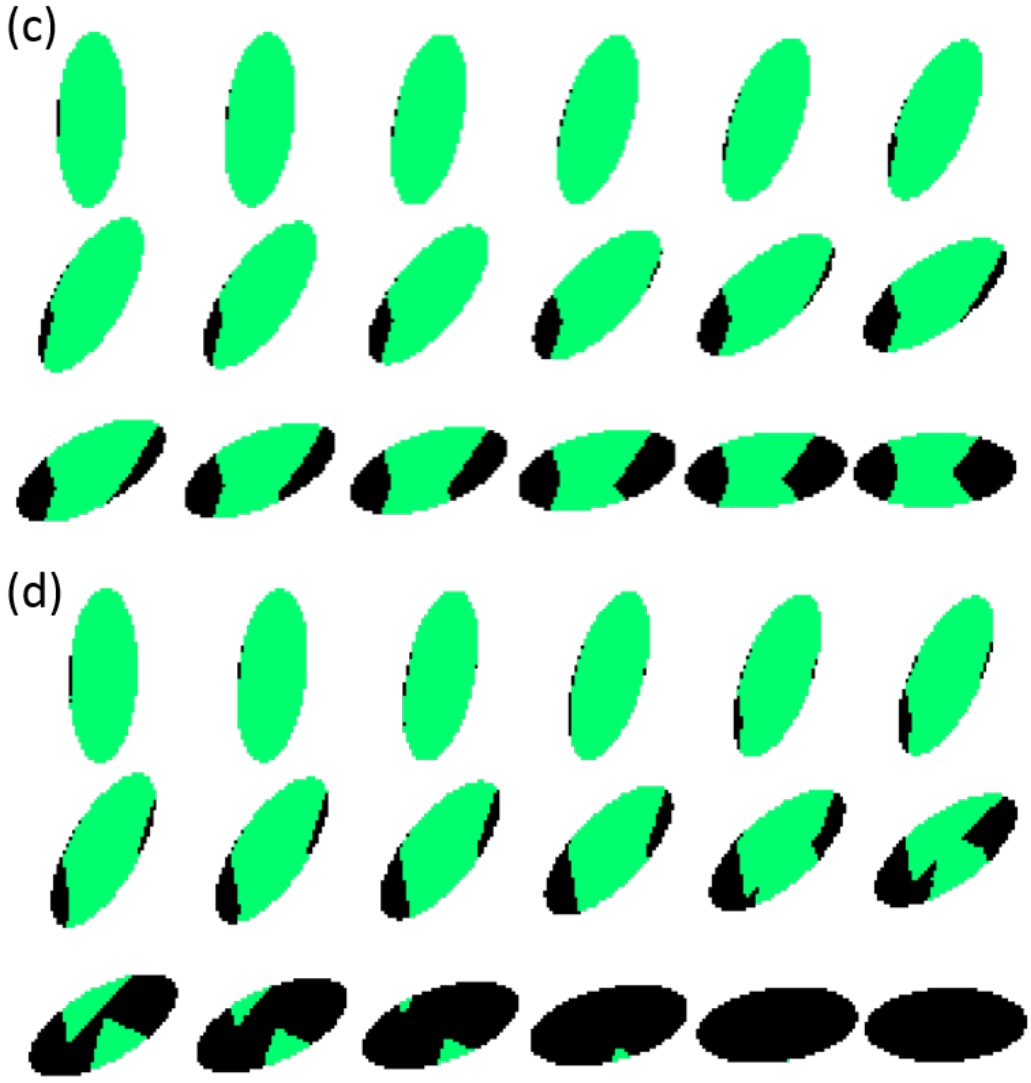

Figure 4.4: Selected FoVs of four IRVBs: (c) 6.5-U IRVB, (d) 6.5-L IRVB. Visible plasma-voxel(green), non-visible plasma-voxel(black) and masked region(white).

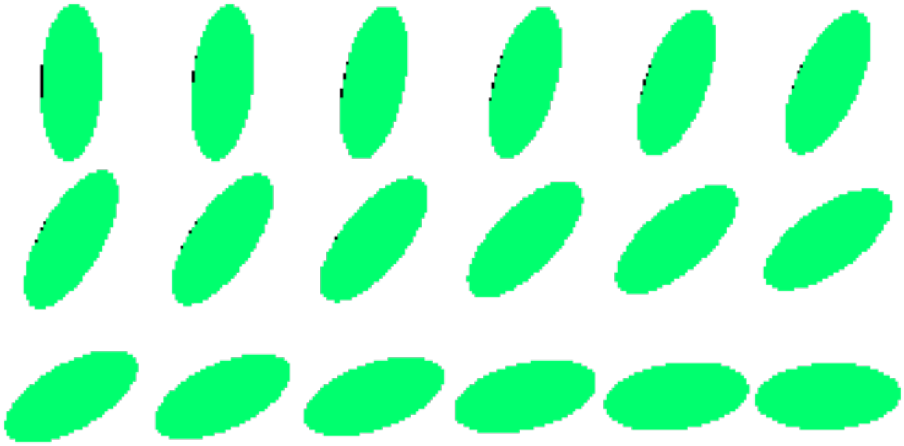

Figure 4.5: Combined FoV of four IRVBs. Visible plasma-voxel(green), non-visible plasma-voxel(black) and masked region(white)

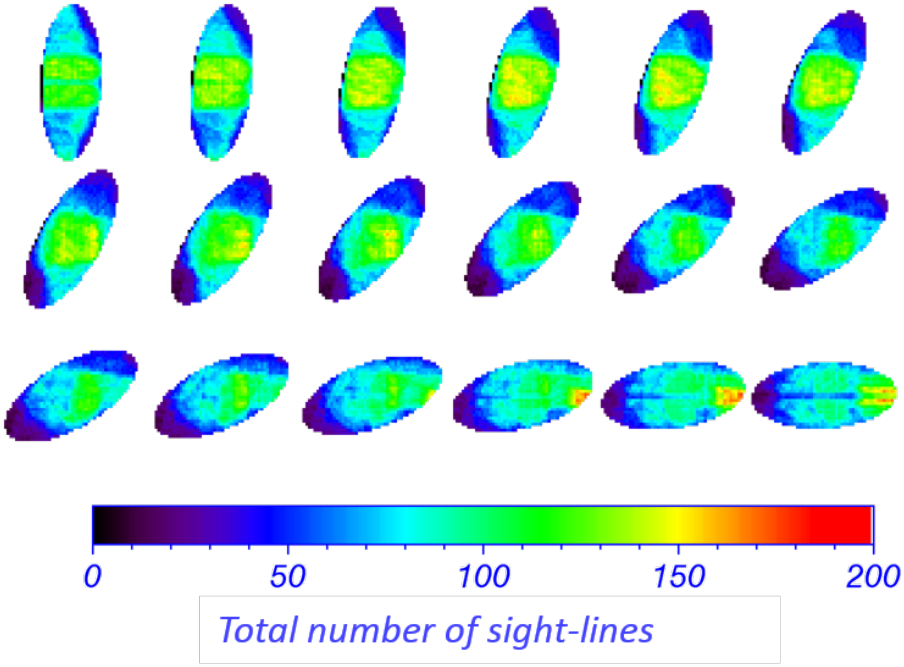

Figure 4.6: Total number of sight-lines that pass through each plasma-voxel

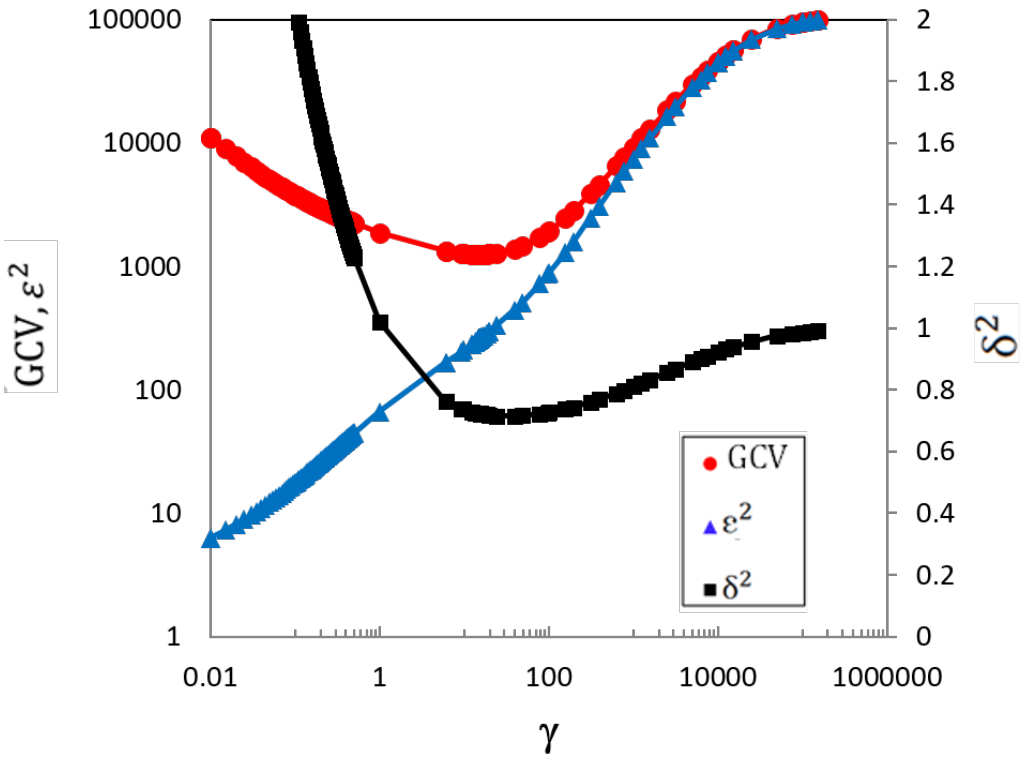

Figure 4.7: Behaviors of GCV (red), projection error $\varepsilon^2(\gamma)$ (blue) and reconstruction error $\delta^2(\gamma)$ (black) with changing γ. Result of Tikhonov regularization for EMC3-EIRENE phantom.

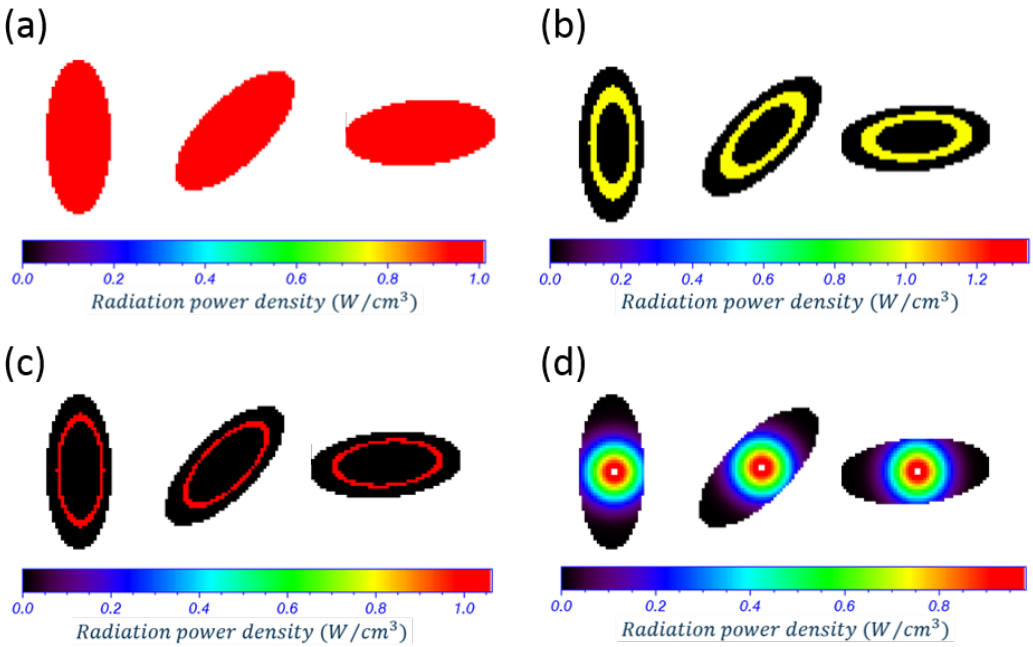

Figure 4.8: Phantoms for numerical test: (a) Uniform phantom, (b) Tube phantom, (c) Thin tube phantom, (d) Core phantom. Profiles are displayed in three poloidal cross sections with ($\phi = 0.5°$, $\phi = 9.5°$, $\phi = 17.5°$).

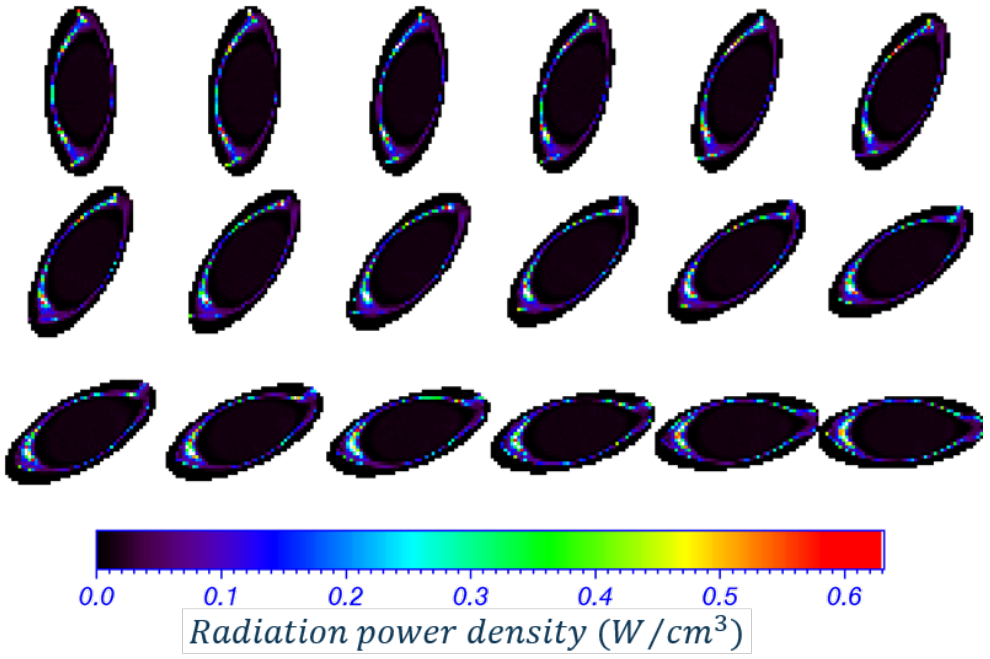

Figure 4.9: EMC3-EIRENE phantom for numerical test

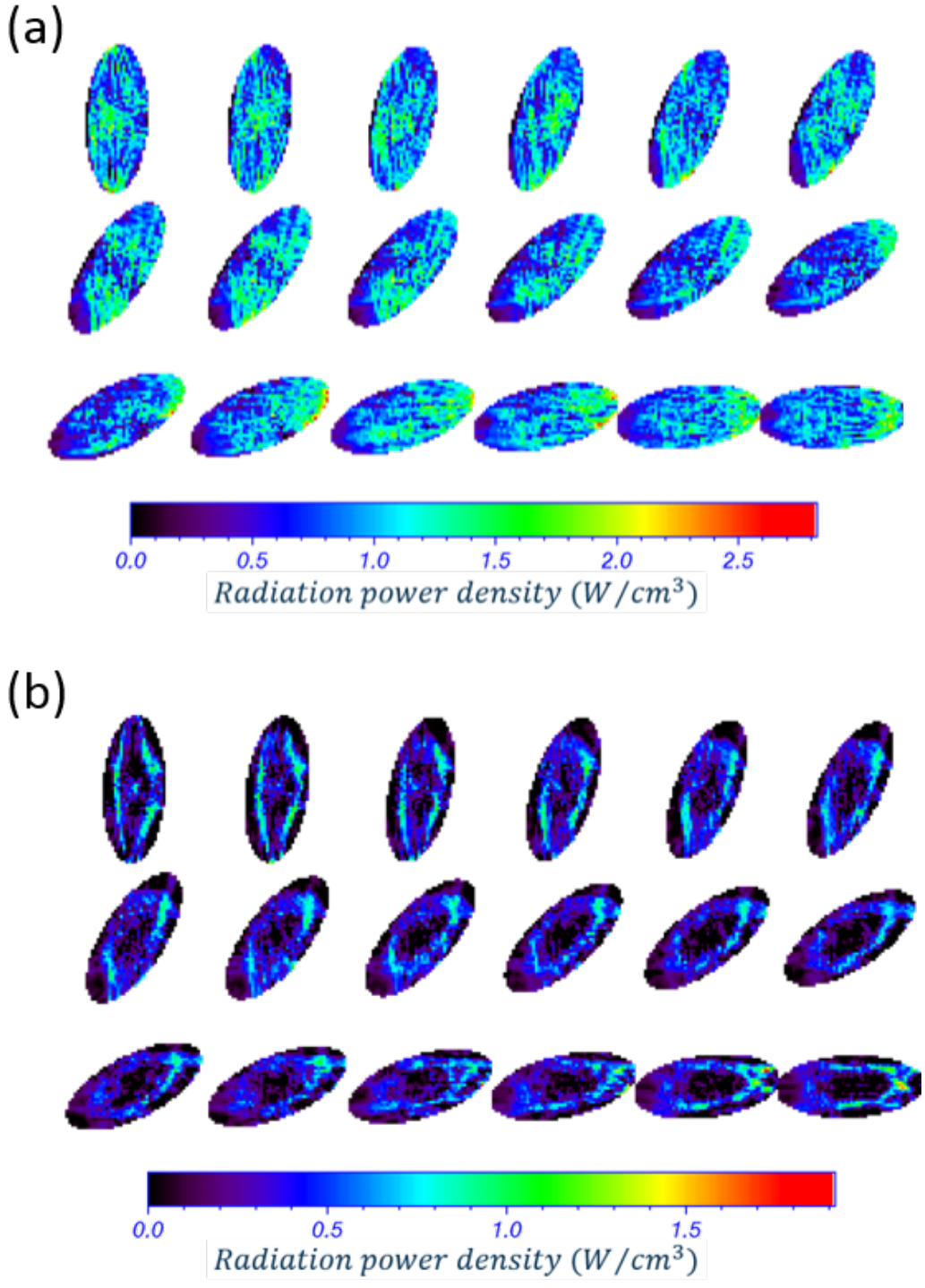

Figure 4.10: Profiles reconstructed by Tikhonov regularization: (a) Uniform phantom, (b) Tube phantom. Negative values are not shown.

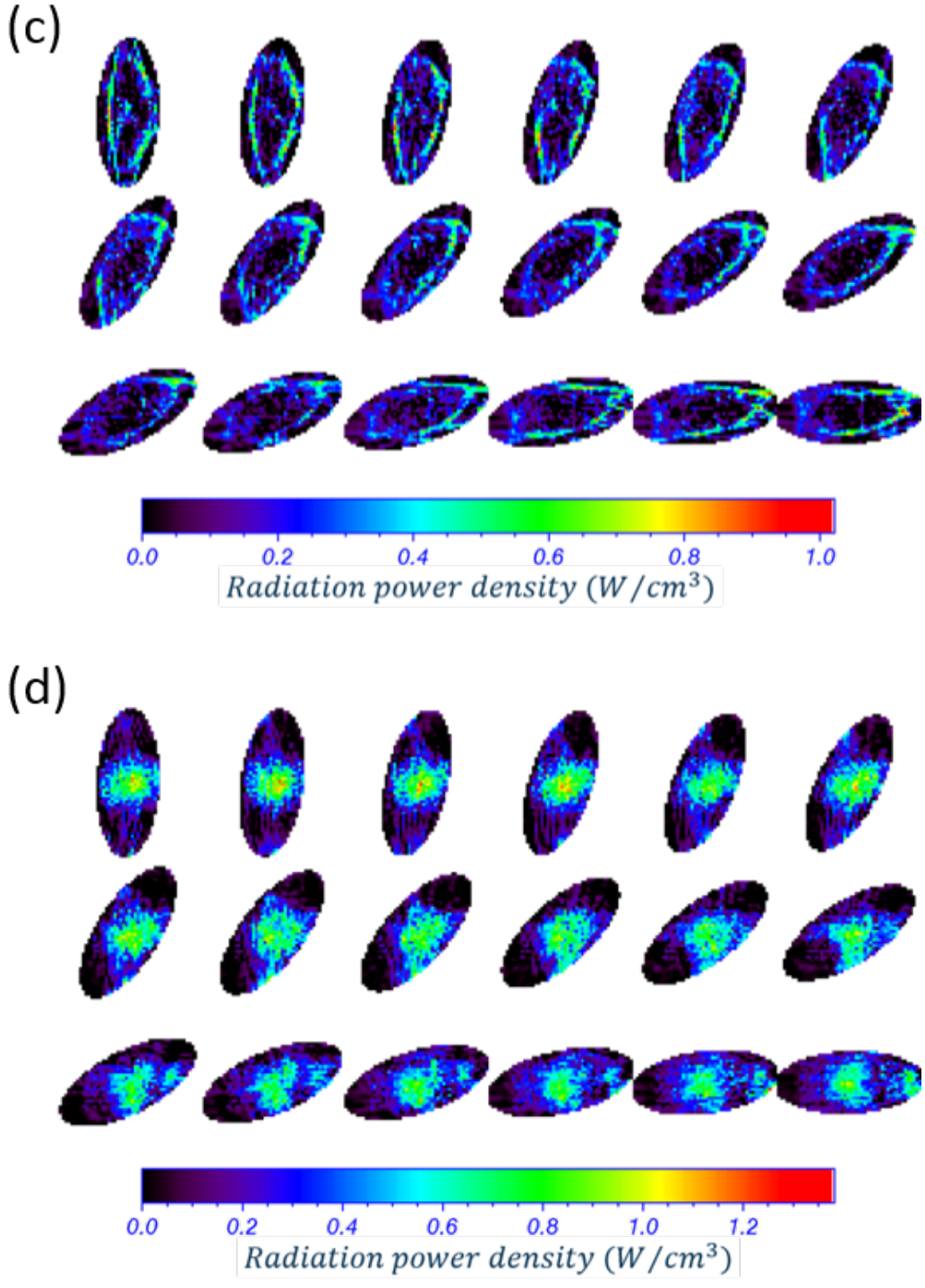

Figure 4.11: Phantoms reconstructed by Tikhonov regularization: (c) Thin tube phantom, (d) Core phantom. Negative values are not shown..

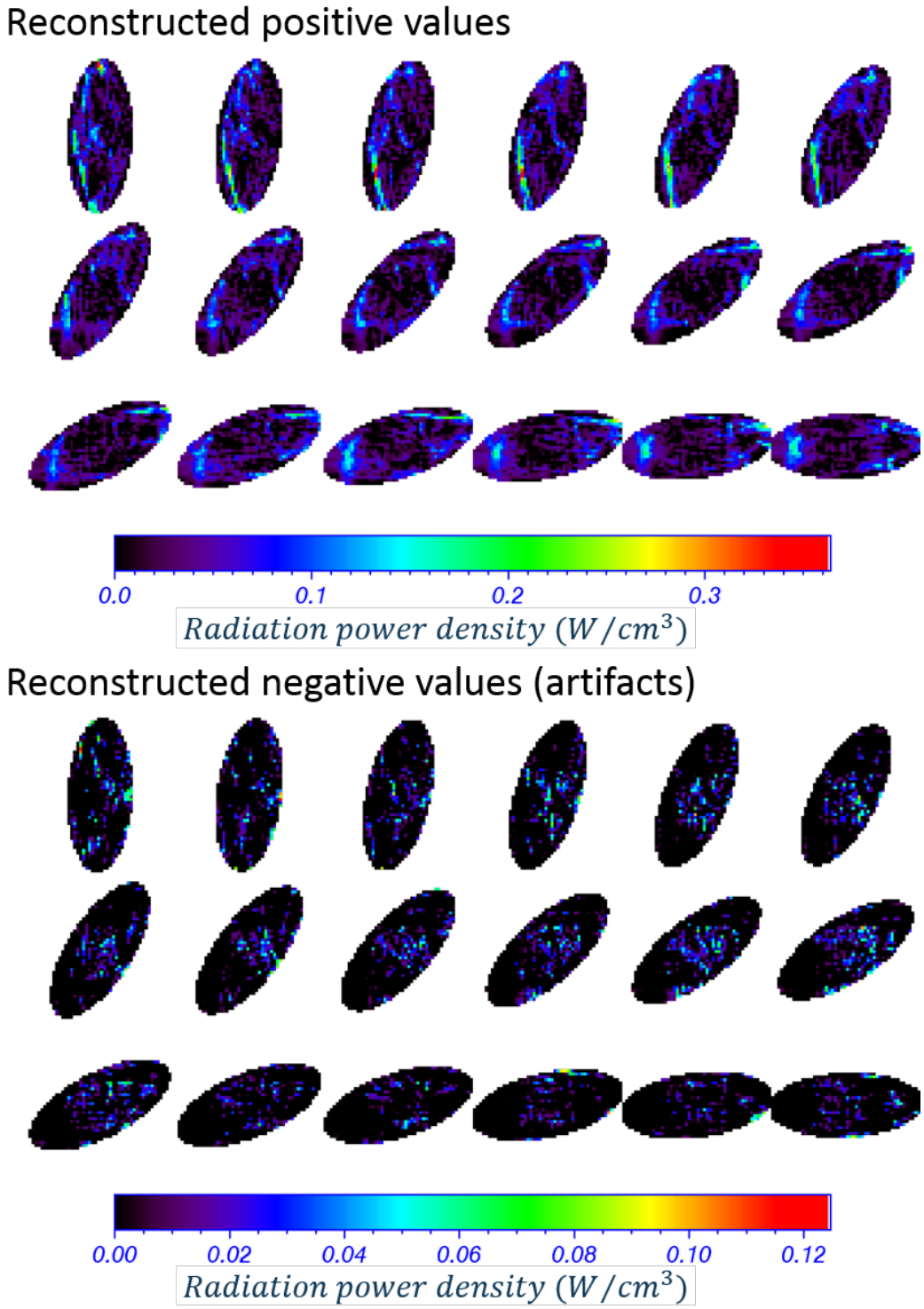

Figure 4.12: EMC3-EIRENE simulated profile reconstructed by Tikhonov regularization; positive values (upper) and negative values (lower).

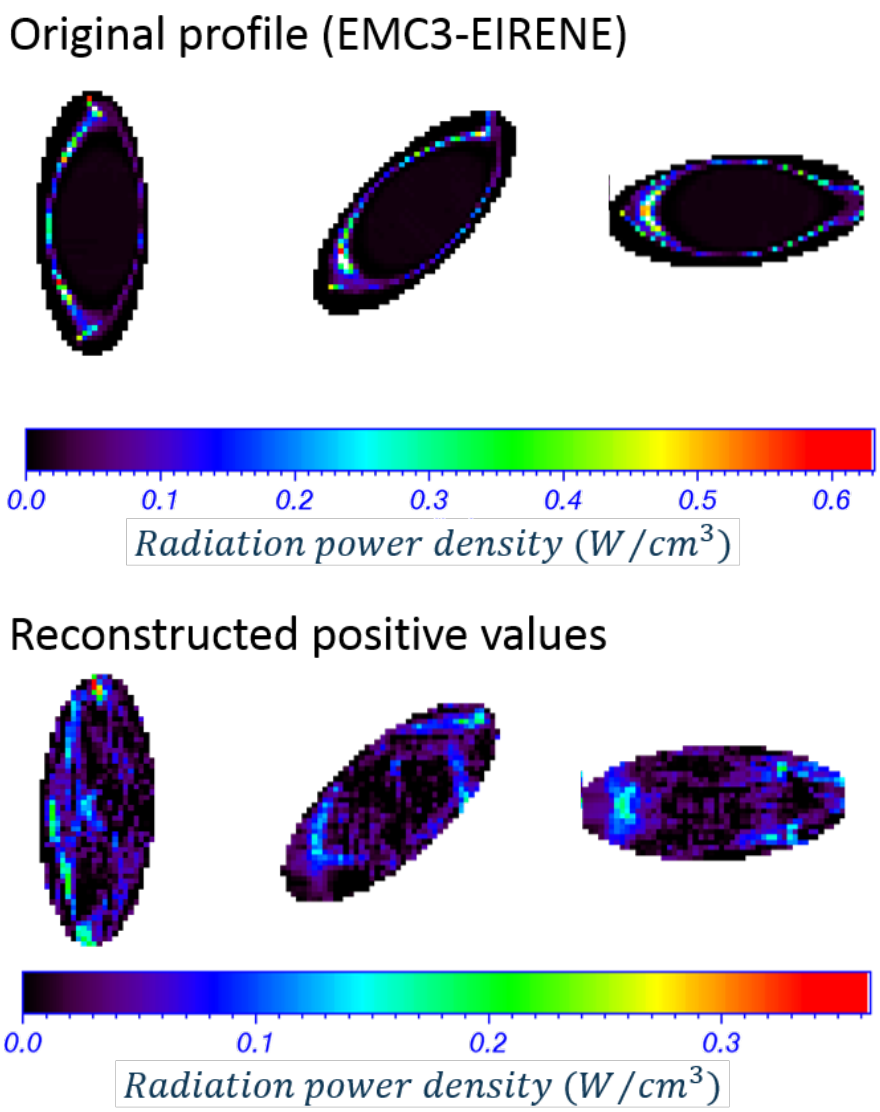

Figure 4.13: Comparison between original EMC3-EIRENE profile (upper) and reconstructed profile (lower) for toroidal angles ($\phi = 0.5°$, $\phi = 9.5°$, $\phi = 17.5°$).

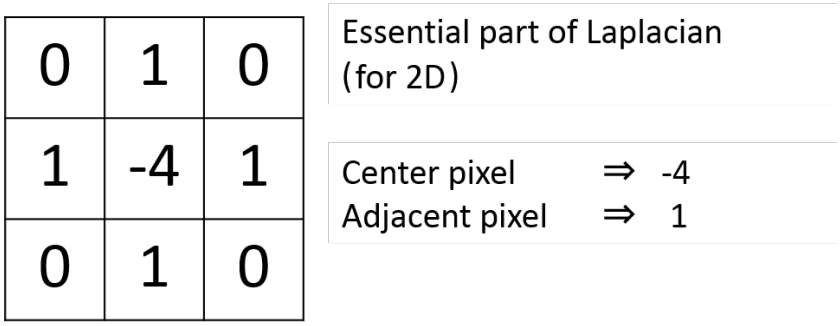

Figure 4.14: Essential part of 2D Laplacian matrix (visual map in real space)

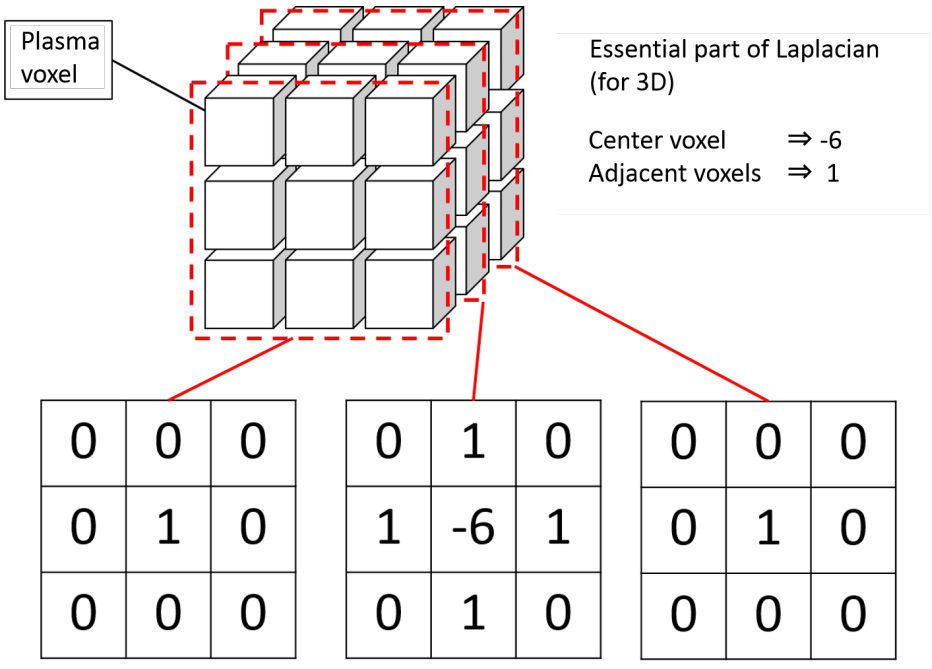

Figure 4.15: Essential part of 3D Laplacian matrix (visual map in real space)

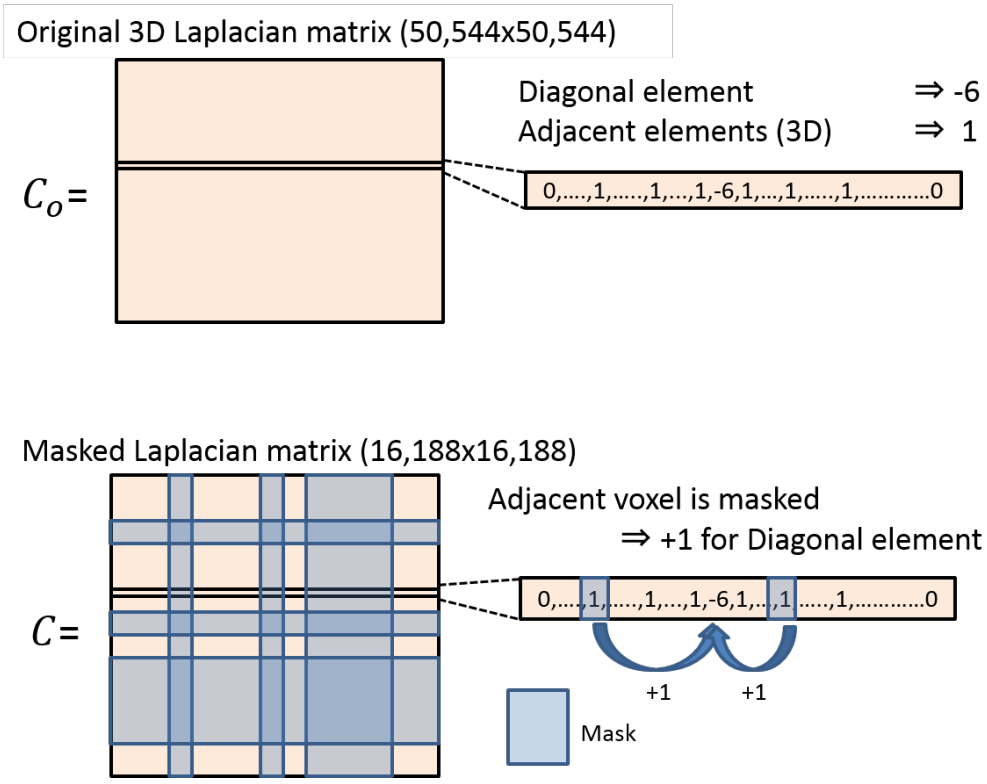

Figure 4.16: Masking of Laplacian matrix for 3D tomography

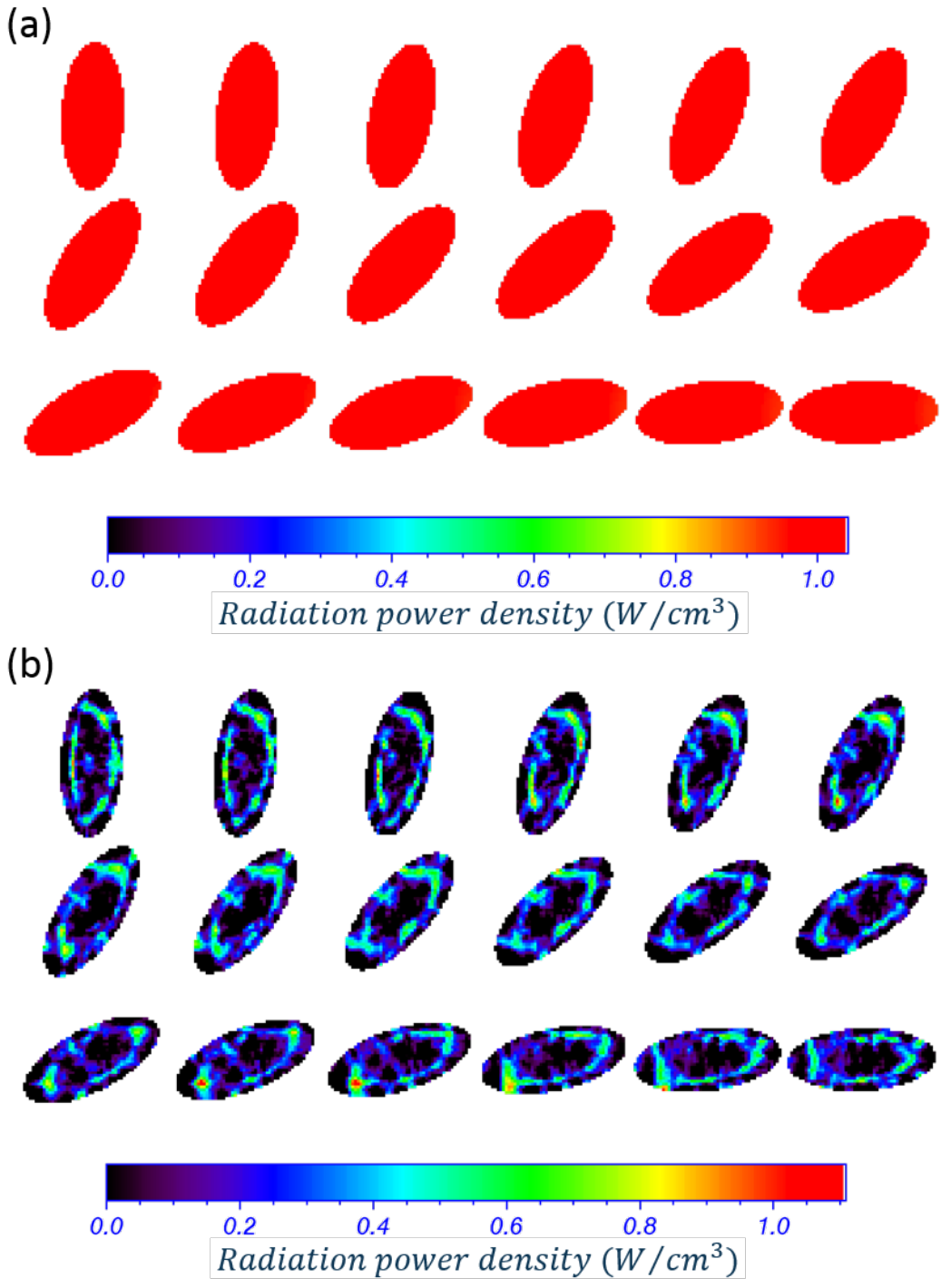

Figure 4.17: Tikhonov reconstruction with Laplacian matrix: (a) Uniform phantom, (b) Tube phantom. Negative values are not shown and never appear for uniform phantom.

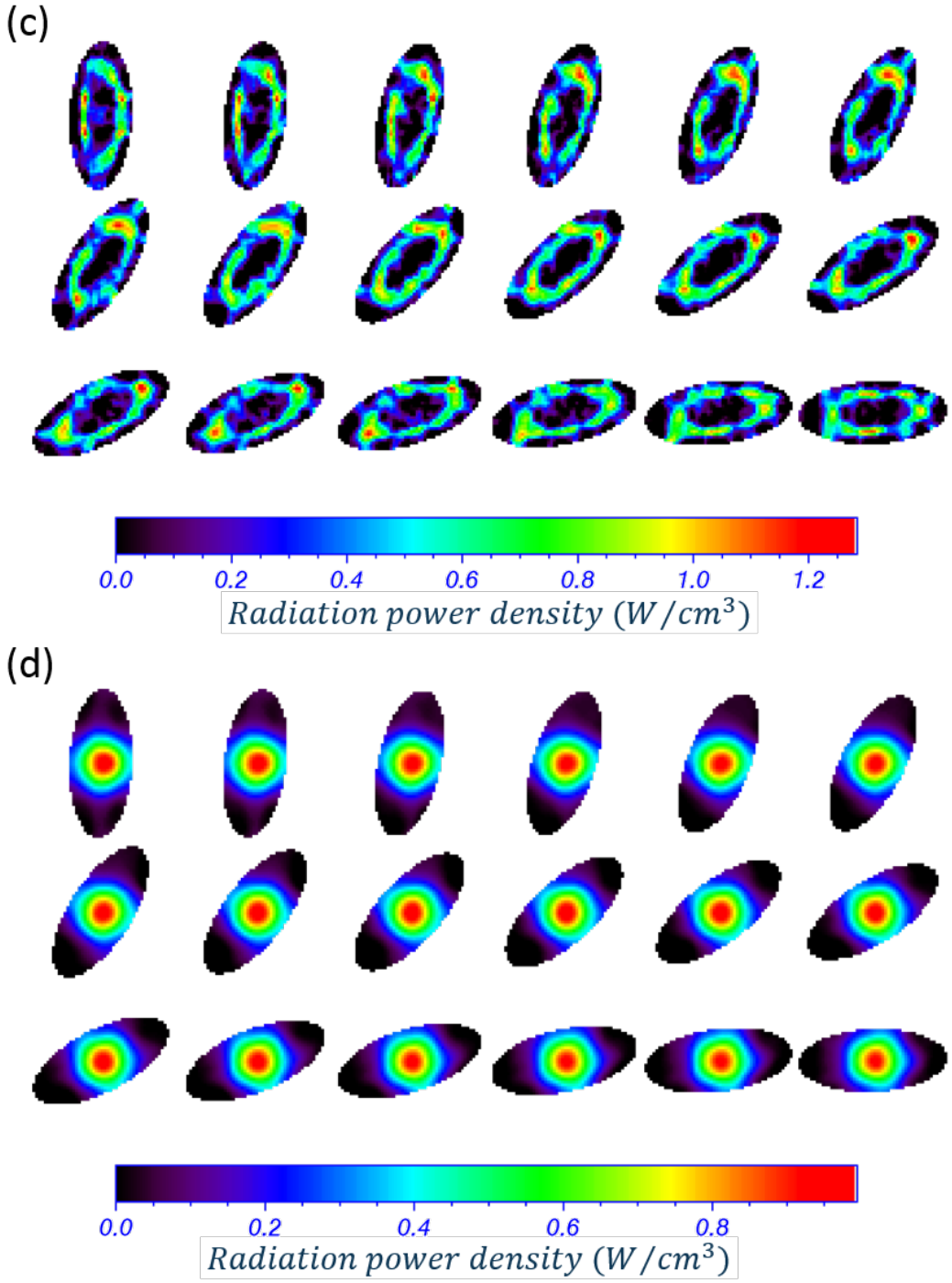

Figure 4.18: Tikhonov reconstruction with Laplacian matrix: (c) Thin tube phantom, (d) Core phantom. Negative values are not shown.

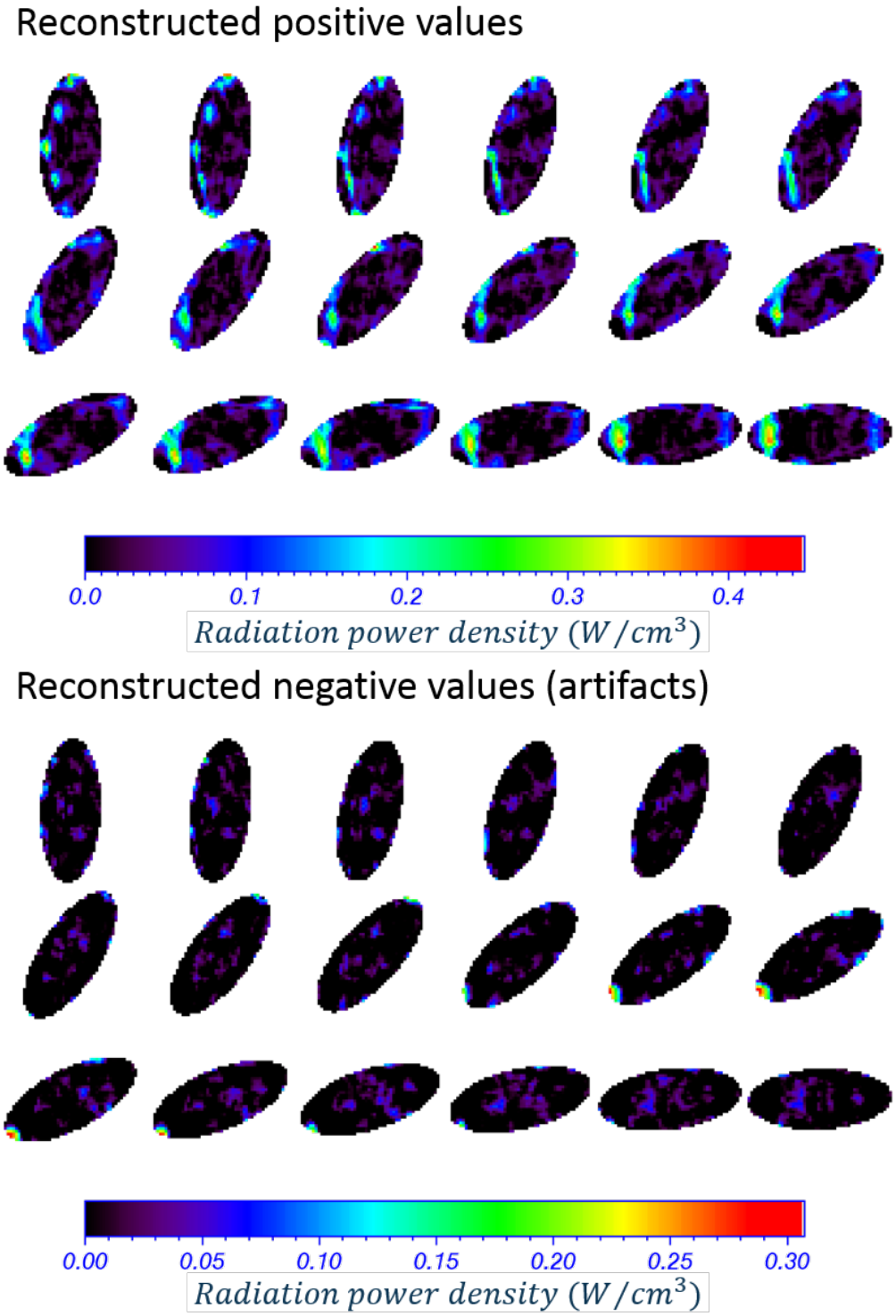

Figure 4.19: EMC3-EIRENE phantom reconstructed by Tikhonov regularization with Laplacian matrix; positive values (upper) and negative values (lower).

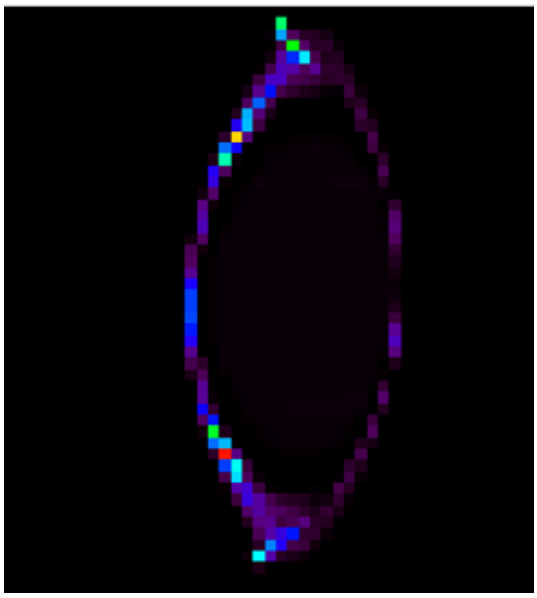

Figure 4.20: Radiation profile calculated by EMC3-EIRENE (data by M. Kobayashi)

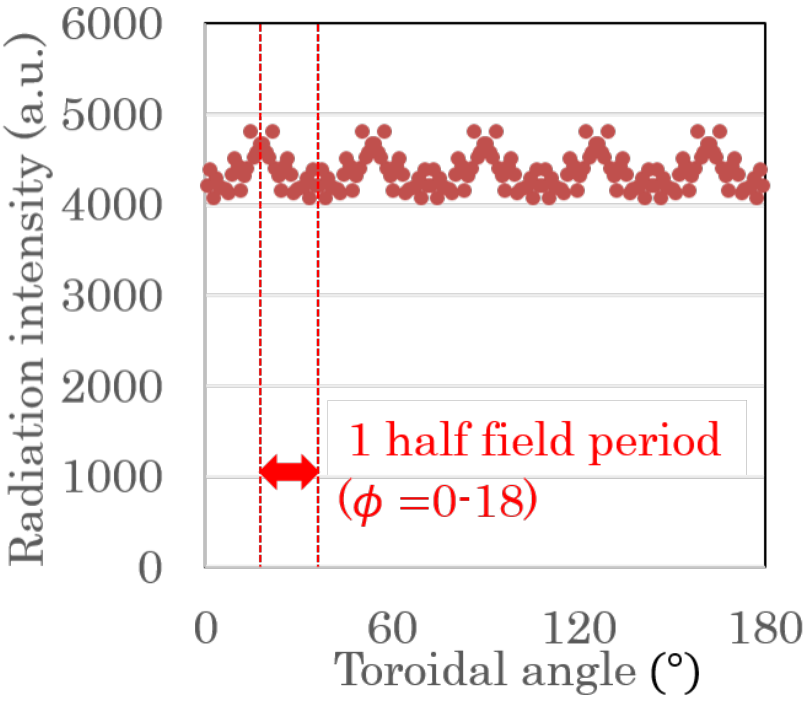

Figure 4.21: Total radiation power in each poloidal cross section; its change with toroidal angle (EM3-EIRENE simulation).

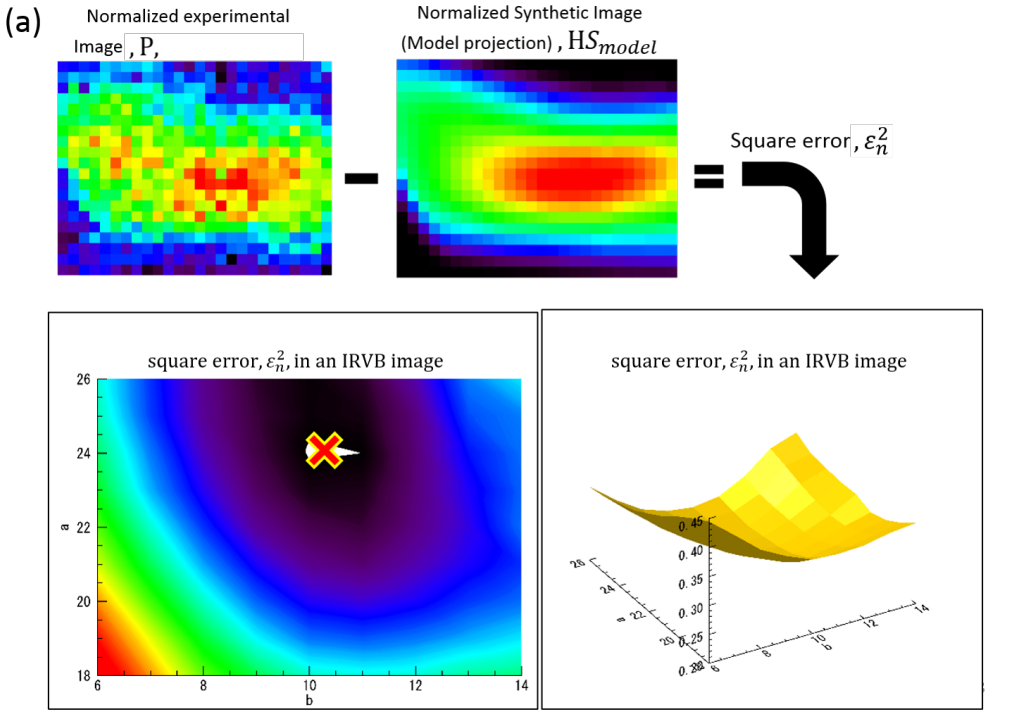

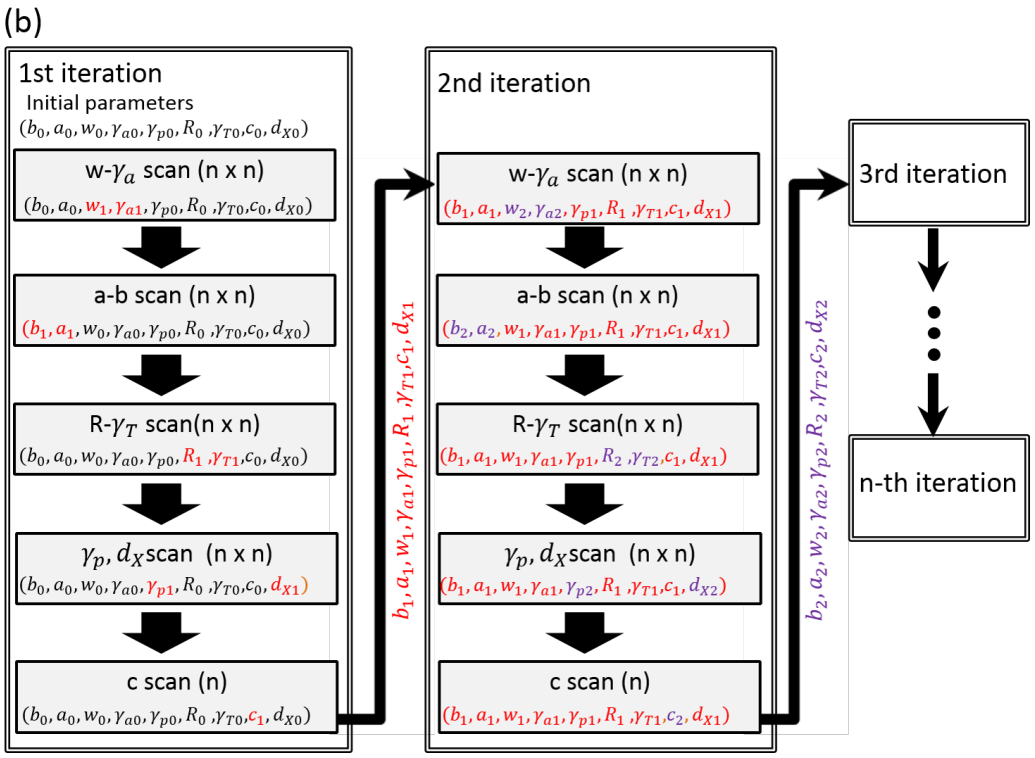

Figure 4.22: (a) Procedure of parameter scanning with 3D radiation model for one IRVB image. Red cross indicates location of minimum in iteration. (b) flow of iterative calculation for parameter scanning with 3D radiation model and IRVB images.

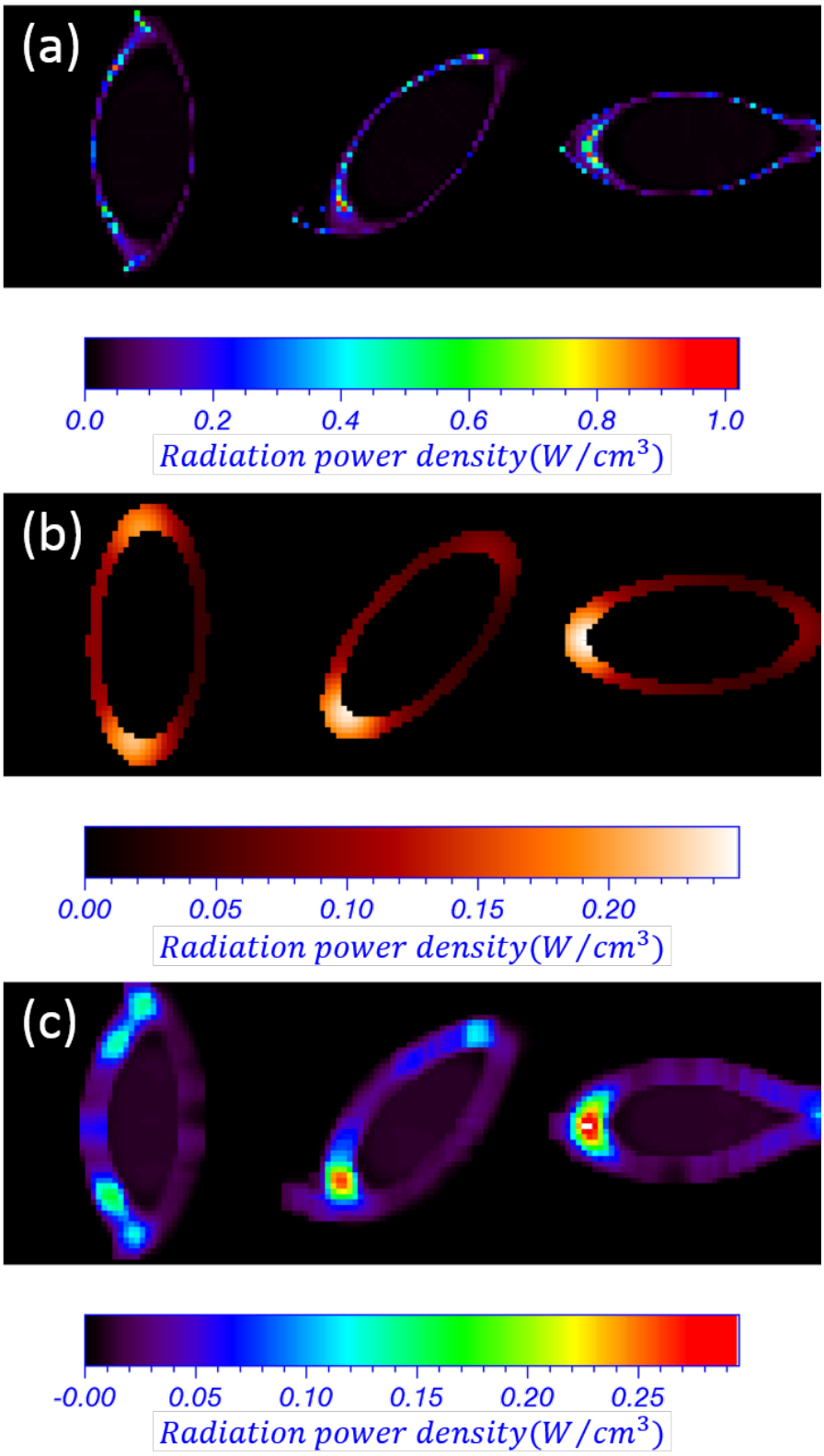

Figure 4.23: Test of model fitting tomography; (a) EMC3-EIRENE phantom, (b) result of reconstruction, (c) smoothed profile of phantom, which are displayed for toroidal angles $\phi = 0.5°, 9.5°, 17.5°$.

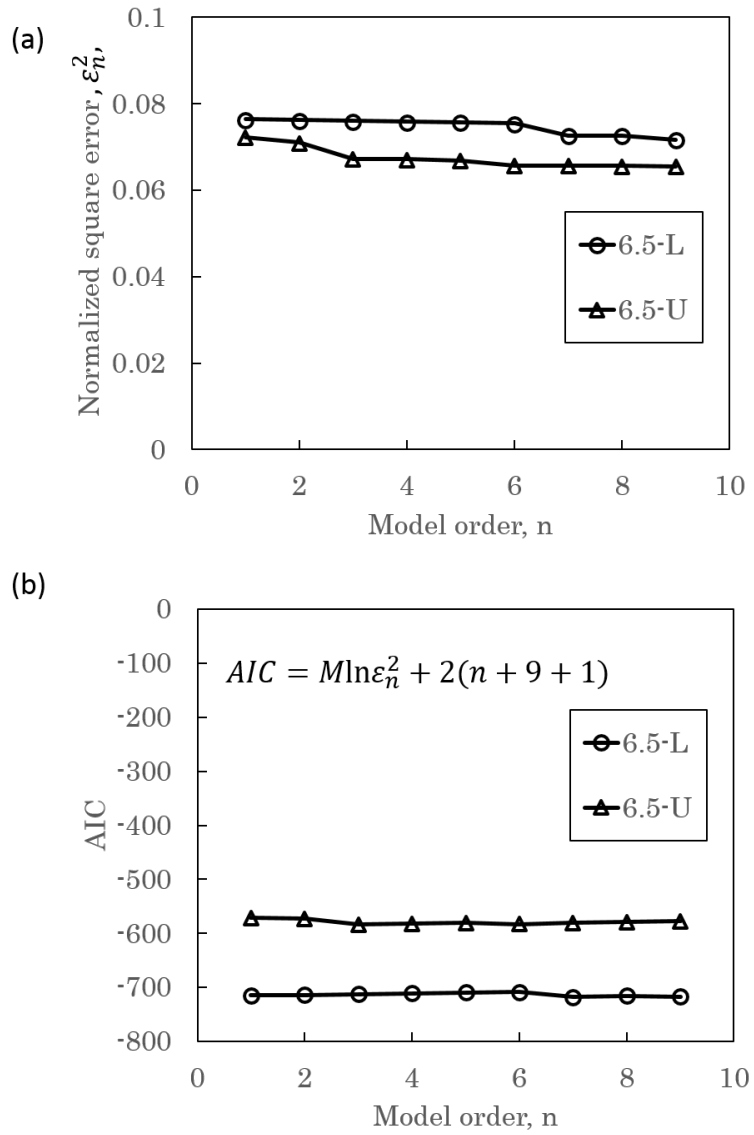

Figure 4.24: Behavior of AIC in 3D function model fitting. (a) Change of normalized square error ϵ_n^2 and (b) change of AIC with number of γ_{in-out} terms, n. M is the number of pixels in each IRVB..

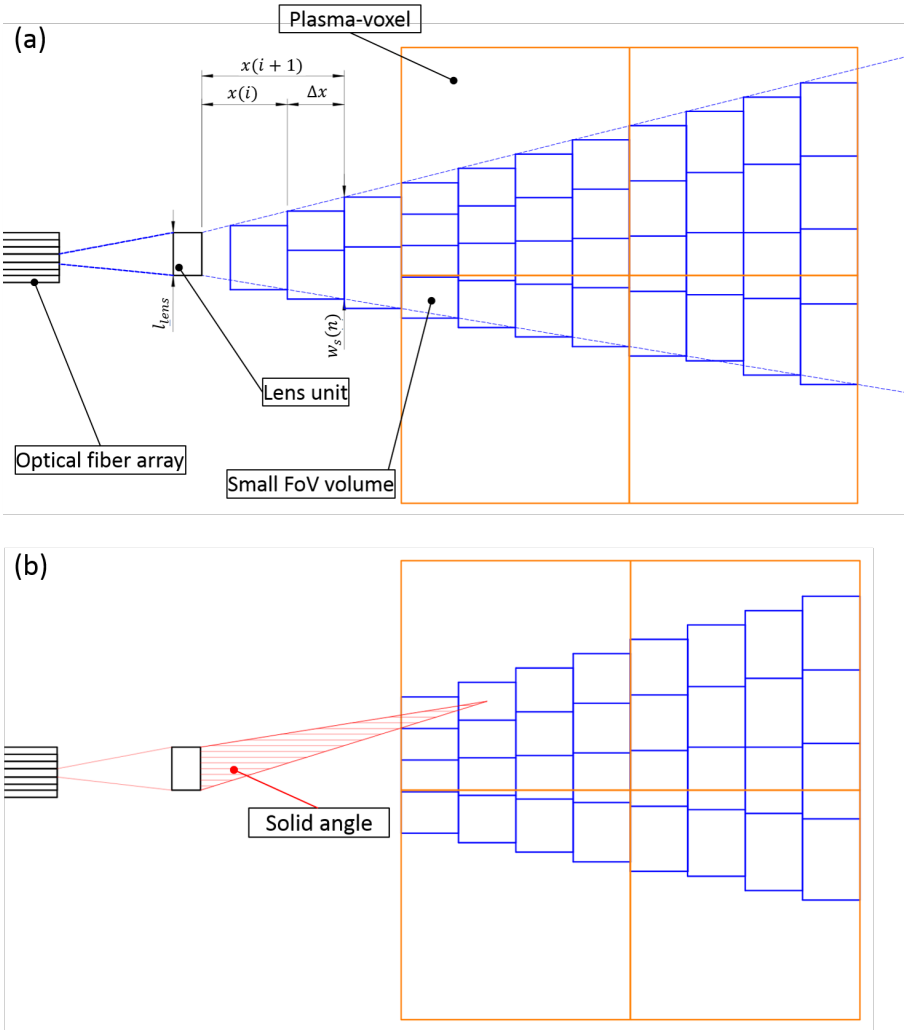

Figure 4.25: Projection matrix calculation for imaging spectrometer. (a) Volume calculation for seen voxel, (b) Solid angle calculation from seen voxel to IRVB pixel.

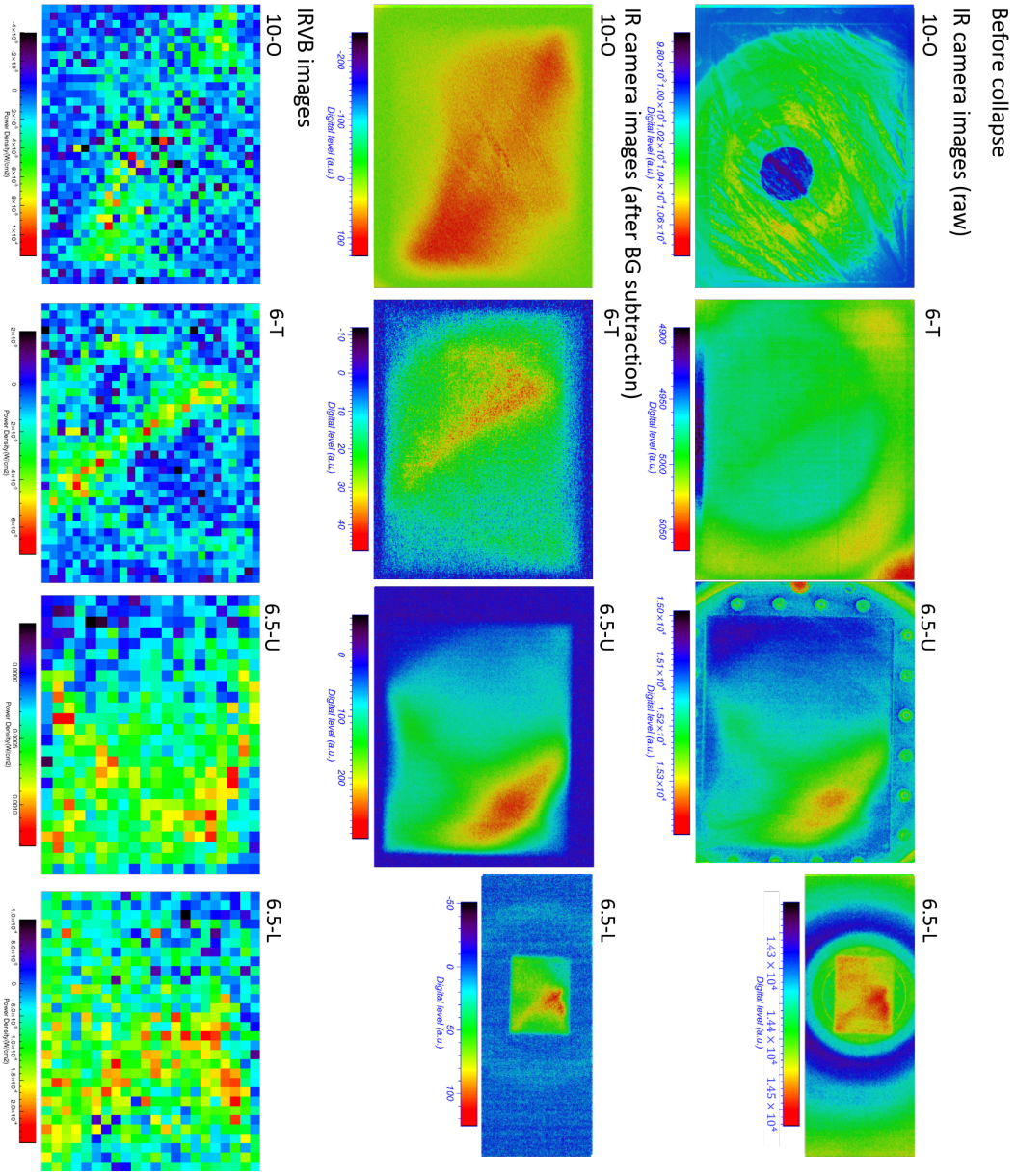

Figure 4.26: IRVB images before radiation collapse (♯1217876.02s). Raw images (upper), background subtracted images (middle), and digitalized images to be analyzed for image reconstruction (lower).

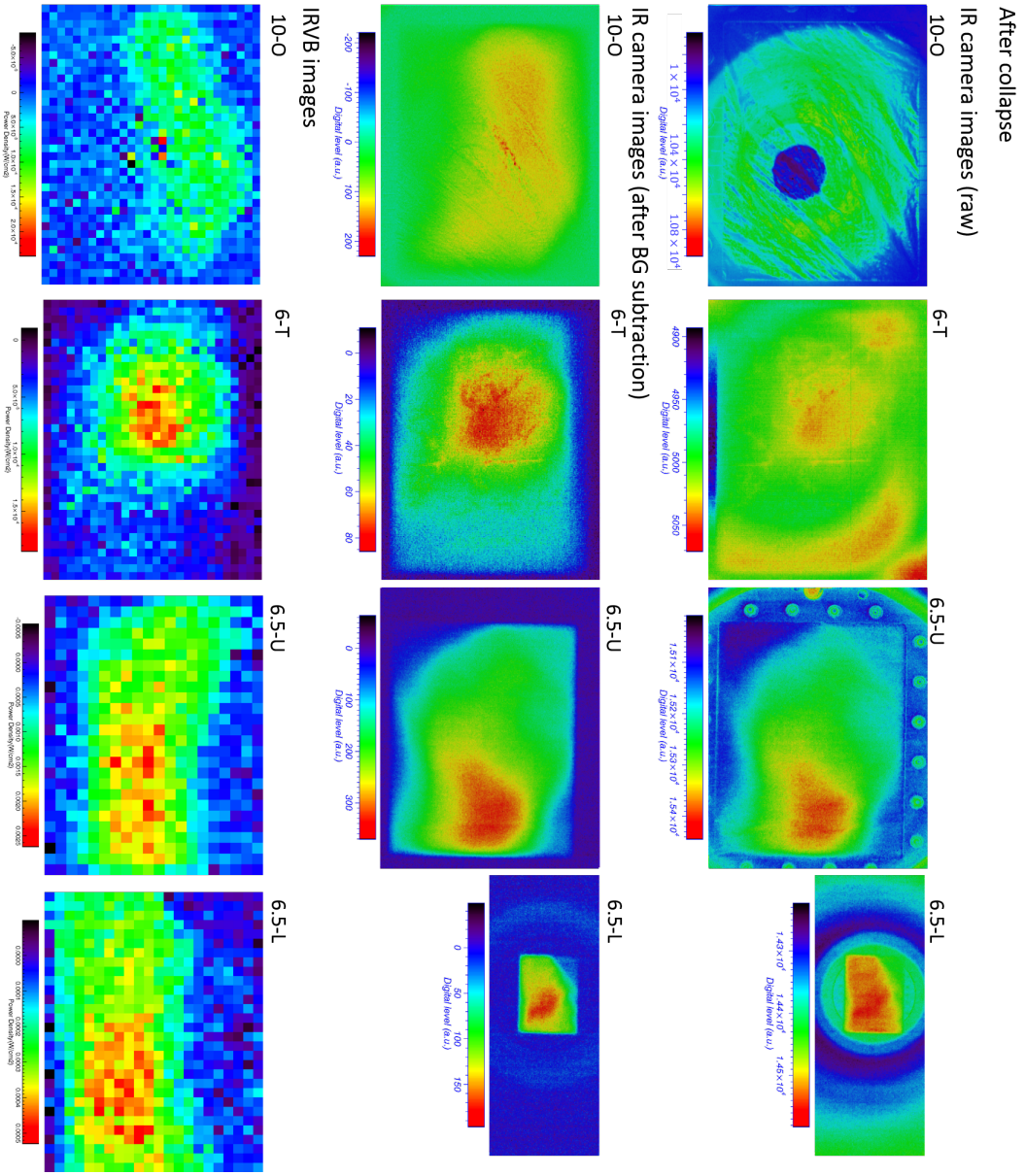

Figure 4.27: IRVB images after radiation collapse (♯1217876.52s). Raw images (upper), background subtracted images (middle), and digitalized images to be analyzed for image reconstruction (lower)

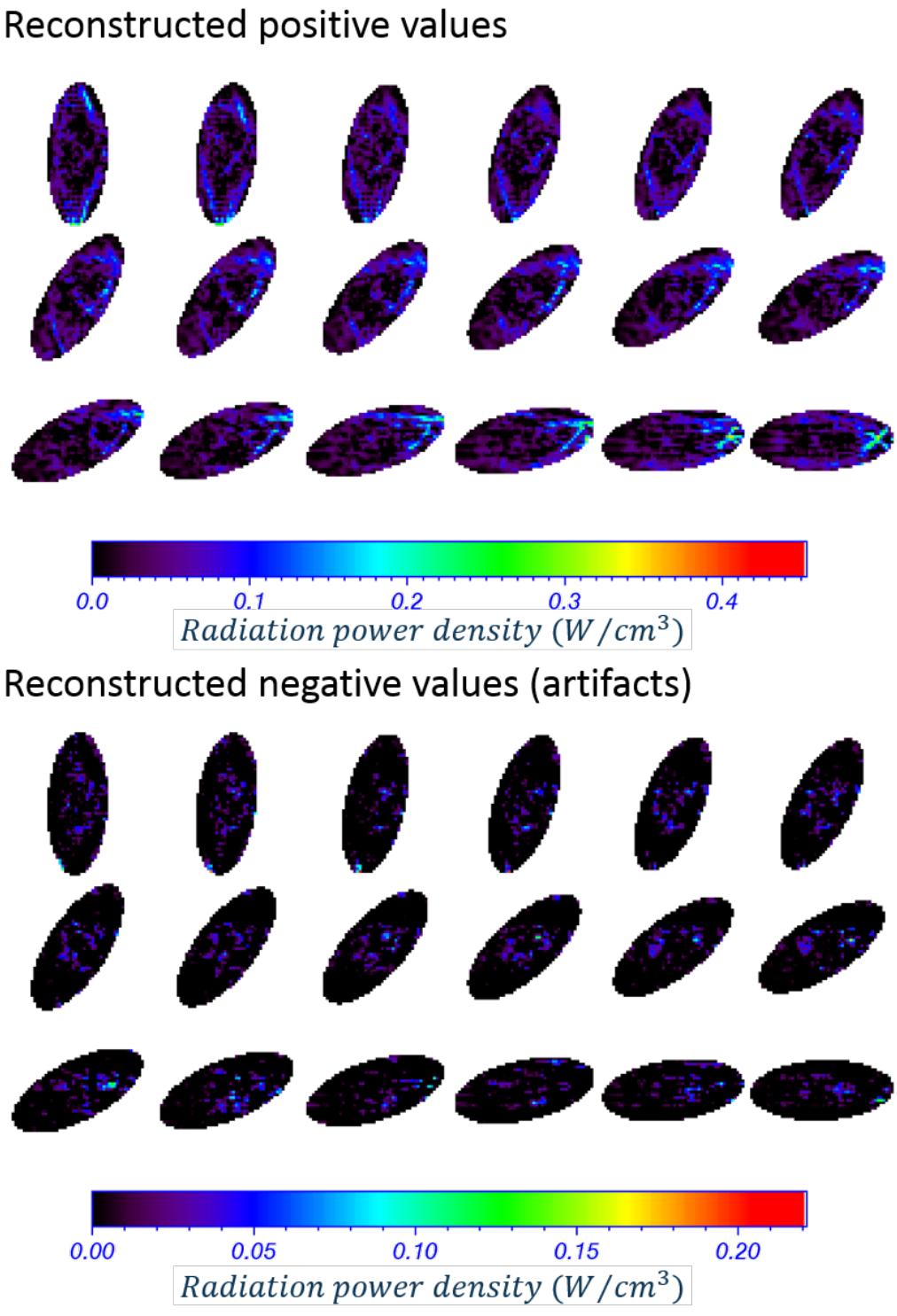

Figure 4.28: Reconstructed profile before radiation collapse (♯1217876.02s), which is obtained from experimental IRVB images by Tikhonov regularization (without relative calibration); positive values (upper) and negative values (lower).

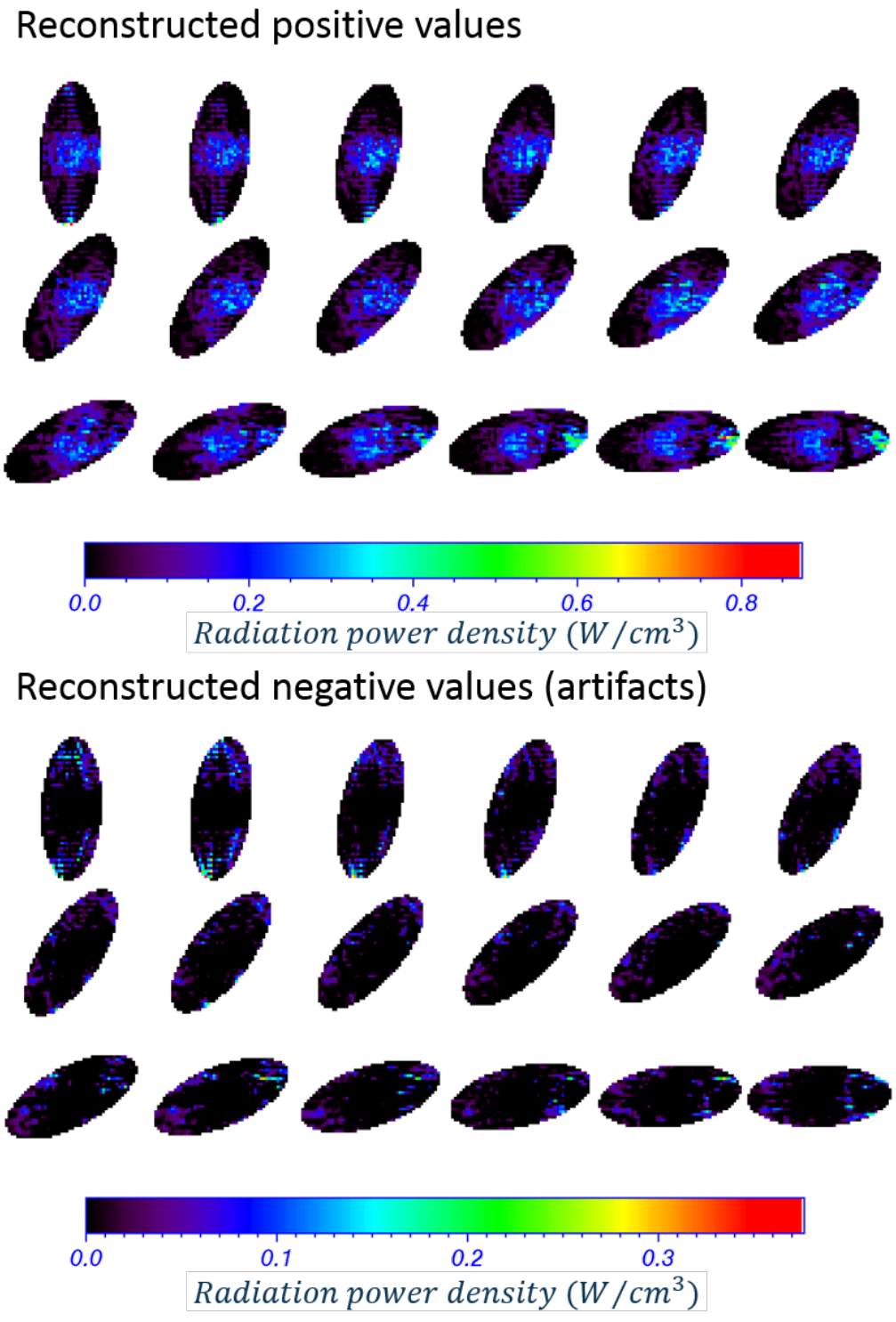

Figure 4.29: Reconstructed profile after radiation collapse (♯1217876.52s), which is obtained from experimental IRVB images by Tikhonov regularization (without relative calibration); positive values (upper) and negative values (lower).

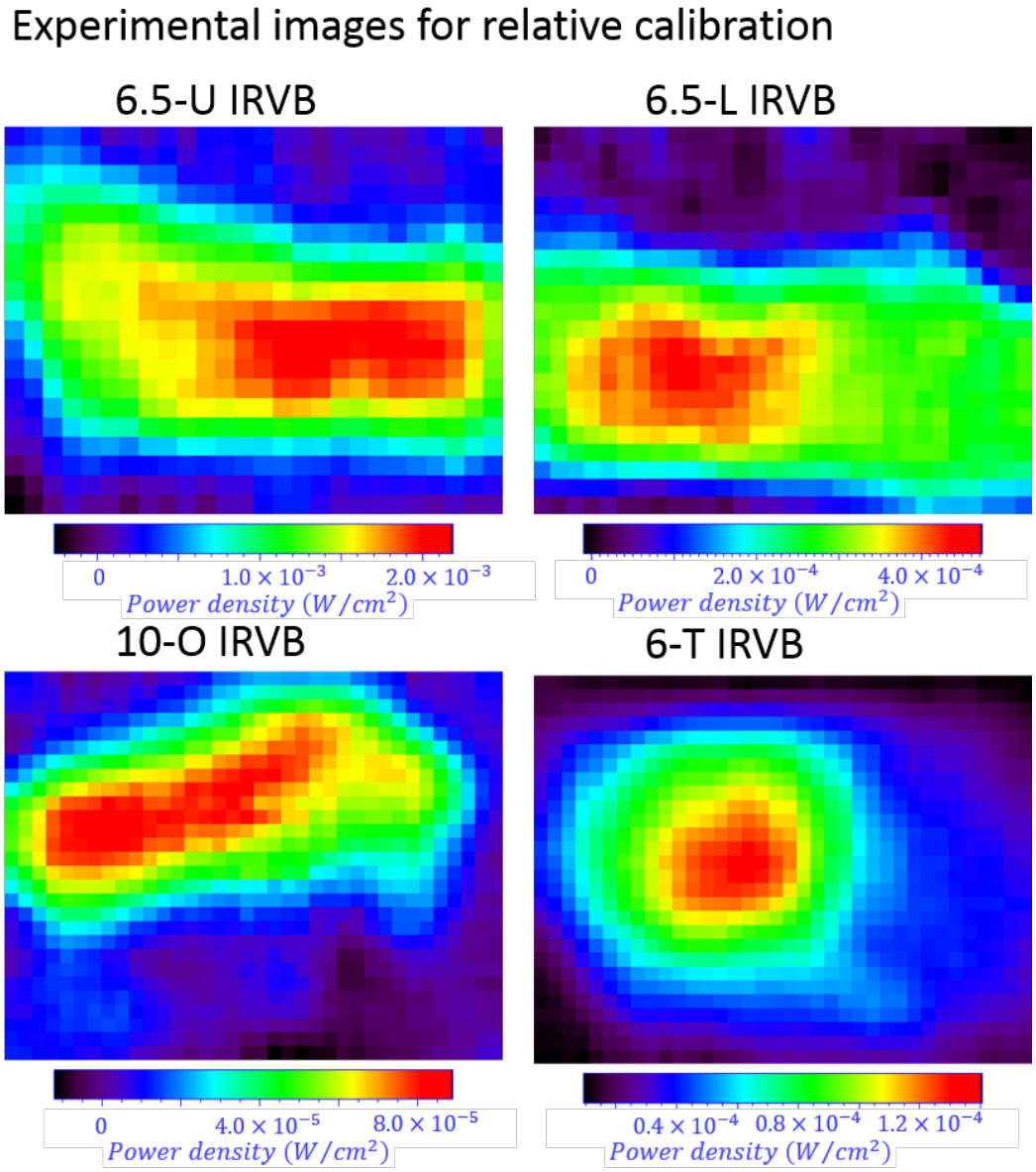

Figure 4.30: Experimental IRVB images for relative calibration, which have been measured in ♯121787 discharge at 6.5s (after collapse)

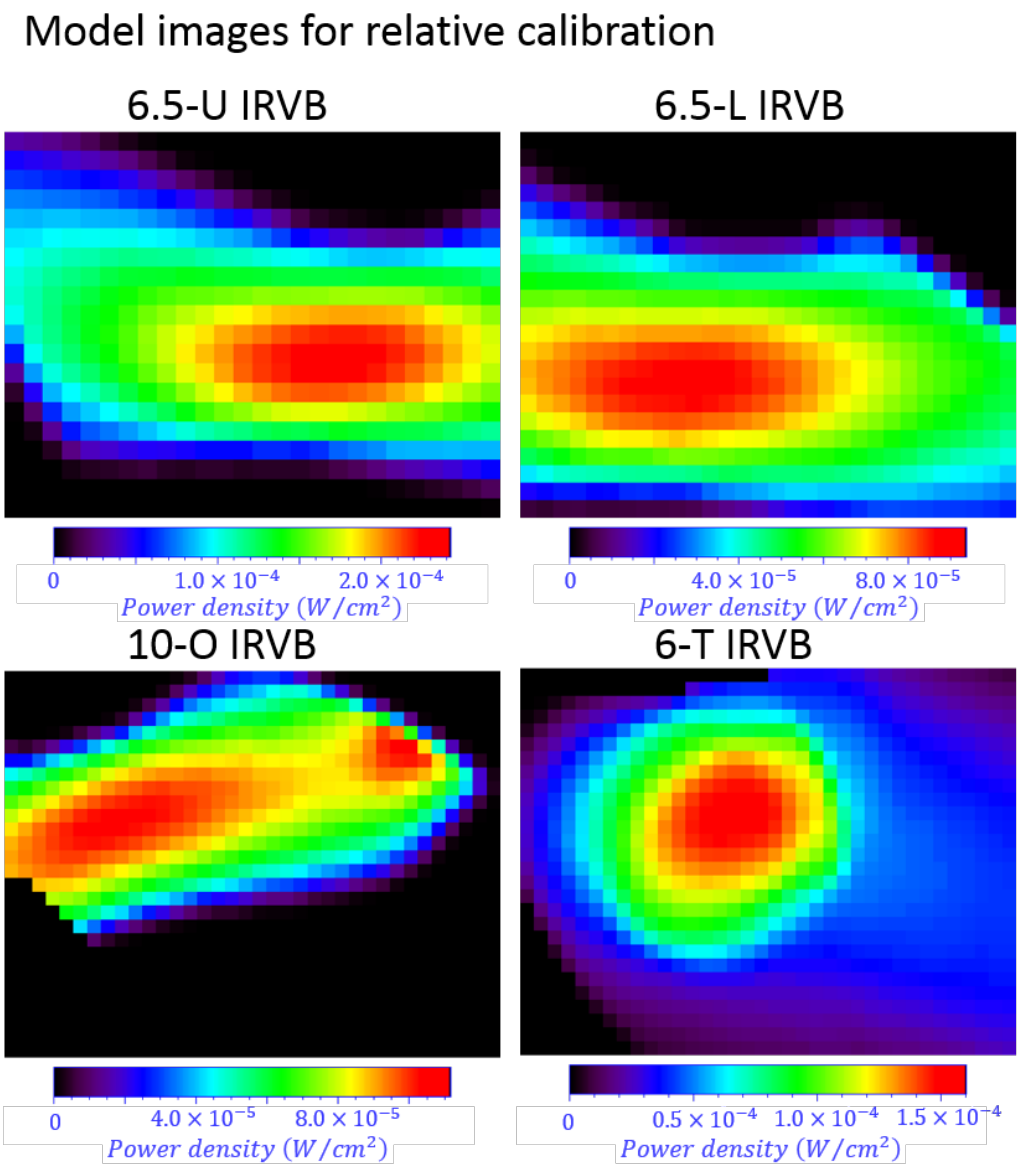

Figure 4.31: Synthetic IRVB images for relative calibration, which are calculated from the 3D function model.

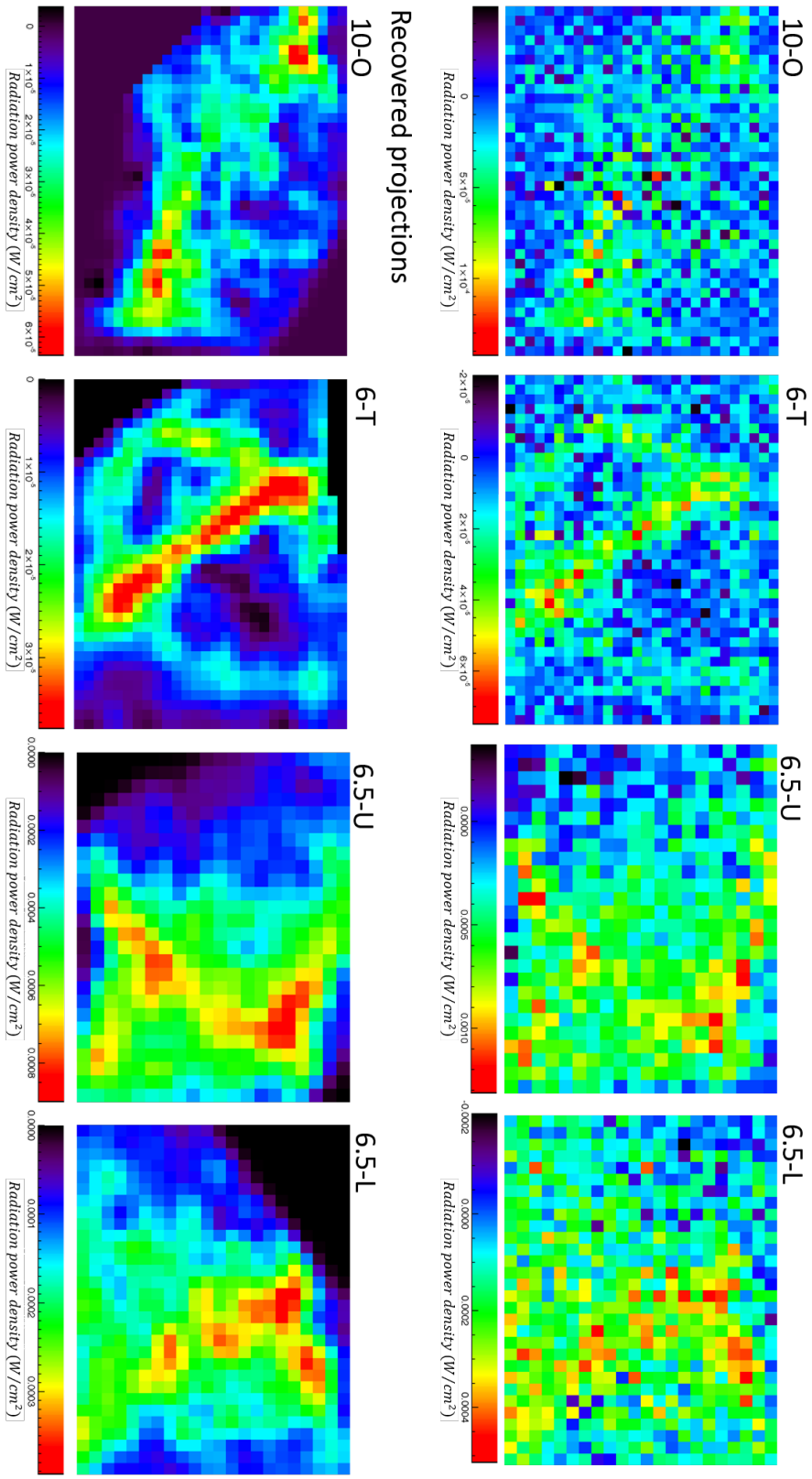

Figure 4.32: Calibrated IRVB image before radiation collapse (♯1217876.02s) (upper) and projections of reconstructed profile with Tikhonov regularization (lower).

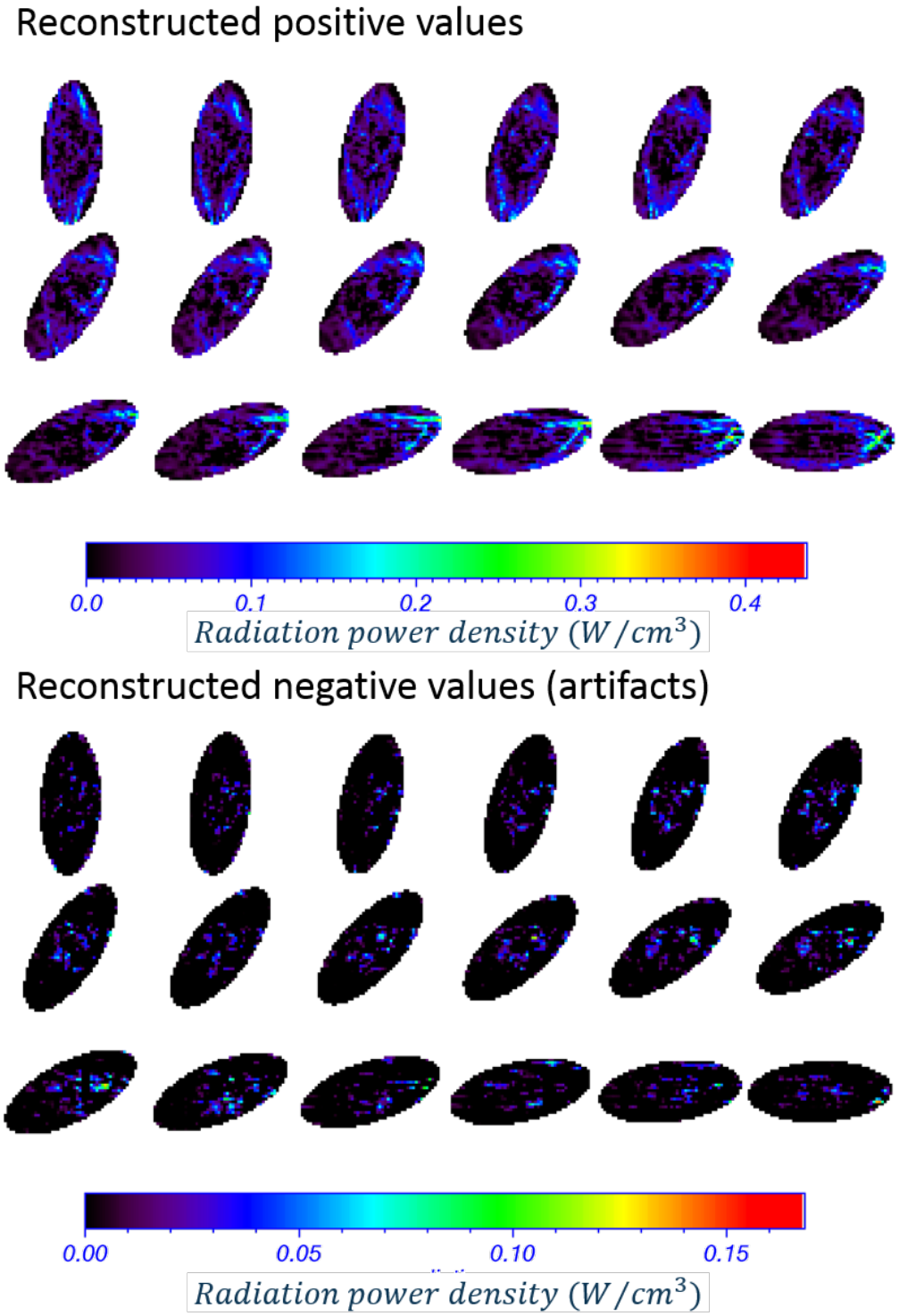

Figure 4.33: Tikhonov reconstruction from calibrated IRVB images before radiation collapse (♯1217876.02s); positive values (upper) and negative values (lower).

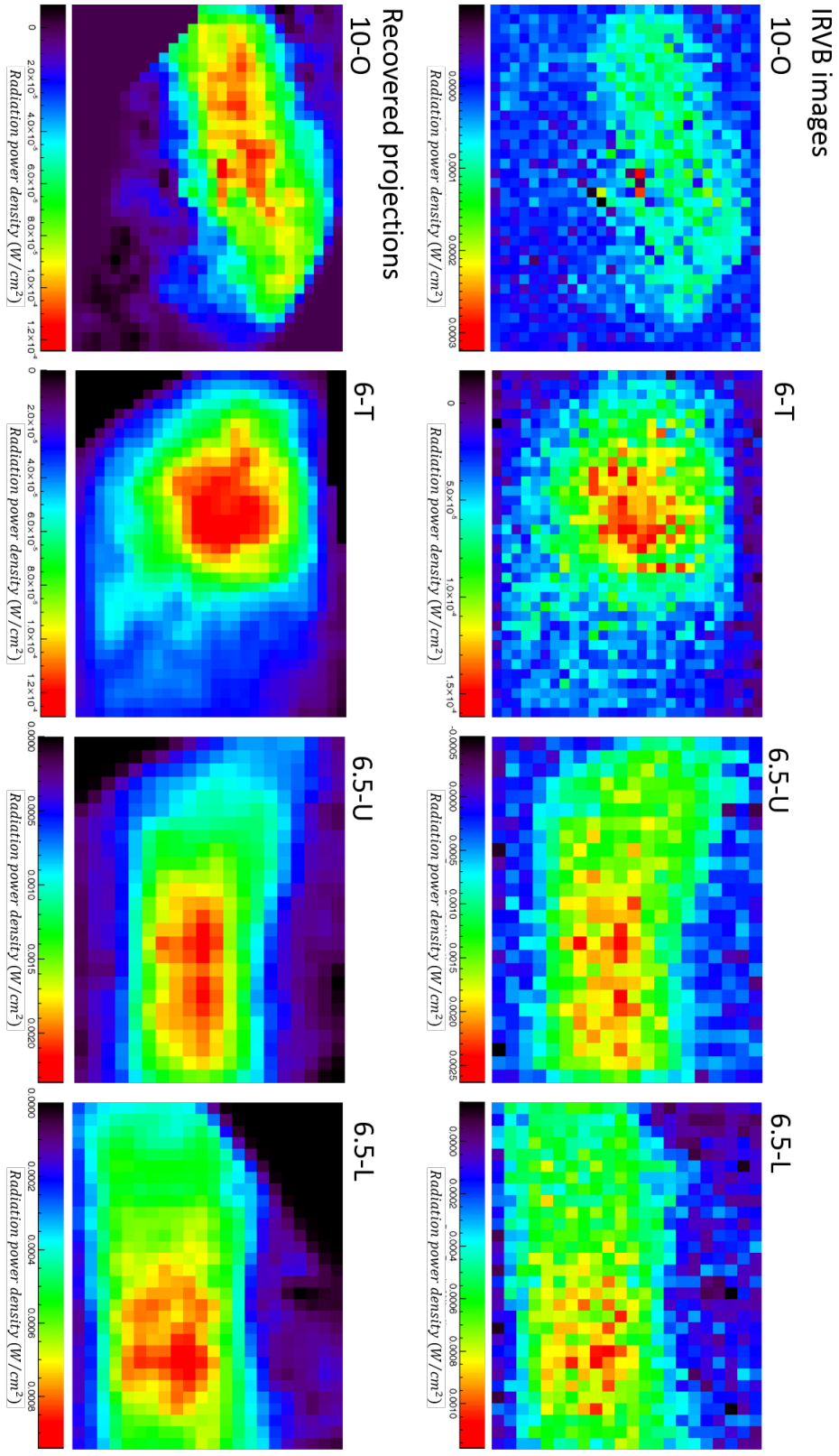

Figure 4.34: Calibrated IRVB images after radiation collapse (♯1217876.52s) (upper) and projections of reconstructed profile with Tikhonov regularization (lower).

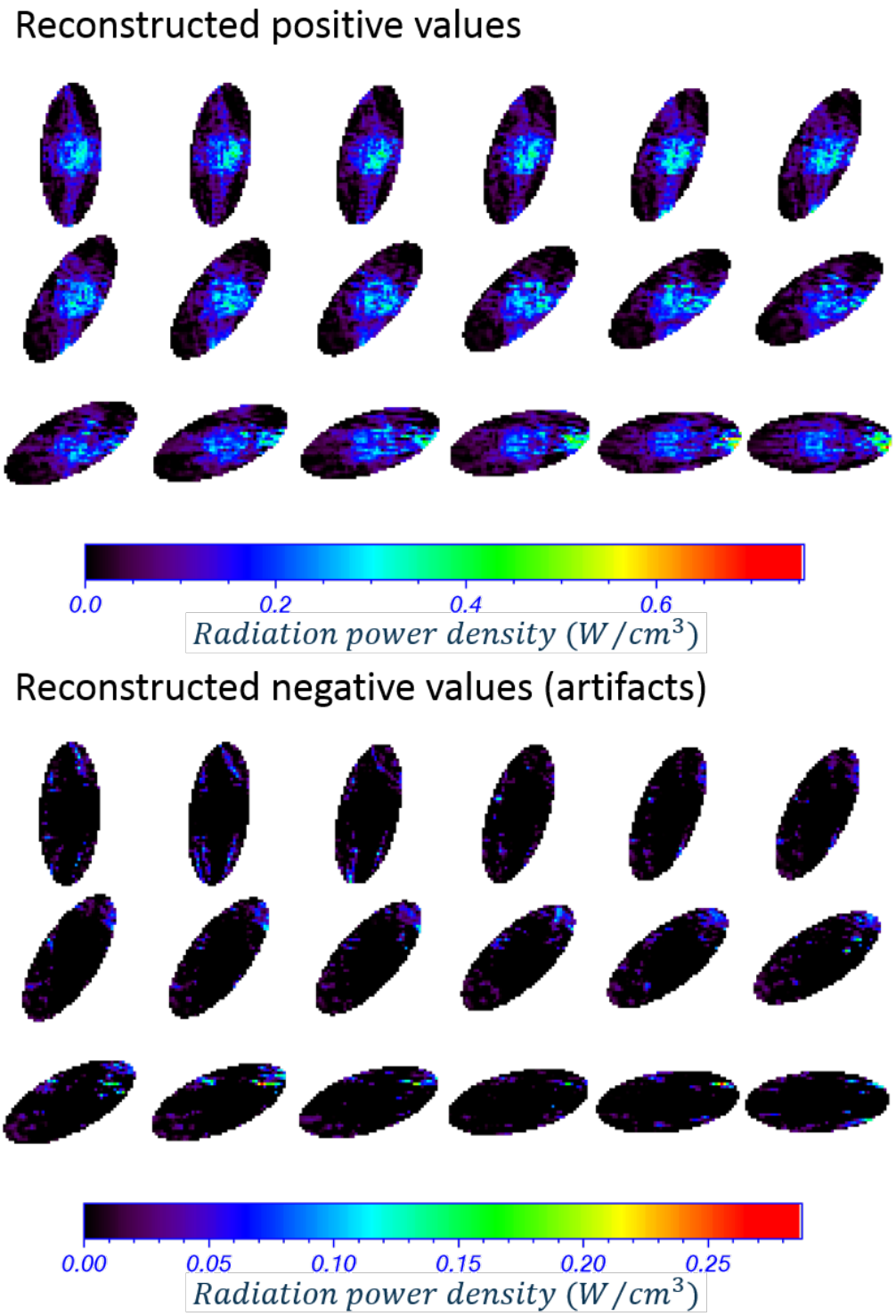

Figure 4.35: Tikhonov reconstruction from calibrated IRVB images after radiation collapse (♯1217876.52s); positive values (upper) and negative values (lower).

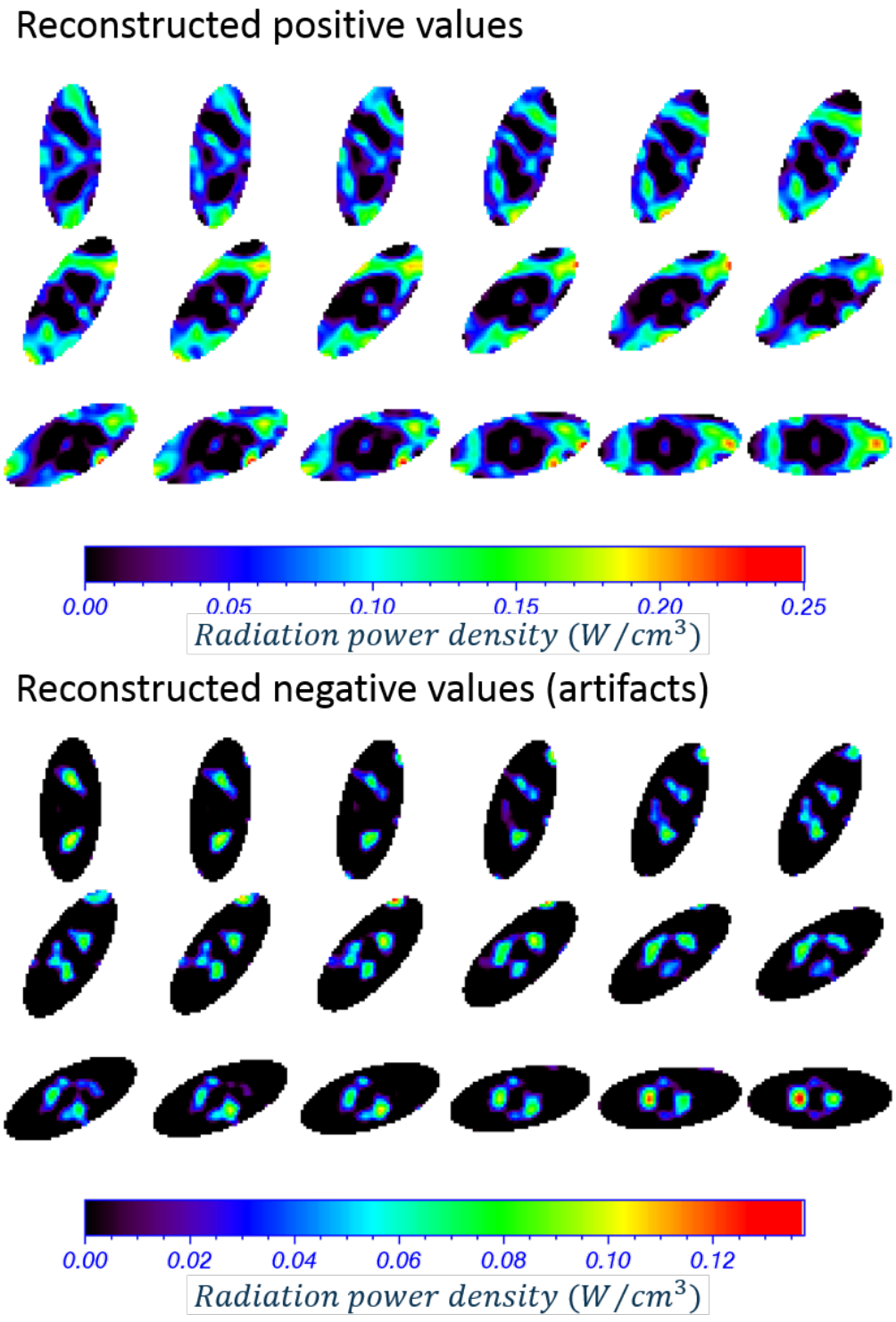

Figure 4.36: Tikhonov reconstruction (Lapalacian matrix) from calibrated IRVB images before radiation collapse ($\sharp 1217876.02s$); positive values (upper) and negative values (lower).

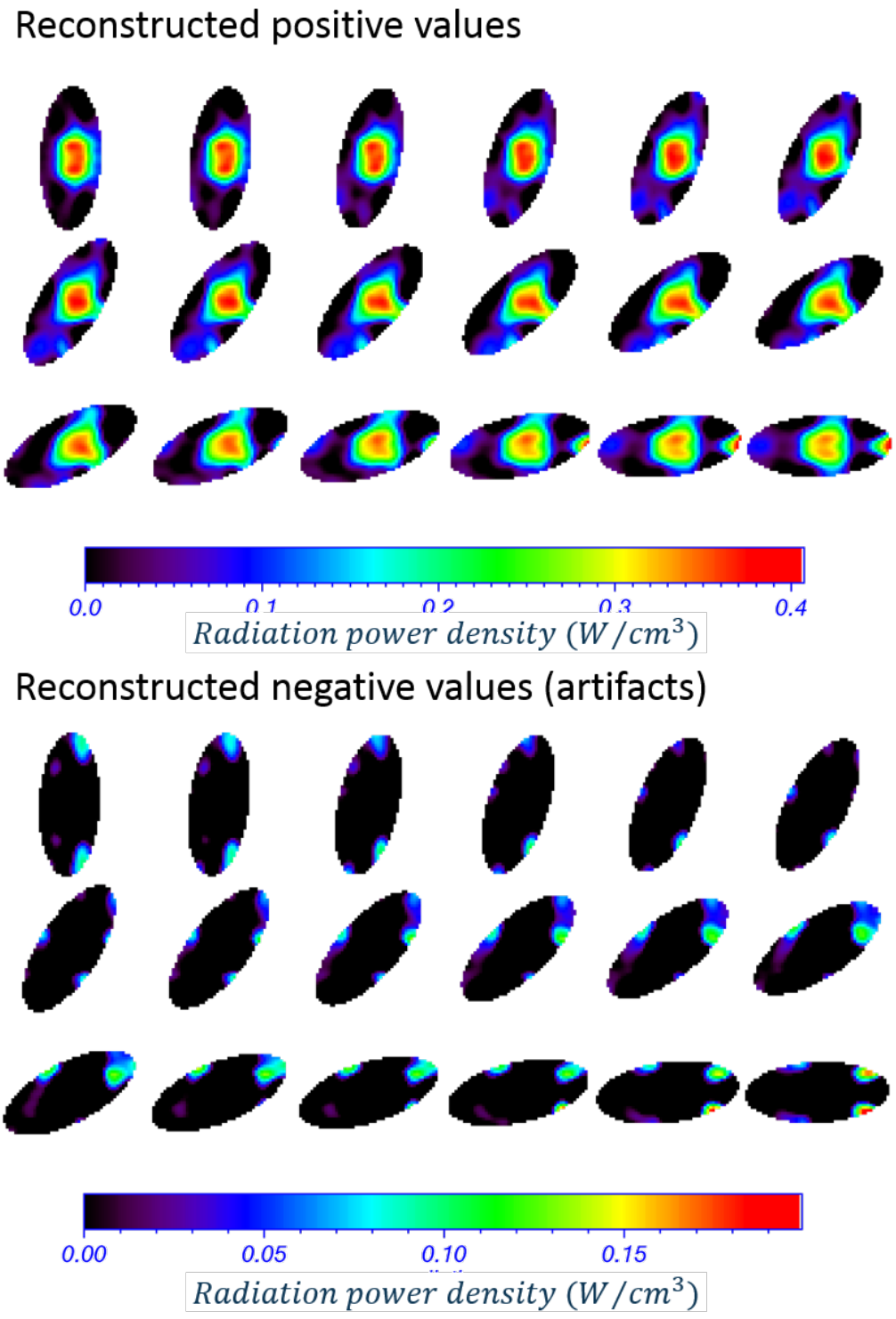

Figure 4.37: Tikhonov reconstruction (Lapalacian matrix) from calibrated IRVB images after radiation collapse (♯1217876.52s); positive values (upper) and negative values (lower).

Bibliography

[1] Y. Feng et al., Contrib. Plasma Phys. 44, 57 (2004).

[2] D. Reiter et al., Fusion Sci. Technol. 47, 172 (2005).

[3] M. Kobayashi et al., Nucl. Fusion 53, 093032 (2013).

[4] R. Sano et al., Plasma Fusion Res. 8, 2402138(2013)

[5] A. C. Kak and M. Slaney, Principles of Computerized Tomographic Imaging (IEEE Press, New York, 1987).

[6] K. Sekihara, Introduction to Statistical Signal Processing (Kyoritsu Shuppan, Tokyo, 2011) (in Japanese)

[7] C. P. Hansen, Discrete Inverse Problems: Insight and Algorithms (SIAM, Philadelphia, 2010).

[8] A.N. Tikhonov, Soviet Math. Dokl. 4, 1035(1963).

[9] G. H. Golub, M. Heath, and G. Wahba, Technometrics 21, 215 (1979).

[10] N. Iwama et al., Appl. Phys. Lett. 54, 502 (1989).

[11] N. Terasaki et al., Fusion Eng. Design 34-35, 801 (1997).

[12] N. Terasaki, N. Iwama, and H. Hosoda, Trans. IEICE J81-D-II, 93 (1998) (in Japanese).

[13] K. Ertle et al., Nucl. Fusion 36, 1477(1996).

[14] N. Iwama et al., J. Plasma Fusion Res. SERIES 8, 691 (2009).

[15] S. Ohdachi et al., Plasma Sci. Technol. 8, 45 (2006).

[16] S. Ohdachi et al., Plasma Fusion Res. 2, S1016 (2007).

[17] T. Ming et al., Plasma Fusion Res. 6, 246120 (2011).

[18] T. Kitagawa, J. Information Processing 11, 263 (1989).

[19] H. Akaike et al., Akaike Information Criterion (Kyoritsu Shuppan, Tokyo, 2007) (in Japanese)

5 Investigation into radiation collapse

In this chapter, radiation from the plasma has been measured with the procedures mentioned in the preceding Chapter.

5.1 IRVB measurement during radiation collapse

Figure 5.2-5.4, 5.8-5.11 and 5.15-5.18 shows sequences of IRVB images which were taken in collapse discharges with the magnetic axis of 3.6m, 3.75m and 3.9m. These images have been smoothed with a $[3 \times 3]$ (for 6.5-U and 6.5-L IRVB images) and $[5 \times 5]$ (for 6.5-U and 6.5-L) averaging window to be easier to understand. These IRVB images show changes on the images before and during collapse. For example, just before a drop of the stored energy IRVB images show fine structure especially on 6.5-U and 6.5-L IRVBs. However, the origin of these changes can not be directly explained by these images, because IRVB images are obtained by line integrated FoVs.

5.2 Application of 3D measurement to radiation collapse

5.2.1 Evolution of nine parameters with 3D model fitting

To investigate the changes of the radiation structures during radiation collapse, the model parameter fitting which is described at Section 4.5 has been applied to the measured IRVB images which are shown in Section 5.1. Figures 5.21-5.28 the show results of the model fitting for the IRVB images. Several parameters show significant changes during radiation collapse. For example, Figures 5.23, 5.26, 5.29 and 5.30 show that the local enhancement of the radiation starts from the inboard side clearly and the evolution of the inboard/outboard asymmetry property γ_{in-out}. γ_{in-out} is significantly increased from a specific timing. It indicates radiation from the inboard side is significantly enhanced, in addition to a decrease in the semi major radius, a, together with a strong increase in c at almost the same timing. The enhancement of the inboard radiation in γ_{in-out} is consistent with previous research that shows strong radiation from the inboard side is obtained during radiation collapse [9]. This behavior is also obtained with other magnetic configurations as Figure 5.31. It indicates that regardless of the magnetic configuration, the inboard enhancement appears at a specific timing during radiation collapse. Therefore, the γ_{in-out} can be used to define a reference timing for the evolution of radiation collapse to investigate the evolution. In this study the initiation of the inboard enhancement is defined as the reference point and the initiation of radiation collapse.

Other parameters also show interesting structural changes during radiation collapse in Figures 5.21-5.27 . Parameter w shows the time evolution of the width of the radiation region. The width is reduced before radiation collapse and increased during radiation collapse. It indicates that the radiation region is concentrated just before radiation collapse. Semi major and minor radii, a and b, show that the radiation shape changed into a circle from an ellipse during radiation collapse. The center of the radiation region, R_{center}, shows the center shifts to the outboard side from the inboard

enhancement, especially in the case of the magnetic axis of 3.9m. Base radiation intensity c indicates that the base radiation is increased before radiation collapse, and the magnitude of the peaking, γ_p, indicates that the radiation is strongly concentrated at a peak during radiation collapse. The toroidal asymmetric parameter $\gamma_{Toroidal}$ also shows a specific behavior. Sometimes $\gamma_{Toroidal}$ increases before the inboard enhancement and decreases after that, suggesting that the 3D structural changes interestingly. The behavior indicates that the radiation from the vertically elongated cross section is slightly enhanced before radiation collapse.

5.2.2 Evolution of reconstructed radiation profile (Tikhonov regularization)

In the last subsection, the results of the 3D model fitting show the characteristics and timings of the evolution of the 3D radiation structure during radiation collapse. However, the 3D model for the model fitting has several restrictions on the description of the 3D radiation structure, because the 3D model has only low order components as model parameters. Especially, when initiation points of the observed asymmetry features (toroidal and in-out) are localized, understanding of the features is difficult. Therefore, to investigate the observed characteristics, the 3D algebraic inversion is applied in analysis of the same discharges as a 3D measurement with less parametric restriction, in other words allowing a more subtle observation. Figure 5.32-5.33 shows the reconstructed profiles by the 3D algebraic inversion (Tikhonov regularization) during radiation collapse. In Figure 5.32-5.33, the radiation profiles in the whole torus are obtained with a repetation of 18 toroidal degrees which is calculated by the 3D algebraic inversion. Reconstructed profiles show the same tendency with the results of the 3D model fitting and show important details on the evolution of radiation structures which can not be or are difficult to observe in the 3D model fitting. Figure 5.33 clearly shows the radiation from the inboard side is enhanced and then the radiation region shrinks. Additionally, as in Figure 5.34 at a timing of 6.00-6.02s the inboard enhancement appears from the inboard side of the vertically elongated cross section and then the inboard enhancement extends to horizontally elongated cross section. This behavior indicates that the inboard enhancement is initiated at the inboard side of the vertically elongated cross section. In LHD, this location is the nearest point to the wall of the vacuum vessel. Figure 5.34 also shows that the extension of the inboard enhancement is along the LCFS of the plasma. These observed behavior of the asymmetries provide enhanced understanding of the model fitting result, such as the evolutions of $\gamma_{Toroidal}$ and γ_{in-out}. In the case of the magnetic axis of 3.75m, the same tendency is also observed in Figure 5.32. Especially, the reconstructed profiles clearly show when the inboard enhancement occurs, radiation structure along the LCFS. Observed evolutions in radiation structures by the 3D model fitting and 3D algebraic inversion indicate that the asymmetries of the radiation structure play an important role in the radiation collapse.

5.2.3 Carbon emission structure

To investigate the carbon emission during the radiation collapse as a main radiator, the $CIII(464.7nm)$ and $CII(426.7nm)$ emissions are measured by the imaging spectrometer at LHD port 7-O. Figure 5.35 -5.36 shows how the radiation structure changes in $CIII(464.7nm)$, $CII(426.7nm)$, H_γ and H_β during radiation collapse with a collapse discharge (♯ 121787). The figures show the following sequence. At 5.80s, the emission of H_β is the strongest emission among four measured emissions and all emissions concentrate around an X point. At 5.95s, the intensity of $CIII(464.7nm)$ is increased as compared with H_β around the X-point. At 6.10s (timing of the inboard enhancement),

H_β and H_β do not show large changes, but the peak locations of $CIII(464.7nm)$ and $CII(426.7nm)$ emission move to near the LCFS from around the X-point. This behavior of the C emission is consistent with the observed behavior of radiation structure by 3D algebraic inversion (radiation structure is along the LCFS). However peak locations of the $CIII(464.7nm)$ and $CII(426.7nm)$ emission are slightly further out than the expected locations from the reconstructed profiles. Therefore, it indicates the possibility that the main radiators are carbon with higher charge states than $CIII$. At 6.25s (after the shrinking phase), $CIII(464.7nm)$ and $CII(426.7nm)$ emission disappeared and the H_β and H_β emission moves into the core region because of the electron temperature decrease and/or loss of carbon source from walls.

5.2.4 Evolution of plasma parameters during radiation collapse

Electron temperature profile

The emission from carbon depends on the cooling rate which is a function of the electron temperature T_e. Therefore the observed change in radiation structures with carbon impurities during radiation collapse indicates the electron temperature is changed at the same timing.To investigate the relation between the evolution of radiation structures and the electron temperature profile, a comparison between the evolution of the optimized model in the model fitting and the measured profile of the electron temperature by a Thomson scattering diagnostics has been carried out.

Figure 5.37 shows the evolution of the 3D model profile at a horizontally elongated cross section and the T_e profile at the same location. The figure shows that the Te profile and the radiation region coinstantaneously shrink. Especially at 6.1s which is the observed timing of the carbon emission moving from the imaging spectrometer, the T_e profile shows shrinking clearly.

Mean free path of electron

The measured evolutions of the radiation structure indicate that the asymmetry in the radiation structure plays an important role in the radiation collapse. The measured asymmetry is obtained even inside the LCFS during radiation collapse. When electrons in the plasma can freely move, this kind of asymmetry should not occur. To investigate these asymmetries in radiation structures, the mean free path (MFP) of electrons has been investigated using theThomson scattering diagnostics. The mean free path of electrons is given by the thermal velocity of the electron and the electron-ion collision frequency, The thermal velocity of electrons, v_{the}, is given as

$$v_{the} = 5.9 \times 10^7 T_e^{0.5} \tag{5-2-1}$$

where T_e is the electron temperature, The electron-ion collision frequency, ν_{ei}, is given as

$$\nu_{ei} = 2 \times 10^{-6} \frac{Z n_e ln\Lambda}{T_e^{1.5}} \tag{5-2-2}$$

where Z is the charge number of ion (=1), n_e is the density of electron and $ln\Lambda$ is the Coulomb logrithm (=20). The mean free path λ_e is given as

$$\lambda_e = v_{the}/\nu_{ei} \tag{5-2-3}$$

The evolution of the mean free path at the plasma edge before radiation collapse has been investigated, Figure 5.38 (lower) shows the relation between the mean free path and

the electron temperature at the plasma edge which is defined before collapse to include 99 percent of the stored energy of the plasma, At first, the mean free path is linearly related with the electron density during steady state phase. This relation is changed before the radiation collapse, In this phase, the mean free path suddenly drops with increasing electron density. The mean free path at which this drop occurs is defined by a 30% gap between the linear extrapolateion and the dropping value. The definition is shown in Figure 5.38.

Figure 5.39 shows how $\lambda_{e,cng}$, is changed with different magnetic axis configurations. The figure indicates that when the mean free path is decreased to $1.5 - 7m$, the change in density dependence is obtained. The timing of this change is before the asymmetry initiation. At the timing of the change, the electron temperature T_e is around $100 - 200eV$ and the electron density is close to the Sudo-density limit. These results indicate the possibility that when the mean free path loses its linear dependence, the asymmetry of radiation structures can no longer be canceled along magnetic field lines by the parallel transport of electrons.

5.3 Summary and scenario of radiation collapse

In this chapter, the developed 3D measurements have been applied to measurement of radiation collapse. Results of 3D measurements indicate that the radiation structures have asymmetries during radiation collapse and these asymmetries start from the inboard side of the vertically elongated cross section where the plasma is closest to the wall. To investigate these asymmetries, the temperature and the mean free path of the electrons have been investigated. By these measurements, several events have been obtained during radiation collapse. With these events, a scenario of radiation collapse with a density ramp up is obtained as follows.

Phase 1 The temperature and the mean free path of electrons drop with increasing electron density and the mean free path loses its linear dependence on density.

Phase 2 When the mean free path become lower than around λ_{chg}, the enhancement of the radiation from the inboard side of the vertically elongated cross section starts. The width of the radiation region is decreased. The radiation intensity start to increase.

Phase 3 The inboard enhancement is extended to the horizontally elongated cross section along the LCFS with decreasing mean free path.

Phase 4 The inboard enhancement covers the whole torus. The radiation region start to shrink.

Phase 5 The radiation region crosses into the LCFS

Phase 6 The total radiation power reaches a peak.

Phase 7 The radiation region is concentrating and peaking in the core region.

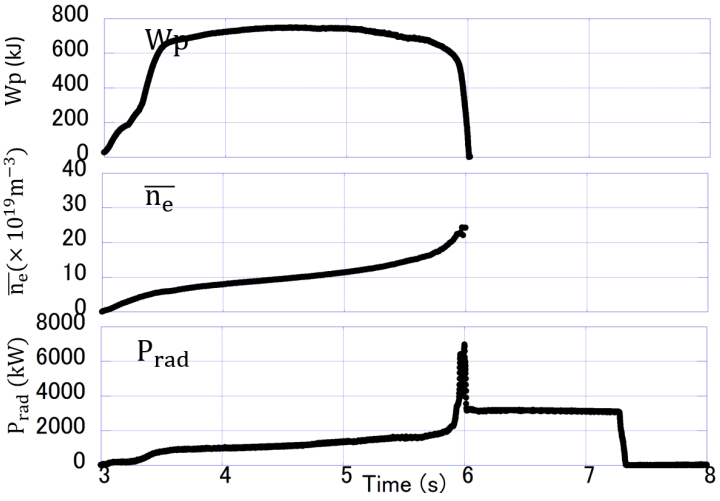

Figure 5.1: Evolution of stored energy, electron density and total radiation power during discharge ♯120928.

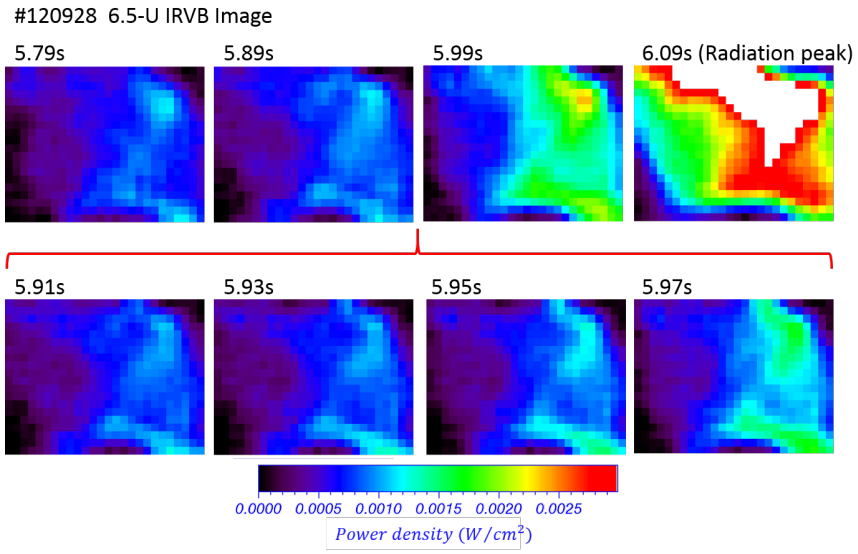

Figure 5.2: Measured 6.5-U IRVB images with collapse discharge (♯120928) under the 3.6m magnetic axis configuration.

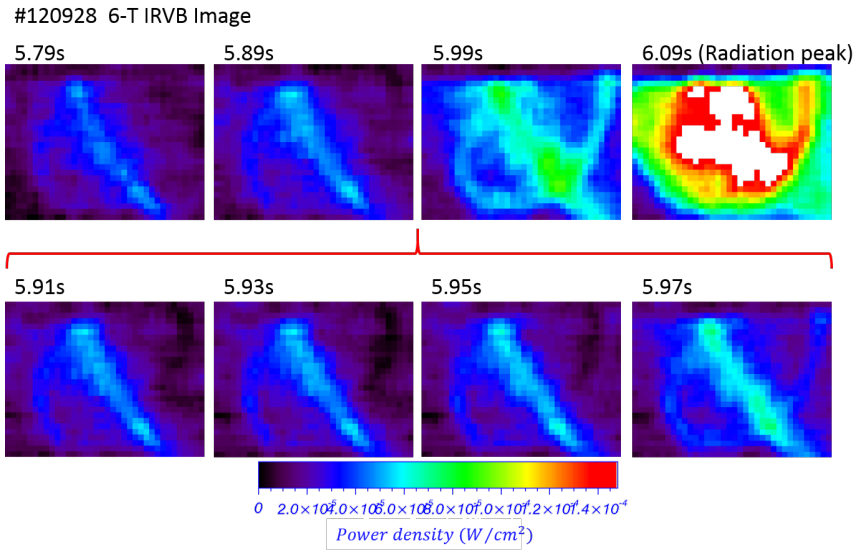

Figure 5.3: Measured 6-T IRVB images with collapse discharge (♯120928) under the 3.6m magnetic axis configuration.

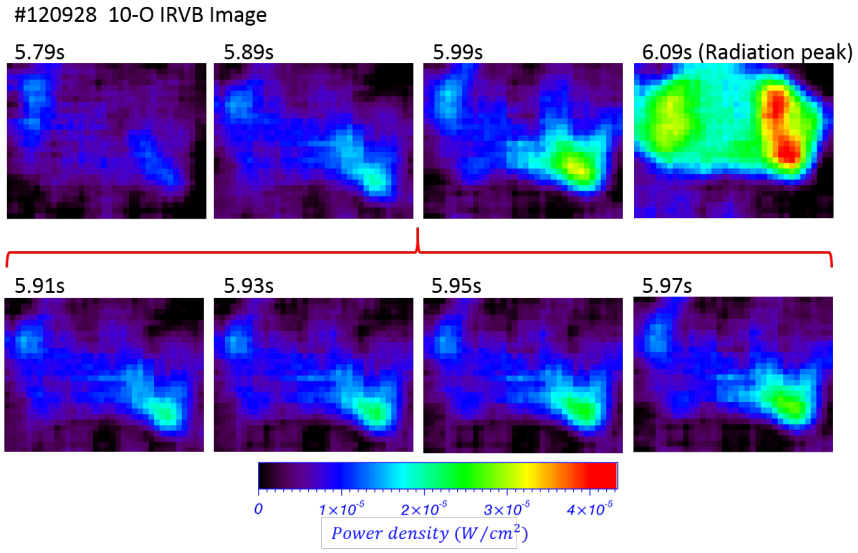

Figure 5.4: Measured 10-O IRVB images with collapse discharge (♯120928) under the 3.6m magnetic axis configuration.

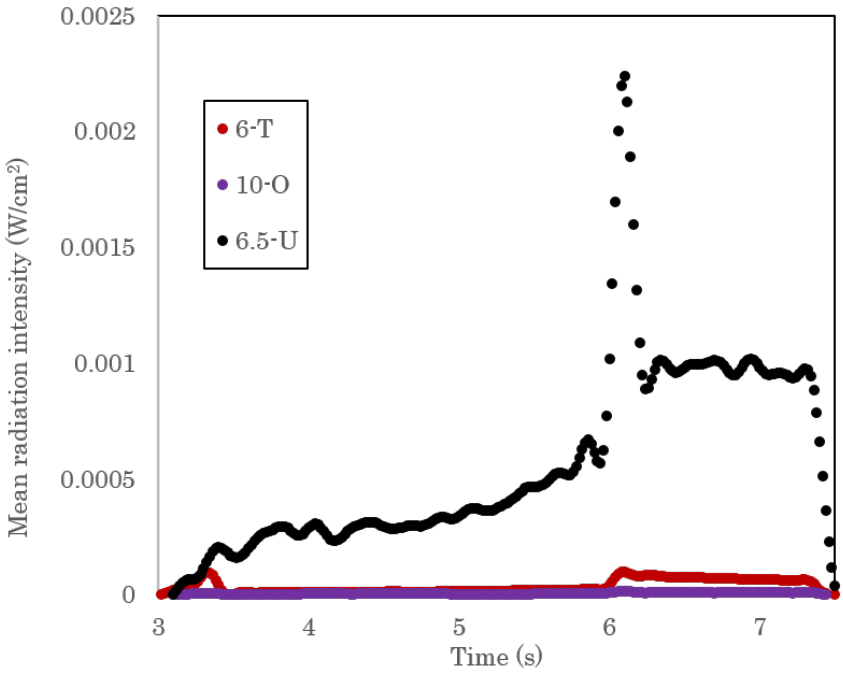

Figure 5.5: Evolution of mean intensity for each IRVB during discharge ♯120928.

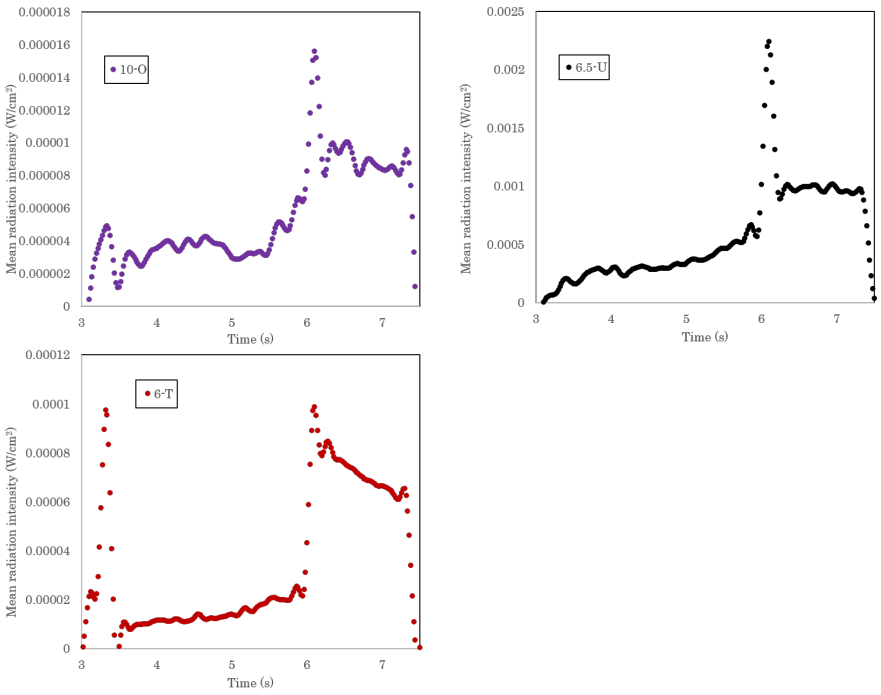

Figure 5.6: Evolution of mean intensity for each IRVB during discharge ♯120928. (6.5-L is not available during this discharge)

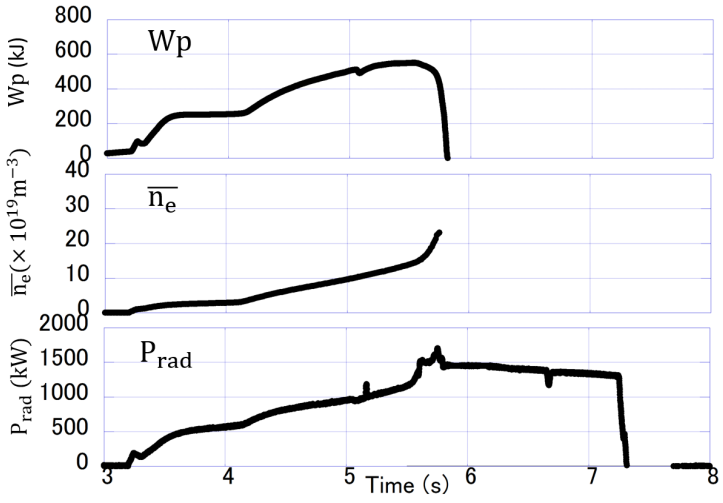

Figure 5.7: Evolution of stored energy, electron density and total radiation power during discharge ♯121835.

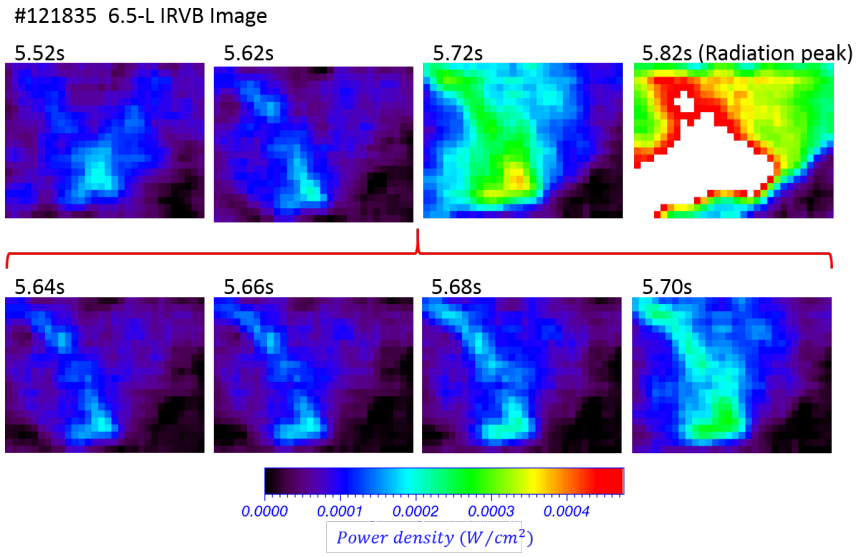

Figure 5.8: Measured 6.5-L IRVB images with collapse discharge (♯121835) under the 3.75m magnetic axis configuration.

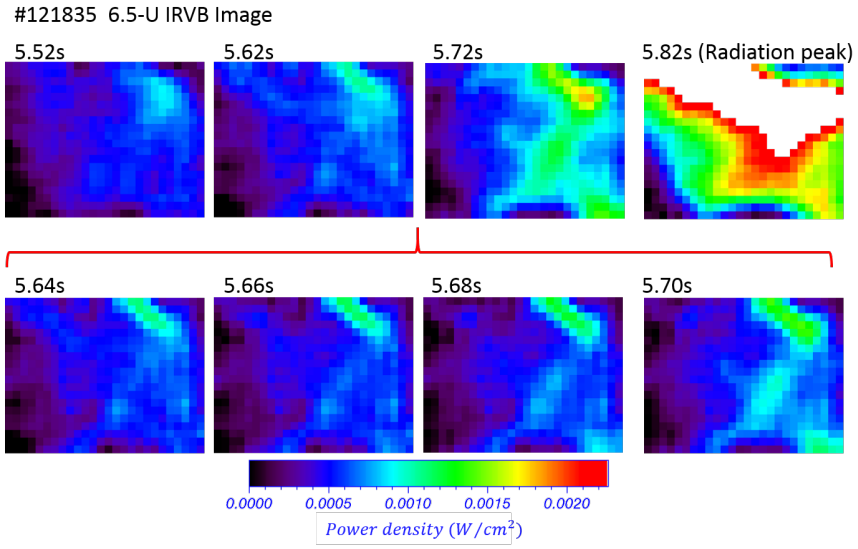

Figure 5.9: Measured 6.5-U IRVB images with collapse discharge (♯121835) under the 3.75m magnetic axis configuration.

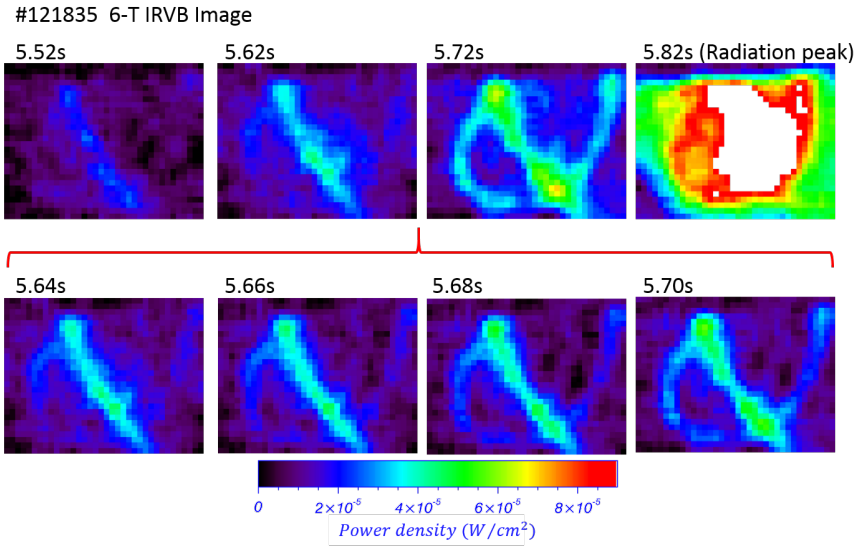

Figure 5.10: Measured 6-T IRVB images with collapse discharge (♯121835) under the 3.75m magnetic axis configuration.

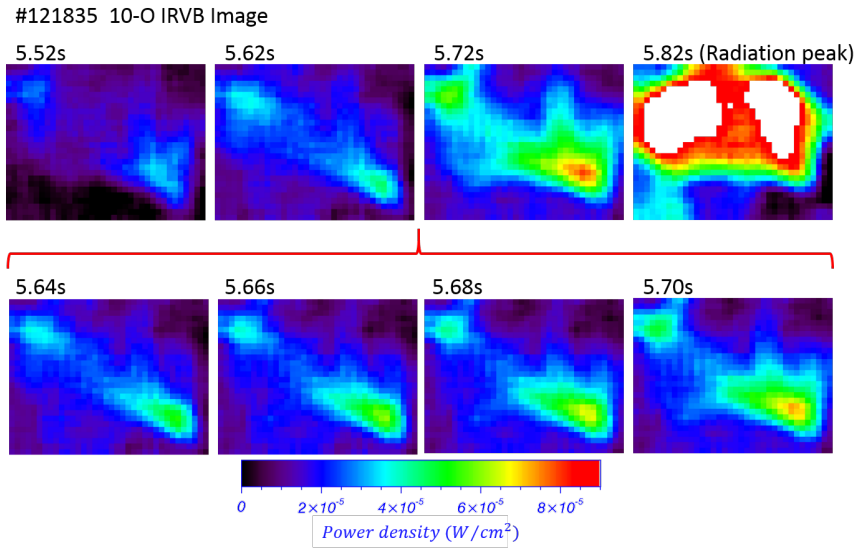

Figure 5.11: Measured 10-O IRVB images with collapse discharge (♯121835) under the 3.75m magnetic axis configuration.

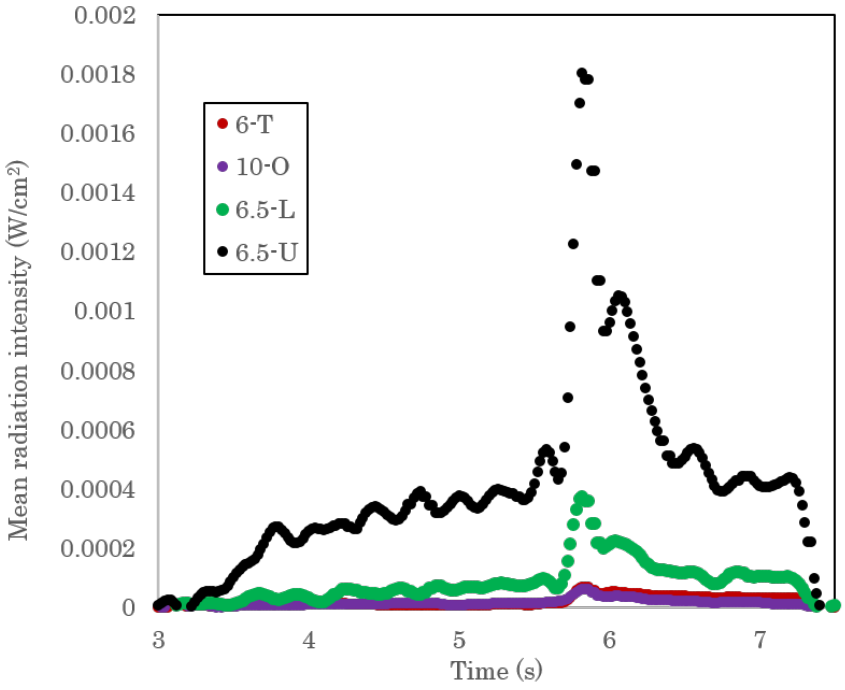

Figure 5.12: Evolution of mean intensity for each IRVBs during discharge ♯121835.

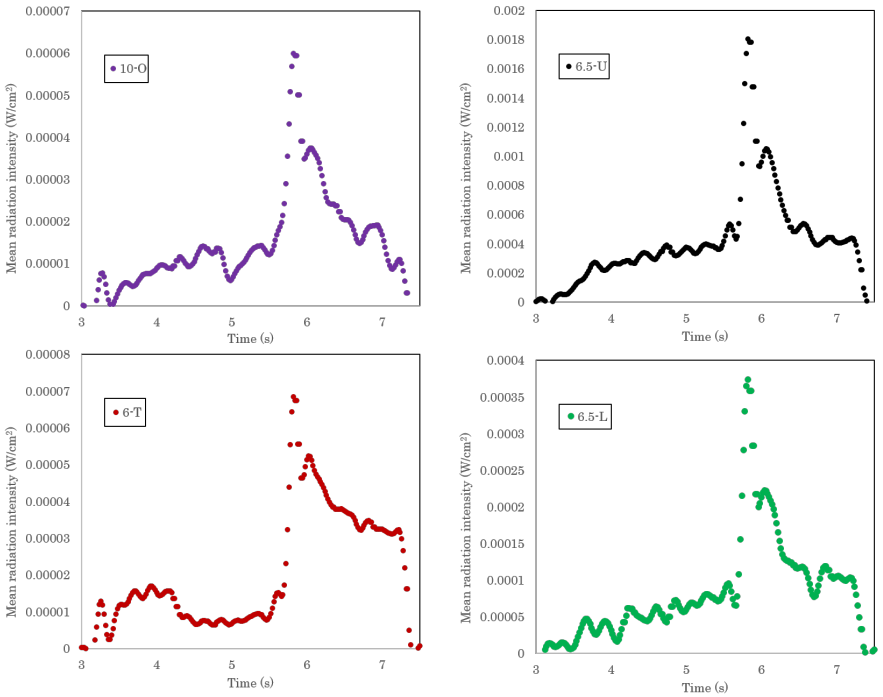

Figure 5.13: Evolution of mean intensity for each IRVBs during discharge ♯121835.

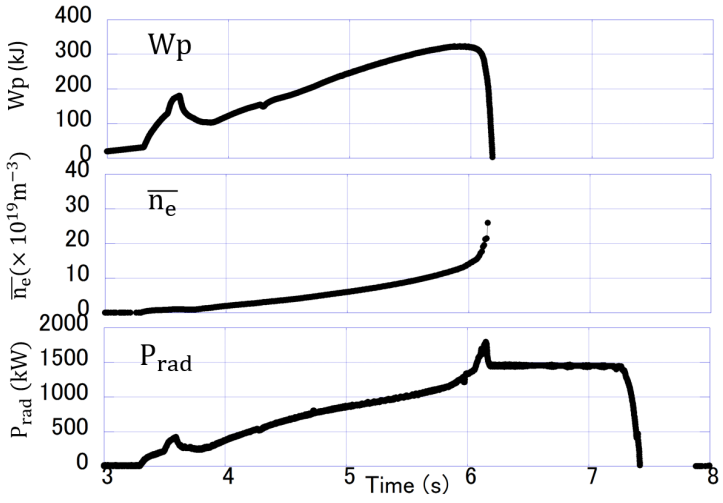

Figure 5.14: Evolution of stored energy, electron density and total radiation power during discharge ♯121787.

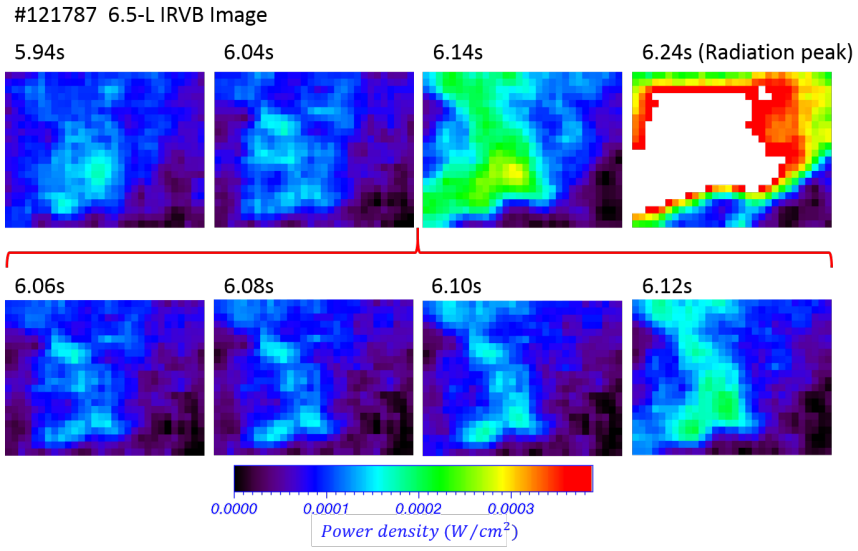

Figure 5.15: Measured 6.5-L IRVB images with collapse discharge (♯121787) under the 3.9m magnetic axis configuration.

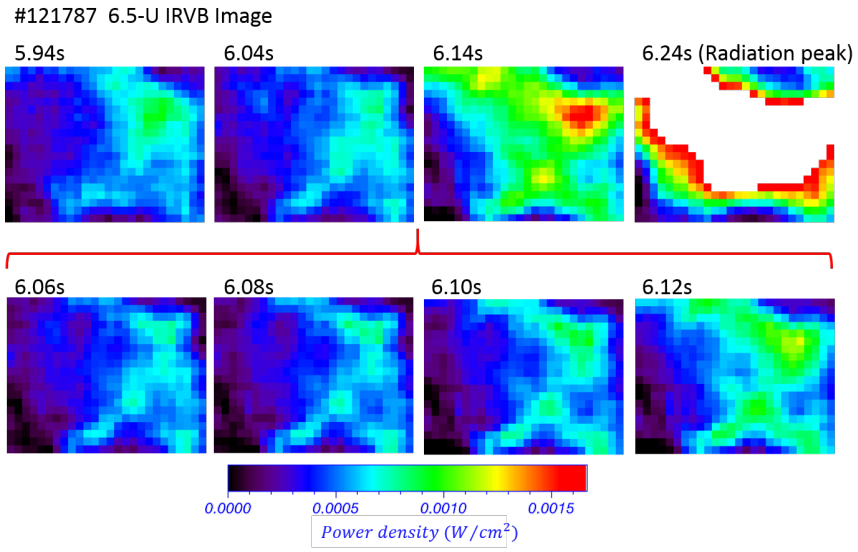

Figure 5.16: Measured 6.5-U IRVB images with collapse discharge (♯121787) under the 3.9m magnetic axis configuration.

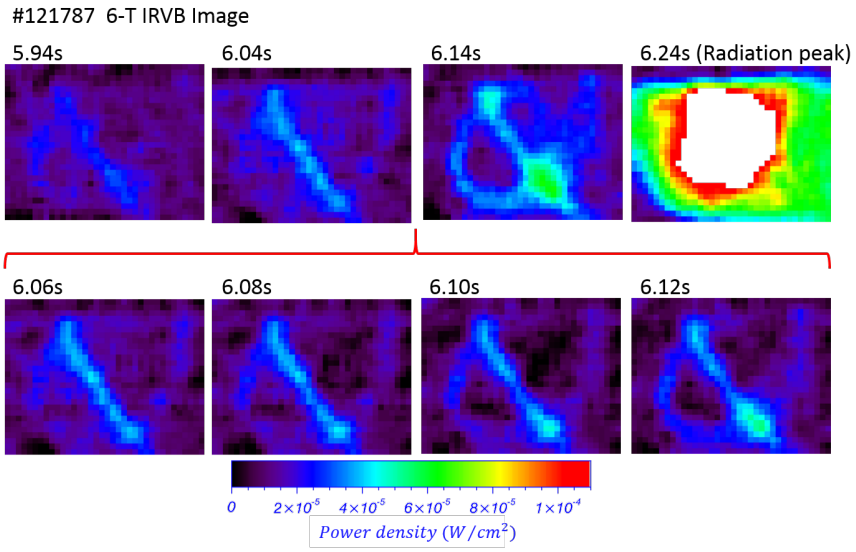

Figure 5.17: Measured 6-T IRVB images with collapse discharge (♯121787) under the 3.9m magnetic axis configuration.

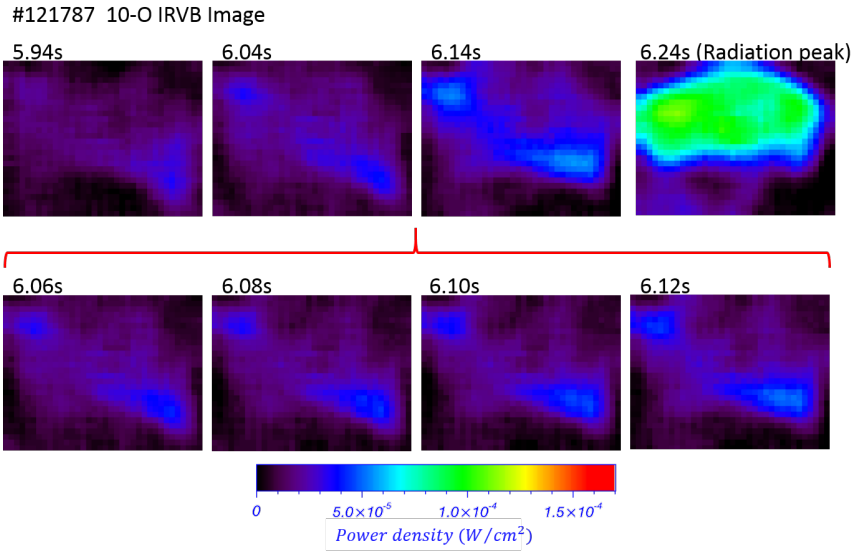

Figure 5.18: Measured 10-O IRVB images with collapse discharge (♯121787) under the 3.9m magnetic axis configuration.

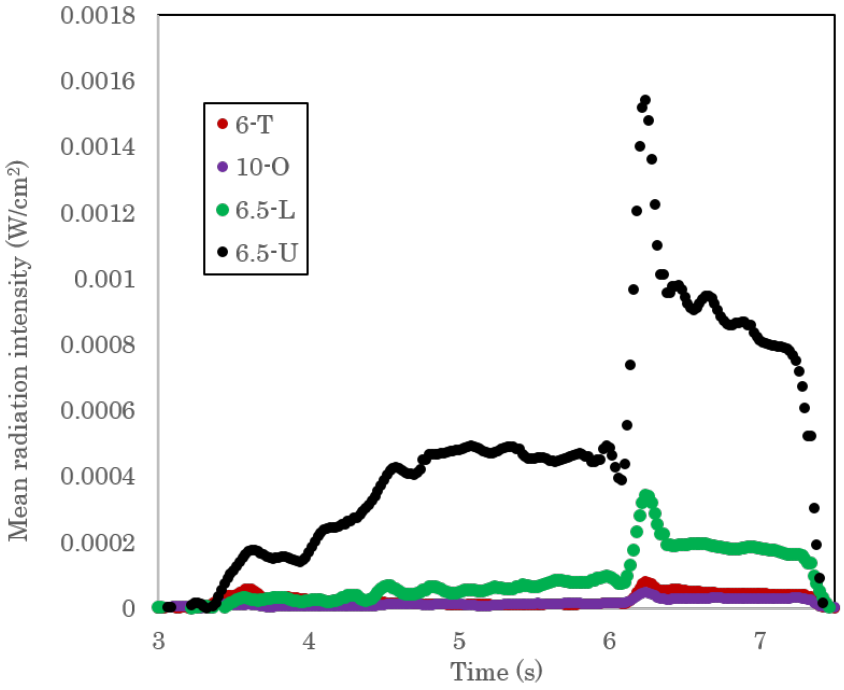

Figure 5.19: Evolution of mean intensity for each IRVBs during discharge ♯121787.

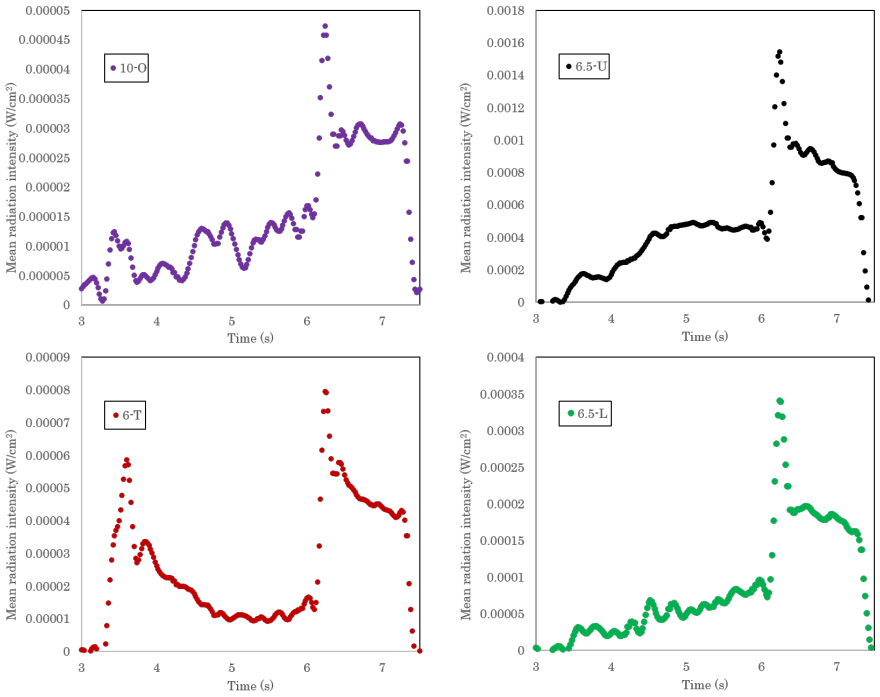

Figure 5.20: Evolution of mean intensity for each IRVBs during discharge ♯121787.

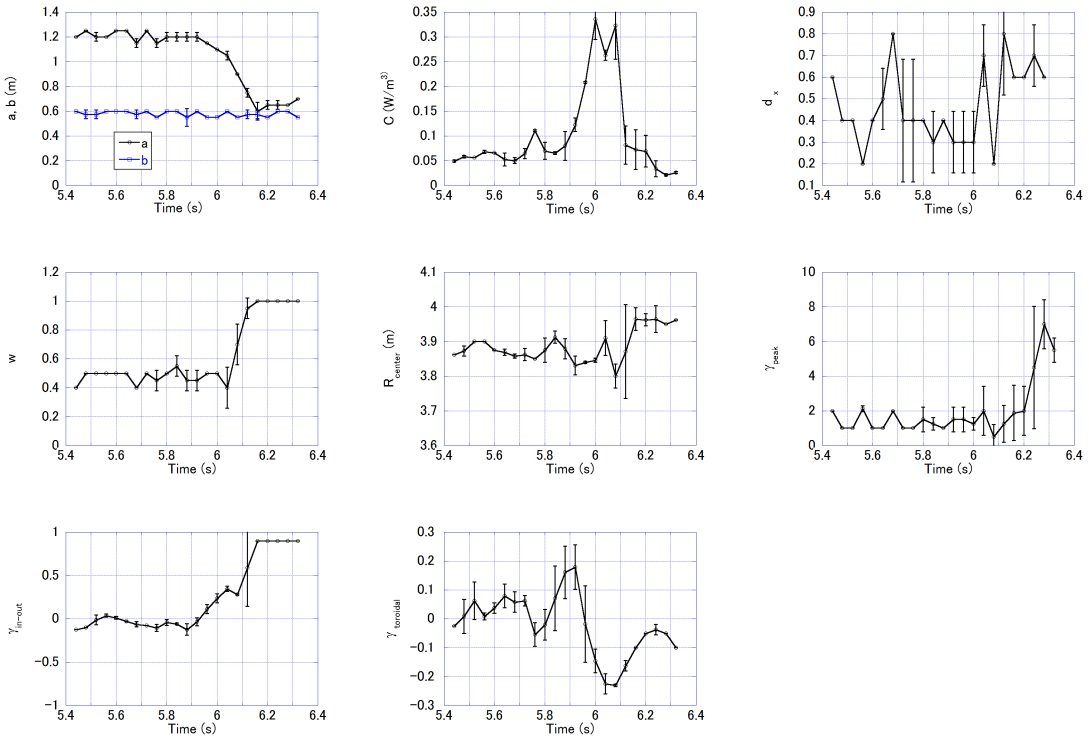

Figure 5.21: Time evolution of obtained model parameters for a collapse discharge (♯ 120928) under the 3.6m magnetic axis configuration.

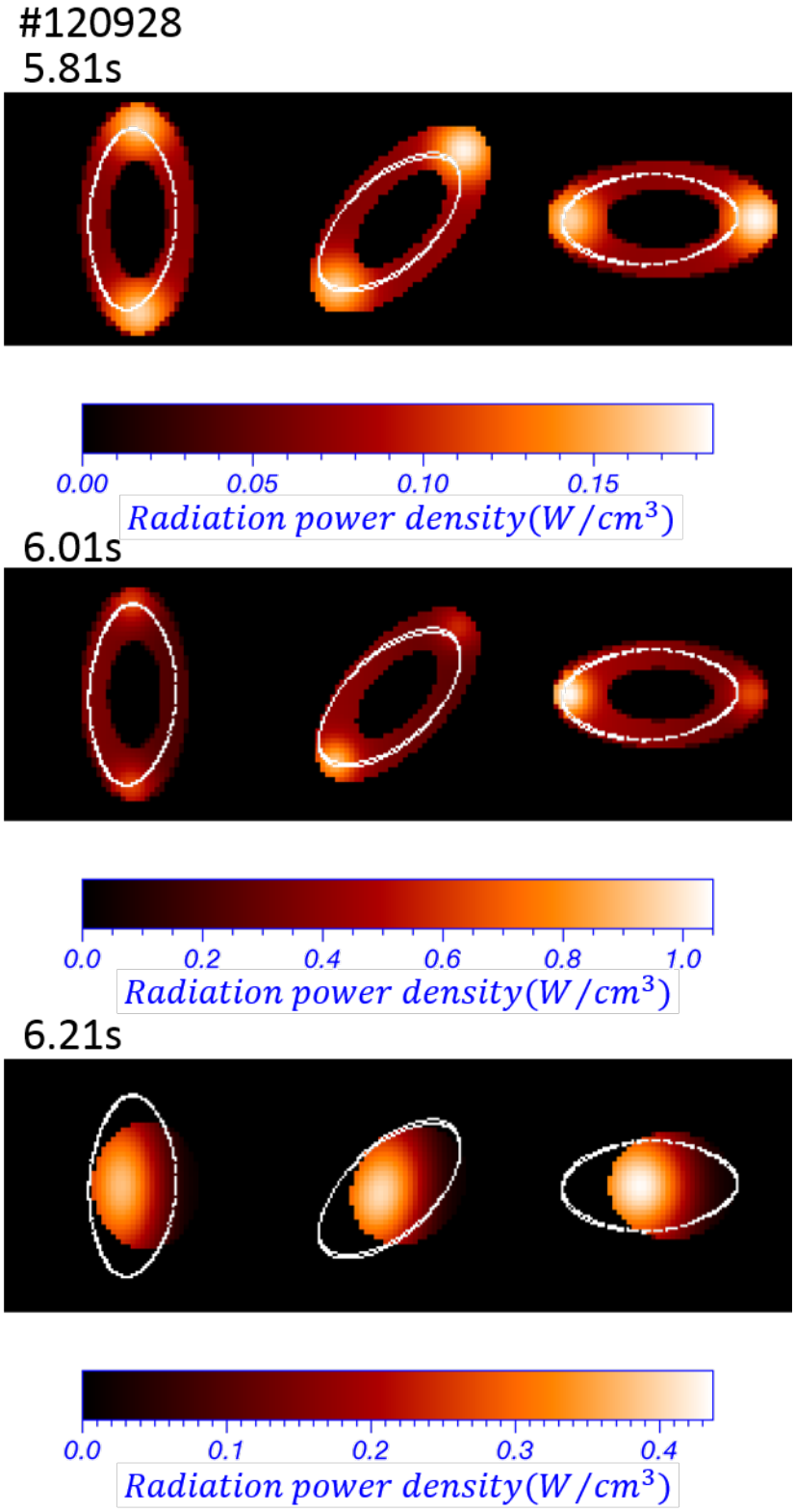

Figure 5.22: Time evolution of 3D model for a collapse discharge (♯ 120928) under the 3.6m magnetic axis configuration.

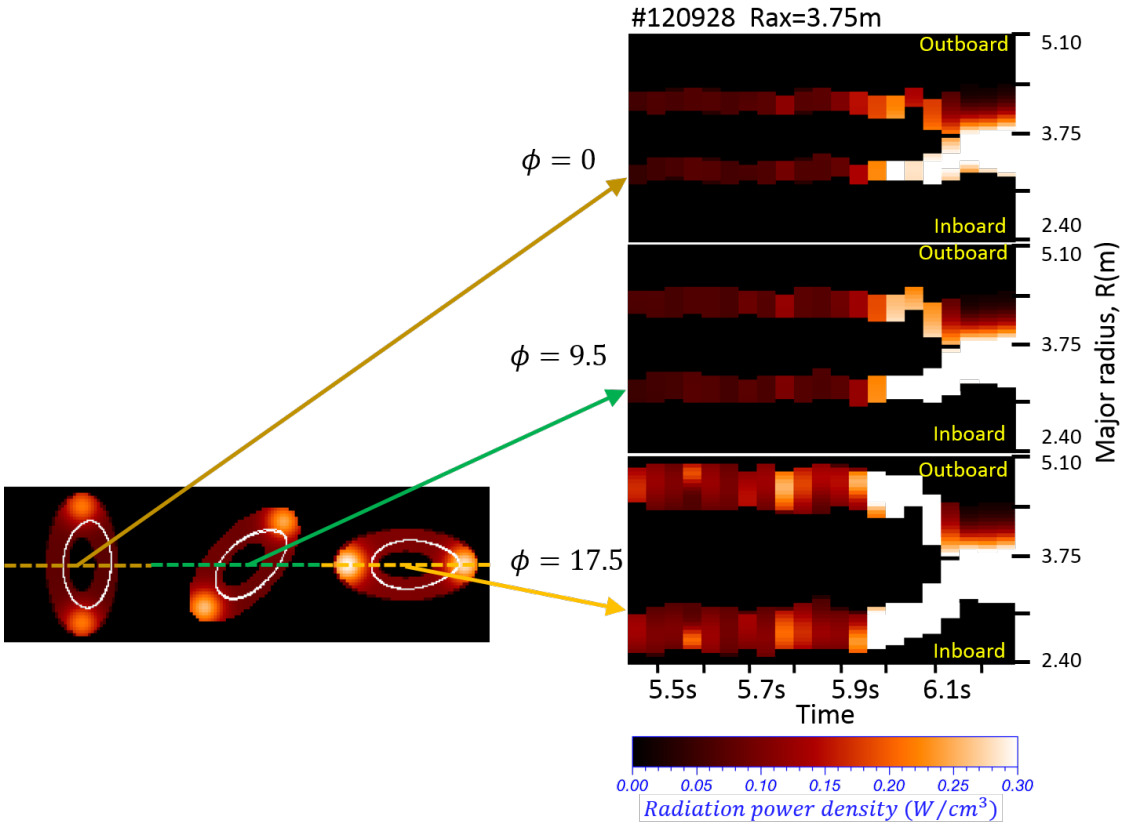

Figure 5.23: Time evolution of 3D model at 0, 9.5, 17.5° poloidal cross sections for a collapse discharge (♯ 120928) under the 3.6m magnetic axis configuration.

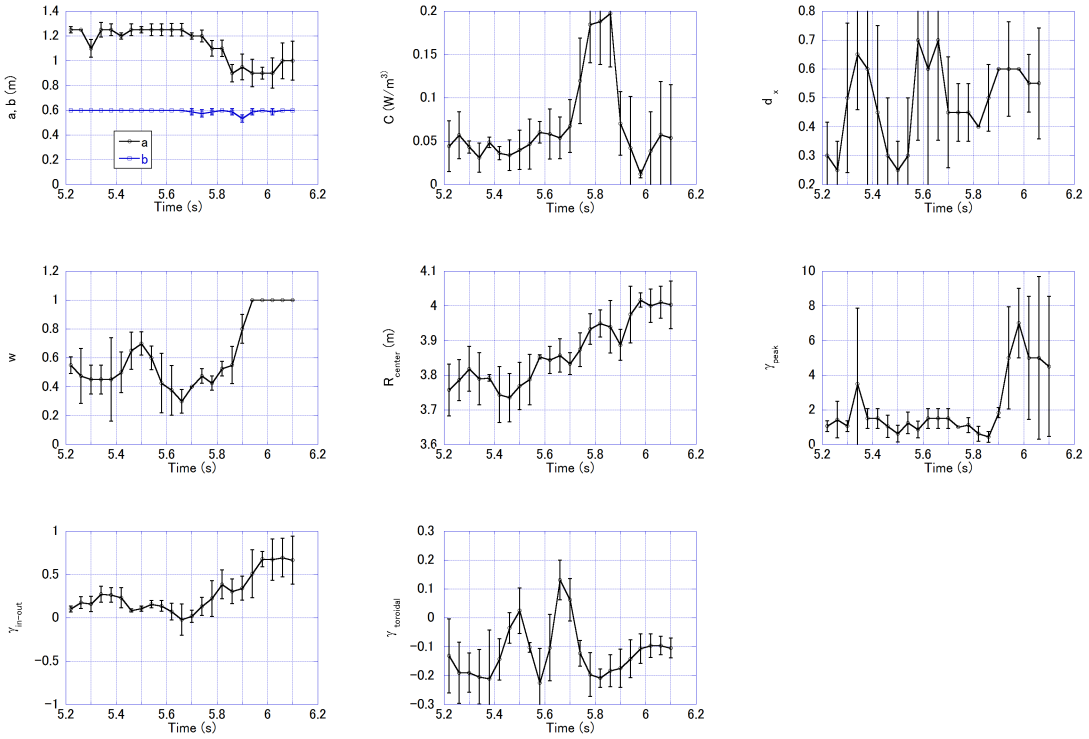

Figure 5.24: Time evolution of obtained model parameters for a collapse discharge (♯ 121835) under the 3.75m magnetic axis configuration.

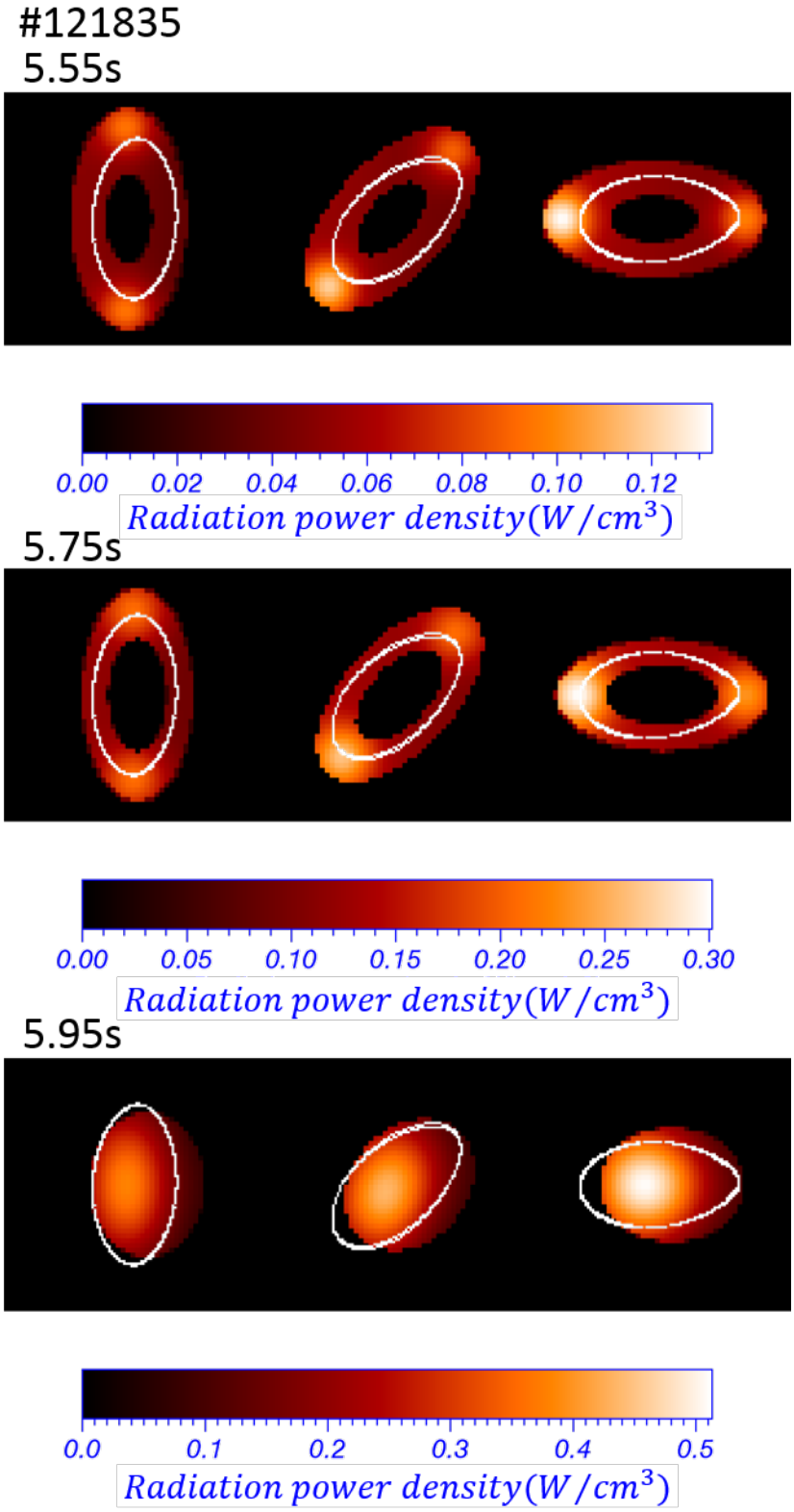

Figure 5.25: Time evolution of 3D model for a collapse discharge (♯ 121835) under the 3.75m magnetic axis configuration.

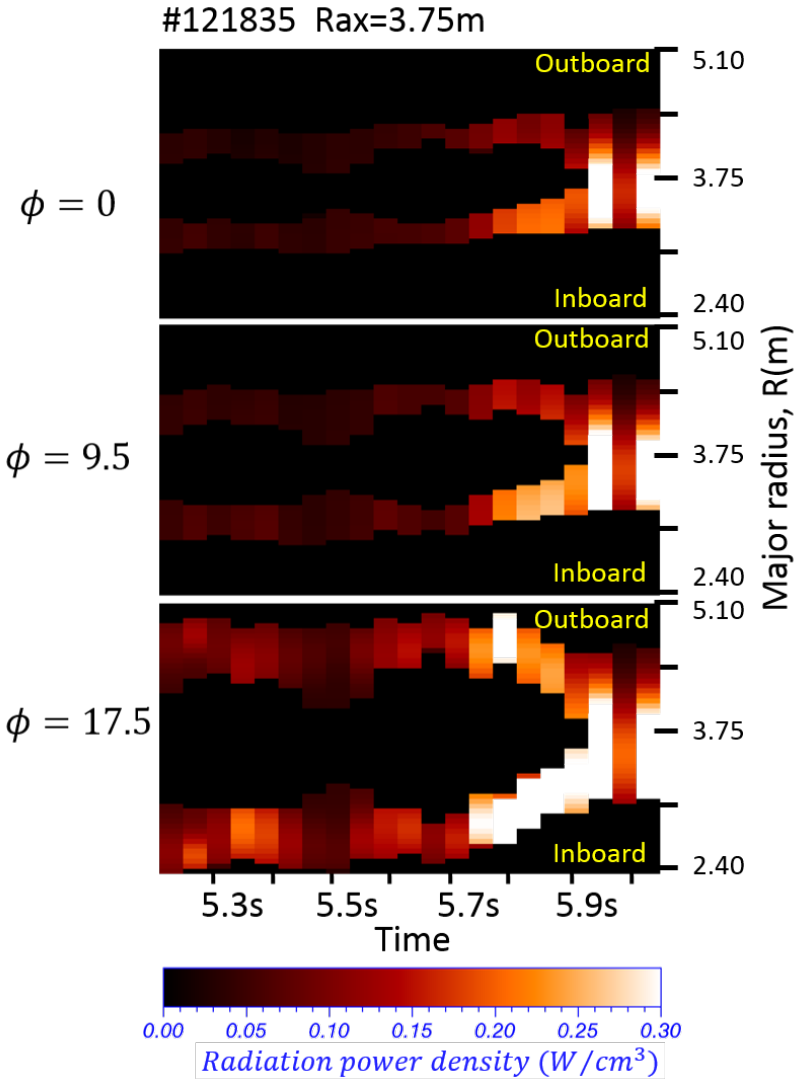

Figure 5.26: Time evolution of 3D model at 0, 9.5, 17.5° poloidal cross sections for a collapse discharge (♯ 121835) under the 3.6m magnetic axis configuration.

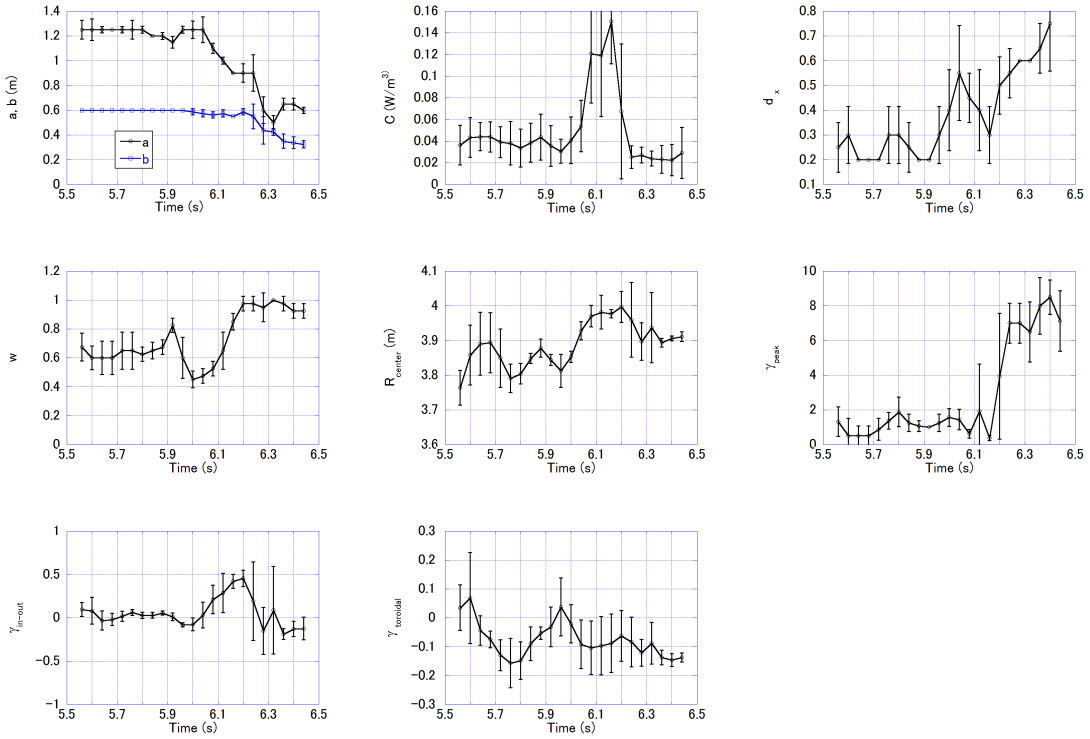

Figure 5.27: Time evolution of obtained model parameters for a collapse discharge (♯ 121787) under the 3.9m magnetic axis configuration.

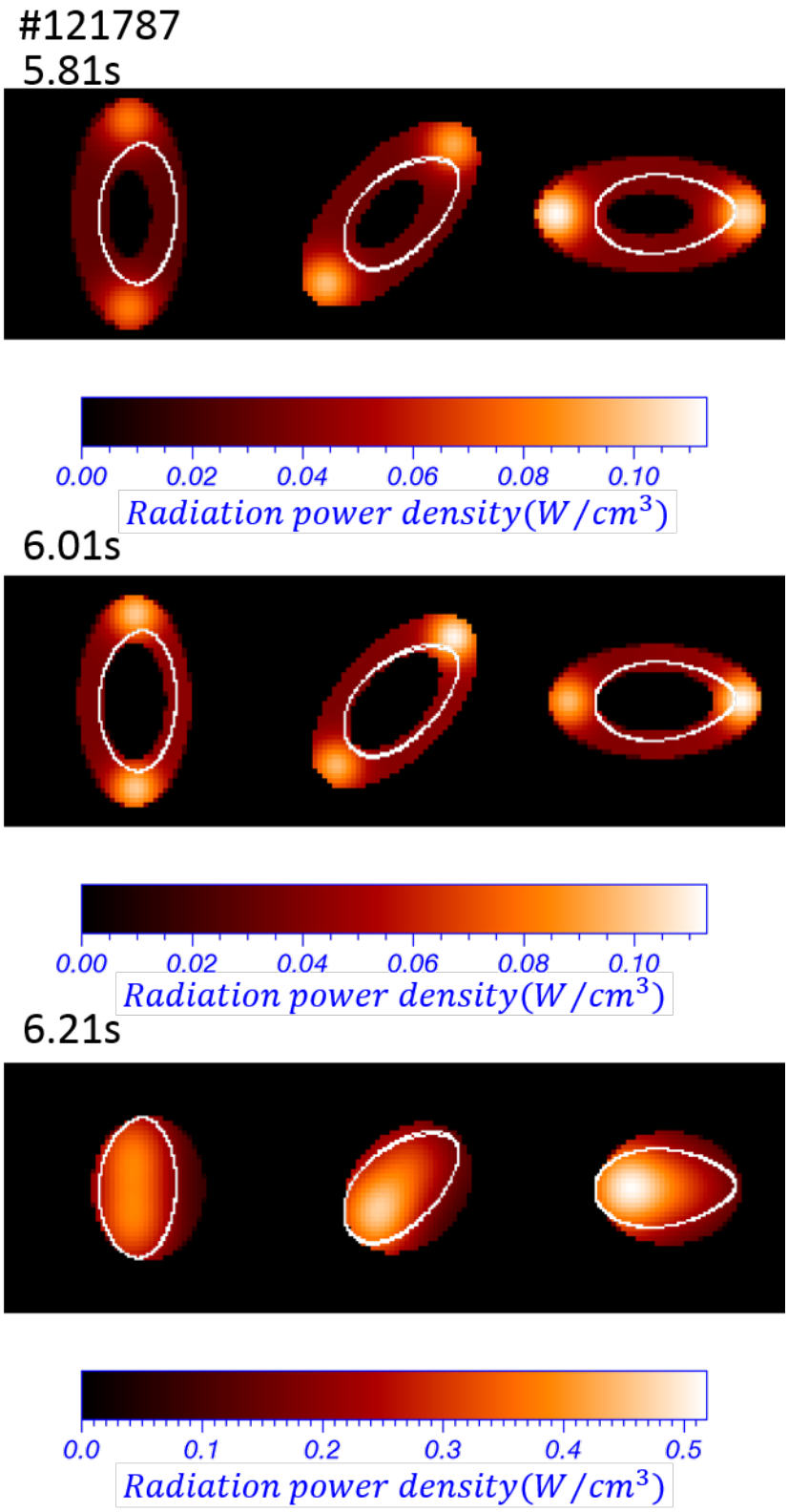

Figure 5.28: Time evolution of 3D model for a collapse discharge (♯ 121787) under the 3.6m magnetic axis configuration.

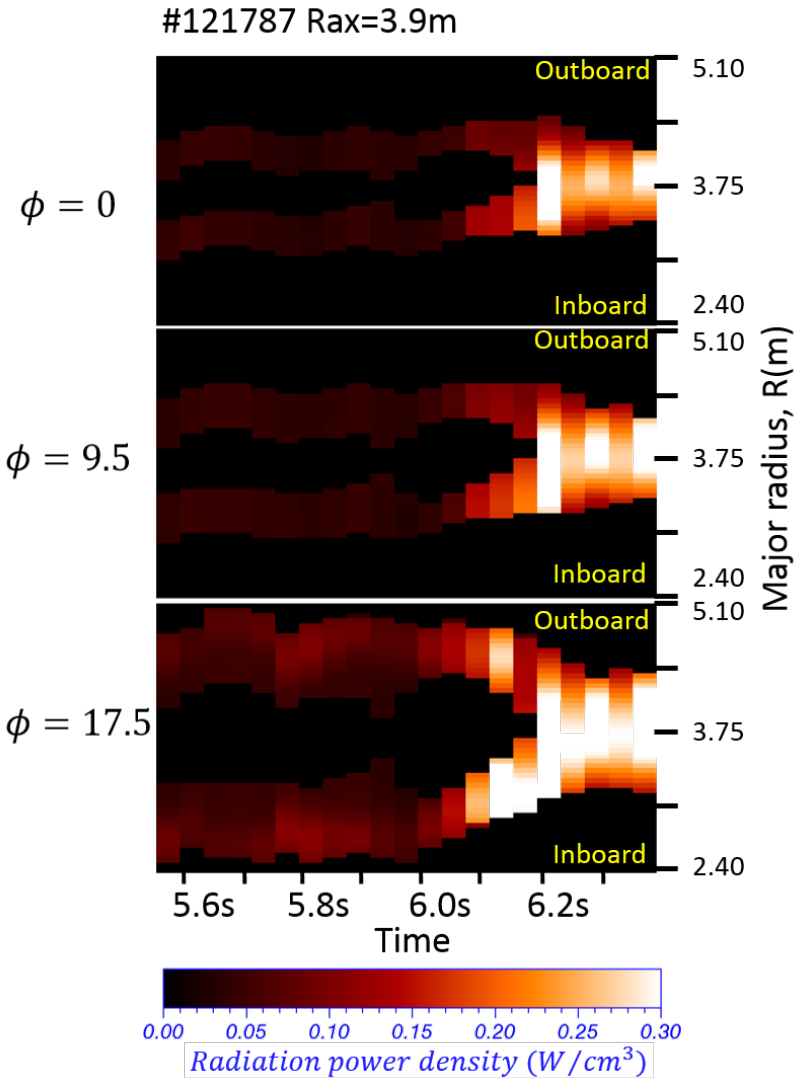

Figure 5.29: Time evolution of 3D model at 0, 9.5, 17.5° poloidal cross sections for a collapse discharge (♯ 121787) under the 3.6m magnetic axis configuration.

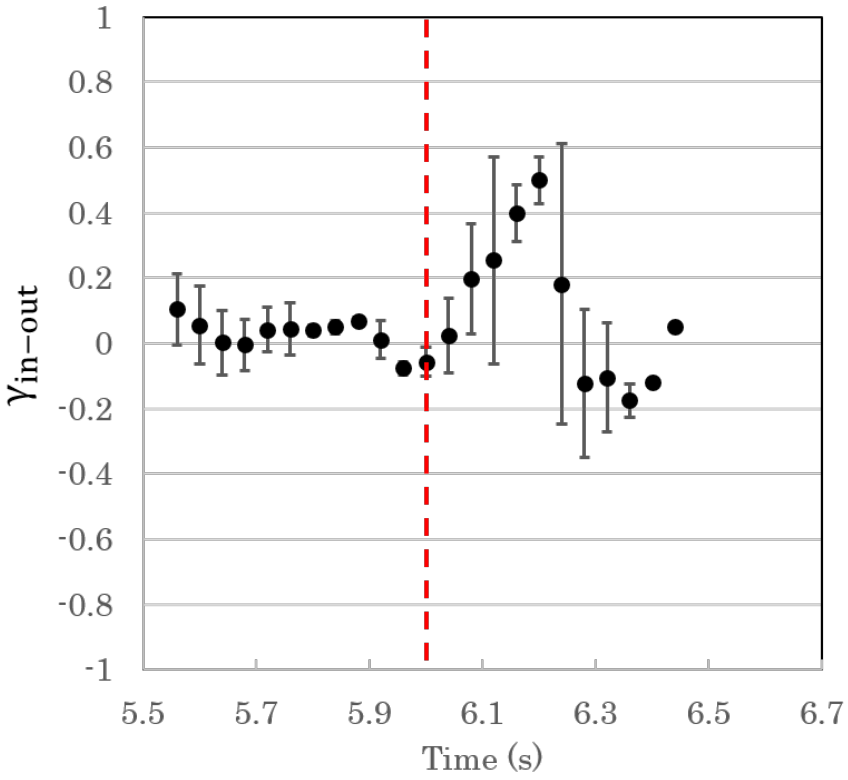

Figure 5.30: Time evolution of width of the radiation region (shot number 121787).

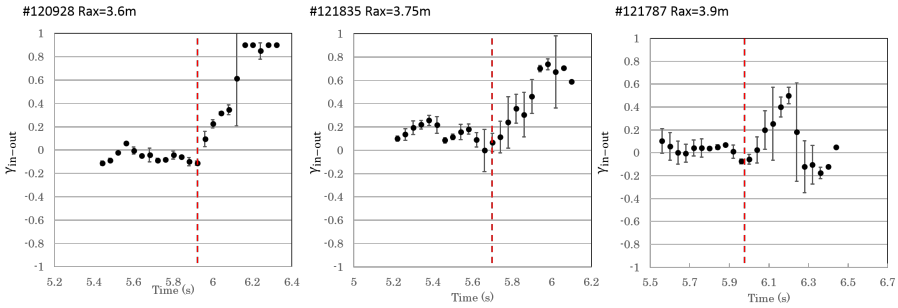

Figure 5.31: Time evolution of asymmetry property with inboard and outboard side (♯120928, ♯121835 ,♯121787). Red line is timing for initiation of inboard enhancement.

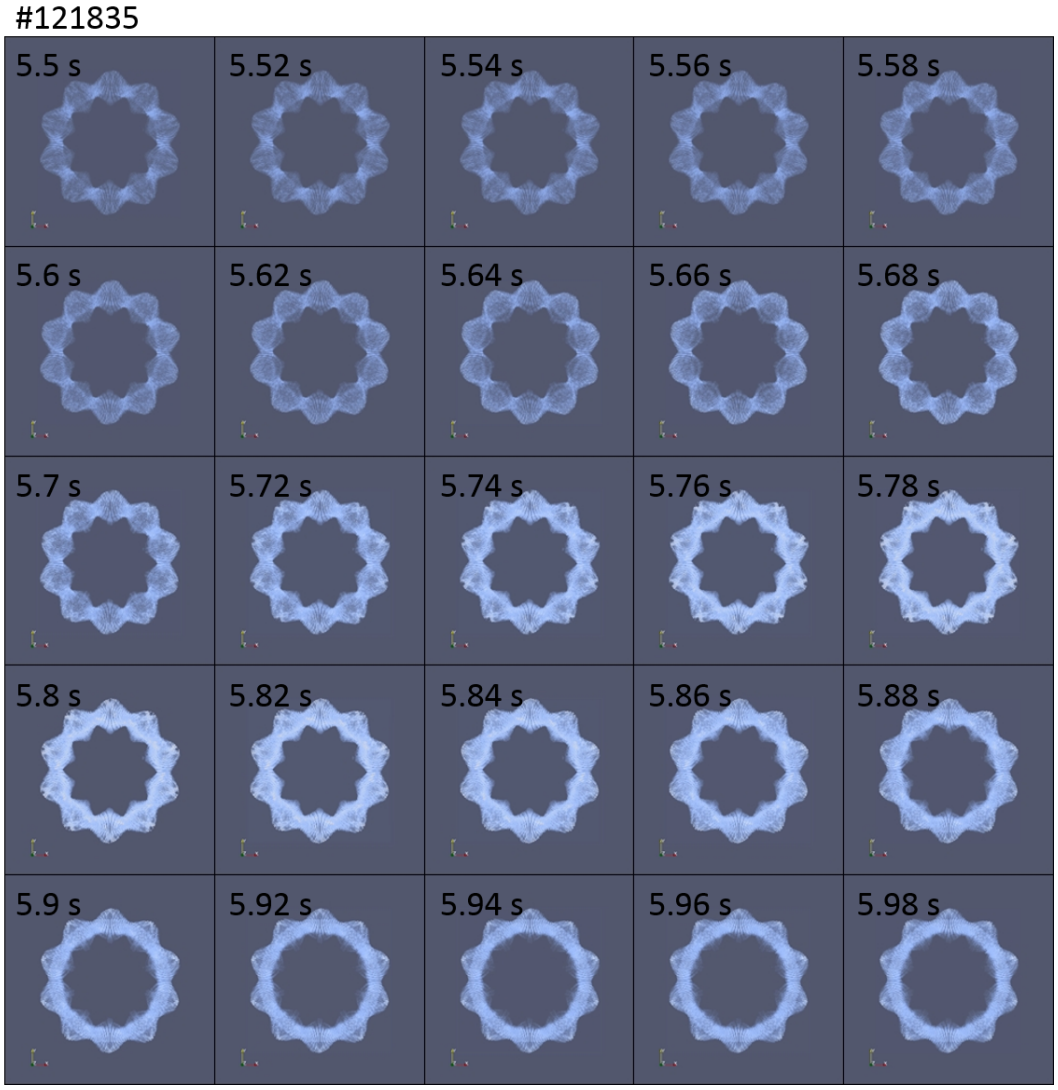

Figure 5.32: Time evolution of reconstructed radiation profile by 3D algebraic inversion (Tikhonov regularization) for a collapse discharge (♯ 121835) under the 3.75m magnetic axis configuration. Point of view is located above torus.

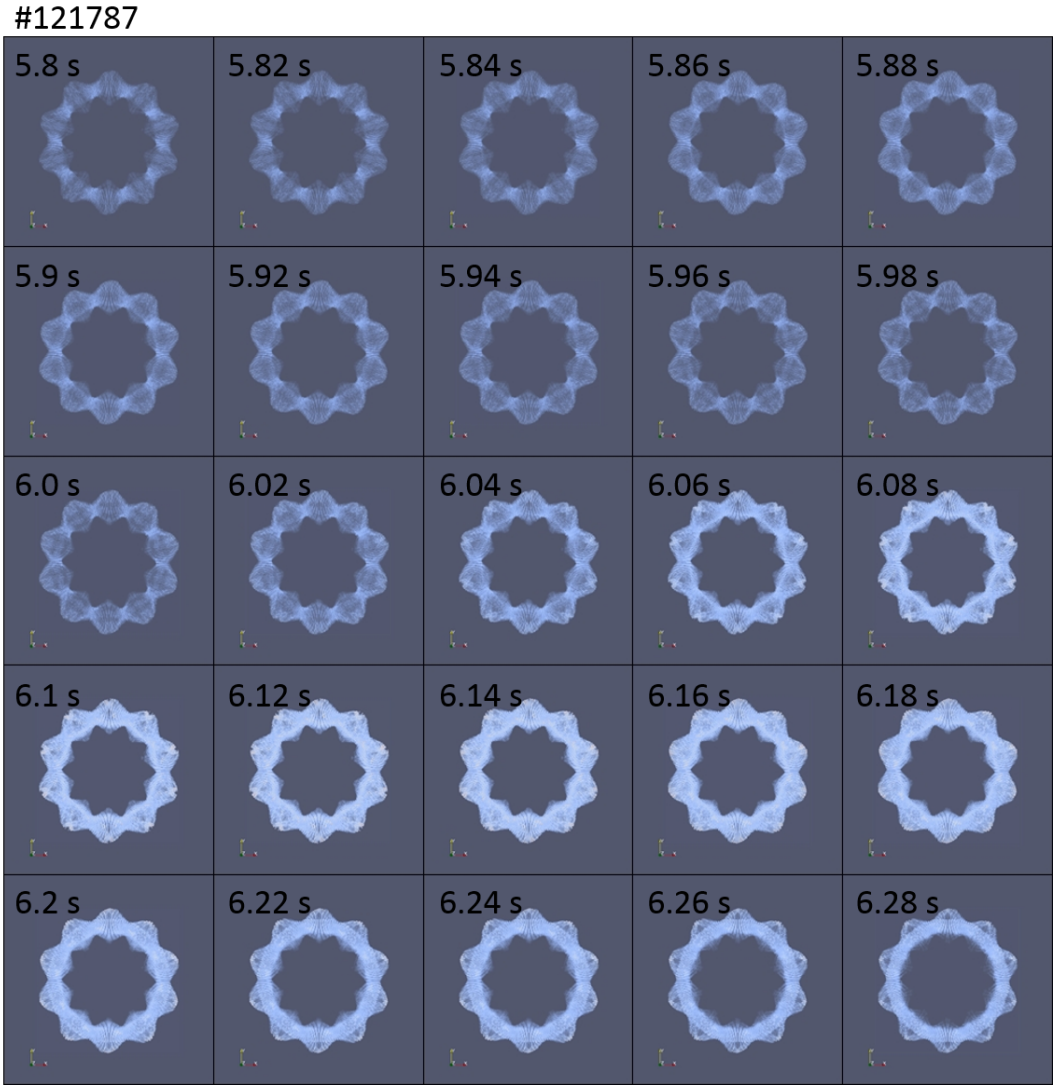

Figure 5.33: Time evolution of reconstructed radiation profile by 3D algebraic inversion (Tikhonov regularization) for a collapse discharge (♯ 121787) under the 3.9m magnetic axis configuration. Point of view is located above torus.

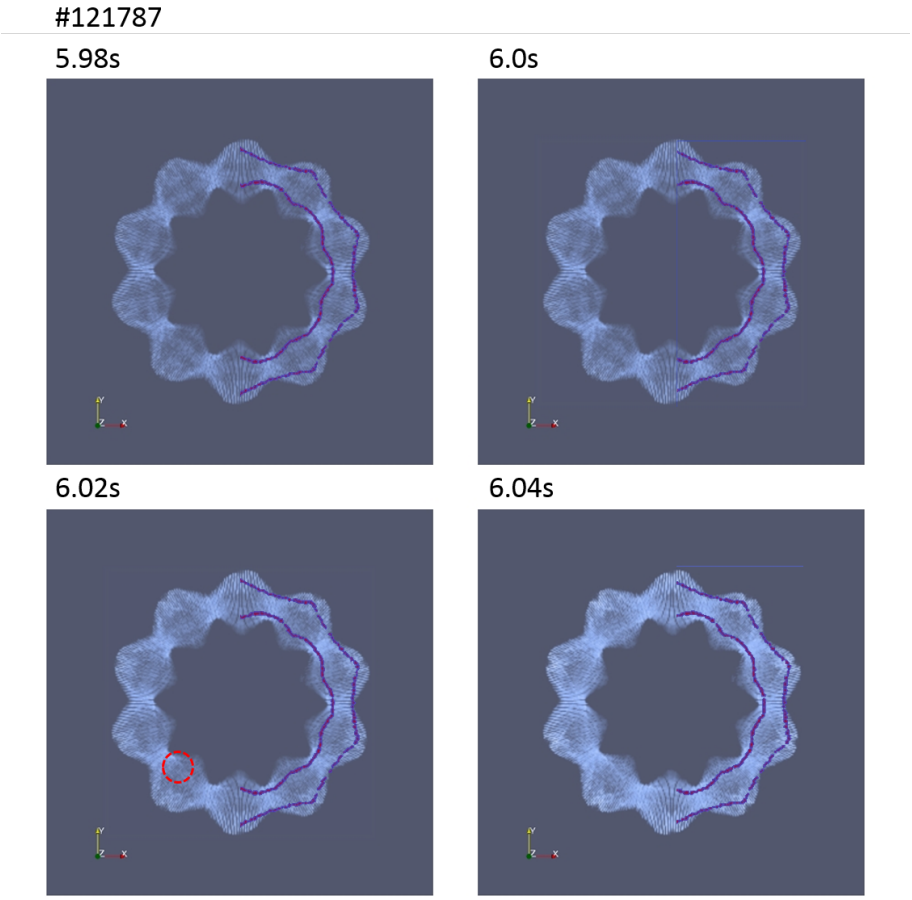

Figure 5.34: Initiation of in-out asymmetry during radiation collapse for a collapse discharge (♯ 121787) under the 3.9m magnetic axis configuration. Red circle is location of extending of inboard enhancement. Point of view is located above torus. Purple lines are LCFS.

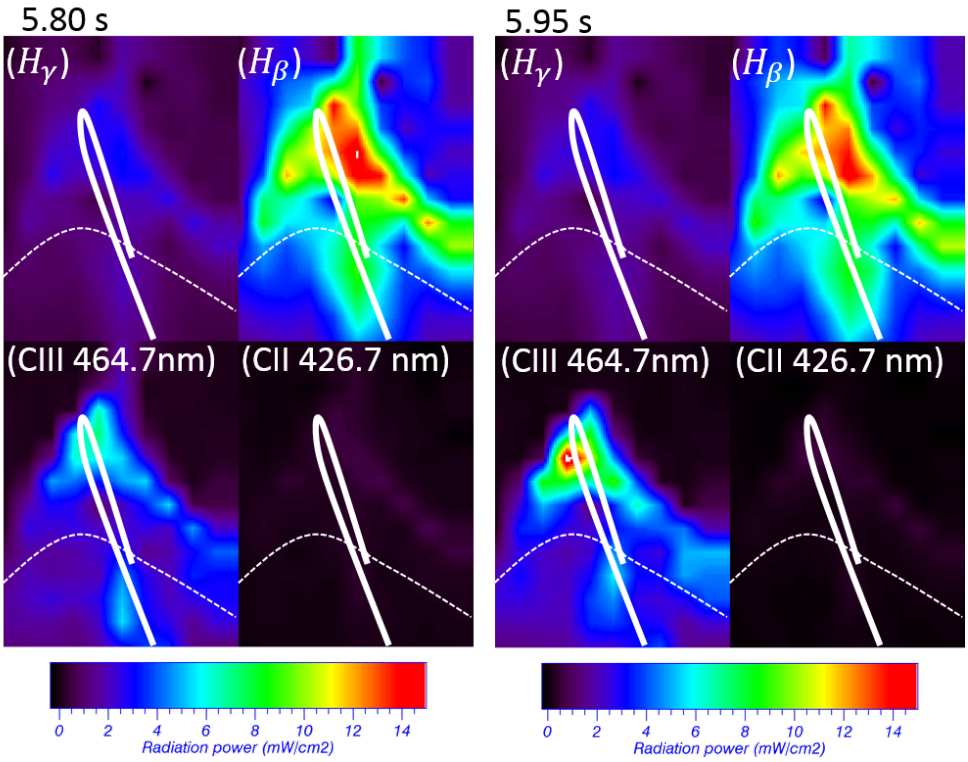

Figure 5.35: Time evolution of $CIII(464.7nm)$, $CII(426.7nm)$, H_γ and H_β emission structure in a collapse discharge (♯ 121787) under the 3.9m magnetic axis configuration. Broken lines are LCFS and solid line is X-point trace.

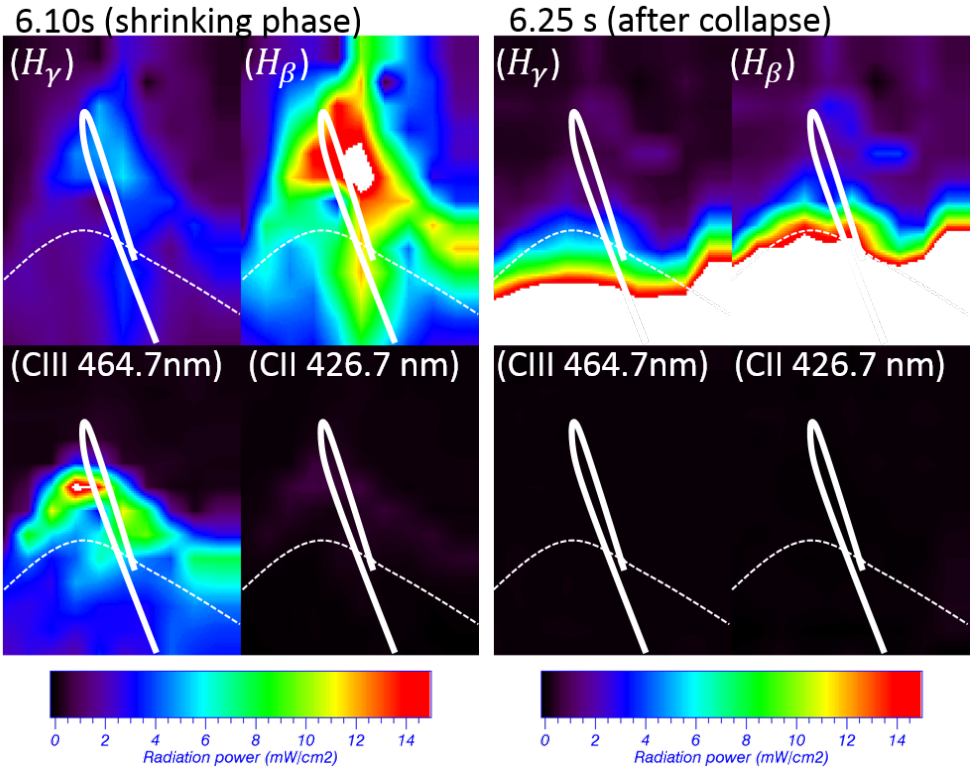

Figure 5.36: Time evolution of $CIII(464.7nm)$, $CII(426.7nm)$, H_γ and H_β emission structure in a collapse discharge (♯ 121787) under the 3.9m magnetic axis configuration. Broken lines are LCFS and solid line is X-point trace.

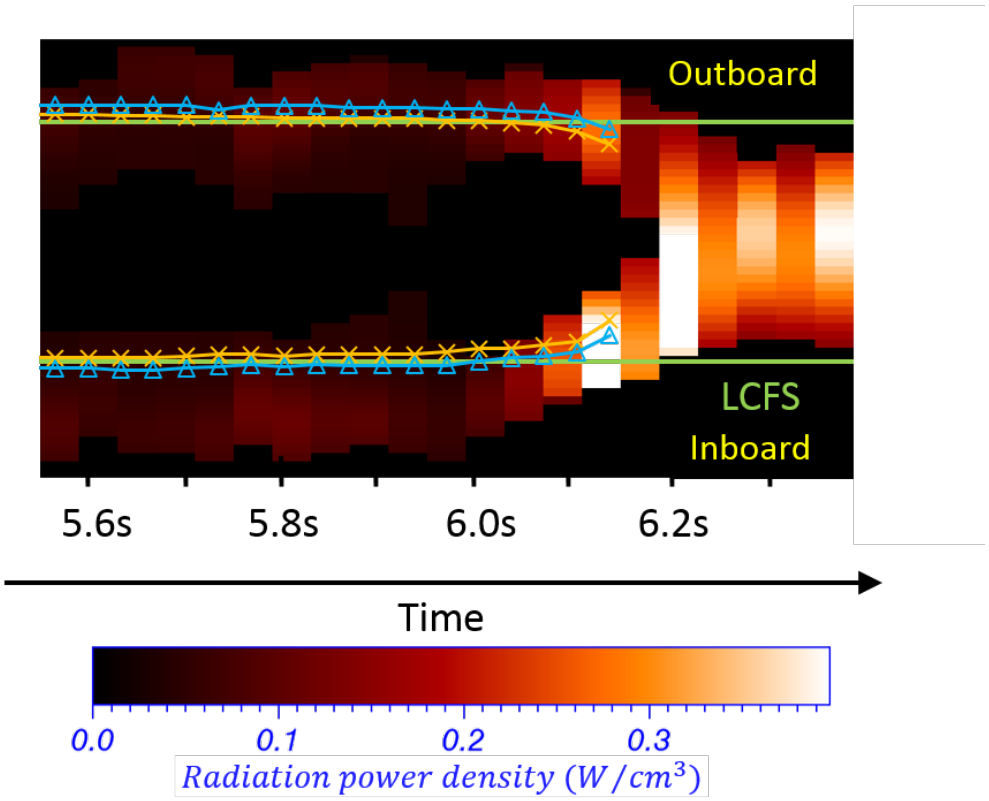

Figure 5.37: Time evolution of model radiation structure and the electron temperature(blue: 100eV, orange: 200eV) at $\phi = 18$.

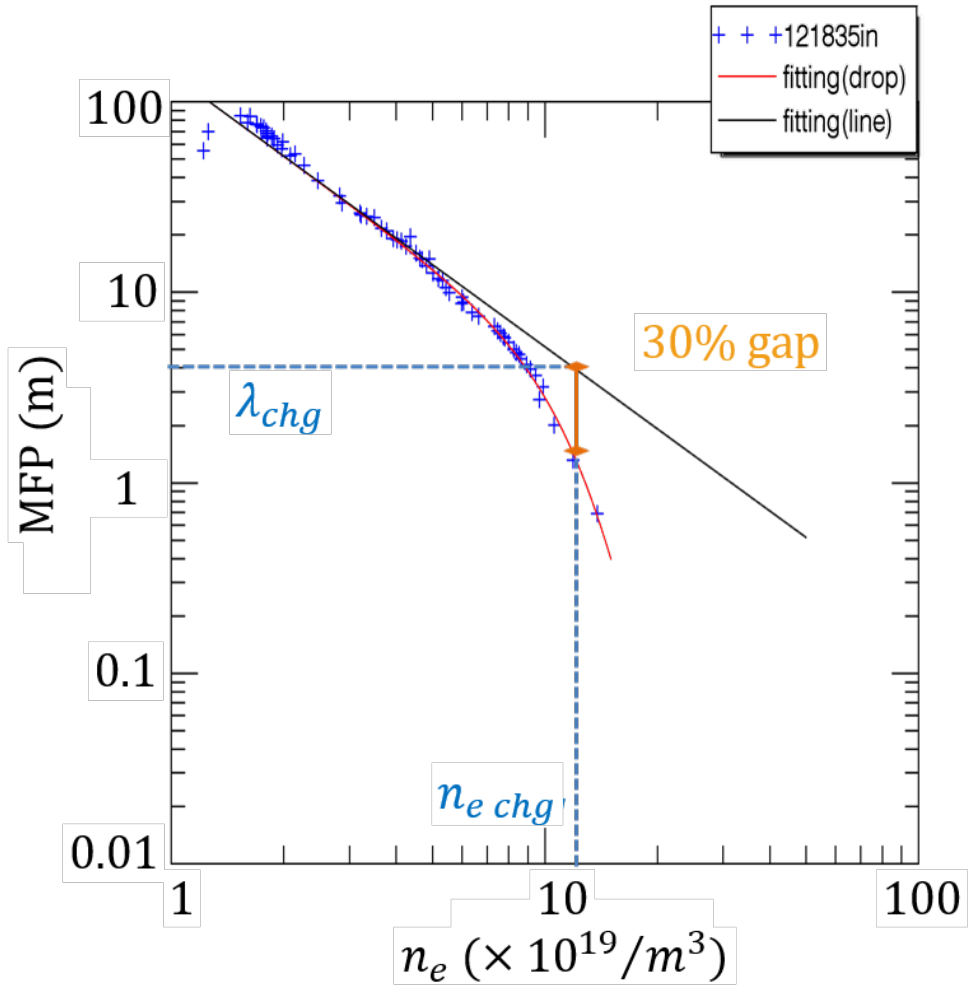

Figure 5.38: Evolution of the mean free path (upper) at the edge which is defined to have 99 percent energy of the plasma. Blue cross is experimental data. Blue line is fitted line for the steady plasma phase. The Red line is the fitted line for the dropping phase. Relation between the mean free path and the electron density at the edge (lower).

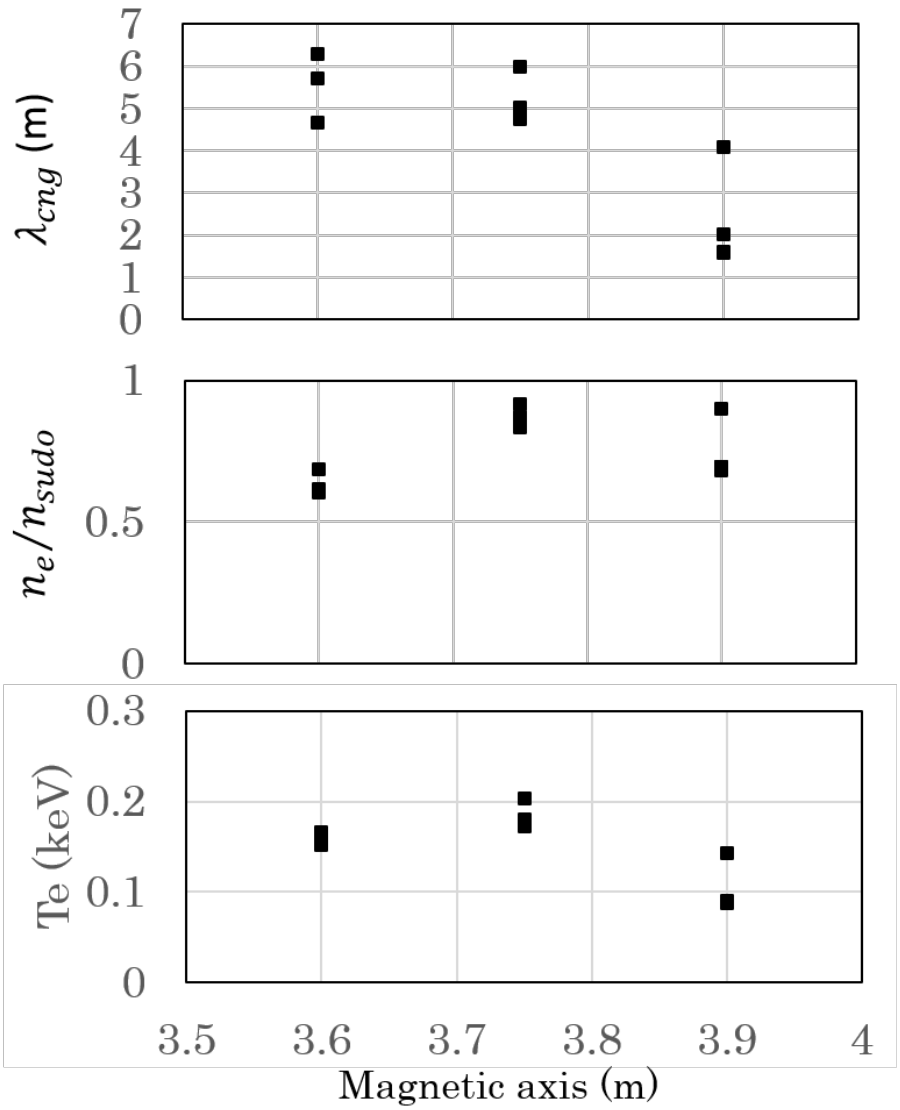

Figure 5.39: The mean free path, $lambda_{e,cng}$ (upper), the normalized electron density (middle) by the Sudo density limit and the electron temperature (lower), from when the relation between the mean free path and the electron density is changed with different magnetic axis configurations.

6 Summary

In this thesis, two 3D tomographic radiation measurements have been developed using improved IRVB measurement.Consequently, 3D tomography measurement of radiation for fusion study has been established for the first time. The measurement results provide a new scenario of radiation collapse.

1 Improvement of the IRVB measurement (foil material selection)

The performance of the IRVB depends on the thermal characteristics of IRVB foil material. To improve the performance of the IRVB measurement, the selection of the foil material has been carried out. In this selection, as the candidates of the foil material, Au, Pt, Ta, W were employed. These candidates were illuminated by a He-Ne laser and their thermal characteristics were evaluated. The evaluation indicated that Pt had the best thermal characteristics and it provides a sensitivity which is twice as large as that of Au which is the prior foil material. Therefore Pt has been selected as the IRVB foil material.

2 Improvement of the IRVB measurement (Development of foil calibration)

The IRVB measurement as an absolute measurement requires the distribution on the foil of 3 foil parameters. However because two of the three parameters, foil thickness and emissivity, had not been evaluated, the IRVB measurement was mainly performed as a qualitative measurement. To evaluate the distribution of the two parameters, a new calibration technique has been developed with comparison between a Finite Element Method (FEM) analysis and the actual foil. The calibration technique evaluates the effective thickness and effective emissivity distribution on the foil. The evaluated distribution of the effective foil thickness and the effective emissivity made possible for the first time a quantitive measurement using an IRVB.

3 Calculation of projection matrix

The 3D measurement requires a 3D knowledge of the relation between each IRVB channels signal and 3D space. To obtain the relation, a projection matrix is calculated with the contribution of the radiation from each plasma volume element to the field of view of each IRVB channel. The fields of view of the IRVBs are designed to have complete coverage of the plasma using the calculated projection matrix.

4 Tikhonov regularization

As a 3D tomographic radiation measurement, 3D reconstruction with Tikhonov regularization with the statistical criterion of minimum GCV has been carried out with s huge and complicated helical geometry, and applied to a plasma measurement for the first time. The reconstruction has been numerically and experimentally examined. The simulated radiation profile using the EMC3-EIRENE code has been used as a numerical phantom in a numerical test of the reconstruction and has been reproduced with the reconstruction process. In reconstruction tests with experimental data which are taken before and after the plasma collapse, reconstruction results have responded to changes in the plasma condition.

5 3D function model fitting

To evaluate the characteristics for the evolution of the 3D radiation structure which are difficult to evaluate with the Tikhonov regularization result, a 3D function model fitting has been developed. The model for the model fitting has been designed with consideration of the radiation shape, as well as inboard-outboard, local peaking and toroidal asymmetries. Model parameters are optimized with a criterion of minimum mean square error between an experimental IRVB image and a synthetic IRVB image which is calculated from the model. The model fitting quantifies the radiation structure changes as changes in nine model parameters.

6 Elucidation of radiation structure evolution during radiation collapse

The developed 3D measurements have been applied to measurements of radiation collapse. The 3D model fitting provides information on the global evolutions in the radiation structures and their timing. More detailed evaluation for the evolution by the reconstruction with Tikhonov regularization has been carried out. Several events during the radiation collapse evolution have been observed from these measurement. Especially, these measurements indicate that toroidal and inboard-outboard asymmetries of the radiation structure play important roles during radiation collapse. The radiation structure can be seen from any view points and cross sections by 3D measurements. Comparison between Thomson scattering measurement data and the measured 3D radiation structure indicates that these obtained events are related to the electron temperature and the mean free path of the electron. When the mean free path at the plasma edge drops below a liner dependence on density which depends on the confinement of plasma, the mean free path suddenly drops and then the paralell transport becomes low. As a result, the growing of the asymmetries is possible and then radiation collapse occurs. By relating these events, a scenario for the radiation collapse has been obtained. That is the main result of this thesis. The developed 3D measurement techniques and improvement in the IRVB will also be applicable in the future to enhancing the understanding of radiation collapse and other radiation phenomena.

Acknowledgements

First of all, the author would like to express his appreciation to Professor B. J. Peterson and Associate professor Junichi Miyazawa who have been greatly tolerant and supportive throughout my graduate study at the National Institute for Fusion Science (NIFS) and the Graduate University for Advanced Studies (SOKENDAI), Department of Fusion Science.

The author would like to gratefully acknowledge Associate Professor Masahiro Kobayashi for his providing the simulated data. The author also gratefully acknowledges Professor Naofumi Iwama of NIFS, Associate Professor Masaru Teranishi of Hiroshima Institute of Technology and Professor Yousuke Hosoda of Fukui University for significant suggestions and discussion about tomography. The author is particularly grateful for the assistance given by Dr. Kiyofumi Mukai of NIFS and Dr. Shwetang Pandya of Institute for Plasma Research (formerly of SOKENDAI) for discussion and suppot of the experiment. The author also gratefully thanks Professor Suguru Masuzaki, Associate Professor Gen Motojima, Associate Professor Tsuyoshi Akiyama and the LHD experimental group of NIFS for their kind support of my experiment. The author would like to express my gratitude to Mr. Haruki Kojima of NIFS for support in understanding with CAD drawings. The author is deeply grateful to Mr. Hiromi Hayashi, Mr. Yasuyuki Tuchibushi, Dr. Takashi Kobuchi, Mr Kouji Okada and Mr. Teruki Nishimura for support in the manufacture of IRVB compornents and installation of IRVBs. The author also gratefully acknowledge Professor Tomoaki Hino, Associate Professor Yuji Yamauchi and Dr. Yuji Nobuta of Hokkaido University for their support of the collaboration study and encouragement. The author would like to express my gratitude to Dr. Shigeru Konoshima for significant suggestions. The author thanks Professor Hiroshi Yamada for serving as the head of the thesis examination committee and smoothly guiding process me through the examination. The author also gratefully thanks Mr Muneji Itomi for discussion and support of experimental data taking. Funding from the JSPS scholarship Foundation is gratefully acknowledged.